

LIISA-IDA SORSA

Full-Wave Radar Tomography of Complex, High-Contrast Targets

Imaging the Interior Structure
of a Small Solar System Body

LIISA-IDA SORSA

Full-Wave Radar Tomography
of Complex, High-Contrast Targets

Imaging the Interior Structure
of a Small Solar System Body

ACADEMIC DISSERTATION

To be presented, with the permission of
the Faculty of Engineering and Natural Sciences
of Tampere University,
for public discussion in the auditorium TB209
of the Tietotalo building, Korkeakoulunkatu 1, Tampere,
on 29 October 2021, at 12 o'clock.

ACADEMIC DISSERTATION

Tampere University, Faculty of Engineering and Natural Sciences
Finland

*Responsible
supervisor
and Custos*

Associate Professor
Sampsa Pursiainen
Tampere University
Finland

Pre-examiners

Associate Professor
Amélie Litman
Fresnel Institute
France

Professor
Paul Sava
Colorado School of Mines
USA

Opponent

University Researcher
Anne Virkki
University of Helsinki
Finland

The originality of this thesis has been checked using the Turnitin OriginalityCheck service.

Copyright ©2021 author

Cover design: Roihu Inc.

ISBN 978-952-03-2126-0 (print)

ISBN 978-952-03-2127-7 (pdf)

ISSN 2489-9860 (print)

ISSN 2490-0028 (pdf)

<http://urn.fi/URN:ISBN:978-952-03-2127-7>

PunaMusta Oy – Yliopistopaino
Joensuu 2021

PREFACE

The research presented in this thesis was carried out in the inverse problems research group in the Computing Sciences Unit in the Faculty of Information Technology and Communication Sciences at Tampere University Hervanta Campus. I am grateful for the funding received from Academy of Finland through the Centre of Excellence in Inverse Modelling and Imaging 2018-2025 (project number 312341), and Academy of Finland ICT 2023 programme (FETD-Based Tomographic Full-Wave Radar Imaging of Small Solar System Body Interiors, project number 336151). I am also grateful to Emil Aaltonen Foundation for the young researcher's grant awarded to me in 2020, covering the funding for the final year of this thesis. I would also like to mention the financial support given by Tampere University Library for covering the article processing charges for open access publishing of the Publications IV and VI of this thesis.

I would like to express my deepest appreciation to my supervisor, Associate Professor Sampsa Pursiainen for the invaluable advice and encouragement throughout this process. This thesis is a continuation of the work he has started over six years ago and the forward simulations and inversion computations presented in this thesis were carried out by the methods he has developed over the years.

I am deeply grateful to my pre-examiners Professor Paul Sava and Associate Professor Amélie Litman for accepting the task and taking the time to evaluate this work. I would also like to sincerely thank University Researcher Anne Virkki for dedicating her time to serve as my opponent in the coming public examination of this thesis.

I am extremely grateful to Associate Professor Christelle Eyraud and her group for the close collaboration we started in late 2018, including a visit to Fresnel Institute in Marseille, France, in November 2018, leading to Publications III-VI of this thesis. The collaboration between our group, Prof. Eyraud and Dr. Jean-Michel Geffrin led to major advances in validating the time and frequency domain solvers for experimental asteroid analogue microwave radar measurements. I am also grate-

ful to Prof. Alain Hérique for the valuable discussions on space missions and the Juventas Radar experiment, providing the context to the work of this thesis.

I would also like to extend my sincere thanks to all my co-authors for the collaboration and support during this project. Special thanks to Dr. Jakob Deller, Dr. Esa Vilenius, Dr. Jessica Agarwal, and Mr. Patrick Bambach for welcoming me to Max Planck Institute for Solar System Research in Göttingen, Germany, for a visit in February-March 2019. The opportunity to participate in the development of the AI3 – Asteroid Interior Investigation 3-way mission proposal for the European Space Agency’s first Fast Class mission call during my stay in Göttingen was an invaluable experience in setting the context for the numerical work we had done so far, and providing an outlook for the research in the future. This collaboration also led to the Publications I and II.

Finally, I want to thank my family and friends for everything that is outside of the world of science.

Hämeenkyrö, 9 September 2021

Liisa-Ida Sorsa

ABSTRACT

Full-wave radar tomography of complex small solar system bodies, such as asteroids, presents a challenging mathematical and computational inverse problem starting from the selection of the method of how to compute the forward problem of wave propagation through the target domain, and continuing to the selection of the appropriate inversion technique. The challenge is further augmented when such tomographic measurement is conducted in deep space with radar-carrying satellites with limited power supply and positional control. This leads to a set-up in which data can be measured in a sparse measurement configuration, and there are a number of possible sources of error starting from the ambiguity of the exact measurement position and orientation, and continuing to the measurement noise caused not only by the instrument but also the cosmic radiation environment.

The aim of this thesis is to advance the mathematical and computational methods for full wave radar tomography by applying the finite element time domain (FETD) method to compute wave propagation in realistic asteroid interior models built inside the shape of the asteroid Itokawa. Tomographic reconstructions of the simulated forward data are computed with the total variation inversion procedure, which is shown to detect the deep interior details such as voids, cracks, boulders, and low contrast details within the asteroid model. Higher-order Born approximation was formulated and implemented to the 2D FETD solver to investigate the effect of the higher-order scattering and measurement configuration on the quality of the reconstructions. To validate the numerical results with the Itokawa model, permittivity-controlled asteroid analogues were manufactured to compare the simulation results to laboratory measurements with microwave radar on the same target shape and structure. The computational tools to model wave propagation in the 2D and 3D target domains, and a toolbox to create a wireframe structure with controlled permittivity distribution for 3D-printing, were published as open source software packages.

The numerical results show that a low-frequency tomographic radar can detect deep interior details inside a realistic asteroid interior model with the shape and size of the asteroid Itokawa, in which the largest dimension is 535 meters. The bistatic and multistatic measurement configurations provide more robust reconstructions in comparison to the monostatic case. The laboratory experiment was designed to investigate a 5 MHz centre frequency and 2 MHz bandwidth radar for an Itokawa-sized target. Based on the results, the simulations model the measured time domain signal well, and the interior details can be detected in the locations predicted by wave traveltimes, giving evidence that numerical simulations can be used to model the real measurements in such a target. Furthermore, it was shown that even a single-point backprojection of the measured data can reveal interior details such as a void.

The current methodology and computational resources can model the full-wave radar tomographic problem for low frequency radars operating at 10 MHz for a target of size 260 meters, or 20 MHz for a target which size is approximately 130 meters. To increase the target size, the memory requirement for the computations may present a limit depending on the available high-performance computing resources. Increasing the measurement frequency to 50-60 MHz would require refining the finite element mesh to increase the accuracy of the forward modelling stage. This would also increase the system size and hence memory requirement, and requires specialised high-performance computing resources and further development of the presented solvers to fully utilise the now available and developing high-performance computing capacity.

TIIVISTELMÄ

Muodoltaan epäsäännöllisten pienten taivaankappaleiden, kuten asteroidien, koko aallon tutkatomografiasovellus on monimutkainen matemaattinen ja laskennallinen inversio-ongelma. Sitä varten on valittava sopiva menetelmä, jolla simuloidaan suora malli eli aallon kulku kohteen sisällä. Lisäksi tarvitaan inversiomenetelmä, jolla voidaan laskea suoran mallin datan perusteella rekonstruktio kohteen sisäosan rakenteelle. Haastetta lisää asteroidikuvantamiseen läheisesti liittyvät rajoitteet siitä, että tutkamittaus suoritetaan avaruudessa satelliiteilla, joilla on käytössään rajattu määrä energiaa. Lisäksi niiden tarkkaa sijaintia ja suuntausta on vaikea ohjata. Tämän vuoksi tutkatomografiset mittaukset tuottavat harvan mittapistekonfiguraation eli kyseessä on myös rajoitetun datan ongelma. Lisäksi mittaukseen liittyy useita virhelähteitä, joista mittapisteen tarkkaan sijaintiin liittyvät ovat vain ensimmäiset. Mittalaitteen kohinan lisäksi mittausympäristössä on kosmista säteilyä, joka voi vaikuttaa heikkoihin tutkasignaaleihin.

Tämän tutkimuksen tarkoitus on edistää koko aallon tutkatomografian matemaattisia ja laskennallisia menetelmiä. Työssä käytetään aikatason elementtimenetelmää (*finite element time domain*, FETD) laskemaan aallon eteneminen realistisen kohdeasteroidimallin sisällä. Tämä malli perustuu Itokawan muotomalliin ja sen sisälle on rakennettu olemassa olevan tiedon perusteella permittiivisyysjakauma. Datatutkimukset lasketaan kokonaisvariaatiomenetelmällä, jonka toimivuus tähän sovellukseen näytetään vertaamalla saatuja rekonstruktioita alkuperäiseen tarkkaan jakamaan. Korkeamman kertaluokan sironnan vaikutusta rekonstruktioihin tutkittiin implementoimalla korkeamman asteen Bornin approksimaatio kaksiuolitteiseen FETD-ratkaisijaan. Samalla tutkitaan mittauskonfiguraation vaikutusta rekonstruktioiden laatuun. Itokawa-mallilla tehtyjen laskennallisten tulosten validointia varten kehitettiin menetelmä valmistaa 3D-tulostimella laskennallista mallia sekä muodoltaan, rakenteeltaan että sähköisiltä ominaisuuksiltaan vastaava pienoismalli, jota tutkittiin laboratoriossa tomografisella mikroaaltotutkalla. Näin saatuja laboratoriomit-

taustuloksia voitiin verrata laskennalliseen dataan. Työssä käytetyt laskentatyökäluut, joilla aaltopropagaatiota voidaan mallintaa 2D- ja 3D-alueissa sekä valmistaa pienoismalli valmistusta varten, julkaistiin avoimen lähdekoodin ohjelmistopaketteina.

Laskennalliset tulokset osoittavat, että matalataajuuksinen tomografinen tutka voi havaita asteroidin sisärakenteen onkalot, halkeamat, tiheät lohkarieet ja hyvin huokoiset yksityiskohdat muodoltaan monimutkaisessa, asteroidi Itokawan muotoon perustuvassa ja vastaavan kokoisessa (535 metriä) asteroidissa. Bistaattinen ja multistaattinen mittauskonfiguraatio johtavat luotettavampaan rekonstruktioon monistaattiseen mittaukseen verrattuna. Laboratoriomittauksella tutkittiin erityisesti Itokawa-kokoisen kohdeasteroidin tomografiaa tutkalla, jonka keskitaajuus oli 5 MHz and kaistanleveys 2 MHz. Kokeellisen ja laskennallisen datan vertailun perusteella laskennallinen data mallintaa mitattua aikatazon tutkasignaalia hyvin. Signaalista voidaan erottaa signaalin matka-ajan avulla jokainen mallin sisärakenteen kohta, joten simulaation avulla voidaan saada luotettavia tuloksia signaalin kulusta kohteen sisällä. Lisäksi näytetään, että käyttämällä vain yhdenkin pisteen takaisinprojektiota, on mahdollista saada kohtuullinen rekonstruktio, josta sisäosien onkalo voidaan havaita.

Tässä työssä käytetyillä menetelmillä ja nykyisillä laskentaresursseilla voidaan simuloida koko aallon tutkatomografinen ongelma matalataajuuksisella tutkalla sellaiselle tapaukselle, jossa tutkan keskitaajuus on 10 MHz ja kohteen koko noin 260 metriä, tai tapaukselle jossa tutkan taajuus on 20 MHz and kohteen koko on noin 130 metriä. Mikäli kohteen kokoa halutaan kasvattaa, ongelman koko ja sitä kautta vaatimus laskentamuistin määrälle kasvaa yli työtä tehdessä käytössä olleen laskentakapasiteetin. Tutkan keskitaajuuden kasvattaminen 50-60 MHz:iin vaatisi lisäksi käytetyn elementtiverkon tihentämisen näille taajuuksille sopivammaksi, jolloin ongelman koko kasvaisi jälleen. Myös tällöin vaatimus teholaskennan entistä suuremmalle muistiresurssin käytölle kasvaa. Kehittämällä edelleen tässä työssä käytettäviä ratkaisijoita sopivaksi nykyisille ja tuleville teholaskentateknologioille, voidaan simuloida myös korkeampia taajuuksia ja suurempia ongelmia.

CONTENTS

1	Introduction	17
1.1	Background	17
1.2	Objectives	20
1.3	Summary of the original publications	20
1.4	Organisation of the thesis	23
2	Radar tomography with time domain signals	25
2.1	Electromagnetic wave propagation in material	25
2.1.1	Maxwell's equations	25
2.1.2	Time-harmonic forms of Maxwell's equations	27
2.2	The forward model	30
2.2.1	Evaluation of wave propagation in a domain	32
2.2.2	Born approximation and higher-order scattering	34
2.2.3	Discretisation of the forward problem	35
2.2.4	Formulation of the higher-order Born approximation	38
2.2.5	Multiresolution approach for the forward and inverse solvers	39
2.3	Inversion procedure	39
2.3.1	Linearisation of the discretised forward problem	39
2.3.2	Deconvolution regularisation parameter	41
2.3.3	Total variation	42
2.3.4	Tomographic backprojection	43
2.4	The radar equation and range resolution	44
3	Asteroid analogues for microwave radar measurement	47

3.1	Asteroid Itokawa model	47
3.2	From a finite element mesh to a 3D-printable object	50
3.3	Controlling the electric permittivity of an analogue object	51
3.4	Manufacturing and validating the 3D-printed analogue target	54
4	Computational implementation of the radar tomography model	57
4.1	The 2D computational model structure	57
4.2	The 3D computational model structure	58
4.3	Measurement point configuration	61
4.3.1	Numerical study	61
4.3.2	Laboratory measurement configuration	62
4.4	Transmitted signal pulse	64
4.5	Time-frequency analysis of the measured scattered field	65
4.6	Identification of scattering zones within the analogue	67
4.7	Studied signal frequencies	69
4.8	Computational implementation: GPU-ToRRe-3D	69
4.8.1	Preprocessing module	71
4.8.2	Forward Modelling module	72
4.8.3	Inverse Modelling module	73
5	Results	75
5.1	Tomographic inversion of simulated data	75
5.2	The effect of the higher-order Born approximation on reconstruction quality	79
5.3	3D-printing of complex-shaped analogue objects	80
5.4	Comparison of simulated and measured tomographic radar signals	83
5.5	Tomographic backpropagation of measured microwave radar data	86
6	Discussion	91
7	Conclusion	97
	References	99

Publication I	111
Publication II	125
Publication III	139
Publication IV	153
Publication V	167
Publication VI	181

List of Figures

2.1 A schematic representation of regularised deconvolution	34
2.2 Schematic representation of the first- and second-order BA	35
3.1 The detailed and the smoothed asteroid Itokawa surfaces	48
3.2 The structural FE model	49
3.3 Mixture permittivity and attenuation predictions	53
3.4 Analogue interior during the 3D printing process and final objects . .	54
4.1 The 2D computational domain and the target	58
4.2 The computational model showing the domains Ω_1 , Ω_2 , and \mathcal{D}	61
4.3 The measurement point configuration and wave path from one point	62
4.4 The experimental set-up used in the CCRM in Marseille	63
4.5 The laboratory measurement configurations.	63
4.6 The QAM signal pulse, its amplitude, and spectrum	66
4.7 Scattering zones in the DM based on two-way signal traveltime	68
4.8 High-level flowchart of the modules in GPU-ToRRe-3D	70
4.9 The functionalities of the Preprocessing module	71
4.10 The functionalities of the Forward Modelling module	72
4.11 The functionalities of the Inverse Modelling module	73

5.1	The normalised numerical backscattering difference signals	76
5.2	3D cut-views of the reconstructions of the void and crack models. . .	77
5.3	The effect of noise on the reconstructions of the void model	78
5.4	Reconstruction of the permittivity distribution	81
5.5	The measured permittivities and loss angles	82
5.6	Comparison between the measurement and simulation data	85
5.7	The effect of the deconvolution regularisation parameter on the BA .	87
5.8	The numerical data at the spatial points	88
5.9	Tomographic backprojection of the measured microwave radar data .	90

List of Tables

2.1	Scaling between the unitless and SI-units	31
3.1	The target permittivities and the volume fractions	54
4.1	Sizing of the unitless 2D computational domain	58
4.2	Details in the asteroid models (A)–(E)	60
4.3	Sizing of the unitless 3D computational domain	61
4.4	Scattering zones and time points in the analogue	68
4.5	The studied signals and scaling to target sizes	69
5.1	Quantitative quality measures for the reconstructions	78
5.2	Quantitative quality measures of the reconstructions in Figure 5.4 . .	80
5.3	The measured permittivity, loss angle and attenuation for the analogue	83

ABBREVIATIONS

BA	Born approximation
CONSERT	Comet Nucleus Sounding Experiment by Radiowave Transmission
DBI	Distorted Born Iterative (method)
DGF	Dyaic Green's Function
DISCUS	Deep Interior Scanning CubeSat
DM	Detail Model: asteroid interior model containing structural interior details with a specified electric permittivity distribution
ESA	European Space Agency
FETD	Finite Element Time Domain
FWI	Full Waveform Inversion
GPU	Graphics Processing Unit
HM	Homogeneous Model: asteroid interior model containing constant permittivity
JAXA	Japan Aerospace Exploration Agency
JUICE	Icy moons of Jupiter mission
JuRa	Juventas Radar
LRS	Lunar Radar Sounder
MAE	Minimum Absolute Error
MAE-R	Relative Minimum Absolute Error
MARSIS	Mars Advanced Radar for Subsurface and Ionospheric Sounding

MRO	Mars Reconnaissance Orbiter
MSE	Minimum Square Error
NASA	National Aeronautics and Space Administration, the United States federal government agency
PCG	Preconditioned Conjugate Gradient
POBA	Physical Optics based Born Approximation
QAM	Quadrature Amplitude Modulation
REASON	Radar for Europa Assessment and Sounding: Ocean to Near-surface
RIME	Radar for Icy Moon Exploration
ROE	Relative Overlap Error
RT	Ray Tracing
SAR	Synthetic Aperture Radar
SHARAD	Shallow Radar
SNR	Signal-to-Noise Ratio
SSIM	Structural Similarity
SSSB	Small Solar System Body

ORIGINAL PUBLICATIONS

- Publication I L.-I. Sorsa, M. Takala, P. Bambach, J. Deller, E. Vilenius and S. Pursiainen. Bistatic full-wave radar tomography detects deep interior voids, cracks and boulders in a rubble-pile asteroid model. *The Astrophysical Journal* 872.1 (2019), 44. DOI: 10.3847/1538-4357/aafba2.
- Publication II L.-I. Sorsa, M. Takala, P. Bambach, J. Deller, E. Vilenius, J. Agarwal, K. Carroll, Ö. Karatekin and S. Pursiainen. Tomographic inversion of gravity gradient field for a synthetic Itokawa model. *Icarus* 336 (2020), 113425. DOI: 10.1016/j.icarus.2019.113425.
- Publication III L.-I. Sorsa, M. Takala, C. Eyraud and S. Pursiainen. A Time-Domain Multigrid Solver with Higher-Order Born Approximation for Full-Wave Radar Tomography of a Complex-Shaped Target. *IEEE Transactions on Computational Imaging* 6 (2020), 579–590. DOI: 10.1109/TCI.2020.2964252.
- Publication IV L.-I. Sorsa, C. Eyraud, A. Hérique, M. Takala, S. Pursiainen and J.-M. Geffrin. Complex-structured 3D-printed wireframes as asteroid analogues for tomographic microwave radar measurements. *Materials & Design* 198 (2021), 109364. ISSN: 0264-1275. DOI: <https://doi.org/10.1016/j.matdes.2020.109364>.
- Publication V C. Eyraud, L.-I. Sorsa, J.-M. Geffrin, M. Takala, G. Henry and S. Pursiainen. Full Wavefield Simulation vs. Measurement of Microwave Scattering by a Complex 3D-Printed Asteroid Analogue. *Astronomy & Astrophysics* 643 (2020), A68. DOI: 10.1051/0004-6361/202038510.

Publication VI L.-I. Sorsa, S. Pursiainen and C. Eyraud. Analysis of full microwave propagation and backpropagation for a complex asteroid analogue via single-point quasi-monostatic data. *Astronomy & Astrophysics* 645 (2021), A73. DOI: 10.1051/0004-6361/202039380.

Author's contribution

- Publication I Created and implemented the numerical Itokawa finite element model structures including the Gaussian random field implementation, ran the numerical analysis, created figures, wrote the manuscript together with SP, and served as the corresponding author.
- Publication II Created and implemented the numerical finite element model structures, ran the numerical analysis, created figures, wrote the manuscript together with SP, and served as the corresponding author.
- Publication III Participated in deriving the concept of higher-order Born approximation together with SP. Run the numerical analysis, analysed the results, and wrote the manuscript together with SP and CE, and served as the corresponding author.
- Publication IV Created the numerical finite element model, participated in conceptualising the manufacturing process and the design of the experiment. Wrote the manuscript together with SP, CE, and J-MG, served as the corresponding author.
- Publication V Created the numerical Itokawa model, performed the time-domain computations and analysis, wrote the manuscript together with SP, CE, and J-MG.
- Publication VI Performed the numerical time-domain computations, analysed and visualised the results, wrote the manuscript together with CE and SP, and served as the corresponding author.

1 INTRODUCTION

1.1 Background

Our understanding of the internal structure of asteroids are based on direct measurements of bulk properties [20], asteroid spin rates, light curve analysis, and spectral measurements, as well as on impact and other simulation studies such as [24, 41] suggesting internal structures which fit the observed parameters. However, direct measurements of electromagnetic wave propagation and scattering in small solar system bodies (SSSB) are required to confirm the hypotheses which have been formed based on numerical experiments, and to validate the results obtained by bulk measurements of physical quantities such as mass, density, and surface materials [38]. The concept of probing the subsurface features by electromagnetic waves is not new, as the Apollo 17 mission used a three-wavelength synthetic-aperture radar at the frequencies 5, 15, and 150 MHz to probe the internal geological structures of the Moon already in 1972 [59]. In 2003, a tomographic radar was proposed to map the interior structure of a near-Earth asteroid [4]. Radars have also been previously used or suggested for use in space exploration to map subsurface features of planets or other smaller bodies [14, 34, 36, 42, 45, 46, 58].

The classical radar sounding experiments on planets or moons during space missions have thus far been carried out with monostatic Synthetic Aperture Radar (SAR) where the electromagnetic waves are transmitted and the reflected signal received by the same orbiting satellite. The European Space Agency's (ESA) mission Mars Express and its Mars Advanced Radar for Subsurface and Ionospheric Sounding instrument (MARSIS) [57] sounded the area near the south pole of the planet between May 2012 and December 2015. MARSIS operated at four frequency bands between 1.3 and 5.5 MHz, and a 1 MHz instantaneous bandwidth. Anomalously bright subsurface reflections detected by the radar led the group to interpret the feature as a stable body of liquid water [57]. Other low frequency radars used in interior inves-

tigations are the 20 MHz center frequency and 10 MHz bandwidth Shallow Radar (SHARAD) onboard the NASA mission Mars Reconnaissance Orbiter (MRO) [70], the 5 MHz Lunar Radar Sounder (LSR) onboard SELENE spacecraft by Japanese Aerospace Exploration Agency (JAXA) for subsurface mapping of Moon [56], the 9 MHz centre frequency and 3 MHz bandwidth Radar for Icy Moon Exploration (RIME) onboard ESA's mission to explore the icy moons of Jupiter (JUICE mission) [17]. Moreover, the dual-frequency Radar for Europa Assessment and Sounding: Ocean to Near-surface (REASON) by NASA emitting 9 MHz and 60 MHz signals for concurrent sounding of deep and shallow structures of Jupiter's moon Europa [54] has been scheduled to be launched in 2024.

The first attempt to measure the deep interior structure of an SSSB was Comet Nucleus Sounding Experiment by Radio-wave Transmission (CONSERT), an experiment which was a part of ESA's Rosetta mission to explore the comet 67P/Churyumov-Gerasimenko. In the experiment, a 90 MHz center frequency and 8 MHz bandwidth radar signal was transmitted by the Rosetta orbiter through the target comet nucleus. This signal was received by the lander Philae and retransmitted back to the orbiter, creating a bistatic measurement configuration where the signal travelled through the comet nucleus twice, yielding multiple source and receiver point pairs enabling radar tomographic imaging [44, 45, 46]. The reported analysis of the results shows that the average relative permittivity of the comet is approximately 1.26, suggesting a volumetric dust/ice ratio of 0.4 to 2.6 and a porosity of 75 to 85 % [46].

The next candidate mission to deploy a radar tomography system to explore the deep interior of an SSSB is ESA's Asteroid Impact Mission Hera [53] which is due to launch in 2024. The target asteroid of the mission is the binary near-Earth asteroid system 65803 Didymos consisting of the primary asteroid and its smaller satellite body Dimorphos. At the core of the mission is to map the deep interior structure of Dimorphos, which, albeit being a small object with a diameter of 160 m, would be big enough to destroy an entire city if it were to collide with Earth. The radar experiment onboard Hera is the Juventas Radar (JuRa), a tomographic monostatic radar operating at a centre frequency of 60 MHz and a bandwidth of 20 MHz [40]. Unlike comets, which are composed of an icy mix of silicates and organics with electric permittivity close to free space [39, 46], asteroids are expected to be composed of rocky materials which real part of the electric permittivity typically varies between 3 to 10 [38]. Such permittivity values have a significant effect on the speed of the

electromagnetic wave travelling in the material, leading to a high contrast between the possible free space within the asteroid interior structure and the constitutive material, as well as on the material interface on the surface of the body.

Full tomography of an asteroid interior requires sufficient measurement point coverage [7, 30] and is significantly improved by multiple source positions [61]. Numerical studies [64, 74, 75] and Publication I of this thesis have shown that low-frequency bistatic computed radar tomographic measurements can be used to detect internal voids inside an asteroid interior model from realistic orbiting distances. Further validation of the concept has been obtained in microwave radar laboratory experiments on a scaled comet model and other similar targets [29, 30]. From an engineering perspective, obtaining sufficient measurement point coverage is a challenge as the the radar-carrying satellite needs to be carefully steered on its orbit to perform the measurements with as low a noise and as accurate positioning of the satellite as possible. Manoeuvring around an SSSB with a very limited and unstable gravitational field heavily consumes the limited power available, leading to a sparse measurement point coverage. The possibilities are further limited by the constraints of radar power consumption limiting the realistic signal bandwidth.

In planetary scientific radar applications, at least six different methods have been applied to numerically investigate full-wave propagation in the tomographic imaging problem. Most of them are very naturally linked to the CONSERT experiment as it is currently the only realised measurement on an SSSB. Initially, the experiment was modelled by Physical Optics based Born Approximation (POBA) to better define and describe the instrument needed to achieve the science goals of the experiment [44]. Later, the Ray Tracing Method (RT) was first implemented and validated in 2D in [9] and later used for the experiment simulations in 3D [8], and finally used in the final data analysis of the experiment [22]. The Finite Difference Time Domain (FDTD) approach has been used to investigate radar wave propagation through seven different comet nuclei models [18]. The Dyaic Green's Function (DGF) method has been used to simulate the full wavefield in experiments with laboratory data on a scale comet model [30]. More recently, full waveform inversion (FWI) method, which is typically used in seismic waveform modelling, has been shown to perform well in generating high resolution tomographic images of comet type nuclei with complex shape and internal permittivity distribution [68]. Finally, the method used in this thesis is the Finite Element Time Domain (FETD) simula-

tion which has been shown to yield good tomographic reconstructions in asteroid-type high-contrast models in 2D and 3D test domains [64, 74, 75].

1.2 Objectives

The objectives of this thesis are:

1. Advance the mathematical methodology of full-wave radar tomography in applications where the measurement set is sparse, the target structure and shape is complex, and the interior permittivity distribution of the target has high contrast.
2. Create a 3D-printed analogue model based on a numerical finite element mesh to measure microwave scattering data in a laboratory.
3. Validate obtained numerical radar tomography results with data obtained from laboratory measurements performed on the manufactured analogue model.
4. Provide the research community with open source software tools to carry out numerical analysis of tomographic inversion problems.
5. Support space mission proposals which science goals require radar tomography or tomographic inversion of other geophysical fields such as the gravity gradient field.

1.3 Summary of the original publications

The six published scientific articles included in this thesis investigate the imaging of the interior of solar system bodies by using the FETD method to simulate the forward problem in electromagnetic wave propagation. The publications introduce complex-shaped asteroid interior models built inside the surface shape of the asteroid 25143 Itokawa (from now on: Itokawa) to investigate tomographic inversion in an asteroid target having a higher internal permittivity contrast than the extensively studied comet nucleus models [22, 30, 68]. The FETD solver was initially formulated and presented in [64, 74, 75], but it has been further developed during this work and has also been made openly available in GitHub [62, 63]. The numerical investigations with the solver are further validated with data from microwave radar

experiments performed in a laboratory on a permittivity-controlled asteroid analogue which was manufactured to match the numerical model. The measured data is also used to investigate and validate the performance of the selected forward and inversion methods to yield meaningful tomographic reconstructions.

Publication I investigates the tomographic inversion of a 2 MHz bandwidth radar signal with five different interior structures, each containing mantle and deep interior details modelling void space, cracks or a high-density boulder in addition to modelling the rubble-pile nature of the other parts of the interior with a Gaussian random field. The specification of the radar simulation was based on the suggested Deep Interior Scanning CubeSat (DISCUS) mission [6] which was further developed to a comprehensive space mission proposal AI3 – Asteroid Interior Investigation - 3way mission [5]. The mission proposal participated in European Space Agency’s (ESA) fast class mission call in 2019, and it was among the best six proposals in the call, although was not eventually selected. The results presented in Publication I provided the key evidence for the AI3 mission proposal showing that a bistatic CubeSat measurement configuration equipped with tomographic radar can detect deep interior voids, cracks, and boulders in an Itokawa-sized asteroid model, and that the numerical experiments could be performed with the then available computing resources within a reasonable amount of time.

Publication II concerns not radar tomography, but the tomographic inversion of the gravity gradient field in two different asteroid Itokawa models. This publication was used to strengthen the science case of the AI3 mission proposal, where the interior of the target asteroid would not only be investigated by a tomographic radar, but also augmented with a gravimetric measurement and seismic waves after the impact experiment. The goal of Publication II was to advance the mathematical inversion methodology in gravimetric measurements, and it sought to find feasibility constraints for resolution, noise, and orbit selection for future space missions utilising gravimetric instruments.

To advance the mathematical methodology in radar tomography, Publication III introduces the formulation, implementation, and evaluation of a higher-order Born approximation in a multigrid FETD framework enabling nonlinear tomographic radar imaging. The introduced method is similar to the frequency-domain solver utilising the distorted Born iterative (DBI) technique [21, 35, 49, 50] in that it relies on sequential linearised approximations with respect to the sought permittivity dis-

tribution. However, unlike the previous literature, the methodology introduced in Publication III has been developed for arbitrary spatial domains and full-wave modelling for a complex-shaped target and a sparse set of measurement points in the time domain. The computations were carried out in a 2D test domain previously used in [75] introducing the multigrid methodology for a linearised forward and inverse solver in the tomographic radar problem.

To validate the results of the numerical experiments reported in Publication I, permittivity-controlled, complex-shaped analogue objects were manufactured by 3D-printing. The method and results of this work are reported in Publication IV. A fused fabrication filament material with suitable dielectric properties was found, and material mixing models were used to match the electric permittivity of the final object with the expected permittivity of an asteroid. The same simplified interior void model within the Itokawa shape as in Publication I was used, and the analogue size was matched so that it could be used for experimental tomographic microwave radar measurements to validate the permittivity and attenuation properties of the manufactured objects, and to perform tomographic radar measurements in the laboratory. The methodology of creating 3D-printable wireframes with given electric properties was developed alongside this work and published as an open source Asteroid Wireframe Package [65].

Publication V reports the comparison of full wavefield simulations to microwave radar measurements. The asteroid analogue manufactured and reported in Publication IV was used as the tomographic target in the laboratory experiments. A modulated pulse matching a 10-20 MHz centre frequency radar to a real-scale Itokawa-size target was used to simulate the laboratory radar measurement. At the core of Publication V is the close international collaboration between two groups with two different solvers, one in the time domain, on which this thesis concentrates on, and the other in the frequency domain, allowing the comparison of two different numerical simulation approaches on laboratory measurements and the cross-validation between the simulation methods.

The close collaboration between the time and frequency domain approaches continued in Publication VI, extending the analysis of full microwave propagation and backpropagation for the complex analogue model by investigating a single-point quasi-monostatic data. This final article in this thesis investigates the wave interaction at given points inside the target body and analyses the effect of direct and

higher-order scattering phenomena on the data and the simple backprojection inversion carried out for both the simulated and measured data.

1.4 Organisation of the thesis

The FETD forward modelling approach of the full wave propagation within a complex spatial domain is explained in Chapter 2 starting with a review of electromagnetic wave propagation in material media and proceeds to present the forward model and the inversion methodologies applied in this thesis. The Born approximation, its use in the linear inverse problem, and its extension to the nonlinear case are also presented. The chapter concludes with the essential topics on radar equation and range resolution, explaining the effect of radar specifications on the imaging capability, and the relation between the resolution, permittivity distribution and radar bandwidth.

Chapter 3 concerns the creation of the 3D-printable analogue object. It justifies the selected electric permittivity distributions inside the model, explains how to control the permittivity of the analogue object, and shows the methodology of how to create a manufacturable object from a finite element mesh.

The computational implementation of the numerical experiments is given in Chapter 4 including the specifications for both the 2D and 3D computational domains, the measurement point configurations in numerical studies, and laboratory experiments. It also discusses the transmitted signal pulse, how to perform time-frequency analysis of the measured and simulated signals, and how to relate the received time domain signal to spatial locations within the target. The chapter also summarises the signal frequencies studied in this thesis, and how they relate to real-scale measurements and target sizes. Chapter 4 is concluded by the description of the implementation of the three-dimensional full wave forward and inverse solvers which have been used to simulate and analyse the data in Publications I, V, and VI.

Chapter 5 summarises the main results of this thesis showing the feasibility of tomographic reconstruction of numerical data and the single-point analyses of the experimental data. Discussion of the results is given in Chapter 6. Finally, Chapter 7 concludes this thesis.

2 RADAR TOMOGRAPHY WITH TIME DOMAIN SIGNALS

2.1 Electromagnetic wave propagation in material

2.1.1 Maxwell's equations

The electromagnetic phenomena are governed by the four fundamental Maxwell equations linking the physical quantities of the electric field $\vec{\mathcal{E}}$, the magnetic field $\vec{\mathcal{B}}$, the electric flux density $\vec{\mathcal{D}}$, the magnetic field intensity $\vec{\mathcal{H}}$, the electric current density $\vec{\mathcal{J}}$, and the volumetric electric charge density $\tilde{\rho}$. In the differential form, these equations are

$$\nabla \times \vec{\mathcal{E}} = -\frac{\partial \vec{\mathcal{B}}}{\partial t} \quad (2.1)$$

$$\nabla \cdot \vec{\mathcal{D}} = \tilde{\rho} \quad (2.2)$$

$$\nabla \times \vec{\mathcal{H}} = \vec{\mathcal{J}} + \frac{\partial \vec{\mathcal{D}}}{\partial t} \quad (2.3)$$

$$\nabla \cdot \vec{\mathcal{B}} = 0. \quad (2.4)$$

The first equation of Maxwell equations (Eq. 2.1) is the Faraday's law of induction which is based on the experimental fact that a time-changing magnetic flux induces electromotive force. Hence a spatially varying, and also time-varying, electric field is always accompanied with a time-varying magnetic field. The equation 2.2, Gauss's law, states that the electric flux per unit volume in space is equal to the volumetric electric charge density at that point. The volume charge density $\tilde{\rho}$ therefore represents the source from which electric fields originate. In a source-free

medium this equation takes the form $\nabla \cdot \vec{\mathcal{D}} = 0$. A generalisation of Ampère's law (Eq. 2.3) states that magnetic fields can be generated by an electric current and changing electric fields, predicting that a changing magnetic field induces an electric field and vice versa. The fourth Maxwell equation (Eq. 2.4) states that there are no magnetic charges and that magnetic field lines always close on themselves.

The medium-independent quantities \mathcal{D} and \mathcal{H} are related to the electric and magnetic fields in a dielectric medium through an electric permittivity ε and a magnetic permeability μ by

$$\vec{\mathcal{D}} = \varepsilon \vec{\mathcal{E}} \quad \text{and} \quad \vec{\mathcal{H}} = \frac{\vec{\mathcal{B}}}{\mu}. \quad (2.5)$$

The current density $\vec{\mathcal{J}}$ in the equation 2.3 is given by

$$\vec{\mathcal{J}} = \vec{\mathcal{J}}_s + \vec{\mathcal{J}}_c, \quad (2.6)$$

where $\vec{\mathcal{J}}_s$ represents the source current such as that in a transmitting antenna, and $\vec{\mathcal{J}}_c$ the conduction current flowing in a medium which conductivity $\sigma \neq 0$, whenever there is an electric field present. The conduction current $\vec{\mathcal{J}}_c$ is given by

$$\vec{\mathcal{J}}_c = \sigma \vec{\mathcal{E}}. \quad (2.7)$$

The parameters ε , μ , and σ describe the relationships between macroscopic field quantities. They are constants only for simple material media, which are linear, homogeneous, time-invariant and isotropic. For complex materials, these quantities may depend on the magnitudes of the field quantities $\vec{\mathcal{E}}$ and $\vec{\mathcal{B}}$ (non-linear media), on spatial coordinates (inhomogeneous), on time (time-variant), or on the orientations of $\vec{\mathcal{E}}$ and $\vec{\mathcal{H}}$ (anisotropic).

When substituting the medium-independent quantities $\vec{\mathcal{D}}$ and $\vec{\mathcal{H}}$ with the medium-specific quantities given by the equation 2.5 to emphasise the contributions of the medium in the fields, the Maxwell equations 2.1-2.4 in a source-free medium take the form

$$\nabla \times \vec{\mathcal{E}} = -\frac{\partial \vec{\mathcal{B}}}{\partial t} \quad (2.8)$$

$$\nabla \cdot \varepsilon \vec{\mathcal{E}} = 0 \quad (2.9)$$

$$\nabla \times \vec{\mathcal{B}} = \mu \vec{\mathcal{J}} + \varepsilon \mu \frac{\partial \vec{\mathcal{E}}}{\partial t} \quad (2.10)$$

$$\nabla \cdot \vec{\mathcal{B}} = 0. \quad (2.11)$$

Taking the curl of the equation 2.8 yields

$$\nabla \times \nabla \times \vec{\mathcal{E}} = \nabla(\nabla \cdot \vec{\mathcal{E}}) - \nabla^2 \vec{\mathcal{E}} = -\nabla \times \frac{\partial \vec{\mathcal{B}}}{\partial t}. \quad (2.12)$$

Substituting equation 2.10 to the equation 2.12, using the equations 2.6 and 2.7 to expand the current density, and assuming a source-free medium ($\nabla \cdot \vec{\mathcal{E}} = 0$), the equation yields

$$\varepsilon \mu \frac{\partial^2 \vec{\mathcal{E}}}{\partial t^2} + \sigma \mu \frac{\partial \vec{\mathcal{E}}}{\partial t} - \nabla^2 \vec{\mathcal{E}} = \mu \frac{\partial \vec{\mathcal{J}}_s}{\partial t}. \quad (2.13)$$

This equation can be recognised as a hyperbolic wave equation for the electric field and it will be used as the basis for building the forward model for the radar tomographic inverse problem.

2.1.2 Time-harmonic forms of Maxwell's equations

In radar tomography performed in space, the radar antenna acts as a source of electromagnetic waves. The target SSSB is the dielectric medium surrounded by free space. Hence, an amplitude-modulated radar operating at a carrier frequency f_c can be treated as a source of steady-state sinusoidal waves, with its amplitude modulated within a narrow bandwidth B around the carrier frequency. Assuming that the characteristics of the propagation medium do not vary significantly over the bandwidth, the propagation behaviour of the radar signal can be described by a single sinusoidal carrier wave.

Maxwell's equations 2.1-2.4 allow the field vectors $\vec{\mathcal{E}}$, $\vec{\mathcal{D}}$, $\vec{\mathcal{H}}$, and $\vec{\mathcal{B}}$ be time-variant. To obtain the time-harmonic (sinusoidal steady-state) forms of the equa-

tions, these fields and the current density $\vec{\mathcal{J}}$ are replaced with the time-invariant complex phasors $\vec{\mathbf{E}}$, $\vec{\mathbf{D}}$, $\vec{\mathbf{H}}$, $\vec{\mathbf{B}}$, and $\vec{\mathbf{J}}$. The former can be obtained from the latter by multiplying by $e^{j\omega t}$, and taking the real part thereof. For example, $\vec{\mathcal{E}}(x, y, z, t) = \text{Re}\{\vec{\mathbf{E}}(x, y, z)e^{j\omega t}\}$. Substituting the field vectors in the equations 2.1-2.4 with the corresponding phasors leads to the time-harmonic forms of Maxwell's equations:

$$\nabla \times \vec{\mathbf{E}} = -j\omega \vec{\mathbf{B}} \quad (2.14)$$

$$\nabla \cdot \vec{\mathbf{D}} = \rho \quad (2.15)$$

$$\nabla \times \vec{\mathbf{H}} = \vec{\mathbf{J}} + j\omega \vec{\mathbf{D}} \quad (2.16)$$

$$\nabla \cdot \vec{\mathbf{B}} = 0. \quad (2.17)$$

Using the phasor equivalents of the quantities in the equation 2.5, the above equations 2.14-2.17 can be written as

$$\nabla \times \vec{\mathbf{E}} = -j\omega \vec{\mathbf{B}} \quad (2.18)$$

$$\nabla \cdot \varepsilon \vec{\mathbf{E}} = \rho \quad (2.19)$$

$$\nabla \times \vec{\mathbf{B}} = \mu(\vec{\mathbf{J}}_s + \sigma \vec{\mathbf{E}} + j\omega \varepsilon \vec{\mathbf{E}}) \quad (2.20)$$

$$\nabla \cdot \vec{\mathbf{B}} = 0. \quad (2.21)$$

The phasor current $\vec{\mathbf{J}} = \vec{\mathbf{J}}_s + \vec{\mathbf{J}}_c = \vec{\mathbf{J}}_s + \sigma \vec{\mathbf{E}}$ (Eq. 2.20) is the sum of the antenna source current $\vec{\mathbf{J}}_s$ and material conduction current $\vec{\mathbf{J}}_c$ as in the equations 2.6 and 2.7. In a conducting media, the equation 2.20 can be rearranged to

$$\begin{aligned} \nabla \times \vec{\mathbf{B}} &= \mu[\vec{\mathbf{J}}_s + \sigma \vec{\mathbf{E}} + j\omega \varepsilon \vec{\mathbf{E}}] = \mu \left[\vec{\mathbf{J}}_s + j\omega \left(\frac{\sigma}{j\omega} + \varepsilon \right) \vec{\mathbf{E}} \right] \\ &= \mu \left[\vec{\mathbf{J}}_s + j\omega \left(\varepsilon - \frac{j\sigma}{\omega} \right) \vec{\mathbf{E}} \right], \end{aligned} \quad (2.22)$$

where the term $(\varepsilon - j\sigma/\omega)$ can be interpreted as the effective complex permittivity ε_c of the medium.

Permittivity ε is a measure of the electric polarisability of a material. Together with the magnetic permeability μ they determine the phase velocity v of electro-

magnetic waves in the medium by

$$v = \frac{1}{\sqrt{\varepsilon\mu}}. \quad (2.23)$$

In free space, the electric permittivity and magnetic permeability have constant values of $\varepsilon_0 = 8.854 \cdot 10^{-12}$ F/m, and $\mu_0 = 4\pi \cdot 10^{-7}$ H/m, respectively.

In lossy media, permittivity of a material is often expressed by the relative permittivity ε_r , which is the ratio of the absolute permittivity of the material ε and the permittivity of the free space ε_0 :

$$\varepsilon_r = \frac{\varepsilon}{\varepsilon_0}. \quad (2.24)$$

With these notations, the effective complex permittivity in the equation 2.22 can be formulated as:

$$\varepsilon_c = \varepsilon - \frac{j\sigma}{\omega} = \varepsilon_0 \left[\varepsilon_r - j \frac{\sigma}{\omega \varepsilon_0} \right] = \varepsilon_0 \varepsilon_{cr}, \quad (2.25)$$

where ε_{cr} is the complex relative permittivity of the medium. The complex relative permittivity is often also expressed as

$$\varepsilon_{cr} = \varepsilon'_r - j\varepsilon''_r. \quad (2.26)$$

This notation has been used in Publication IV of this thesis. The equation 2.22 can hence be written more concisely as

$$\nabla \times \vec{\mathbf{B}} = \mu(\vec{\mathbf{J}}_s + j\omega\varepsilon_c\vec{\mathbf{E}}). \quad (2.27)$$

To obtain the time-harmonic formulation of the equation 2.13, the procedure again starts by taking the curl of the equation 2.20:

$$\begin{aligned} \nabla \times \nabla \times \vec{\mathbf{E}} &= -j\omega \nabla \times \vec{\mathbf{B}} = -j\omega(\mu\vec{\mathbf{J}}_s + j\omega\mu\varepsilon_c\vec{\mathbf{E}}) \\ &= -j\omega\mu\vec{\mathbf{J}}_s + \omega^2\mu\varepsilon_c\vec{\mathbf{E}}. \end{aligned} \quad (2.28)$$

Using the vector identity $\nabla \times \nabla \times \vec{\mathbf{E}} = \nabla(\nabla \cdot \vec{\mathbf{E}}) - \nabla^2\vec{\mathbf{E}}$ and assuming a source-free

medium ($\nabla \cdot \vec{\mathbf{E}} = 0$), the equation 2.28 yields

$$\begin{aligned} -\nabla^2 \vec{\mathbf{E}} &= -j\omega\mu\vec{\mathbf{J}}_s + \omega^2\mu\epsilon_c\vec{\mathbf{E}} \\ \omega^2\mu\epsilon_c\vec{\mathbf{E}} + \nabla^2 \vec{\mathbf{E}} &= j\omega\vec{\mathbf{J}}_s. \end{aligned} \quad (2.29)$$

The equation 2.29 is recognized as the inhomogeneous Helmholtz equation which can be solved by specifying a suitable boundary condition at infinity, such as the Sommerfeld radiation condition, and calculating the convolution with the Green's function of the equation.

2.2 The forward model

The forward model is formulated based on the hyperbolic wave equation 2.13. The formulation is shown here for the two-dimensional case where the transmitted signal produces a transverse electric field perpendicular to the direction of propagation. The reason for choosing to present the two-dimensional case is that the higher-order Born approximation developed during this thesis (Publication III) was formulated for the two-dimensional case. The three-dimensional formulation of the forward problem including the polarization terms resulting from electromagnetic wave interaction with medium interfaces is given in [74]. To match the notations in the original publications introducing the forward model [64, 74, 75], and Publications I, III, V, and VI of this thesis, the electric field $\vec{\mathcal{E}}$ is denoted by the scalar potential u . The antenna current density $\vec{\mathcal{J}}_s$ acting as the source function for the radar pulse signal transmitted from the antenna is given by $f(t)$. The forward model can hence be expressed as

$$\epsilon\mu\frac{\partial^2 u}{\partial t^2} + \sigma\mu\frac{\partial u}{\partial t} - \Delta u = \mu\frac{\partial f}{\partial t}. \quad (2.30)$$

The equation 2.30 is sought in a form emphasizing the recovery of the real part of the relative electric permittivity ϵ_r . By expanding $\epsilon = \epsilon_r\epsilon_0$ (Eq. 2.24), and assuming that the magnetic permeability of the medium $\mu = \mu_0$, it is written as

$$\epsilon_r\epsilon_0\mu_0\frac{\partial^2 u}{\partial t^2} + \sigma\mu_0\frac{\partial u}{\partial t} - \Delta u = \mu_0\frac{\partial f}{\partial t}. \quad (2.31)$$

Table 2.1 Spatial scaling of SI-units to the unitless computational domain. The spatial scaling factor is s and the wave velocity $c = 1/\sqrt{\varepsilon_0\mu_0} = 1$ when $\varepsilon_r = 1$. The physical constants $\varepsilon_0 = 8.85 \cdot 10^{-12}$ F/m is the electric permittivity, and $\mu_0 = 4\pi \cdot 10^{-7}$ H/m the magnetic permeability of vacuum.

Quantity	Unitless	SI-units
Time	t	$(\varepsilon_0\mu_0)^{1/2}st$
Position	\vec{x}	$s\vec{x}$
Velocity	$c = 1$	$(\varepsilon_0\mu_0)^{-1/2}c$
Frequency	f	$(\varepsilon_0\mu_0)^{-1/2}s^{-1}f$
Electric permittivity	ε_r	ε_r
Electric conductivity	σ	$(\varepsilon_0/\mu_0)^{1/2}s^{-1}\sigma$

To simplify the numerical parameters, the computational problem is solved with a unitless set of parameters of time t , frequency f , space \vec{x} , electric permittivity ε_r , conductivity σ and velocity c by choosing that the wave velocity in free space ($\varepsilon_r = 1$) is $c = (\varepsilon_0\mu_0)^{-1/2} = 1$.

By multiplying both sides of the equation 2.31 by $(\varepsilon_0\mu_0)^{-1} = 1$ to obtain the unitless system, and by simplifying the resulting equation, the forward model takes the form

$$\varepsilon_r \frac{\partial^2 u}{\partial t^2} + \sigma \frac{\partial u}{\partial t} - \Delta u = \frac{\partial f}{\partial t} \quad \text{for all } (t, \vec{x}) \in [0, T] \times \Omega \quad (2.32)$$

with the initial conditions $u|_{t=0} = u_0$ and $(\partial u / \partial t)|_{t=0} = u_1$. The signal source $\partial f / \partial t$ is given by

$$\frac{\partial f(t, \vec{x})}{\partial t} = \delta_{\vec{p}}(\vec{x}) \frac{\partial \tilde{f}(t)}{\partial t}, \quad (2.33)$$

where the notation $\tilde{f}(t)$ refers to the time-dependent part of f , and $\delta_{\vec{p}}(\vec{x})$ is the Dirac's delta function with respect to the signal transmission point \vec{p} .

The quantities which contain spatial dependency are scaled by the spatial scaling factor s obtained by the ratio of the real SI-unit size of the target object divided by the unitless size of the target domain \mathcal{D} . The parameters in the equation 2.32 can be scaled to SI-units according to Table 2.1.

By defining an auxiliary function \vec{g} as

$$\vec{g} = \int_0^t \nabla u(\tau, \vec{x}) d\tau, \quad (2.34)$$

the hyperbolic wave equation 2.32 can be expressed as the first-order differential system

$$\varepsilon_r \frac{\partial u}{\partial t} + \sigma u - \nabla \cdot \vec{g} = f \quad (2.35)$$

$$\frac{\partial \vec{g}}{\partial t} - \nabla u = 0 \quad (2.36)$$

in the domain $\Omega \times [0, T]$. To obtain the weak form of this system, the equation 2.35 is multiplied by the test function $v : [0, T] \rightarrow H^1(\Omega)$, and the equation 2.36 by the test function $\vec{w} : [0, T] \rightarrow L_2(\Omega)$ followed by integration by parts yields the weak formulation of the system:

$$\frac{\partial}{\partial t} \int_{\Omega} \varepsilon_r u v d\Omega + \int_{\Omega} \sigma u v d\Omega + \int_{\Omega} \vec{g} \cdot \nabla v d\Omega = \begin{cases} \tilde{f}(t) & \text{if } \vec{x} = \vec{p} \\ 0 & \text{otherwise} \end{cases} \quad (2.37)$$

$$\frac{\partial}{\partial t} \int_{\Omega} \vec{g} \cdot \vec{w} d\Omega - \int_{\Omega} \vec{w} \cdot \nabla u d\Omega = 0. \quad (2.38)$$

This weak form has the unique solution $u : [0, T] \rightarrow H^1(\Omega)$ when the domain and the parameters are regular enough [27].

2.2.1 Evaluation of wave propagation in a domain

The problem of full wave propagation in the domain Ω can be associated with a situation where a signal $\tilde{f}(t)$ is transmitted from the point \vec{p}_1 and received at the point \vec{p}_2 . The received signal $\tilde{d}(t)$ at the receiver point \vec{p}_2 can be expressed as the linear convolution

$$\tilde{d}(t) = \mathcal{G}_{\vec{p}_1, \vec{p}_2} * \tilde{f}(t) = \int_{-\infty}^{\infty} \mathcal{G}_{\vec{p}_1, \vec{p}_2}(t - \tau) \tilde{f}(\tau) d\tau, \quad (2.39)$$

where $\mathcal{G}_{\vec{p}_1, \vec{p}_2}$ is the Green's function $\mathcal{G} = \mathcal{G}(\varepsilon, \epsilon)$, a functional of the permittivity ε and a nuisance parameter ϵ , and representing the impulse response to an infinitely short monopolar pulse transmitted from \vec{p}_1 and received in \vec{p}_2 . The nuisance parameter ϵ is related to the uncertainties in the numerical model, including signal attenuation due to, for example, conduction losses, reflections and refractions, and also numerical modelling errors. These uncertainties can be modelled with an additive error term ϵ resulting in a simplified expression for the Green's function as

$$\mathcal{G}(\varepsilon, \epsilon) = \mathcal{G}(\varepsilon) + \epsilon. \quad (2.40)$$

The equation 2.39 expresses the wavefield in a domain with constant permittivity distribution ε . In realistic scenarios, the domain includes electromagnetic scatterers, perturbations ρ to the overall permittivity distribution ε . To investigate the effect of such small scattering obstacles, assume one at point \vec{r} causing a local perturbation ρ in the overall permittivity distribution ε . The permittivity at that point is then defined as

$$\varepsilon_{\vec{r}} = \varepsilon + \rho. \quad (2.41)$$

An electromagnetic wavefield signal $\tilde{\mathbf{f}}$ transmitted from the point \vec{p}_1 and travelling through the point \vec{r} which contains the permittivity perturbation, is altered at that point. The point \vec{r} can therefore be considered to act as a new point source transmitting an altered signal $\tilde{\mathbf{h}}$. Because the wavefield is altered only at \vec{r} , the Green's function equals $\mathcal{G}(\varepsilon)$ elsewhere. The perturbed wavefield $\tilde{\mathbf{d}}$ received at the point \vec{p}_2 is hence

$$\tilde{\mathbf{d}} = \mathcal{G}(\varepsilon)_{\vec{p}_1, \vec{p}_2} * \tilde{\mathbf{f}} + c(\rho) \mathcal{G}(\varepsilon)_{\vec{r}, \vec{p}_2} * \tilde{\mathbf{h}}, \quad (2.42)$$

where $c(\rho)$ is a constant contrast factor whose numerical dependence on the perturbation ρ is determined later in the section 2.3.2, and the wavefield

$$\tilde{\mathbf{h}} = \mathcal{G}(\varepsilon_{\vec{r}})_{\vec{p}_1, \vec{r}} * \tilde{\mathbf{f}}. \quad (2.43)$$

Due to the uncertainties included in the error term ϵ (Eq. 2.40), the exact form of the Green's function is not known. However, it is approximated numerically by using a regularised deconvolution process (Figure 2.1) which proceeds according to

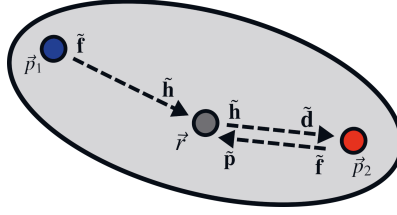


Figure 2.1 A schematic presentation of regularised deconvolution which is applied in computing wave propagation between points \vec{p}_1 and \vec{p}_2 where there is a scattering detail altering the wave-field at point \vec{r} . Adapted from Publication III. Reprinted with permission.

the following steps:

1. Propagate a single wave from both \vec{p}_1 and \vec{p}_2 and evaluate the terms $\tilde{\mathbf{h}} = \mathcal{G}(\varepsilon)_{\vec{p}_1, \vec{r}} * \tilde{\mathbf{f}}$ and $\tilde{\mathbf{p}} = \mathcal{G}(\varepsilon)_{\vec{p}_2, \vec{r}} * \tilde{\mathbf{f}}$ for each scattering point \vec{r} .
2. Use the Tikhonov-regularised deconvolution with a suitably chosen regularisation parameter ν to estimate the Green's function

$$\tilde{\mathbf{g}} = \mathcal{G}(\varepsilon)_{\vec{r}, \vec{p}_2} = \mathcal{G}(\varepsilon)_{\vec{p}_2, \vec{r}}. \quad (2.44)$$

3. Estimate the wavefield originating from \vec{r} at \vec{p}_2 by $\tilde{\mathbf{d}} = \tilde{\mathbf{g}} * \tilde{\mathbf{f}}$.

The principle of reciprocity of wave propagation ensures that the equation 2.44 holds. The entries of the vectors $\tilde{\mathbf{f}}$, $\tilde{\mathbf{h}}$, $\tilde{\mathbf{p}}$, $\tilde{\mathbf{g}}$, and $\tilde{\mathbf{d}}$ contain the pointwise time evolution of the corresponding variables. Backscattering data is obtained when $\vec{p}_1 = \vec{p}_2$.

2.2.2 Born approximation and higher-order scattering

In a complex, bounded geometry, a propagating wavefield may experience multiple scattering events related to the same perturbation. Such events can be modelled with the Born series. The first-order term of the series is called Born approximation, where the total field is replaced by the incident field and this incident field is assumed to be the driving field at each point in the scatterer (Figure 2.2). Therefore, the Born approximation (BA), or the first-order term of the Born series, can be obtained by substituting $\mathcal{G}(\varepsilon_{\vec{r}})$ in the equation 2.43 with the corresponding Green's function of the incident field $\mathcal{G}(\varepsilon)$:

$$\mathbf{h}^{BA,1} = \mathcal{G}(\varepsilon)_{\vec{p}_1, \vec{r}} * \tilde{\mathbf{f}}. \quad (2.45)$$

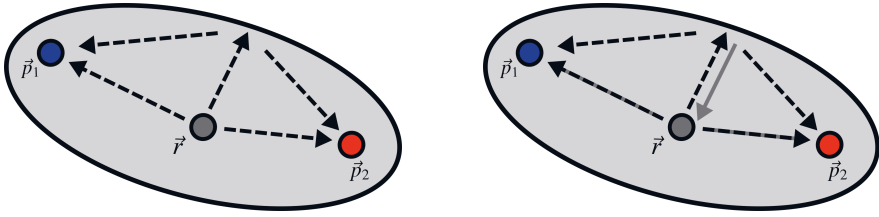


Figure 2.2 Schematic representation of the first-order BA (left) and second-order BA (right). The first-order BA accounts for the scattered wavefields (black, dashed arrows) which originate from a single point and its interaction with \vec{r} with respect to the details in the computational geometry. The second-order BA accounts for the wavefields which have scattered twice from \vec{r} (solid grey arrows). Adapted from Publication III. Reprinted with permission.

The higher-order terms of the series modelling the secondary, tertiary, and higher order scattering events from the same scatterer are derived analogously to the equation 2.42 from the recursive equation

$$\tilde{\mathbf{h}}^{BA,n} = \mathcal{G}(\varepsilon)_{\vec{p}_1, \vec{r}} * \tilde{\mathbf{f}} + c(\rho) \mathcal{G}(\varepsilon)_{\vec{r}, \vec{r}} * \tilde{\mathbf{h}}^{BA,n-1}, \quad (2.46)$$

where n gives the order of the scattering event. As the first-order Born approximation is based on \mathcal{G} alone, the nonlinear wave propagation effects are only recovered by the higher order terms where the total field is replaced by the incident field as given by the equation 2.43.

2.2.3 Discretisation of the forward problem

The forward problem 2.32 and its weak form are solved numerically by the finite element time domain (FETD) method, where the spatial d -dimensional ($d = \{2, 3\}$) domain Ω is discretised into a d -simplex finite element mesh \mathcal{T} consisting of m elements $\{T_1, T_2, \dots, T_m\}$. Each of these elements T_i , $i = 1, \dots, m$ is associated with an element indicator function $\chi_i \in L_2(\Omega)$. Here, the discretisation is presented for the two-dimensional case. The mesh \mathcal{T} consists of a set of n mesh nodes $\{\vec{r}_1, \vec{r}_2, \dots, \vec{r}_n\}$ identified with piecewise linear nodal basis functions $\{\varphi_1, \varphi_2, \dots, \varphi_n\} \in H^1(\Omega)$. The potential and gradient fields in equations 2.35 and 2.36 are approximated in each dimension of the mesh \mathcal{T} as finite sums

$$u = \sum_{j=1}^n p_j \varphi_j \quad \text{and} \quad \vec{g} = \sum_{k=1}^d g^{(k)} \vec{e}_k, \quad (2.47)$$

where $g^{(k)} = \sum_{i=1}^m q_i^{(k)} \chi_i$, the weighted sum of the element indicator functions $\{\chi_1, \chi_2, \dots, \chi_m\} \in L_2(\Omega)$.

By defining the test functions $v : [0, T] \rightarrow (V) \subset b^1(\Omega)$ and $\vec{w} : [0, T] \rightarrow \mathcal{W} \subset L_2(\Omega)$ with $\mathcal{V} = \text{span}\{\varphi_1, \varphi_2, \dots, \varphi_n\}$ and $\mathcal{W} = \text{span}\{\chi_1, \chi_2, \dots, \chi_m\}$, the weak form (Eqs 2.35-2.36) is expressed in the discretised Ritz-Galerkin form [15]:

$$\frac{\partial}{\partial t} \mathbf{Cp} + \mathbf{Rp} + \mathbf{Sp} + \sum_{k=1}^d \mathbf{B}^{(k)T} \mathbf{q}^{(k)} = \mathbf{f} \quad (2.48)$$

$$\frac{\partial}{\partial t} \mathbf{Aq}^{(k)} - \mathbf{B}^{(k)} \mathbf{p} + \mathbf{T}^{(k)} \mathbf{q}^{(k)} = 0, \quad (2.49)$$

where $\mathbf{p} = (p_1, p_2, \dots, p_n)$ and $\mathbf{q}^{(k)} = (q_1^{(k)}, q_2^{(k)}, \dots, q_m^{(k)})$ are the coordinate vectors associated with the finite sums in the equations 2.47 which contain the scalar potential field u , and its gradients \vec{g} . The elements in the matrices $\mathbf{A} \in \mathbb{R}^{m \times m}$, $\mathbf{B} \in \mathbb{R}^{m \times n}$, $\mathbf{C} \in \mathbb{R}^{n \times n}$, $\mathbf{S} \in \mathbb{R}^{n \times n}$, and $\mathbf{T} \in \mathbb{R}^{m \times m}$ are defined in the two-dimensional case as:

$$C_{i,j} = \int_{\Omega} \varepsilon_r \varphi_i \varphi_j d\Omega \quad (2.50)$$

$$R_{i,j} = \int_{\Omega} \sigma \varphi_i \varphi_j d\Omega \quad (2.51)$$

$$B_{i,j} = \int_{T_i} \vec{e}_k \cdot \nabla \varphi_j d\Omega \quad (2.52)$$

$$f_i = \int_{\Omega} f \varphi_i d\Omega \quad (2.53)$$

$$A_{i,i} = \int_{T_i} d\Omega \quad A_{i,j} = 0 \quad \text{if } i \neq j \quad (2.54)$$

$$S_{i,j} = \int_{\Omega} \xi \varphi_i \varphi_j d\Omega \quad (2.55)$$

$$T_{i,i}^{(k)} = \int_{T_i} \zeta^{(k)} d\Omega \quad T_{i,j}^{(k)} = 0 \quad \text{if } i \neq j. \quad (2.56)$$

The matrices \mathbf{S} and $\mathbf{T}^{(k)}$ are additional matrices associated with the split-field perfectly matched layer which is defined for the outermost part of the computational domain Ω to eliminate reflections from the boundary $\partial\Omega$ back to the inner part of

Ω . The outermost part is defined as $\{\vec{x} \in \Omega | \varrho_1 \leq \max_k |x_k| \leq \varrho_2\}$. The parameters ξ and $\zeta^{(k)}$ are absorption parameters of the form $\xi(\vec{x}) = \varsigma$, when $\varrho_1 \leq \max_k |x_k| \leq \varrho_2$, and $\zeta^{(k)}(\vec{x}) = \varsigma$, when $\varrho_1 \leq |x_k| \leq \varrho_2$. In other parts of the model $\xi(\vec{x}) = \zeta^{(k)}(\vec{x}) = 0$.

The time domain $[0, T]$ is discretized by the standard finite difference approach into Δt -spaced regular grid of N time points. The temporal discretization of the spatially discretized weak formulation equations 2.48 and 2.49 yields the leapfrog time integration system:

$$\mathbf{p}_{\ell+1} = \mathbf{p}_{\ell} + \Delta t \mathbf{C}^{-1} \left(\mathbf{f}_{\ell} - \mathbf{R}\mathbf{p}_{\ell} - \mathbf{S}\mathbf{p}_{\ell} - \sum_{k=1}^d \mathbf{B}^{(k)T} \mathbf{q}_{\ell+\frac{1}{2}}^{(k)} \right) \quad (2.57)$$

$$\mathbf{q}_{\ell+\frac{1}{2}}^{(k)} = \mathbf{q}_{\ell-\frac{1}{2}}^{(k)} + \Delta t \mathbf{A}^{-1} \left(\mathbf{B}^{(k)} \mathbf{p}_{\ell} - \mathbf{T}^{(k)} \mathbf{q}_{\ell-\frac{1}{2}}^{(k)} \right), \quad (2.58)$$

in which $\ell = 1, 2, \dots, N$ are the time points used to simulate the signal propagation in the spatial domain Ω , and $\mathbf{q}_{\ell-\frac{1}{2}}^{(k)}$ is the gradient of \mathbf{p}_{ℓ} integrated over time.

By defining the auxiliary time-evolution vectors

$$\mathbf{a}_{\ell-\frac{1}{2}}^{(k)} = \mathbf{A}^{-1} \left(\mathbf{B}^{(k)} \mathbf{p}_{\ell} - \mathbf{T}^{(k)} \mathbf{q}_{\ell-\frac{1}{2}}^{(k)} \right) \quad (2.59)$$

$$\mathbf{b}_{\ell+\frac{1}{2}} = -\mathbf{R}\mathbf{p}_{\ell} - \mathbf{S}\mathbf{p}_{\ell} - \sum_{k=1}^d \mathbf{B}^{(k)T} \mathbf{q}_{\ell+\frac{1}{2}}^{(k)}, \quad (2.60)$$

the equations 2.57 and 2.58 can be expressed in a more concise form, emphasizing the permittivity-containing mass matrix \mathbf{C} . The electromagnetic field is hence solved in the Cartesian components by the leapfrog iteration

$$\mathbf{p}_{\ell+1} = \mathbf{p}_{\ell} + \Delta t \mathbf{C}^{-1} \left(\mathbf{f}_{\ell} + \mathbf{b}_{\ell+\frac{1}{2}} \right) \quad (2.61)$$

$$\mathbf{q}_{\ell+\frac{1}{2}}^{(k)} = \mathbf{q}_{\ell-\frac{1}{2}}^{(k)} + \Delta t \mathbf{a}_{\ell-\frac{1}{2}}^{(k)}. \quad (2.62)$$

2.2.4 Formulation of the higher-order Born approximation

The matrix \mathbf{C} in the leapfrog formulation of the time-evolution of the wavefield propagation (Eq. 2.61) is a permittivity-weighted positive definite mass matrix which entries are given by the equation 2.50. To formulate this matrix in the similar way the point-wise permittivity is formulated as the sum of the overall permittivity distribution and perturbation (Eq. 2.41), the matrix \mathbf{C} can be decomposed as the difference

$$\mathbf{C} = \mathbf{C}_1 - \mathbf{C}_2, \quad (2.63)$$

where \mathbf{C}_1 and \mathbf{C}_2 correspond to ε and ρ , respectively. When the perturbation ρ is small enough so that $\|\mathbf{C}_1^{-1}\mathbf{C}_2\| < 1$, the inverse of \mathbf{C} can be expanded as a geometric series for $(\mathbf{I} - \mathbf{C}_1^{-1}\mathbf{C}_2)^{-1}$ as

$$\begin{aligned} \mathbf{C}^{-1} &= (\mathbf{C}_1 - \mathbf{C}_2)^{-1} = (\mathbf{I} - \mathbf{C}_1^{-1}\mathbf{C}_2)^{-1}\mathbf{C}_1^{-1} \\ &= (\mathbf{I} + \mathbf{C}_1^{-1}\mathbf{C}_2 + \mathbf{C}_1^{-2}\mathbf{C}_2^2 + \dots)\mathbf{C}_1^{-1}. \end{aligned} \quad (2.64)$$

Substituting the first-degree polynomial approximation $\mathbf{C}^{-1} \approx (\mathbf{I} + \mathbf{C}_1^{-1}\mathbf{C}_2)\mathbf{C}_1^{-1}$ of the equation 2.64 in the leapfrog equation 2.61, the numerical leapfrog iteration formulae (Eqs 2.61 and 2.62) are formulated as

$$\mathbf{p}_{\ell+1} = \mathbf{p}_{\ell} + \Delta t \mathbf{C}_1^{-1} \left(\mathbf{h}_{\ell} + \mathbf{f}_{\ell} + \mathbf{b}_{\ell+\frac{1}{2}} \right) \quad (2.65)$$

$$\mathbf{q}_{\ell+\frac{1}{2}}^{(k)} = \mathbf{q}_{\ell-\frac{1}{2}}^{(k)} + \Delta t \mathbf{a}_{\ell-\frac{1}{2}}^{(k)}, \quad (2.66)$$

where the term $\mathbf{h}_{\ell} = \mathbf{C}_2\mathbf{C}_1^{-1}(\mathbf{f}_{\ell} + \mathbf{b}_{\ell+\frac{1}{2}})$ is an auxiliary source vector. It can be interpreted as the source vector originating from the perturbation point and hence as the first-order BA of the system. Therefore, it is labelled as

$$\mathbf{h}_{\ell}^{BA,1} = \mathbf{C}_2\mathbf{C}_1^{-1}(\mathbf{f}_{\ell} + \mathbf{b}_{\ell+\frac{1}{2}}). \quad (2.67)$$

The higher order Born approximations are obtained by applying equation 2.67 recursively. Physically, this corresponds to replacing the total field with the incident field at each step at the point of perturbation. The auxiliary source term for the

higher-order BA is thus given by

$$\mathbf{h}_\ell^{BA,n} = \mathbf{C}_2 P_n(\mathbf{C}_1^{-1} \mathbf{C}_2) \mathbf{C}_1^{-1} (\mathbf{f}_\ell + \mathbf{b}_{\ell+\frac{1}{2}}), \quad (2.68)$$

where $P_n(\mathbf{C}_1^{-1} \mathbf{C}_2) = \mathbf{I} + \mathbf{C}_1^{-1} \mathbf{C}_2 + \dots + \mathbf{C}_1^{-n+1} \mathbf{C}_2^{n-1}$ is a matrix-valued polynomial. The detailed derivation of the equation 2.68 and its convergence is shown in Publication III.

2.2.5 Multiresolution approach for the forward and inverse solvers

To speed up the forward model computation, a multiresolution approach [15, 64, 75] is adopted. The fine mesh \mathcal{T} (section 2.2.3) with n nodes is used as basis to recover a coarser, nested d-simplex mesh \mathcal{T}' with M elements $\{T'_1, T'_2, \dots, T'_M\}$ and N nodes $\{\vec{r}_1, \vec{r}_2, \dots, \vec{r}_N\}$, which are shared by the fine mesh ($N < n$). While the resolution of the fine mesh \mathcal{T} is determined by the geometrical constraints of the forward simulation such as the domain structure and the applied wavelength, the resolution of the coarse mesh \mathcal{T}' is chosen based on the desired precision of the reconstruction.

The electric permittivity distribution of the domain is sought in the form

$$\varepsilon = \varepsilon_{bg} + \varepsilon_\rho, \quad (2.69)$$

where ε_{bg} is a constant, fixed, background distribution and ε_ρ a variable perturbation. The permittivity distribution ε within the domain is defined with respect to the elements of the coarse mesh T' and is given by $\varepsilon = \sum_{j=1}^M c_j \chi'_j$. Assuming a piecewise constant permittivity distribution in the fine mesh \mathcal{T} , the permittivity distribution of the fine mesh is given by $\varepsilon = \sum_{j=1}^m c_j \chi_j$. Such a nested mesh structure leads to a natural conclusion that the maximal theoretical reconstruction resolution is lower than that which is used in propagating a wave through the domain.

2.3 Inversion procedure

2.3.1 Linearisation of the discretised forward problem

To solve the forward problem efficiently, the leapfrog formulas (Eqs 2.57 and 2.58) are linearised with respect to the permittivity entry c_j at the permittivity distribution ε as:

$$\frac{\mathbf{p}_{\ell+1}}{\partial c_j} = \frac{\partial \mathbf{p}_\ell}{\partial c_j} + \Delta t \mathbf{C}^{-1} \left(\mathbf{h}_\ell^{\text{diff}} + \frac{\partial \mathbf{b}_{\ell+\frac{1}{2}}}{\partial c_j} \right) \quad (2.70)$$

$$\frac{\partial \mathbf{q}_{\ell+\frac{1}{2}}^{(k)}}{\partial c_j} = \frac{\partial \mathbf{q}_{\ell-\frac{1}{2}}^{(k)}}{\partial c_j} + \Delta t \frac{\partial \mathbf{a}_{\ell-\frac{1}{2}}^{(k)}}{\partial c_j}, \quad (2.71)$$

where $\mathbf{h}_\ell^{\text{diff}}$ is an auxiliary source function originating from the scattering point and defined by

$$\mathbf{h}_\ell^{\text{diff}} = -\frac{\partial \mathbf{C}}{\partial c_j} \mathbf{C}^{-1} (\mathbf{f}_\ell + \mathbf{b}_{\ell+\frac{1}{2}}). \quad (2.72)$$

The more detailed derivation of this linearised form is provided in [64] and in Publication III.

Based on the definition of the permittivity distribution (Eq. 2.69) and the entries of the matrix \mathbf{C} (Eq. 2.50),

$$\left(\frac{\partial \mathbf{C}}{\partial c_j} \right)_{k,l} = \int_{T_j} \varphi_k \varphi_l d\Omega. \quad (2.73)$$

This means that the differential entry $(\partial \mathbf{C} / \partial c_j)_{k,l}$ is non-zero only where φ_k and φ_l are supported on T_j , the elements of the fine mesh \mathcal{T} . The differential of the equation 2.73 can therefore be interpreted as a special case of the first-order BA (Eq. 2.67). Also, the multigrid formulation of the permittivity distribution is valid because the differential update $(\partial \mathbf{C} / \partial c_j)$ to the permittivity distribution differs from zero only at the coarse mesh element $T'_j \in \mathcal{T}'$.

In the reconstruction procedure, the relation between the permittivity vector $\mathbf{x} = (c_1, c_2, \dots, c_M)$ and the discretised electric potential field \mathbf{p} is approximated by

the linearised forward model

$$\mathbf{p}[\mathbf{x}] = \mathbf{p}[\mathbf{x}_0] + \mathbf{J}[\mathbf{x}_0](\mathbf{x} - \mathbf{x}_0), \quad (2.74)$$

in which \mathbf{x}_0 is an *a priori* estimate for the permittivity, and $\mathbf{J}[\mathbf{x}_0]$ the Jacobian matrix consisting of partial derivatives $\partial \mathbf{p}_\ell / \partial c_j$ evaluated at \mathbf{x}_0 and formulated as

$$\frac{\partial \mathbf{p}_\ell}{\partial c_j} = \sum_{\vec{r}_i \in T_j, i \leq n} \mathbf{d}_\ell^{(i,j)}. \quad (2.75)$$

The entries $\mathbf{d}_\ell^{i,j}$ can be computed by solving an auxiliary system which follows from the leapfrog time integration system (Eqs 2.57 and 2.58) by placing $\mathbf{h}_\ell^{\text{diff}}$ (Eq. 2.72) as the source. This procedure is formulated in [75]. The number of the terms in the sum of the equation 2.75 depends on the density of the fine mesh \mathcal{T} , relating to the number of nodes $\vec{r}_i \in \mathcal{T}$. To reduce the number of terms, and the computational work requirement in simulating the model, the multigrid approach is used to redefine the sum 2.75 with respect to the coarse mesh \mathcal{T}' as

$$\frac{\partial \mathbf{p}_\ell}{\partial c_j} \approx \sum_{\vec{r}_i \in T'_j, i \leq N} \mathbf{d}'_\ell^{(i,j)} = \sum_{k=1}^{d+1} \mathbf{d}'_\ell^{(i_k,j)}, \quad (2.76)$$

where the number of terms $d + 1$ is the number of nodes \vec{r}_i belonging to the coarse mesh element T'_j

2.3.2 Deconvolution regularisation parameter

The selection of the contrast factor $c(\rho)$ in the equations 2.42 and 2.46 is related to the permittivity perturbation ρ at the point \vec{r} . As the source term $\tilde{\mathbf{h}}^{BA,n}$ is linear with respect to the perturbation, and the BA is found through the Tikhonov-regularised deconvolution process, the selection of the magnitude of the permittivity perturbation ρ can be associated with choosing an appropriate Tikhonov deconvolution regularisation parameter ν (Publication III). Hence, an update of the form $\rho \rightarrow \gamma \rho$ with $\gamma > 0$ corresponds to $\mathbf{h}^{BA,n} \rightarrow \gamma \mathbf{h}^{BA,n}$. If the estimate to \mathbf{p}_ℓ is updated as $\mathbf{p}_\ell \rightarrow \gamma \mathbf{p}_\ell$, the corresponding deconvolution regularisation parameter is updated as $\nu \rightarrow \gamma^{-1} \nu$. This means that the same effect which follows from a decrease in the perturbation

can be achieved by an increase in the regularisation parameter ν . Therefore, in the numerical evaluation of the BA, any perturbation can be assumed to be $\rho = 1$, and the deconvolution regularisation parameter can be selected with respect to that.

2.3.3 Total variation

In the inversion stage, the linearised forward model (Eq. 2.74) can be written as the linear system

$$\mathbf{y} - \mathbf{y}_0 = \mathbf{L}(\mathbf{x} - \mathbf{x}_0) + \mathbf{n}, \quad (2.77)$$

where \mathbf{y} is the actual data vector relating to the perturbed permittivity distribution, \mathbf{y}_0 relates to the data on the background permittivity distribution ε_{bg} , \mathbf{L} is the Jacobian matrix for the constant *a priori* guess \mathbf{x}_0 , and \mathbf{n} is a noise vector including both modelling and measurement errors. The regularised solution for \mathbf{x} is then obtained by the iteration

$$\mathbf{x}_{\ell+1} = \mathbf{x}_0 + (\mathbf{L}^T \mathbf{L} + \alpha \mathbf{D} \Gamma_\ell \mathbf{D})^{-1} \mathbf{L}^T (\mathbf{y} - \mathbf{y}_0), \quad (2.78)$$

in which Γ_ℓ is a weighting matrix satisfying $\Gamma_0 = \mathbf{I}$ and $\Gamma_\ell = \text{diag}(|\mathbf{D}[\mathbf{x}_\ell - \mathbf{x}_0]|)^{-1}$ for $\ell \geq 1$. The constant α is a regularisation parameter which value is commonly adjusted to the same order of magnitude as $\|\mathbf{y} - \mathbf{y}_0\|^2$. The matrix \mathbf{D} is a regularisation matrix of the form

$$D_{i,j} = \beta \delta_{i,j} + \frac{\ell^{(i,j)}}{\max_{(i,j)} \ell^{(i,j)}} (2\delta_{i,j} - 1), \quad (2.79)$$

$$\delta_{i,j} = \begin{cases} 1 & \text{if } j = i \\ 0 & \text{otherwise.} \end{cases} \quad (2.80)$$

The first term of the equation 2.78 is a weighted identity operator which limits the total magnitude of \mathbf{x} , and the second term penalises the jumps of \mathbf{x} over the edges of the coarse mesh \mathcal{T}' multiplied by the edge length $\ell^{(i,j)} = \int_{T'_i \cap T'_j} ds$. If the regularisation constant $\beta = 0$, the regularisation procedure yields the total variation of \mathbf{x} . If $\beta > 0$ then also the norm of \mathbf{x} is regularised at each iteration step.

Following the detailed derivation in [64], the inversion process minimises the regularising function

$$F(\mathbf{x}) = \|\mathbf{L}(\mathbf{x} - \mathbf{x}_0) - (\mathbf{y} - \mathbf{y}_0)\|_2^2 + 2\sqrt{\alpha}\|\mathbf{D}(\mathbf{x} - \mathbf{x}_0)\|_1, \quad (2.81)$$

which is the sum of the total variation of the estimate and the L2-norm penalty term. The former of these corresponds to the Euclidean norm of the permittivity gradient integrated over \mathcal{D} , while the latter penalises the total magnitude of the distribution. The regularisation parameter α affects the reconstruction quality, and β ensures the numerical stability of the inversion process bounding the reconstruction values. A characteristic of the total variation (TV) regularisation procedure is to yield a low-noise reconstruction with large connected areas close to constant, because the length of the boundary curve between jumps is regularised. This is especially useful in the context where clear-contrast inclusions are sought from a constant background. In the present context, such inclusions would be internal voids, cracks, other higher-contrast details, and the surface layer of the asteroid target.

The multigrid approach [15, 75] can also be used in the inversion stage to reconstruct coarse details before the finer ones. The coarse-to-fine inversion routine alternates between finding the coarse resolution inverse estimate to $\mathbf{x}_{\ell+1}^{\text{coarse}}$ and the fine resolution inverse estimate $\mathbf{x}_{\ell+1}^{\text{fine}}$, in which the variables in the equation 2.78 are computed for both the resolutions separately. The inverse estimate is the sum of the coarse and the fine solutions $\mathbf{x}_{\ell+1} = \mathbf{x}_{\ell+1}^{\text{coarse}} + \mathbf{x}_{\ell+1}^{\text{fine}}$. The validity and details of the approach are explained in [75].

2.3.4 Tomographic backprojection

In tomographic reconstruction, a signal measured in a projection of the target is re-distributed to the image space. Backprojection is a central concept in this procedure. In the presented problem of full-wave tomography, the Born approximation defined in the section 2.2.2 can be interpreted as a differential of the full wave signal with respect to the perturbed permittivity distribution ε (Eq. 2.41). The resulting BA matrix can be associated with an array of the form $\mathbf{L} = [d_1, d_2, \dots, d_N]$, where each column \mathbf{d}_j denotes the BA evaluated at a perturbation point \mathbf{r}_j , as also specified by the Eq. 2.75. Consequently, by defining the perturbed permittivity distribution as $\Delta\mathbf{c} = [\Delta c_1, \Delta c_2, \dots, \Delta c_N]^T$, the signal perturbation $\Delta\mathbf{s}$ corresponding to the per-

mittivity perturbation can be approximated numerically by the product

$$\Delta \mathbf{s} = \mathbf{L} \Delta \mathbf{c}. \quad (2.82)$$

A rough backpropagated reconstruction can be obtained by interpreting the adjoint operation of BA as the tomographic backprojection. The multiplication $\mathbf{L}^T \Delta \mathbf{s}$ is obtained from the equation

$$\Delta \mathbf{s}^T (\mathbf{L} \Delta \mathbf{c}) = \Delta \mathbf{c}^T (\mathbf{L}^T \Delta \mathbf{s}). \quad (2.83)$$

The nonzero entries of the resulting backpropagation matrix correspond to the locations at which a permittivity perturbation contributes to the signal $\Delta \mathbf{s}$ at the specified time interval.

2.4 The radar equation and range resolution

In free space, the radar signal velocity corresponds to the speed of light c through

$$c = \frac{1}{\sqrt{\varepsilon_0 \mu_0}}. \quad (2.84)$$

In an dielectric medium, the signal velocity follows the phase velocity v given in the equation 2.23. In a dielectric medium such as the asteroid interior, the signal velocity can be expressed through the relative electric permittivity of the medium by combining equations 2.23 and 2.24 to yield

$$v = \frac{1}{\sqrt{\varepsilon_r}} \frac{1}{\sqrt{\varepsilon_0 \mu}}, \quad (2.85)$$

where the first term is separated from the second to emphasise the inverse square root dependence of the wave velocity on the relative permittivity of the medium. In applications where the magnetic permeability of the propagation medium can be considered close to that of free space ($\mu \approx \mu_0$), the signal velocity is given by

$$v = \frac{1}{\sqrt{\varepsilon_r}} c. \quad (2.86)$$

In radar signal transmission, an oscillating electric current is supplied to the transmitting antenna, which creates an oscillating electric field around the antenna ele-

ments. The energy of the electric field radiates into the surrounding space as moving electromagnetic waves, and the reflected waves are received by the receiving antenna. The power P_r returning to the receiver is described by the radar equation

$$P_r = \frac{P_t G_t G_r \lambda^2 \sigma_R F^4}{(4\pi)^3 R_t^2 R_r^2}, \quad (2.87)$$

in which P_t is the power of the transmitter, G_t and G_r the gains of the transmitter and the receiver, respectively, λ is the transmitted signal wavelength, σ_R the radar cross-section (or the scattering coefficient of the target), R_t and R_r are the distances from the transmitter and receiver to the target, respectively. The pattern propagation factor F in the equation accounts for complex scattering, multipath, and antenna pattern effects. It is defined by $F = |E/E_0|$, where E is the electric field in the medium and E_0 is the electric field in the free space. For free space with no multipath effect, $F = 1$. In the presence of multipath effects, the value of $F = [0, 2]$, assuming a flat surface for the second reflection in the indirect path, and free space for wave propagation [52]. The propagation factor can also be viewed to describe the constructive and destructive interference of the wave diffracted from surfaces and predicting or controlling it is the most complex task when estimating the signal power returning to the receiver in realistic cases.

The ability of a radar system to distinguish between two or more targets depends on the transmitted signal pulse, the type and size of the targets, and the efficiency of the receiver. The theoretical maximum resolution of a well-designed radar system is one-half of the pulse width time. In radar systems, the transmitted signal pulse is modulated to increase the range resolution as well as improve the signal to noise ratio, and the actual pulse is therefore transmitted in its modulated carrier frequency. In such systems, the range resolution of the radar is not determined by the modulated pulse carrier frequency, but the bandwidth B of the transmitted pulse. The radar range resolution δ_r in a medium is given by

$$\delta_r = \frac{v}{2B}. \quad (2.88)$$

Combining this with the equation 2.86 yields the form distinguishing the effect of

the relative permittivity of the dielectric medium on the range resolution:

$$\delta_r = \frac{1}{\sqrt{\varepsilon_r}} \frac{c}{2B}. \quad (2.89)$$

3 ASTEROID ANALOGUES FOR MICROWAVE RADAR MEASUREMENT

3.1 Asteroid Itokawa model

The Hayabusa spacecraft sent by Japan Aerospace Exploration Agency (JAXA) observed the near-Earth asteroid 25143 Itokawa (Itokawa from now on) during the interval from September through early December 2005. The onboard instruments measured a variety of data to determine the shape, mass, and surface topography, as well as the spectral properties of the asteroid. On 20 and 26 November 2005, the spacecraft landed on the Muses-C region of the asteroid to capture dust particles from the surface. The sample capsule landed back to Earth in Woomera, South Australia, on 13 June 2010. The analysis of the sampled dust particles confirmed the earlier terrestrial remote sensing classification [11] and the remote sensing observation of Hayabusa [1] of Itokawa being an S-type asteroid composed of ordinary LL4 to LL6 chondrites, and indicated that the particles had suffered from long-term thermal annealing and subsequent impact shock, suggesting that Itokawa is a rubble-pile asteroid made of reassembled pieces of the interior portions of a once larger asteroid [55].

The shape of Itokawa resembles a potato or a sea otter. It has a clear "head" region and a "body" region separated by a "neck". The Muses-C region, where the dust samples were collected, is located in the concave part, close to the neck of the asteroid. The surface is smoother in that region, whereas in other parts the terrain is significantly rougher, consisting mainly of numerous boulders. Based on remote sensing spectral analysis [1], there is no substantial difference in the mineralogical composition over the asteroid's surface although the roughness of the terrain varies. Figure 3.1 shows the high-resolution surface model [37] of the asteroid in three directions rotated around the x axis, and the corresponding smoothed surfaces, which

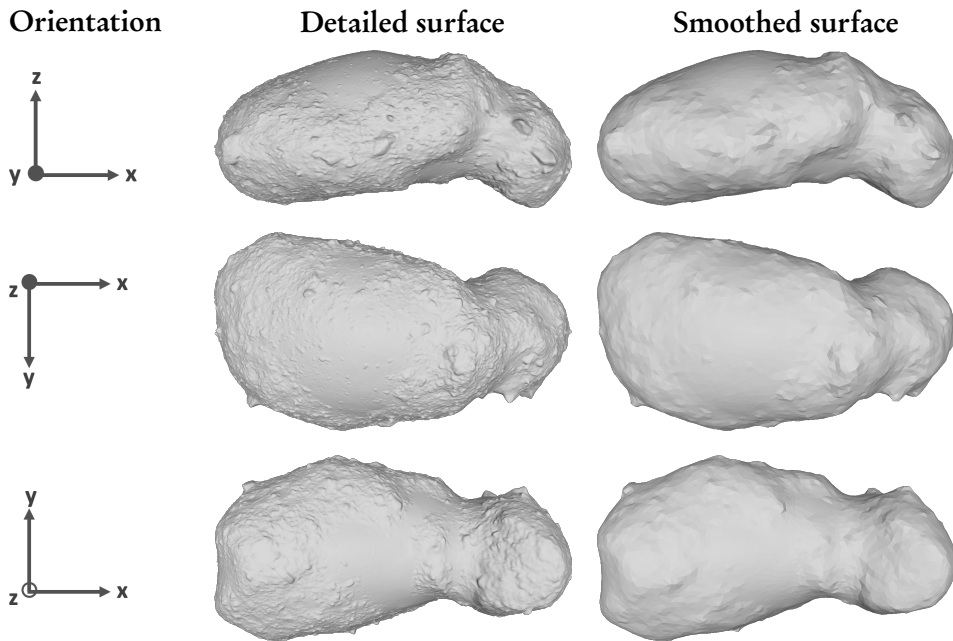


Figure 3.1 The detailed the smoothed model surfaces of the asteroid Itokawa from different views. The smoothed surface was used as the surface for the FE model. The smooth Muses-C region is clearly visible in the bottom views of the asteroid. The data for depicting the high-resolution surface has been obtained from [37].

are used here as a basis for the numerical asteroid model, and the 3D-printed asteroid analogue.

During the rendezvous with Itokawa, the instruments on Hayabusa determined the basic physical characteristics of the asteroid. The orthogonal axes of Itokawa are 535, 294, and 209 meters in the x, y, and z directions, respectively, and the rotational period 12.1 hours [33]. The mass of the asteroid was measured as $(3.58 \pm 0.18) \cdot 10^{10}$ kilograms, and the volume approximately $(1.84 \pm 0.09) \cdot 10^7 \text{ m}^3$ [1]. The estimated bulk density of the asteroid was hence $1.95 \pm 0.14 \text{ g/cm}^3$, which is significantly less than that of S-type asteroids on average [16], suggesting a significant level of macroporosity of up to approximately 40 % of the total volume [33].

To enable a creation of a conforming tetrahedral finite element mesh, the smoothed Itokawa surface (Figure 3.1, right column) was used. The interior structure of the model was based on the physical measurements by Hayabusa on Itokawa [1, 33, 55, 66], and impact simulations, which suggest that the internal porosity of the asteroid

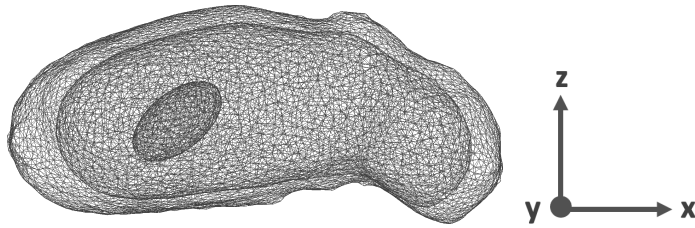


Figure 3.2 The structural FE model of the Detail Model (DM) target domain based on asteroid Itokawa's surface model, showing the different structural compartment surfaces in the ellipsoidal void structure.

varies, and that it increases towards the centre implying a slightly more porous surface [20, 24, 41]. Therefore, the target asteroid domain \mathcal{D} for the three-dimensional Detail Model (DM) based on Itokawa's surface model was constructed to include an interior structure where there is a surface layer (mantle), and a deep interior compartment containing interior details such as an ellipsoidal void. The surfaces of each of the finite element model compartments were meshed with triangular elements providing the nodes and edges for volumetric tetrahedral meshing. The triangular surface mesh structure of the asteroid containing a mantle and an ellipsoidal void is shown in Figure 3.2. The Homogeneous Model (HM), which was used as the background permittivity distribution in the computations, only includes the outer surface of the target domain \mathcal{D} , and a homogeneous permittivity distribution within the interior.

The dielectric permittivity of the model was chosen based on the data on the porosity and mineralogical composition of the model asteroid. The permittivity values of rocky materials found on Earth exhibit some correlation with density. Compact rocks with little porosity usually have relative permittivity values between 3.0 and 10.0 [3] while highly porous materials are found in the lower end of the range. For S-type asteroids, the real part of the electric permittivity is between 7.0 and 10.0 for solid, non-porous material, and the value decreased as the porosity increases, being between 3.7 and 4.8 when the porosity is 40 % [38]. The loss tangent ranges for the solid and 40 % porous materials are 0.010 and 0.007, respectively [38]. Considering that the analysis of the CONCERT signal revealed that the overall real part of the permittivity of the comet 67P/Churyumov-Gerasimenko was 1.27 ± 0.05 , and that the permittivity of dust including 30 percent porosity was less than 2.9 [39], the relative permittivity values for the Itokawa model used here were chosen accord-

ingly thus producing a complex-shaped, high-contrast target for radar tomographic investigations.

The mantle of the asteroid model based on the Itokawa shape was thus assigned the real permittivity value of 3.0, and the interior compartment the value of 4.0. The permittivity of the deep interior ellipsoidal void detail was that of free space, 1.0. These values were used as the target references when constructing the 3D-printed analogue object using the finite element mesh and choosing the appropriate dielectric plastic materials for model printing purposes.

3.2 From a finite element mesh to a 3D-printable object

At the time when 3D-printed analogue objects were being manufactured, the initial numerical results of Publication I on the same Itokawa target domain \mathcal{D} were available, and the initial tetrahedral mesh suitable for carrying out numerical computations existed. The goal of creating the permittivity-controlled 3D-printed wireframe object was to achieve the same target domain structure with details while maintaining the 3D printability of the resulting structure.

The sizing of the analogue was a balance between choosing the maximum target size and weight that could robustly be manufactured with the available conventional single-nozzle fused filament fabrication printer, given that the analogue was to be measured in the quiet zone of the anechoic chamber of Centre Commun de Ressources en Microondes (CCRM), Marseille, which microwave radar covers a frequency band of 2-18 GHz. In the measurement chamber, the target is mounted on a tall polystyrene mast which can hold a mass up to a few kilograms, limiting the total size and weight of the analogue. Furthermore, to allow repeatability of the measurements and accurate positioning of the analogue, the complex-sized target object needs a suitable stand which holds the object accurately in place.

The chosen printing material was the commercially available Preperm ABS450 dielectric filament (Premix Oy, Finland) which diameter is 1.7 mm, density 1.52 g/cm³, and the complex relative permittivity $\varepsilon_{cr} = 4.5 + j0.019$ (loss angle $\varepsilon''_r/\varepsilon'_r = 0.0042$) at 2.4 GHz according to the manufacturer's specifications [60]. This filament was considered suitable because the target real parts of the relative permittivities of the target object were to be $\varepsilon'_r = 4.0$ in the interior compartment, and $\varepsilon'_r = 3.0$ in the mantle. Also the loss angle of the material, accounting for the signal attenuation

was in the appropriate range.

The three-dimensional structure of the analogue was built based on the finite element wireframe mesh, in which the edges of the tetrahedral mesh were inflated by substituting them with prisms, leading to a structure with complex-shaped apertures. The edge length for these apertures depends on the applied edge width and needs to be smaller than $\lambda/4$ of the maximal applied measurement wavelength in order for the structure to appear as a solid with the desired permittivity, and the wireframe mesh not to cause systematic measurement errors. The exact procedure of how this was achieved is given in Publication IV. The described edge inflation procedure results in a volumetric filling of the mesh, slightly affecting the size and shape of the details. However, it is this volumetric filling ratio controlled by the edge width, which allows adjusting the desired permittivity of the object and the local control of permittivity in the three-dimensional structure. The volumetric filling ratio is used as a parameter in material mixing laws which were used to predict the permittivity of the 3D-printed analogue.

3.3 Controlling the electric permittivity of an analogue object

The effective permittivity of an M -component mixture of materials can be estimated by the classical exponential mixture model

$$\varepsilon_{r,m}^a = \sum_{i=1}^M f_i \varepsilon_{r,i}^a, \quad (3.1)$$

in which $\varepsilon_{r,i}$ is the permittivity of the i -th component, f_i is its volumetric filling ratio, and a is an exponential constant which is determined by the application. For soil-water mixtures, the constant $a = \frac{1}{2}$ [13], and for dry snow $a = \frac{1}{3}$ [72]. For a mixture of snow, soil and water the constant is the average of the previous two, $a = \frac{5}{12}$ [71].

Hence, the permittivity $\varepsilon_{r,m}$ of a two-component mixture formed by a dielectric material and air, the exponential mixture model can be written as

$$\varepsilon_{r,m} = \left(1 + (\varepsilon_{r,p}^a - 1)f_p\right)^{1/a}, \quad (3.2)$$

where $\varepsilon_{r,p}$ is the relative permittivity and f_p the volume fraction of the dielectric

plastic.

An alternative model to estimate the dielectric permittivity of a plastic-air mixture is the Maxwell Garnett approximation, in which the effective medium consists of a material matrix with ε_p and air inclusions with ε_i . The electric permittivity of such a mixture is given by

$$\varepsilon_{r,m} = \varepsilon_p \frac{2f_i(\varepsilon_i - \varepsilon_p) + \varepsilon_i + 2\varepsilon_p}{2\varepsilon_p + \varepsilon_i - f_i(\varepsilon_i - \varepsilon_p)}, \quad (3.3)$$

where f_i is the volume fraction of the inclusions given by $f_i = 1 - f_p$ [51].

Wave attenuation in the material is caused by absorption and multiple diffuse Rayleigh and Mie scattering phenomena within the material structures. Absorption rate can be estimated by the distance where the wave field intensity decreases by the factor e^{-1} , the skin depth [77], given by

$$\delta = \frac{1}{2\pi f} \sqrt{\frac{2}{\mu_0 \varepsilon_0 \varepsilon_r'} \left(\sqrt{1 + \left(\frac{\varepsilon_r''}{\varepsilon_r'} \right)^2} - 1 \right)^{-1}}. \quad (3.4)$$

Here, f is the signal centre frequency, and ε_0 and μ_0 are the electric permittivity and magnetic permeability of the vacuum, respectively. The real and imaginary parts of permittivity are denoted by ε' and ε'' , respectively.

The approximate loss rate translating to attenuation in decibels is calculated based on the skin depth δ by

$$\frac{20 \log_{10} e}{\delta}. \quad (3.5)$$

By combining equations 3.4 and 3.5, it is easy to see that the attenuation is directly proportional to the frequency.

With the dielectric specifications of the printing filament (section 3.2), the mixing model equations 3.2 and 3.3 can be used to determine the volume fractions which are required to achieve the target permittivities for analogue objects. Figure 3.3 shows the predicted behaviour of the real and imaginary components of the relative permittivity of the air-plastic mixture and the resulting attenuation in the mixture. The maximum relative error of the real part of permittivity between the exponential model (with $a = \frac{5}{12}$) and Maxwell Garnett is 5.6 %, whereas the maximum error

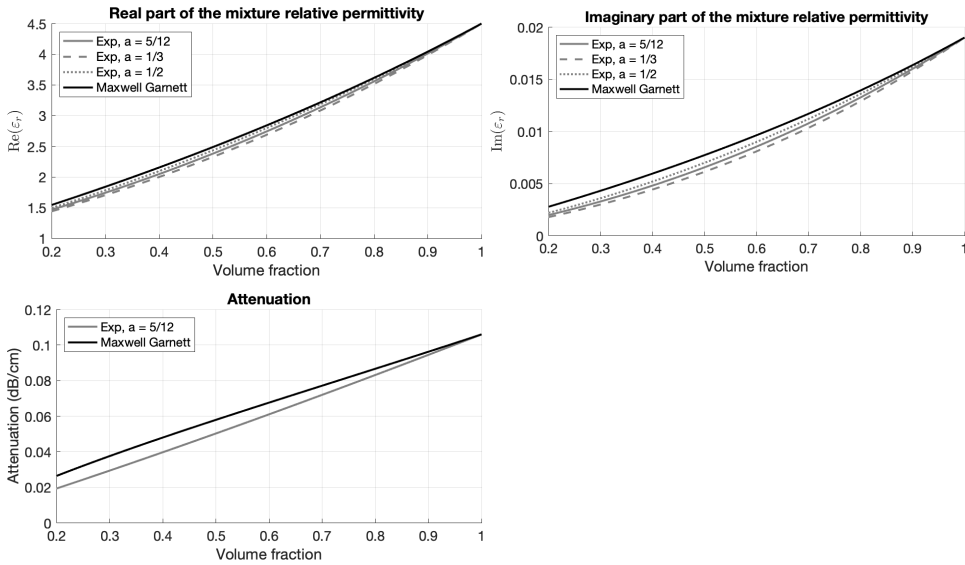


Figure 3.3 The predictions of the real (top left), imaginary (top right) parts of air-plastic permittivities, and attenuation (bottom left) as a function of the plastic volume filling ratios. The permittivity predictions are given based on the exponential model (grey) with three different values of the parameter a , and the Maxwell Garnett model (black). The attenuation predictions have been calculated with the exponential model with the parameter $a = 5/12$ corresponding to the snow-air-water mixture and with Maxwell Garnett model assuming 13 GHz centre frequency.

in the imaginary part may be as large as 40 %. This shows well also in the attenuation curve, where the maximum relative difference between the two models is 37 %. The differences between the permittivity and attenuation predictions are greatest in the lower end of volume fractions, and the values converge towards the filament specifications when the plastic volume fraction approaches 1.

The structural model of asteroid Itokawa used in the numerical computations and building the analogue (Figure 3.2) comprises three compartments: the mantle, the interior, and the deep interior ellipsoidal void, for which the real part of the relative permittivities are 3.0, 4.0 and 1.0, respectively. Based on the evaluation through the mixing laws combined with the chosen filament material, these target permittivities result in volume fractions of 0.66 and 0.90 for the mantle and the interior, respectively. The volume fraction in the void space is 0.0. These targets and predicted values are summarised in Table 3.1.

The open source Matlab (Mathworks, Inc.) implementation of Asteroid Wireframe Package used to create the permittivity-controlled wireframes described here is available in [65]. The package includes the example targets based on the asteroid

Table 3.1 The target permittivities and volume fractions for the analogue model as predicted by the exponential (Exp) and the Maxwell Garnett (MG) mixing laws.

Compartment	Target ε_r	f_p	Prediction model	
			Exp ($a = \frac{5}{12}$)	MG
Mantle	$3.0 + j0.010$	0.66	$2.98 + j0.010$	$3.06 + j0.012$
Interior	$4.0 + j0.016$	0.90	$4.01 + j0.016$	$4.04 + j0.016$



Figure 3.4 Analogue interior structure during the 3D printing process (left) and the final object on the support plate (right). The mantle and the void structures are clearly visible during the additive manufacturing process. During the printing process, the object is surrounded by a support structure which is removed after the printing. The different filling levels of the surface layer and the interior around the void are clearly visible, as is the inflated edge structure. The surface of the final object is fairly smooth despite the wireframe structure being clearly visible. Photos: Sampsa Pursiainen.

Itoawa shape, and the shape of the asteroid 1998 KY₂₆ which was the other analogue reported in Publication IV.

3.4 Manufacturing and validating the 3D-printed analogue target

The created wireframe analogue objects were printed with a single-nozzle Prusa i3 MK3S printer using a nozzle diameter of 0.4 mm and a rectilinear support pattern to stabilise the object on the build plate. The layer height was set to 0.3 mm and the printing temperature was 270-275 °C at the nozzle and 110-112 °C on the plate. The printing process was carried out in the x-y plane of the model and the total printing

time for an analogue object was approximately 5.5 days.

The structure of the analogue object was easily monitored during printing. As shown in Figure 3.4, the relative differences between the volumetric fillings of the interior and the mantle can also be seen visually. The ellipsoidal void is clearly enclosed in the deep interior and the support structure encloses the object during printing. The final objects, which have been cleared out of the support structure, are shown on the right in Figure 3.4 from two different views on their support plates.

The electric permittivity properties of the manufactured object were validated by performing a bistatic far-field electromagnetic scattering experiment [28, 67] on 35 mm diameter test spheres manufactured from the same material and with the corresponding volumetric filling ratios as the mantle and interior compartments in the actual asteroid analogue. Additionally, a solid test sphere was measured to see if the parameters of the filament predict the dielectric properties of a solid after the manufacturing process.

4 COMPUTATIONAL IMPLEMENTATION OF THE RADAR TOMOGRAPHY MODEL

4.1 The 2D computational model structure

The two-dimensional computational model used in studying the performance of the multigrid solver with higher-order Born approximation in Publication III is the same domain Ω used in the earlier work reported in [75]. In the model, the synthetic asteroid target domain \mathcal{D} is placed in an origo-centric structure in which it is enclosed by a circular orbit Ω_2 where the transmitters are located. The outermost domain Ω_1 is a square and it contains a perfectly matched layer which dampens any echoes which propagate away from the domain.

The electric permittivity in the target domain \mathcal{D} was chosen to roughly match the expected permittivities found in asteroids. The surface layer was assigned the relative permittivity $\varepsilon_r = 3$ and for the interior part of the target $\varepsilon_r = 4$. The deep interior details model void space inside the system and hence $\varepsilon_r = 1$. The more detailed reasoning for these permittivity values are given later in the section 3.1 where the electrical permittivity parameters of the 3D model are discussed.

The sizes of the domains Ω_1 and Ω_2 in the unitless computation system are shown in Table 4.1. It also shows the shortest edge length and the time step applied in the wave iteration. Remembering that in the unitless system the wave velocity in free space is set to $c = 1$, the shortest edge length is also the shortest time between the closest mesh points. The selection of the time step satisfies the Courant condition [23] which ensures that the time steps which are used to compute wave propagation in the mesh is smaller than the time it takes for the wave to travel from one grid point to another. The scaling between the unitless and the SI-system units is given in Table 2.1.

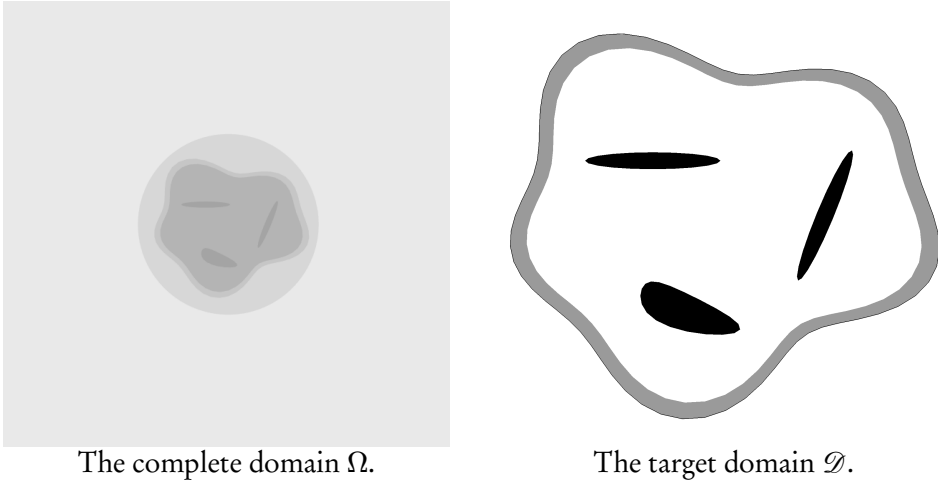


Figure 4.1 The complete computational domain Ω in 2D (left) showing the square domain Ω_1 containing the perfectly-matched layer, and the circular domain Ω_2 which boundary contains the pulse transmitting sources. The target domain \mathcal{D} is enclosed in Ω_2 . The magnification of the target domain \mathcal{D} (right) shows the shape and structure of the target which contains a surface layer (grey) and three internal voids (black).

Table 4.1 Sizing of the unitless 2D computational domain.

Subdomain	Dim.	Unitless size
Square Ω_1	side length	0.80
Circle Ω_2	diameter	0.32
Target \mathcal{D}	[x y]	[0.27 0.24]
Shortest edge		$4.7 \cdot 10^{-4}$
Time step		$2.5 \cdot 10^{-4}$

4.2 The 3D computational model structure

The three-dimensional target domain \mathcal{D} is based on the shape model of asteroid Itokawa [37]. The elongated and complex shape of Itokawa is well suited for testing the capability of the tomographic reconstruction on realistic targets.

In addition to the simple ellipsoidal interior detail model representing a case where the asteroid deep interior would include a significant void cavity or very high contrast material such as metallic boulders, two crack models were created to test whether an irregularly shaped detail could be reconstructed. Additionally, the elec-

tric permittivity of the interior compartment was controlled by a Gaussian random field with a mean $\varepsilon'_r = 4$, standard deviation equal to one, and the correlation between the adjacent lattice points equal to 0.2 to model the rubble-pile nature of the target asteroid with variable density material inside the rubble-pile. The five different asteroid interior models were labelled from (A) to (E) according to Table 4.2. The model (A) forms the general target domain Detailed Model (DM) structure including a mantle and an internal ellipsoidal void, which also formed the basis for creating a 3D-printed analogue described in Publication IV, and was used in Publications V and VI to validate the numerical model with experimental data.

The computational problem is formulated as a far-field model [74] in which an origo-centric cubical domain Ω_1 which encloses the spherical domain Ω_2 is used in the far-field formulation. The target asteroid domain \mathcal{D} is inside the domain Ω_2 (Figure 4.2). The satellites carrying the transmitter and receiver are located in an orbit outside of the domain $\Omega = \Omega_1 \cup \Omega_2$. These transmitter and receiver positions are projected on to the boundary of Ω_2 as shown in [74], and the computational wave propagation is hence initiated at that boundary as a point source transmitting a wave. To simulate an open-field wave propagation and to dampen the wave echoes originating from the boundary of the cubical domain Ω_1 , a perfectly-matched layer was embedded in the domain Ω_1 .

The 3D model allows for a slight variation in the target domain \mathcal{D} size and shape. The sizes of the domains Ω_1 and Ω_2 have been fixed in the unitless system as shown in Table 4.3. For the 3D asteroid Itokawa model, the unitless sizing of the \mathcal{D} is 0.28 in the largest (x coordinate) dimension. The scaling of the unitless parameters to SI-units is the same as with the 2D domain, and is shown in Table 2.1. The quantities which contain spatial dependency are scaled by the spatial scaling factor s obtained by the ratio of the real size of the target divided by the unitless size of the domain \mathcal{D} . The spatial scaling property is particularly useful in designing experiments. The same computational domain can be used in both pure numerical studies and experimental set-ups, where it is possible to scale the simulated quantities to a target size by the spatial scaling coefficient.

In the 3D domain, the total system size increases rapidly with the mesh refinement level and easily reaches the memory limits available for carrying out the computations. In the 3D numerical analysis carried out in this study, the Courant condition is satisfied with the shortest modelled edge length (Table 4.3) which is a balance

Table 4.2 Details in the asteroid models (A)–(E). Sizes are indicated in meters, and with respect to the wavelengths of a 2 MHz signal which was used to investigate the reconstruction quality and resolution in Publication I, and 3.87, and 4.92 MHz signals investigated in Publication V. The Model (A) is referred in this thesis as Detail Model (DM).

Model	Description	Detail	ϵ_r	Detail size		
				Length	Width	Depth
(A)	Single void	Ellipsoid	1	120 m	120 m	55 m
				0.8λ	0.8λ	0.4λ
				1.5λ	1.5λ	0.7λ
				2.0λ	2.0λ	0.9λ
(B)	Highly porous inclusion	Ellipsoid	2	120 m	120 m	55 m
				1.1λ	1.1λ	0.5λ
				2.2λ	2.2λ	1.0λ
				2.8λ	2.8λ	1.3λ
(C)	High-permittivity boulder	Ellipsoid	15	120 m	120 m	55 m
				3.1λ	3.1λ	1.4λ
				6.0λ	6.0λ	2.7λ
				7.6λ	7.6λ	3.5λ
(D)	Deep crack	Crack	1	185 m	10–55 m	10–50 m
				1.2λ	$0.07–0.4\lambda$	$0.07–0.3\lambda$
				2.4λ	$0.1–0.7\lambda$	$0.1–0.6\lambda$
				3.0λ	$0.2–0.9\lambda$	$0.2–0.8\lambda$
(E)	Shallow crack	Crack	1	185 m	10–55 m	10–50 m
				1.2λ	$0.07–0.4\lambda$	$0.07–0.3\lambda$
				2.4λ	$0.1–0.7\lambda$	$0.1–0.6\lambda$
				3.0λ	$0.2–0.9\lambda$	$0.2–0.8\lambda$

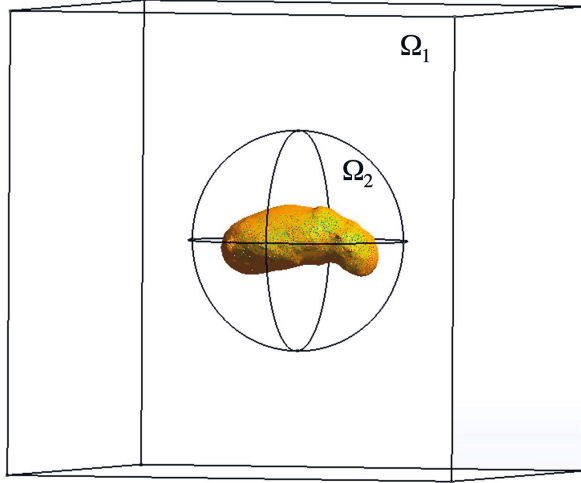


Figure 4.2 The computational model structure showing the cubic domain Ω_1 containing the perfectly-matched layer enclosing the spherical domain Ω_2 and the coloured target domain \mathcal{D} . The radar pulse signal transmitted from outside of the domain Ω_1 is projected onto the spherical boundary of the domain Ω_2 enabling the implementation of the far-field model [74] of signal propagation.

Table 4.3 Sizing of the unitless 3D computational domain.

Subdomain	Dim.	Unitless size
Square Ω_1	side length	0.80
Circle Ω_2	diameter	0.38
Target \mathcal{D}	[x y z]	[0.28 0.15 0.12]
Orbit	distance, r	2.4
Shortest edge		$9 \cdot 10^{-3}$
Time step		$3.1 \cdot 10^{-5}$

between the total system size and a reasonable computation time.

4.3 Measurement point configuration

4.3.1 Numerical study

In the initial numerical study in Publication I, in total 64 measurement point locations with 70 degrees angular coverage between the measurement plane normal and

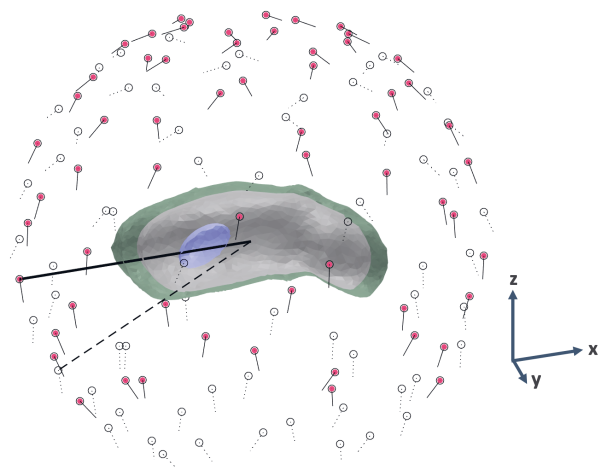


Figure 4.3 The signal configuration used in the numerical study in Publication I showing the 64 transmitter points (coloured dots), the corresponding bistatic receiver points (black circles), and the antenna orientations at each point. The backscattering wave path which data is shown later in Figure 5.1 is shown as a solid black line. The dashed line indicates the wave path to the receiver in the bistatic measurement. The target is shown as a cut-view to reveal the interior structure and the wave path inside the target. It is not in scale with respect to the measurement distance.

the asteroid spin (assumed to spin around the z axis) were evenly distributed on a sphere of radius $r = 2.4$ (Figure 4.3). The measurement was assumed to be carried out by two satellites, of which one acts as both a transmitter and a receiver, providing monostatic measurement of the backscattering data, and the other as a receiver only to yield bistatic reception. The bistatic angle between the satellite antennas was 25 degrees in the longitudinal axis and the orientations were assumed to be tangential with respect to the measurement sphere.

4.3.2 Laboratory measurement configuration

Laboratory measurements on the 3D asteroid analogue were carried out with a microwave radar in the anechoic chamber of the CCRM in Marseille. These source and receiver antenna positions were translated into the numerical model. In the laboratory set-up, the signal is measured by a transmitter-receiver pair with a fixed-angle separation of 12 degrees. The antenna pair was positioned at a fixed distance r from the target and could be moved along the latitudinal and longitudinal axes, resulting in the azimuth and polar angles θ and Φ , respectively. The location of the transmitter

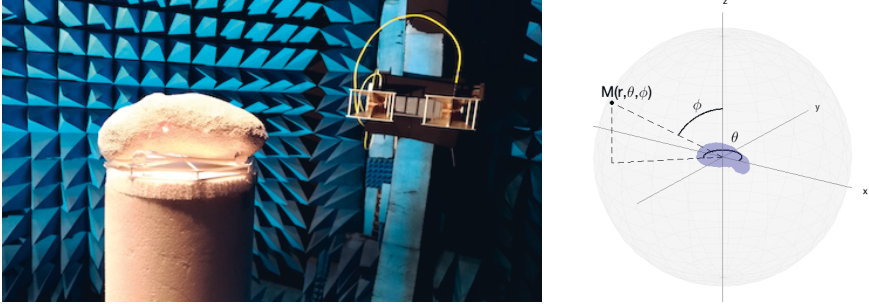


Figure 4.4 The experimental set-up used in the CCRM in Marseille. **Left:** A photograph of the anechoic chamber measurement with the two parallel antennas and the target object. Photo: Jean-Michel Geffrin. **Right:** The definitions of the spherical coordinate angles of the measurement showing the azimuth (θ) and the polar (Φ) angles.

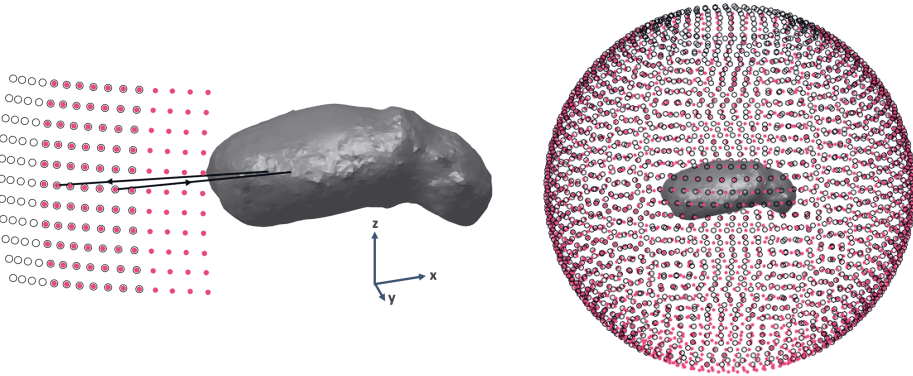


Figure 4.5 The initial laboratory measurement configuration with 121 points covering a small section of the target (left). The source positions are shown in coloured dots and the receivers as black circles. The high-coverage measurement configuration containing 2372 source positions for attempting tomographic imaging of the analogue object (right). The target size and the measurement distance are not in scale, but the spacing between the measurement points is.

was thus defined by the spherical coordinates $M(r, \theta, \Phi)$ (Figure 4.4).

The initial measurement for investigating the validity of the numerical model with respect to the measured data, and to validate the time-domain analysis method against the frequency-based modelling carried out earlier in [30, 31], had a limited-angle coverage of 121 points (Figure 4.5, left). Later, a new, more complete and near-full-coverage laboratory measurement was carried out to enable tomographic imaging of the target (Figure 4.5, right).

4.4 Transmitted signal pulse

The radar pulse of duration T_0 is modelled with a Blackmann-Harris (BH) window for $t \in [0, T_0]$ as

$$h(t) = 0.359 - 0.488 \cos\left(\frac{2\pi t}{T_0}\right) + 0.141 \cos\left(\frac{4\pi t}{T_0}\right) - 0.012 \cos\left(\frac{6\pi t}{T_0}\right), \quad (4.1)$$

and $h(t) = 0$ otherwise. In the unitless quantities, the pulse duration was chosen as $T_0 = 0.12$.

For the low-frequency and bandwidth-based modelling carried out in Publication I, the transmitted signal pulse was a simple BH window function. To model higher frequencies and introduce the carrier wave into the simulation, the pulse is modulated by the Quadrature Amplitude Modulation (QAM) method, which allows amplitude-preserving modulation and demodulation of the signal by a specified carrier frequency f . It is therefore a suitable method for radar signal transmission and measurement.

The quadrature-amplitude-modulated signal $s_f(t)$ is composed of two components, the in-phase component $s_{f,I}(t)$ and the quadrature component $s_{f,Q}(t)$:

$$s_f(t) = [s_{f,I}(t) \ s_{f,Q}(t)]. \quad (4.2)$$

These two components have the mutual phase difference of $\pi/2$. The amplitude of the modulated signal A_f is given by

$$A_f = \sqrt{s_{f,I}^2(t) + s_{f,Q}^2(t)}, \quad (4.3)$$

and the two components are defined as

$$s_{f,I}(t) = \frac{1}{2\pi f} \frac{d}{dt} (s_Q \cos(2\pi f t)) = s_I \cos(2\pi f t) - s_Q \sin(2\pi f t) \quad (4.4)$$

$$s_{f,Q}(t) = \frac{1}{2\pi f} \frac{d}{dt} (s_Q \sin(2\pi f t)) = s_I \sin(2\pi f t) - s_Q \cos(2\pi f t), \quad (4.5)$$

where s_I and s_Q are the in-phase and the quadrature components of the corresponding unmodulated signal $s(t) = [s_I(t) \ s_Q(t)]$. The unmodulated in-phase component

is defined by s_I , and the quadrature component is given by

$$s_Q = 2\pi f \int_0^t s_I(\tau) d\tau \quad \text{with} \quad \max_t |s_Q(t)| \geq \max_t |s_I(t)|. \quad (4.6)$$

The quadrature component s_Q can therefore be modelled by the BH window and the in-phase component s_I with its time derivative according to the equation 4.6. Consequently, the amplitude of the unmodulated signal $s(t)$ is equal to that of the QAM signal $s_f(t)$:

$$A_s = \sqrt{s_I^2(t) + s_Q^2(t)} = \sqrt{s_{f,I}^2(t) + s_{f,Q}^2(t)} = A_f. \quad (4.7)$$

The original signal $s(t)$ can hence be obtained from the modulated signal components through a demodulation process, where the phase ϕ of the carrier wave is sought by maximising the function

$$\begin{aligned} \tilde{s}(t, \psi) &= s_{f,I} \cos(2\pi f t + \psi - \phi) + s_{f,Q} \sin(2\pi f t + \psi - \phi) \\ &= s_I \cos(\psi - \phi) + s_Q \sin(\psi - \phi) \end{aligned} \quad (4.8)$$

at the point $t_{\max} = \operatorname{argmax}_t |s_Q(t)|$ with respect to the demodulation phase ψ translating to $\phi = \operatorname{argmax}_\psi |\tilde{s}(t_{\max}, \psi)|$.

The in-phase and quadrature components of s can therefore be obtained as $s_I = \tilde{s}(t, \phi - \pi/2)$ and $s_Q = \tilde{s}(t, \phi)$. Following from the equation 4.6, the in-phase component $s_I(t_{\max}) = 0$ implying that ϕ maximises the second term in the equation 4.8. Therefore, the signal amplitude A_s and the quadrature component amplitude $|s_Q|$ are maximised at the same point where $A_s = |s_Q|$ and s_I vanish.

4.5 Time-frequency analysis of the measured scattered field

The laboratory measurements yielded the frequency domain scattered field in response to the transmitted continuous waves between the frequency range between 2 and 18 GHz with 0.05 GHz increment. Calibration was done at each frequency so that the incident electric field at the origin had an amplitude of 1 S/m and a null phase, leading to a case where the measurements at a given location correspond to a flat-spectrum point source. Therefore, any time domain pulse shape can be synthe-

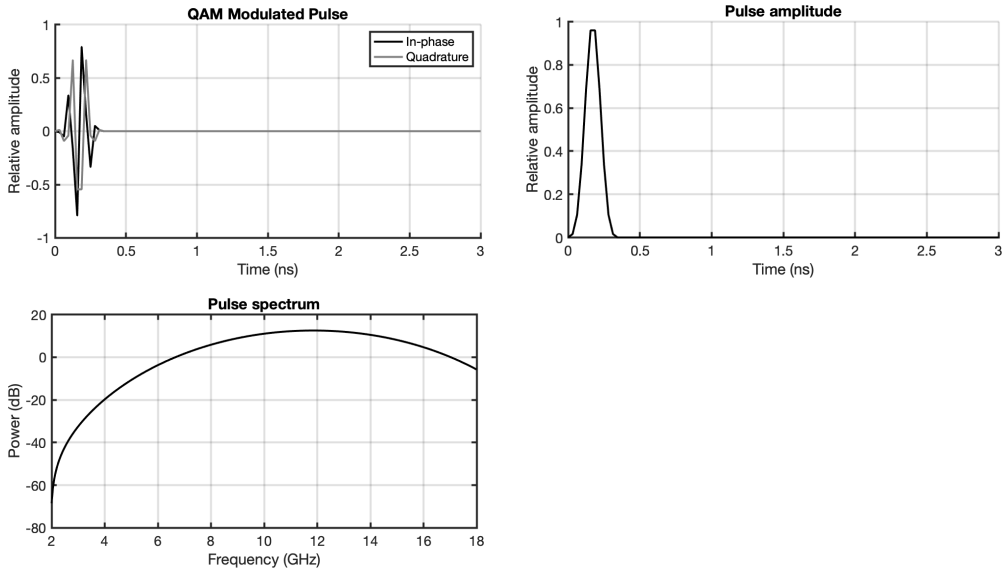


Figure 4.6 The QAM modulated signal pulse with centre frequency of 12.9 GHz and bandwidth of 5.70 GHz showing the in-phase and the quadrature components of the signal, and its spectrum. This pulse was used to convert the scattered fields measured in the laboratory to time domain signals.

sised based on the measurement data.

A quadrature amplitude modulated (QAM) signal pulse can be used as the time domain pulse. In the Publication V, a QAM pulse based on the Blackman-Harris window with $f_c = 12.9$ GHz and 5.70 GHz bandwidth was used. The in-phase and quadrature components, amplitude, and spectrum for such a pulse over the measured frequency range are shown in Figure 4.6. This pulse covers the investigated frequency range regarding the spectrum intensity from -10 to 0 dB with respect to the pulse amplitude. The limit -10 dB was selected to ensure that the signal bandwidth is contained within the measured frequency range.

The scattered field $\mathbf{E}_s(\mathbf{r}; f)$ measured in the frequency domain can be expressed in time domain as a response to a signal pulse s as

$$\mathbf{E}_s(\mathbf{r}; t) = \mathcal{F}^{-1}[\mathbf{E}_s(\mathbf{r}; f)\mathcal{F}[s](f)](t), \quad (4.9)$$

where \mathcal{F} and \mathcal{F}^{-1} are the Fourier transform and its inverse, respectively.

The point-wise scattering effects can be analysed by applying the Born approximation (BA) which gives an estimate for the effect of a single-point permittivity per-

turbation within the target object. It can be formulated via Tikhonov-regularised deconvolution between a wave $u(t)$ originating from the transmitting antenna and the reciprocal wave $p(t)$ emitted by the receiving antenna. At the point of scattering, Born approximation, denoted by $d(t)$, can be formulated as

$$d(t) = \mathcal{F}^{-1} \left[\frac{\mathcal{F}[p](f) \mathcal{F}[u](f)}{\mathcal{F}[s](f) + \nu} \right] (t), \quad (4.10)$$

where the transmitted signal is denoted by s , and the deconvolution regularisation parameter by ν . For any given time point, BA approximates the distribution of the permittivity perturbation effect over the target body. Hence, the time evolution of this distribution reflects the balance between the direct and higher-order scattering events.

4.6 Identification of scattering zones within the analogue

The signal registered at each time point by the receiver is the full wave resulting from scattering events in the object, including direct scattering and multipath effects. The signal traveltime can be used to estimate the locations where direct scattering can have occurred and hence to identify scattering zones within the target. Scattering can be expected to occur at least at the interfaces where the electric permittivity changes. In the DM analogue model, the temporal domain can be divided into four direct scattering zones: (i) Mantle I, in which reflections arise from the air-mantle and mantle-interior interfaces, (ii) Void, in which there are interior-void, and void-interior interfaces, (iii) Mantle II, which is the interior-mantle and mantle-air interfaces, and (iv) Higher-order scattering zone containing the second and higher order reflections within the target. These scattering zones and direct scattering locations are shown in Figure 4.7, and the corresponding time intervals in the measurement configuration used in Publication V are listed in Table 4.4. The scattering zones found in the HM include only the air-interior, interior-air, and higher-order reflections.

The two-way traveltimes at each reflection interface shown in Table 4.4 were determined based on the plane wave propagation predicted by geometrical optics, and accounting for the different paths involving a primary or secondary reflection. The

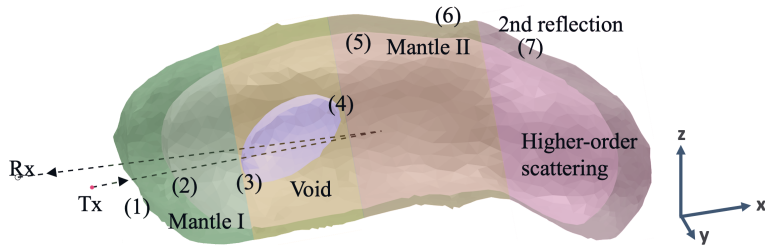


Figure 4.7 The scattering zones in the DM identified based on the two-way signal traveltimes listed in Table 4.4. The dashed black line shows the direct signal path between the transmitter–receiver (Tx–Rx) pair used in Publication V through the origin of the model. The Mantle I zone with the air-mantle (1) and mantle-interior (2) interfaces is shown in green, the Void zone with the interior-void (3) and void-interior (4) interfaces in yellow, the Mantle II zone with the interior-mantle (5) and mantle-air (6) interfaces in nude, and the 2nd reflections containing Higher-order scattering zone with the interface (7) shown in lilac. The target size with respect to the Tx/Rx distance is not in scale and the model has been rotated slightly, as shown by the coordinate axes, to show the angle between the transmitter and receiver.

widths of the zones were calculated based on the duration of the signal pulse and are based on the arrival time of the signal to the receiver. The signal associated temporally with the Higher-order scattering zone involves mainly multipath and multiple scattering effects. In the analysis of the received signal, the time points (1) to (7) are considered of specific interest as they should be identifiable as peaks and used to cross-check the validity between the measured and simulated signals.

Table 4.4 The scattering zones and time points corresponding to the volumetric compartments in the analogue, and their boundaries illustrated in Figure 4.7. The reflections at interfaces (1) to (7) concern the DM, whereas only the interfaces (1), (6), and (7) can be found in the HM. The times are two-way traveltimes and correspond to the laboratory scale measurement.

Zone	Range (ns)	Point ID	Time (ns)	Boundary
Mantle I	11.50–12.12	(1)	11.86	Air–Mantle
		(2)	12.05	Mantle–Interior
Void	12.12–12.71	(3)	12.22	Interior–Void
		(4)	12.48	Void–Interior
Mantle II	12.71–13.50	(5)	12.87	Interior–Mantle
		(6) ^{DM}	13.06	Mantle–Air
		(6) ^{HM}	13.33	Mantle–Air
(2nd reflection)	14.00–15.07	(7) ^{DM}	14.27	Mantle–Air
		(7) ^{HM}	14.80	Mantle–Air

Table 4.5 The studied signal frequencies, bandwidths, measurement distances, and scaling to target sizes. The four last lines give estimates on the target sizes at the listed centre frequencies and bandwidths corresponding to the studied ones in Publication V (lines 4 and 5 of the table).

f_c	Bandwidth	Scale	Size	Size in λ	Distance	Publication
	2.0 MHz	Itokawa	535 m	12.8λ	4.59 km	I
10.1 GHz	5.45 GHz	Analogue	20.5 cm	11.0λ	1.85 m	V
12.9 GHz	5.70 GHz			14.8λ		
3.87 MHz	2.09 MHz	Itokawa	535 m	12.8λ	4.83 km	V
4.92 MHz	2.20 MHz			16.3λ		
10 MHz	5.40 MHz	Any	207 m	11.0λ	1.87 km	V
	4.42 MHz	target	264 m	14.8λ		
20 MHz	10.8 MHz		104 m	11.0λ	0.94 km	
	8.84 MHz		132 m	14.8λ	1.19 km	

4.7 Studied signal frequencies

The studied signal frequencies have been translated to the real target sizes where appropriate in Table 4.5. Furthermore, the target sizes achievable with the studied system sizes are given for 10 MHz and 20 MHz centre frequency radars, as these have been envisioned as possible low-frequency radar frequencies for asteroid imaging purposes [6]. The measurement distances relative to these sizes are also given. These are calculated based on the spatial scaling of the studied distances.

4.8 Computational implementation: GPU-ToRRe-3D

The high-level description of the Matlab (Mathworks, Inc.) implementation of the GPU-ToRRe-3D software package [63] intended for GPU-accelerated radar tomographic reconstruction in 3D, and used to compute the simulated results in this thesis, is shown in Figure 4.8. The software comprises three main modules: (1) Preprocessing, (2) Forward Modelling, and (3) Inverse Modelling. The Preprocessing module is used to create the measurement antenna configuration and the signal path between the measurement points based on the chosen antenna locations. The most intensive computation is carried out by the Forward Modelling module,

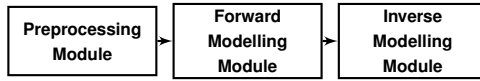


Figure 4.8 The high-level flowchart of the computational implementation of the modules in GPU-ToRRe-3D. The details of the functionalities of each of the modules is given in their dedicated and in Figures 4.9-4.11.

which also contains scripts for computational system creation. The routines in this module refine the finite element mesh given as an input, create the system matrices, and include the routine for GPU-accelerated wave propagation through the system. Each transmitted pulse can be propagated through the system separately, therefore making the computation highly parallelisable, enabling running the simulation in a high-performance GPU computing cluster. The Inverse Modelling module is used to compute the reconstruction of the target based on the forward modelling results. It also includes plotting routines.

The forward computations were carried out in two different high-performance clusters. The forward simulation in the earliest numerical study in Publication I was run in the GPU partition of Tampere Centre for Scientific Computing (TCSC) Narvi cluster (Tampere, Finland) consisting of 8 GPU nodes with 20 CPU cores (4 GPUs in each), totalling altogether 32 NVIDIA Tesla P100 16 GB GPUs. The later forward simulations for Publications V and VI were run in the GPU partition of the Puhti supercomputer of CSC - IT Center for Science Ltd. (Espoo, Finland) containing a total of 80 GPU nodes with a total peak performance of 2.7 petaflops. Each node in Puhti is equipped with Intel Xeon Gold 6230 processors with 20 cores each running at 2.1 GHz. The nodes are each equipped with four NVIDIA Volta V100 GPUs with 32 GB of memory, and with 384 GB of main memory and 3.6 TB of fast local storage.

The local high-performance GPU workstation used to carry out system creation and inversion computations was at first Lenovo P910 equipped with two Intel Xeon E5 2697A 2.6 GHz 16-core processors and 128 GB RAM with two NVIDIA Quadro P6000 GPUs. In autumn 2020, the workstation was upgraded to with Intel Core i9-10900X processors at 3.7 GHz and 256 GB RAM, and with two NVIDIA Quadro RTX 8000 GPUs with 48 GB memory allowing the simulation of either larger systems, or systems with finer mesh and higher frequency.

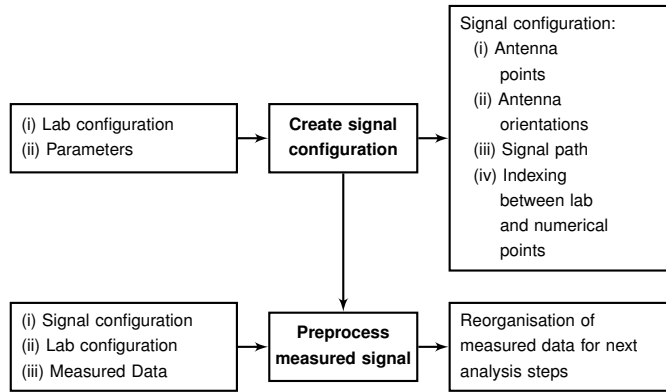


Figure 4.9 The two steps and the outputs of the Preprocessing module which computes the signal transmitter-receiver configurations based on either a laboratory configuration, or user-defined parameters for the transmitter and receiver positions and distances.

4.8.1 Preprocessing module

The Preprocessing module provides scripts which translate the laboratory measurement set-up into the computational domain configuration, or create a theoretical configuration based on the user’s needs. The module also provides methods to preprocess laboratory measurement signals and translates the data into data structures which can later be used in the analysis after the forward modelling step. The produced signal configuration, such as that shown in Figure 4.3, is used as the input for determining the signal transmitter-receiver paths in the forward modelling step.

The work flow in the module is described in Figure 4.9. The left boxes describe the inputs and the right ones the outputs of each of the consecutive stages shown in the middle.

During the preprocessing phase, the discretisation of the full computational domain Ω containing also the target \mathcal{D} is carried out with a suitable 3D meshing software. Here, Gmsh [gmsh] was used for both mesh creation and optimisation. The node and tetrahedral element data were extracted to their separate files which are given as inputs to the system creation script in the Forward Modelling module. There was in total over 2.33 million nodes and 13.7 million tetrahedra in the whole computational domain of the DM of the Model (A) (Table 4.2).

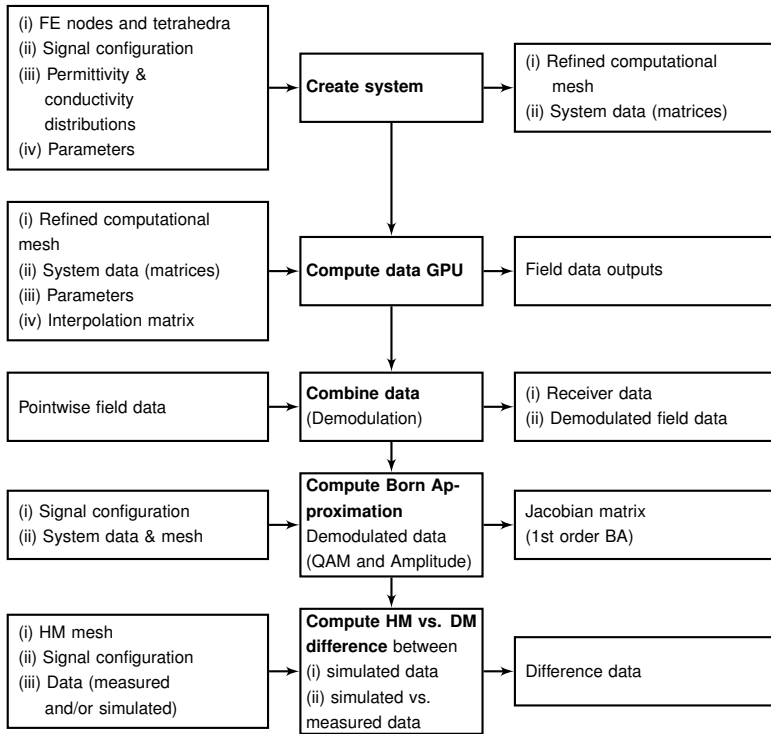


Figure 4.10 Forward Modelling module scripts and functionalities.

4.8.2 Forward Modelling module

The Forward Modelling module is the most computationally intensive part of the package. It includes five main steps (Figure 4.10) starting from system creation (“Create system”) in which the finite element nodes and tetrahedra information and signal configuration created in the earlier step are used to create the fine mesh for the forward computations, and the system matrices \mathbf{C} , \mathbf{R} , and \mathbf{A} given in the equations 2.50, 2.51, and 2.54, respectively.

The second step, the “Compute data GPU” routine, solves the linearised leapfrog time integration system (Eq. 2.70 and 2.71) in which the speed of the iteration is especially affected by finding the inverse of the system matrix \mathbf{C} . The solution to \mathbf{C}^{-1} is sought by using a preconditioned conjugate iteration with a lumped diagonal preconditioner to avoid nonzero entries outside of the diagonal of the matrix and to economise memory consumption. The output of the routine is the field data for each transmitter point. The total maximum memory consumption for each measurement

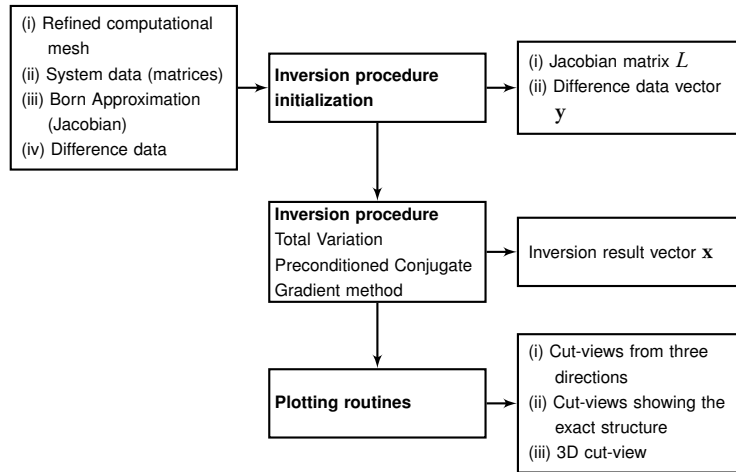


Figure 4.11 Inverse Modelling module scripts and functionalities.

point in the forward simulation in Publications V and VI was 10 GB, and the runtime was approximately 7 hours 50 minutes in the Puhti supercomputer. In Publication I, the system was simulated at a lower frequency and hence the time step was also longer than in the later studies. There, the system size was 4.8 GB and the total runtime for one transmitter point was approximately 3 hours 10 minutes.

Where the signal pulse is modulated to model the carrier frequency rather than only the bandwidth of the pulse, the field data obtained in the second step is demodulated in the third step (“Combine data”). The demodulated data can then be used to compute the Born approximation in the fourth step. Finally, the fifth step in the forward modelling module is the computation of the difference data between the Homogeneous Model and the Detailed Model.

4.8.3 Inverse Modelling module

The Inverse Modelling module (Figure 4.11) currently supports the total variation reconstruction method for computing the inversion of the modelled data. The outputs from the Forward Modelling module are initialised in the first step (“Inversion procedure initialization”) where the Jacobian matrix is reorganised as the lead-field matrix and the difference data vector is constructed. The total variation of the inversion estimate is sought with the preconditioned conjugate gradient (PCG) method. The regularisation parameters α and β in equations 2.79 and 2.81, the number of

total variation iterations, and the number of PCG iterations.

Finally, the inversion result can be plotted with the implemented plotting routines. There are available scripts for plotting cut-views from different directions and positions either with or without the original exact model plotted in the background. Additionally, a 3D cut-view plotting routine is included. For example, the reconstruction result figures presented in the section 5.1 have been created with these routines.

5 RESULTS

5.1 Tomographic inversion of simulated data

Figure 5.1 shows single point backscattering curves for the difference between the simulated Detail Model (DM) (A)–(E) (Table 4.2) and the Homogeneous Model (HM) which contains the constant background permittivity distribution with $\varepsilon'_r = 4$ and lacks any interior details. The time axis has been scaled from the unitless computational system to the SI-units used in a real measurement by using the spatial scaling factor $s = 1911$ and the time scaling formula in Table 2.1. The measurement frequency corresponded to a 2 MHz bandwidth signal, and the measurement distance was to 4.59 kilometres in SI-scale (Table 4.5). The curves show the measured normalised antenna voltages for the signal travelling inside of the target asteroid domain \mathcal{D} and scattering to the receiver. The time axis indicates the two-way traveltime of the signal, starting from the surface of the target. The first peak after $29 \mu s$ can be interpreted to originate from the mantle-interior interface of each of the DMs, as that is the first structural difference between the HM and the DM. The echo from the shallow crack shown in the dashed black line is clearly at approximately $30 \mu s$. The effect it has on the echo is also visible with respect to the other models, as the crack was placed very close to the surface affecting the wave propagation at the mantle-interior interface. The ellipsoidal internal details of the void, highly porous material, and high density boulder are located close to $30.5 \mu s$. The ellipsoidal detail causes the signal to fluctuate, and the effect of the detail permittivity value affects the direction of the signal peak. The deep crack signal is clear at $32 \mu s$, which is the location where it is expected to be seen based on two-way traveltime of the signal in a medium with an average relative permittivity of 4.

Similar curves can be obtained for each of the 64 measurement points in the numerical experiment point cloud (Figure 4.3). The total variation inversion procedure was used to obtain the tomographic inversion of the data. The inversion regularisa-

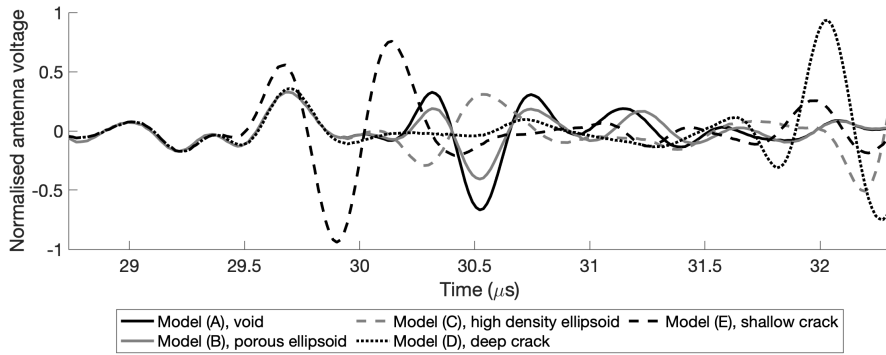


Figure 5.1 The normalised backscattering difference signals between the DM and HM for the five asteroid interior structures shows how the interior details can be interpreted from simple antenna voltage curves. The time axis has been scaled to real size measurement and presents the two-way traveltime from the transmitter to the receiver. The solid black curve indicates the void model (A). The shallow crack (Model (E), dashed black) is easily detectable from the signal alone. The deep crack (Model (D), dotted black) is clearly detectable at $32 \mu s$. The porous ellipsoid (solid grey) gives a signal which is only a slightly different from the void signal, whereas the signal for the high density ellipsoid (dashed grey) clearly is in opposite phase to that of the void.

tion parameters for the models presented here were $\alpha = 0.01$, and $\beta = 0.005$. The parameters were adjusted to these levels based on preliminary experiments in which the goal was to maximise the distinguishability of the interior details and to obtain a range of permittivity values with respect to the exact model.

Figure 5.2 shows the exact model structure and the resulting 3D reconstructions for the models (A), (D), and (E), the void, deep crack, and shallow crack models, respectively. For the void model (A) reconstruction, it also shows the difference between the monostatic and bistatic measurement, where the bistatic measurement appears to give a better-defined and more robust reconstruction of the void detail in comparison to the monostatic one.

The shallow crack (Model (E)) reconstruction was able to localise the crack moderately well, although the shape of the crack could not be reconstructed exactly. This could be expected based on the signal curves in Figure 5.8, because there was such a well-defined echo in the temporal region when the signal was expected to reach the location. The reconstruction for the deep crack (Model (D)) was poor, which is surprising considering how well the crack could be seen in the signal curve. However, as the reconstruction is built from all measured signals, the deep interior details may have such high uncertainty that the exact location and shape of the detail cannot be

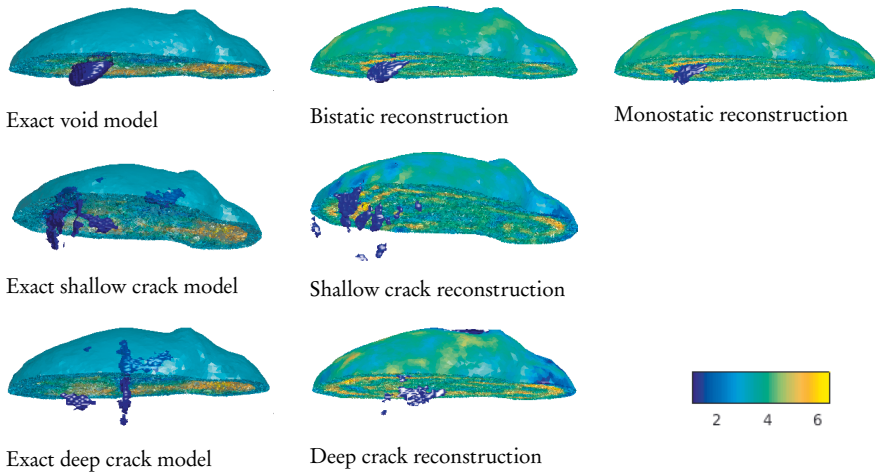


Figure 5.2 3D cut-views of reconstructions of the void and crack models showing the localisation of the details. The colour bar indicates the relative permittivity values in the images.

reconstructed reliably.

The results from the reconstructions were also quantified by calculating the mean square error (MSE), mean absolute error (MAE), and the relative mean absolute error (MAE-R) for the reconstructions (Table 5.1). The MSE and MAE values were computed separately for the interior detail (ellipsoidal anomaly or complex-shaped cracks), the mantle, and the global reconstruction containing the whole structure. The MAE-R was computed for the details only to compare the goodness of detail reconstruction between the models. The errors were noticed to be the greatest in the detail areas and the smallest in the surface layer. This is also evident by visual inspection of the reconstructions, because the majority of the volumes in the void and cracks are not captured in the reconstruction, causing an evident source of error.

Figure 5.2 also shows a comparison between the void detection by a monostatic and bistatic measurement. In the monostatic case, the signal is transmitted and received at the same location, whereas in the bistatic case the signal is transmitted at one point and received at two, giving both the backscattering data and the bistatic data. The reconstruction shows that the bistatic measurement approach provides a slightly more robust reconstruction, as it contains more information on the target during the inversion process.

The effect of noise on the reconstruction was investigated by adding Gaussian noise in the system during inversion. The results are shown with respect to the

Table 5.1 The mean square errors (MSE), mean absolute errors (MAE), and relative mean absolute errors (MAE-R) of the reconstructions for Models (A), (D), and (E) (Table 4.2). The reconstructions for the Models (A), (D), and (E) are shown in Figure 5.2 and reconstructions and these error values for all the models are available in the Publication I.

Model	Error	Detail	Mantle	Global
(A)	MSE	8.21	0.99	1.19
	MAE	2.80	0.89	0.93
	MAE-R	0.93
(D)	MSE	7.10	0.93	1.05
	MAE	2.49	0.89	0.90
	MAE-R	0.83
(E)	MSE	6.86	0.90	1.04
	MAE	2.38	0.87	0.89
	MAE-R	0.79

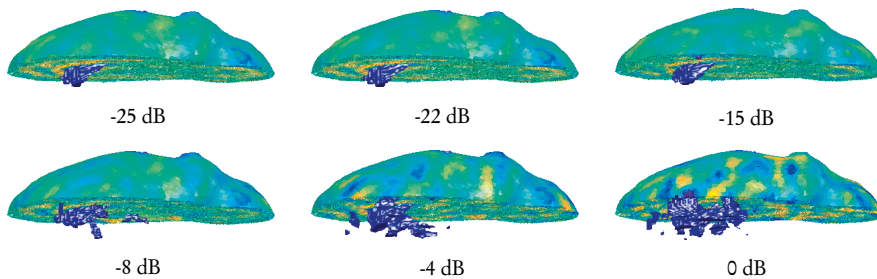


Figure 5.3 The effect of noise on the reconstructions of the void model. The colour scale is as in Figure 5.2.

bistatic measurement of the Model (A) containing the ellipsoidal void (Figure 5.3). The threshold at which noise appears to start affecting the reconstruction is between -15 and -8 dB, between which the localisation and shape detection of the void is lost and the amount of artefacts due to noise increases clearly. This result supports the earlier findings in [74] that the critical noise threshold is around -10 dB.

5.2 The effect of the higher-order Born approximation on reconstruction quality

The effect of the higher-order BA on the reconstruction quality was investigated in the 2D domain (Figure 4.1). The Matlab (Mathworks, Inc.) implementation of the computational routines and the 2D domain is available in GitHub [62]. Four different signal configurations were considered. The Monostatic configuration measurement corresponds to a backscattering experiment where the signal is transmitted and received at the same location. In the Bistatic I configuration, the transmitter and the receiver are separated by a constant 22.5 degree angle. In the Bistatic II configuration, the separating angle is 90 degrees. The Multistatic configuration covers five equally spaced measurement points covering a 90 degree angle, where each two points are separated by a 22.5 angle.

The inversion estimate was sought by total variation (TV, Section 2.3.3) by performing three iteration steps in which a regularised permittivity estimate was found through a single step of the iterative TV regularisation scheme. The TV regularisation parameter values $\alpha = 2\text{E-}1$ and $\beta = 1\text{E-}3$. The Tikhonov regularisation parameter $\delta = 1\text{E-}4$. The parameters were selected based on preliminary tests and experience from [75].

The reconstruction quality was evaluated by visual inspection of the reconstructions (Figure 5.4) as well as by three quantitative measures: (i) the structural similarity (SSIM) between the exact and the reconstructed permittivity distribution, (ii) the mean square error (MSE), and (iii) the relative overlap error (ROE). The relative overlap error was defined as the relative error in overlap between the surface layer and the voids. The MSE and ROE can be used as measures for analysing the value accuracy and localisation of the permittivity details. The values for these quality measures are given in Table 5.2.

Visual evaluation of the reconstructions suggests that both the signal configuration and the order of the BA have a significant effect on the reconstruction quality, and the observation is also supported by the SSIM results showing that the structural similarity between the reconstruction and the exact permittivity distribution increases with the order of BA and when moving from monostatic to bistatic and multistatic measurements. With respect to the measurement configuration, the mul-

Table 5.2 The quantitative quality measures of the reconstruction results in Figure 5.4. The peak-to-peak signal-to-noise ratio (PPSNR) is the relative noise peak level with respect to the amplitude of the difference between the DM and HM data. Structural similarity (SSIM), mean squared error (MSE), and relative overlap error (ROE) were used to measure the quality of the reconstructions. The best value of SSIM is 1 and the best value of MSE and ROE is 0.

Config.	BA order	PPSNR (dB)	SSIM	Global MSE	Void MSE	Surface MSE	Void ROE	Surface ROE
Monostatic	1	13.9	0.896	0.344	0.147	0.102	37.1	22.6
	2	13.9	0.914	0.283	0.171	0.0485	37.3	26.0
	3	13.9	0.918	0.288	0.189	0.0495	34.2	32.0
Bistatic I	1	15.2	0.897	0.419	0.164	0.124	33.6	17.9
	2	15.2	0.916	0.302	0.173	0.0425	39.4	20.6
	3	15.2	0.922	0.285	0.185	0.0387	40.0	23.8
Bistatic II	1	13.9	0.907	0.339	0.140	0.0647	34.2	26.4
	2	13.9	0.916	0.305	0.181	0.0480	38.0	32.6
	3	13.9	0.920	0.303	0.200	0.0493	39.8	36.0
Multistatic	1	-15.2	0.908	0.489	0.232	0.0636	37.7	14.5
	2	-15.2	0.924	0.331	0.208	0.0334	36.5	18.0
	3	-15.2	0.925	0.305	0.209	0.0392	35.9	22.0

tistatic measurement yields superior SSIM results in comparison to monostatic and bistatic configurations.

Increasing the order of BA led to an enhanced global value accuracy for each configuration, as measured by MSE, ROE, and SSIM. Based on a visual evaluation, it also gives a sharper contrast between the structural details and the background. Especially the surface layer is detected better with higher-order BA. For the bistatic configurations, the Bistatic I (22.5 degree angle) performed better than the Bistatic II (90 degree angle) regarding both the MSE and ROE.

5.3 3D-printing of complex-shaped analogue objects

Photographs of the final 3D-printed analogues based on the asteroid Itokawa shape model can be seen in Figures 3.4 and 4.4. The results of the bistatic far-field scattering pattern measurements conducted in the anechoic chamber for the test spheres with

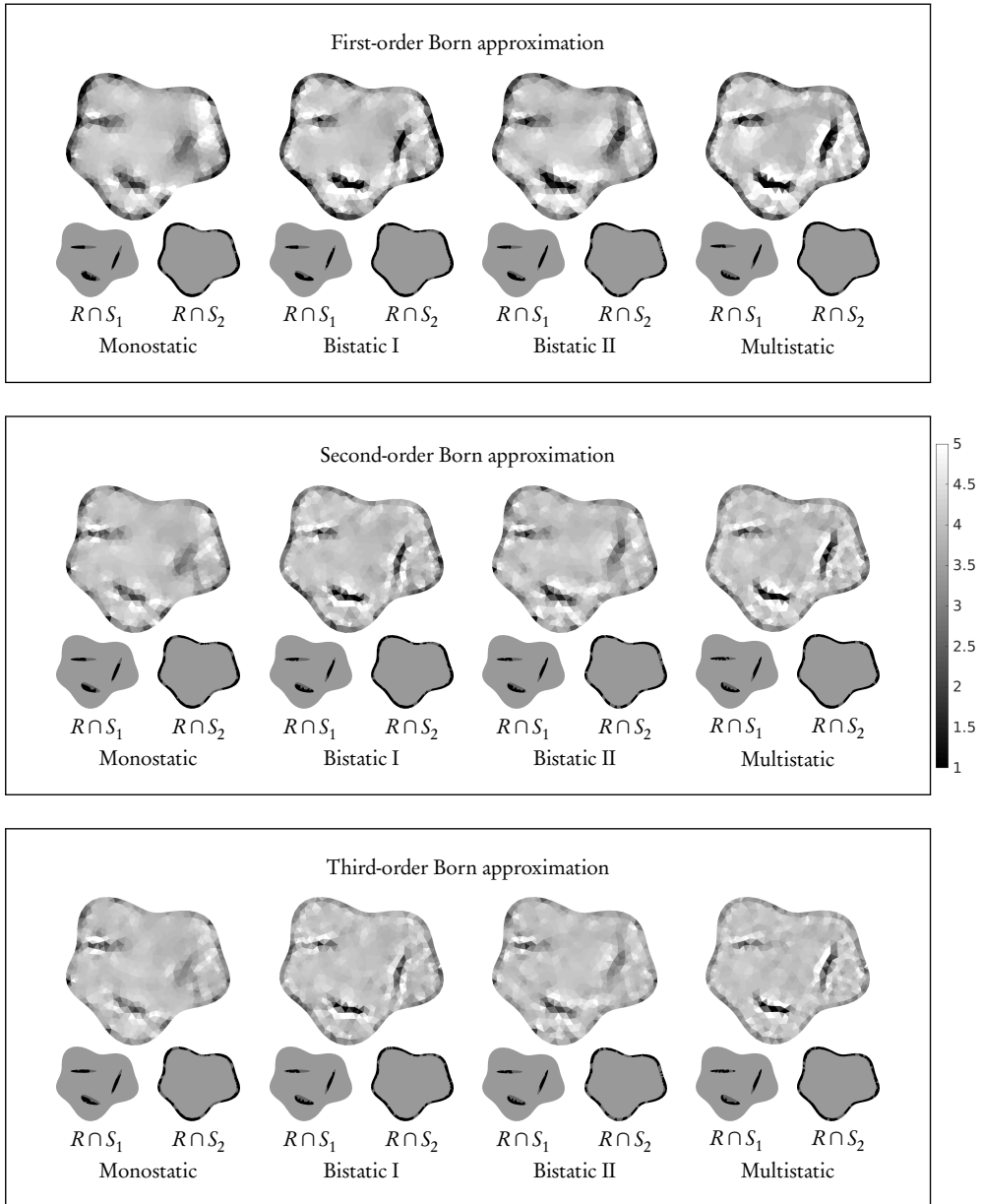


Figure 5.4 The reconstructions of the two-dimensional permittivity distributions for the first, second and third order BAs together with the overlap sets $R \cap S_1$ and $R \cap S_2$. The colour scale is the relative permittivity from 1 (black) to 5 (white). Adapted from Publication III. Reprinted with permission.

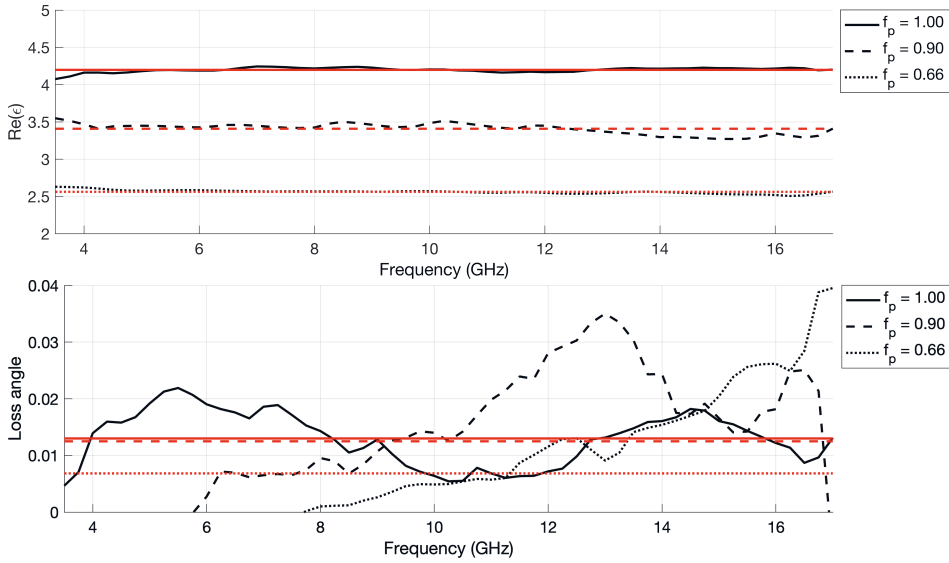


Figure 5.5 The nine-point moving averages of the real part of the relative permittivity (ϵ'_r) and the loss angle (ϵ''_r/ϵ'_r) of the three measured test spheres with different volumetric filling ratios (f_p). The black lines show the actual measurements and the red their corresponding averages.

the volumetric filling ratios corresponding to the ones in the final asteroid analogue surface and interior compartments, are shown in Figure 5.5. The real part of the relative permittivity was fairly stable within the measured frequency range of 2-18 GHz, whereas the imaginary part affecting the conductivity of the material fluctuates strongly within the range, as is described by the loss angle curves. It should also be noted that for the nonsolid test objects, the imaginary part was too low to be discerned by the measurement, especially in the lower end of the frequency range. Therefore, it can be expected that the obtained measurement contains high uncertainty in the imaginary part of the permittivity.

The measured relative permittivities and loss angles in Figure 5.5 are given in Table 5.3 along with the 90 % confidence intervals for the quantities and the expected signal attenuation calculated based on these results by equations (3.4) and (3.5). The results show that the measured 3D-printed object permittivities for the mantle and the interior, $2.56 + j0.02$ and $3.41 + j0.04$, are lower than the predicted target permittivities given by the mixing laws, $3.0 + j0.010$ and $4.0 + j0.016$, respectively (Table 3.1). Furthermore, the signal attenuation in the measured objects was higher than the predicted values (Figure 3.3). However, both the predicted and the measured permittivity and loss values match roughly with the current knowledge about the

Table 5.3 The measured ε_{cr} , and the resulting attenuation, loss angle ($\varepsilon''_r/\varepsilon'_r$) values, and their 90 % confidence intervals for the different volumetric filling fractions f_p . The attenuation values have been determined with respect to a 13 GHz signal centre frequency.

f_p	ε_{cr}	90% conf. of ε_{cr}	Atten. (dB/cm)	Loss angle ($\varepsilon''_r/\varepsilon'_r$)	90% conf. of loss angle
1.00	4.20+j0.05	[4.19+j0.05, 4.21+j0.06]	0.35	0.0130	[0.0119, 0.0141]
0.90	3.41+j0.04	[3.39+j0.03, 3.42+j0.05]	0.22	0.0068	[0.0097, 0.0153]
0.66	2.56+j0.02	[2.56+j0.01, 2.57+j0.02]	0.13	0.0125	[0.0040, 0.0097]

dielectric properties of asteroids [38, 43], and hence, because the relative difference between the permittivities of the two structural compartments is preserved also in the manufacturing phase, this outcome is acceptable. The parameters for the following numerical experiments were adjusted according to these measurement results to match the simulations with the laboratory measurement parameters.

5.4 Comparison of simulated and measured tomographic radar signals

After successful manufacturing of the 3D-printed analogue and determination of the permittivity distribution of the target object, a preliminary tomographic microwave radar measurement was conducted in the anechoic chamber to validate the numerical model with experimental data. A single-point analysis on the match between the measured and simulated full wavefield data was carried out. The wavefields were simulated and measured for both the Homogeneous Model (HM), and the Detail Model (DM), analogues. The resulting frequency-domain measurement data was transformed to the time domain, and the measured data was compared to the simulated data for the HM and DM individually, the difference data between DM and HM were quantified for the simulated and measured data, and the moving peak signal-to-noise ratio was quantified to monitor the quality of the signal in the experiments.

The signal curves in Figure 5.6 show the electric field amplitude at the receiver at each time point specified as the signal round-trip time. The plots also contain colour coding of the zones outlined in Figure 4.7 and Table 4.4 giving a reference to the spatial regions from which the first echo in that time interval can originate from. In the HM data, the outer surface and the backwall echoes are clearly visible and form

the two highest peaks in both the measured and the simulated data. Juxtaposition of the HM and DM data shows that HM lacks most of the peaks observed in the DM data, giving evidence that the interior of the HM indeed is homogeneous and can be seen as the constant permittivity background distribution. In the DM data, the signal peaks are located at the time points predicted by the model zones, and the measurement and simulation peaks coincide very well, although especially the measured peak at the interior-mantle interface in the Mantle II zone (5) produces is nearly double the magnitude of the simulated value. The approximate maximum observed measurement error reflecting the credibility of the measurement is indicated by a shadowed region around the measurement data curves (red line). The deviation between the measurement and simulated data increases along with the time in both the HM and DM data and this is especially prominent in the higher order scattering zone.

The difference curves were calculated between the measured DM and HM data, the measured DM and simulated HM data, and the simulated DM and HM data. The similarity between the first two difference curves and their peaks shown in the middle panel of Figure 5.6 by the blue and red curves, respectively, indicates that the measured and simulated HM signals give similar data, and therefore it could be credible to use the simulated HM data in running the forward model for the background permittivity distribution needed for the inversion stage. However, the magnitude of the amplitudes between the measured and simulated differences is evident as the dashed black difference curve showing data for the simulated difference between the DM and the HM suggests that the measured DM data drives the magnitude of the amplitude data. The difference peaks at the Mantle I and Mantle II zones are the most prominent in the difference data curves containing measurement data, which can be expected as similar peaks are also found in the top panel.

The moving peak signal-to-noise ratio (SNR) in the bottom panel of Figure 5.6 shows the SNR between the measurement and simulation for the DM (dashed blue), HM (solid purple), and the difference between DM and HM (solid brown) signals. The peak SNR comprises the effect of both the measurement and modelling accuracy. The first of these is determined by the laboratory radar performance (SNR > 20 dB), target positioning and orientation errors (≤ 1 mm and ≤ 1 degrees, respectively). The modelling accuracy includes errors in the numerical FETD simulation and in the modelled permittivity distribution, which depends on the accuracy of the

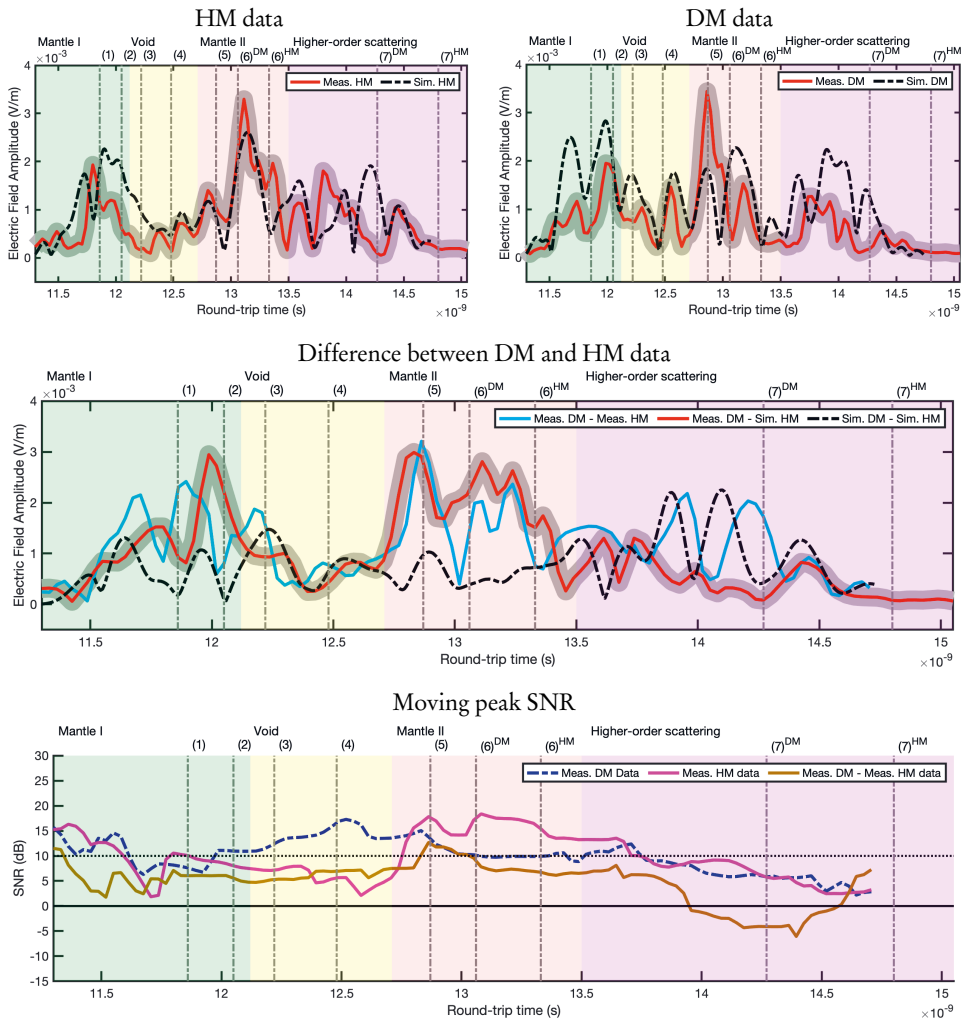


Figure 5.6 A comparison of the between the measurements and finite element time-domain (FETD) simulation data for the centre frequency of 12.9 GHz and vertical ($\Phi\Phi$) polarisation at the central transmitter–receiver position. The approximate maximum observed measurement error is indicated by the shadowed region around the measurement data (red line). The top panel shows the measured and simulated data for the HM (left) and DM (right). The middle panel gives the difference between the DM and HM data in the case of measured or simulated differences. The bottom panel shows the moving peak SNR curves and the reference 10 dB threshold which has been found to enable reliable tomographic inversion of the data. Adapted from Publication V. Reprinted with permission.

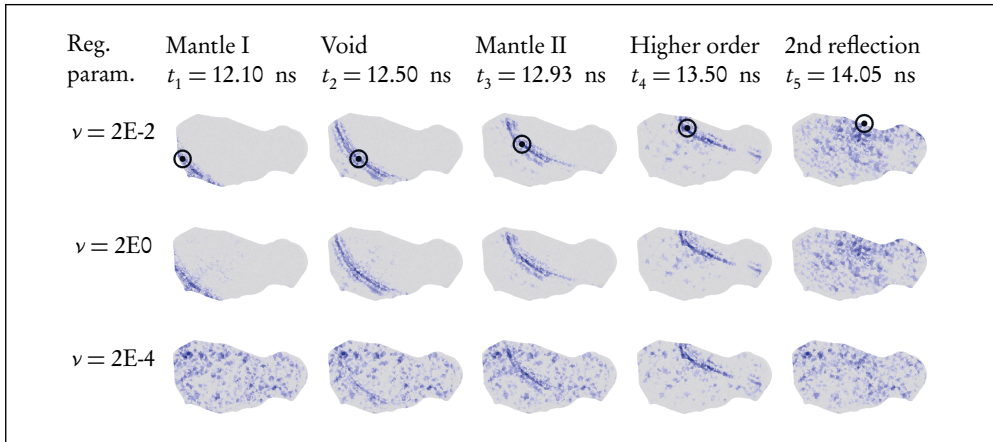
analogue permittivity measurements (Table 5.3), and the accuracy of the analogue mesh edge inflation procedure, which may involve deviations of less than 1.5 % depending on the different surface curvatures of which more details are given in the Publication V. The mean power of the simulated signal was normalised with respect to that of the measured signal, and the length of the moving window is 0.5 ns. The dashed black line in the figure indicates the earlier found 10 dB threshold for obtaining a reasonable reconstruction [74, 75], and also supported by the findings in Figure 5.3 in the Section 5.1) of this thesis and Publication I.

The superior peak SNR is found for the measured DM data in which the peak SNR is maintained at or above 10 dB throughout the interval from 11.95 to 13.4 ns covering the two-way traveltime for the signal from the Mantle I to Void and the major part of the Mantle II zone. Also the early part of the Higher-order scattering zone yields a peak SNR above the threshold. The moving peak SNR for the HM is at its highest in the Mantle II zone, which can be expected from the signal data where the backwall echo is the most prominent source of scattering. The lowest peak SNR is obtained for the difference data between the measured DM and HM data, but also that is above 0 dB except for the later part of the time interval in the Higher-order scattering zone. This can also be expected because the difference data has an overall lower amplitude than either of the DM or HM signals alone.

5.5 Tomographic backpropagation of measured microwave radar data

Figure 5.7 shows the spatial analysis of Born approximation (BA) with different Tikhonov deconvolution regularisation parameters ν in each of the spatial zones identified in Table 4.4 and Figure 4.7. The circled black dots indicate the spatial locations \mathbf{p}_1 - \mathbf{p}_5 giving the maximum absolute value of the wavefield at the identified time points t_1 - t_5 . Overall, the most regular outcome can be achieved with the deconvolution regularisation parameter $\nu = 2E-2$ for both the demodulated QAM and amplitude modulated signal BAs. The overregularised ($\nu = 2E0$) and underregularised ($\nu = 2E-4$) cases are shown for the demodulated QAM signal only. Especially underregularisation gives a noisy BA in comparison to the more optimal regularisation where the propagation of the wavefront is clearly observed throughout the time

Demodulated QAM signal BA



Demodulated Amplitude-based BA

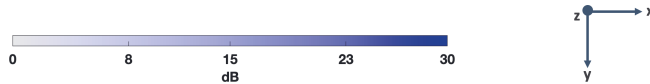
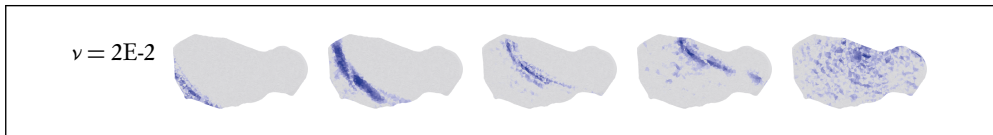


Figure 5.7 The effect of the deconvolution regularisation parameter on the volume-normalised BA of the demodulated QAM and demodulated amplitude-based signals. The circled dot in the top row of the optimally regularised ($\nu = 2E-2$) BA indicates the maximum absolute value of the wavefield at the time point. The overregularised ($\nu = 2E0$) and underregularised ($\nu = 2E-4$) cases are given for the demodulated QAM signal. Adapted from Publication VI. Reprinted with permission.

interval. The BA in the later part of the Higher-order scattering zone accounting for second reflections is noisy despite the regularisation parameter, suggesting that the multipath and complex scattering events yield a wavefield for which differentiating the origins of the components is very difficult.

The curves in the two top panels of Figure 5.8 give time domain data curves for the normalised signal and the normalised amplitude of the signal inside the object at the five spatial points \mathbf{p}_1 – \mathbf{p}_5 . The four bottom panels in the figure show the time domain data for the complete normalised BAs with different deconvolution regularisation parameters.

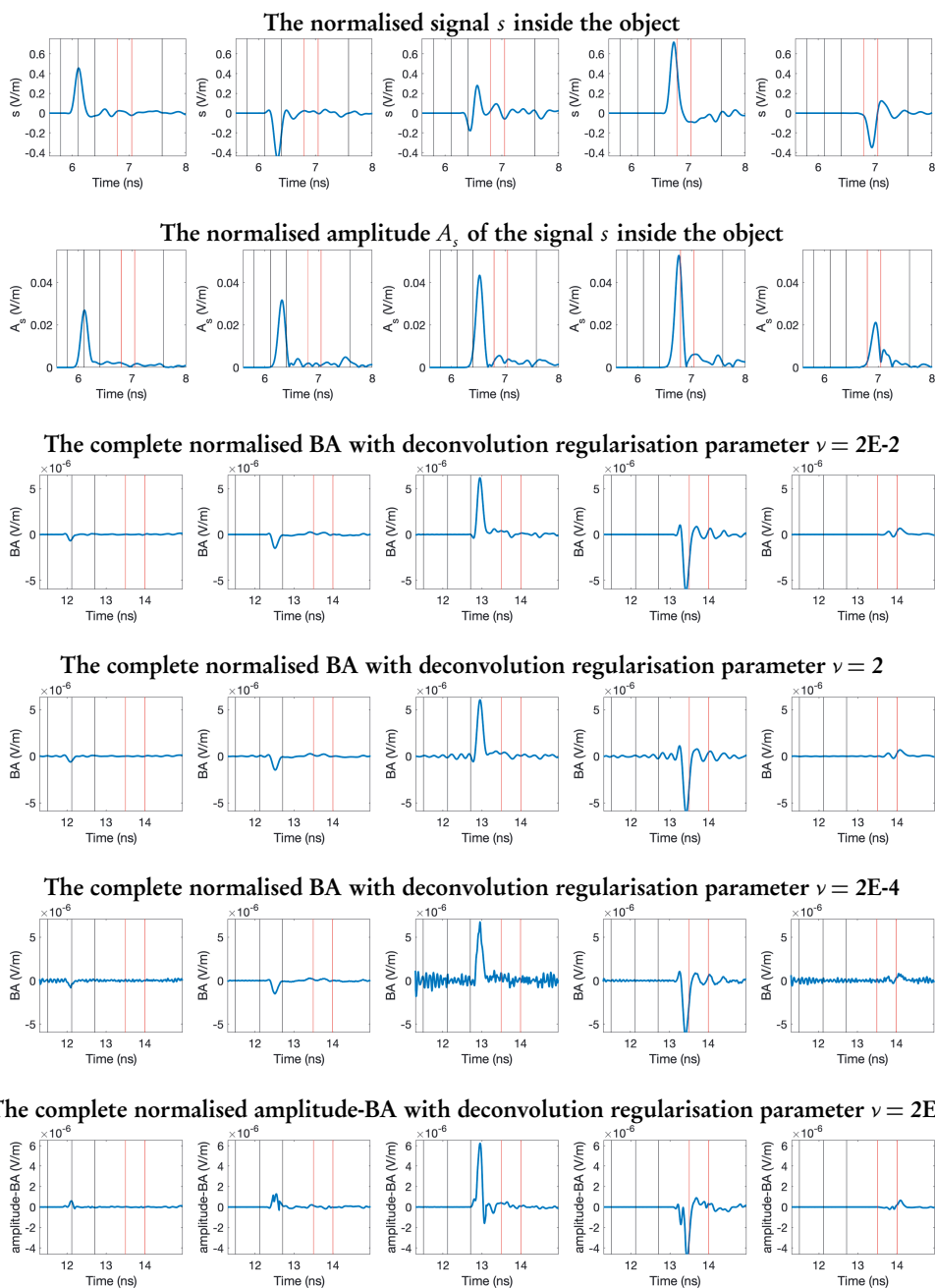


Figure 5.8 The numerical data at the five spatial points p_1 – p_5 , indicated by circled dots in Figure 5.7, showing the wave propagation in time domain and the effect of the deconvolution regularisation parameter on the stability of the signal. Adapted from Publication VI. Reprinted with permission.

Although the difference between the optimal and overregularised BAs is fairly small in the spatial plot in Figure 5.7, the effect of the deconvolution regularisation parameter on the data is evident in the signal curves given in the bottom four panels of Figure 5.8. The optimally regularised data is stable prior to the significant signal peak. In the overregularised and underregularised cases, oscillation artefacts were found to occur, and the frequency of the artefacts increases when the parameter decreases. The overregularised case (Figure 5.8, fourth panel) has preringing artefacts, meaning that fluctuations begin before the actual pulse response occurs. The underregularised case (Figure 5.8, fifth panel) is corrupted by high-frequency noise. The bottom panel of Figure 5.8 gives the optimal regularisation for the demodulated amplitude-based BA. It appears to be less stable than the demodulated QAM BA, and the pulse response is not as smooth as in the case of the demodulated QAM BA.

The optimally-regularised ($\nu = 2E-2$) BAs for the demodulated QAM and amplitude-based signals were used for constructing structural image maps by backpropagation from the measured scattered field obtained in the quasi-monostatic measurement configuration with a single transmitter-receiver pair (Figure 4.5, left). To investigate the effect of the amount of included data as defined by the different scattering zones, the reconstructions were computed and visualised for an increasing amount of time-domain data. The reconstructions are given in Figure 5.9 with the exact DM structure underlaid in the background. The quality of the reconstructions are evaluated visually with respect to the exact structure. The superior reconstruction is obtained when Mantle I to Mantle II, and the Mantle I to Higher-order scattering zone data are included in the inversion (the framed middle panel of the figure). The reconstructions with the demodulated QAM and amplitude-based BAs appear very similar, although the largest differences can be observed in the reconstruction of the mantle, where the reconstruction with the amplitude-based BA appears to be stronger. The reconstruction of the void structure is the most prominent with the demodulated QAM BA, although the localisation of the anomaly is not exact. Some of this deviation may occur due to the absence of the mantle in the HM, which is applied as the reference for the linearisation of the BA. However, because the reconstructions were obtained by single point data, the exact localisation of the interior details cannot be expected.

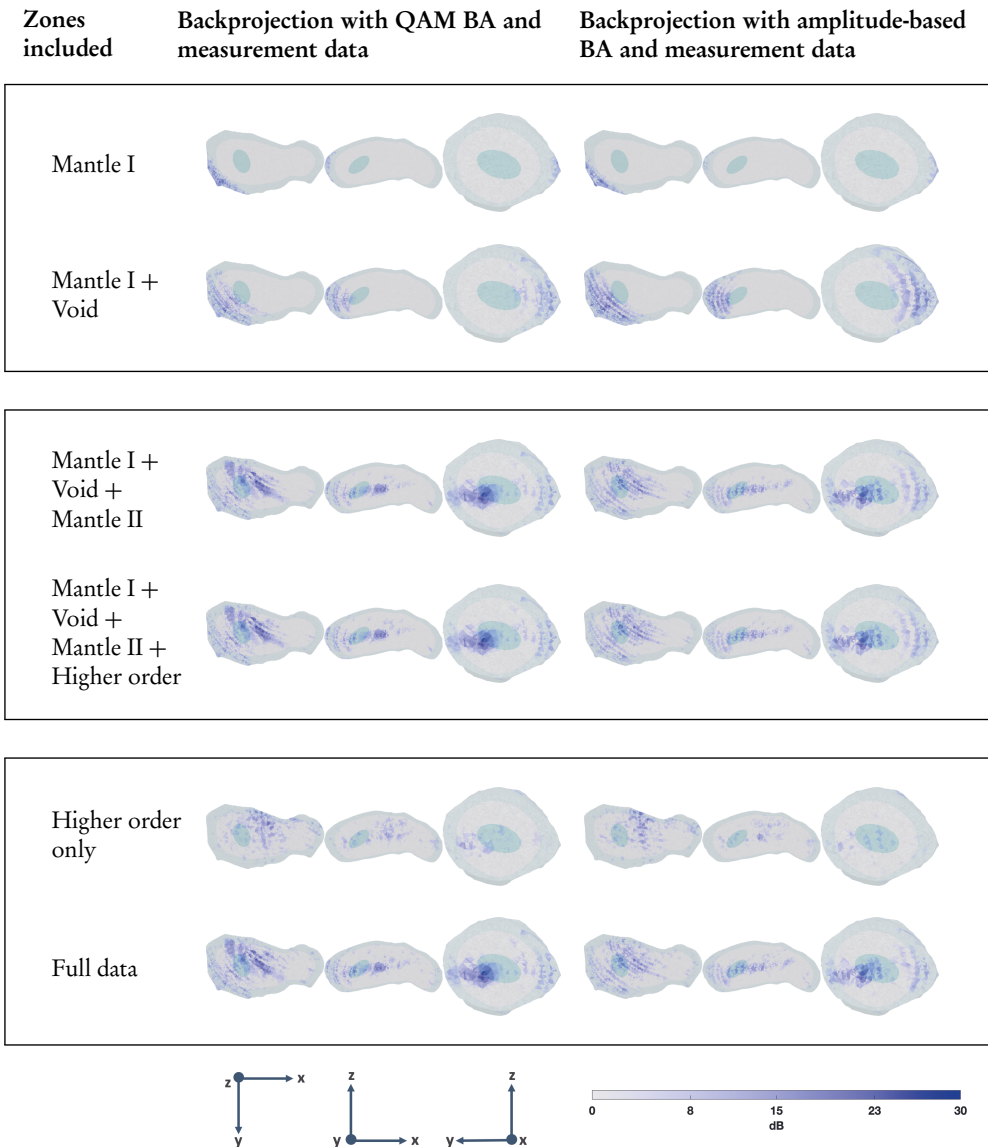


Figure 5.9 Tomographic backprojection of the measured microwave radar measurement data. Reconstructions are shown in blue for both, the demodulated QAM BA (left), and the demodulated amplitude-based BA (right), and for the temporal ranges of data as specified by zones in Table 4.4. The exact DM model structure with the surface layer and the void has been underlaid in the reconstruction background. Adapted from Publication VI. Reprinted with permission.

6 DISCUSSION

This thesis and the publications constituting the thesis use a full-wave approach to investigate the interior structure of asteroids with a low frequency radar operating at 5-20 MHz in a distant orbit, leading to a far-field measurement. The numerical work presented in Publication I shows that computational radar tomographic inversion can be successfully performed on a complex-sized asteroid model, and that internal details such as voids, cracks, and boulders can be detected with a 2 MHz bandwidth signal in an Itokawa-sized target. This means that a tomographic low-frequency radar could be used to investigate the interiors of targets with diameters of up to approximately 500 meters, and that the numerical analysis required to perform the tomographic inversion could be carried out with the currently available high-performance computing resources. In Publications V and VI, a carrier signal was introduced in the modelled pulse enabling the modelling of higher frequencies. The results obtained in these studies, and validated with laboratory measurements by a microwave radar, scale to a 5 MHz centre frequency signal for an Itokawa-size target. Increasing the carrier frequency would lead to a scale-down of the system size so that the doubling of the frequency halves the target size for the feasible computation. The results presented in this thesis can therefore be considered to extend to a 10 MHz radar with a target size of approximately 260 m and 20 MHz radar with a target size of approximately 130 m.

The Juventas Radar, which will be onboard ESA's Hera mission, will operate at 60 MHz centre frequency and 20 MHz bandwidth [40]. The currently available high-performance computing (HPC) graphics processing unit (GPU) resources would allow computing the full-wave tomographic problem for a target of size 40 meters which is a quarter of the size of Dimorphos. Furthermore, to achieve the target centre frequency of JuRa with the present full-wave FETD methodology, the system size will necessarily increase even further, as the higher frequency simulation will also require a higher density finite element mesh in the computational domain and espe-

cially in the target object. Fortunately, advances in the available high-performance computing infrastructures available for researchers will very soon be augmented by LUMI, the EuroHPC supercomputer funded jointly by the EuroHPC Joint Undertaking through the European Union's Connecting Europe Facility, and the Horizon 2020 research and innovation programme. It will start its operations in late 2021. LUMI will be equipped with high bandwidth memory GPU cards enabling significantly higher memory space in comparison to the GPU technologies which were used in the present computations. The technology changes in the HPC infrastructure, and the significant increase in the problem size required by the planetary scientific research questions, will very likely also lead to new HPC implementations of the FETD solver GPU-Torre-3D presented in this thesis.

The reconstruction quality of a radar measurement is impacted by the measurement configuration. The configurations used in the studies in this thesis are sparse in nature, but the number of transmitter-receiver pairs and the locations of the transmitter and receiver with respect to each other were investigated. In Publication I, the bistatic measurement configuration was found to be more robust in comparison to the monostatic one. The optimised bistatic and multistatic configurations yielded superior reconstruction results in comparison to the monostatic and suboptimal bistatic measurements, as reported in Publication III. While most of the radars employed on space missions have been monostatic due to mission payload and especially technology maturity reasons, the development of low-cost miniature satellites may enable the utilisation of fleets of CubeSats in future deep space missions, creating an opportunity for multistatic constellations for tomographic radar experiments in SSSBs [26].

The previous work on full-wave tomography of SSSBs [30, 68] have been done on cometary models with low contrast electric permittivity distributions (the real part of the permittivity has been below 2). The internal permittivity distribution of asteroids can be expected to be significantly higher [38] in comparison to that of comets, which are mainly composed of dust and ice. Therefore, the full-wave inversion problem is presented with new challenges relating to the higher permittivity contrast affecting, for example, more significant attenuation and refraction of the signal inside the body. Moreover, should there be significant void space within the internal structure of an asteroid, the contrast between the free space and the surrounding regolith can be expected to result in interfaces which have high refractory

and reflection properties causing significant changes in both the velocity and the direction of the electromagnetic wave travelling in the medium. The effect of such high contrast regions will result in complex scattering and multipath phenomena both within the body and at the surface of the asteroid. These effects are also more pronounced as the measurement frequency increases, leading to ambiguities in the phase of the wave at the interfaces leading to phase errors affecting the inversion stage. At higher frequencies, the small shift in phase may result in large errors in the final reconstruction, leading to a requirement to use advanced mathematical methods to filter and adjust for these errors during the reconstruction phase. These errors could be handled by, for example, a random sampling procedure in which the independent measurement points are sampled to form sparse subsystems for which reconstructions are computed independently. Averaging these subsystems to produce the final reconstruction would also average the errors, possibly leading to a more robust reconstruction. These multipoint reconstruction methods and handling of higher-frequency phase errors will be an important future research topic in the tomographic reconstruction of complex-shaped and high-contrast targets. They are also necessary for the successful analysis of tomographic radar measurements which will be obtained by the 60 MHz Juventas Radar on Dimorphos.

Time domain modelling of the radar signal is advantageous in that it allows the identification of signal features based on wave traveltime, as was done in Publication V. This can be advantageous especially in the inversion stage because it allows for simple traveltime-based filtering of the data, enabling the exclusion of, for example, second reflections or higher-order scattering which may, especially in the higher frequency signal cases be too noisy for obtaining a reasonable reconstruction without more advanced signal filtering techniques. Additionally, time domain analysis can be used to remove unwanted surface scattering echoes, which, in the event of uneven and irregular surfaces may be a dominant feature in the data masking the weaker signal from the deep interior. The time domain signals of both the measured and the simulated data in this thesis were used to identify the expected scattering interfaces inside the asteroid model, meaning that the outer surface of the mantle, as well as the mantle-interior reflections could be identified in the data. Also the interior-void and void-interior interfaces and especially the interior-mantle and mantle-surface interfaces in the back end of the target yielded high intensity signals.

The missions Hayabusa, Hayabusa-2, and Osiris-REx surveying the asteroids Ito-

ka-wa, 16173 Ryugu, and 1019955 Bennu, respectively, revealed that the surfaces of all these asteroids are covered with a high abundance of boulders and significant size regolith as well as impact craters [33, 73, 76]. For a tomographic radar operating at higher frequencies, such an uneven surface may lead to additional modelling challenges for the simulated signal. The effect of such surface echoes has successfully been investigated by physical optics in [10], and a similar analysis would need to be carried out also with a full-wave approach.

The design requirements of a tomographic radar for investigating the interior structure of a small solar system body need to not only match the parameters given by the measurement environment in the outer space, but also to achieve the appropriate signal penetration depth to ensure sufficient sounding of the target. Signal attenuation depends on the dielectric properties of the target, and on the internal structure causing the multipath and complex scattering phenomena affecting the attenuation. For an asteroid composed of porous materials, the bulk medium attenuation may vary from 8 to 20 dB/km for 50 % porous granite to 10 to 30 dB/km for basalt when sounded with a low-frequency carrier radar operating at 10 MHz [43]. Because the attenuation effects are directly proportional to the frequency, a low-frequency radar operating below the centre frequency of 50 MHz and with a bandwidth of greater than 2 MHz has been suggested for investigating the interior of a near-Earth object with a diameter of less than a few kilometres [12]. Similar parameters, 20-50 MHz centre frequency and 2-5 MHz bandwidth, were suggested for the AI3 mission proposal [5, 6] and formed the initial radar parameters presented in this thesis as well.

Reconstruction of the internal details was feasible up to approximately 10 dB of noise with the realistic 3D asteroid models presented in Publication I. This is similar to the earlier findings in [74, 75] where the similar threshold was found to apply in both 2D and 3D models. Furthermore, a recent study combining envelope inversion with full waveform inversion [25] found the 10 dB threshold to limit the ability to reconstruct the internal details in an asteroid model. For a radar with 20 MHz carrier frequency, the radio noise is dominated by the galactic background noise, which is significantly higher than the antenna thermal noise driving the radar sensitivity to the signal [38, 48]. In the laboratory measurements presented in Publication V, the signal-to-noise ratio was found to be at or above the 10 dB threshold for the most part of the measurement where the signal travelled inside the target suggesting that

the interior details of the surface layer, the deep interior and the internal void in the analogue can be reconstructed. The simple backpropagation analysis of a single-point backscattering data in Publication VI showed a reasonably good localisation of both the mantle and the void. Performing the multipoint tomographic inversion to obtain a reconstruction of this data is the next significant research topic after this thesis.

The radar tomographic measurements can be augmented with other quantities such as gravity field gradient measurements [19, 32], or impact experiments measuring seismic waves [69]. Publication II showed that the gradient of the gravity field can provide meaningful data of the internal distribution of mass, and that this data can be used for tomographic inversion to uncover the internal density distribution of a target object. In contrast to a radar measurement, the investigated gravity field gradient measurements need to be carried out close to the surface of the object to achieve a usable signal-to-noise ratio and to obtain a reconstruction of the internal details such as voids or high density boulders. In practice, manoeuvring a satellite in the close proximity of the target is difficult due to inhomogeneities in the gravity field, and, therefore, in a realistic mission setting, a radioscientific Doppler shift measurement, which has been used for example in the high-precision measurements of the lunar science mission GRAIL (Gravity Recovery and Interior Laboratory) [2, 47, 78], could be employed to obtain gravimetric measurements. The investigation of realistic stable orbits around small target bodies for gravimetric measurements will be an important future research topic in addition to the investigation into how these different data modalities can be combined to improve the inversion result.

Being able to validate numerical results with measurement data is a significant step in increasing the confidence that the results obtained by computational methods also apply in the real astrophysical measurement case. Manufacturing permittivity-controlled, complex-shaped analogue objects with desired interior structures based on a numerical finite element mesh, and performing tomographic radar measurements of the target object in a laboratory, expands the possibilities of studying inversion methods with both simulated and measured data. The developments in commercially available dielectric filament materials ensure that target analogue objects can be manufactured to model a wide range of different permittivity distributions. In this thesis, the investigated interior structure contained a surface layer and a deep interior void. However, the method introduced here can be used to generate any

kind of internal structure, enabling a laboratory measurement of, for example, a crack model.

7 CONCLUSION

The methods and the results presented in this thesis provide the first computational radar tomographic inversion results for complex-shaped and high-contrast target objects providing evidence that tomographic inversion with a sparse measurement set can be successfully carried out for a realistically sized and shaped asteroid. The computational results were also successfully validated with laboratory measurements by a microwave radar on a permittivity-controlled 3D-printed analogue target. The future research will concentrate on multipoint reconstruction of the measured laboratory and computational data, and to investigate the tomographic inversion of signals higher than 20 MHz frequency, up to at least 60 MHz centre frequency and 20 MHz bandwidth. The eventual aim of the research is to support the development of the Juventas Radar onboard ESA's Hera mission, and other planetary scientific missions in the future. This work will hopefully eventually contribute to the inversion of the first direct observations of an asteroid interior.

REFERENCES

- [1] M. Abe, Y. Takagi, K. Kitazato, S. Abe, T. Hiroi, F. Vilas, B. E. Clark, P. A. Abell, S. M. Lederer, K. S. Jarvis, T. Nimura, Y. Ueda and A. Fujiwara. Near-Infrared Spectral Results of Asteroid Itokawa from the Hayabusa Spacecraft. *Science* 312.5778 (2006), 1334–1338. ISSN: 0036-8075. DOI: 10.1126/science.1125718.
- [2] J. C. Andrews-Hanna, S. W. Asmar, J. W. Head, W. S. Kiefer, A. S. Konopliv, F. G. Lemoine, I. Matsuyama, E. Mazarico, P. J. McGovern, H. J. Melosh et al. Ancient igneous intrusions and early expansion of the Moon revealed by GRAIL gravity gradiometry. *Science* 339.6120 (2013), 675–678. DOI: 10.1126/science.1231753.
- [3] A. Annan. Electromagnetic principles of ground penetrating radar. English. *Ground Penetrating Radar Theory and Applications*. Ed. by H. M. Jol. Elsevier Science, 2008. Chap. 1. ISBN: 0444533486;9780444533487;
- [4] E. Asphaug, M. J. S. Belton, A. Cangahuala, L. Keith, K. Klaasen, L. McFadden, G. Neumann, S. J. Ostro, R. Reinert, A. Safaeinili, D. J. Scheeres and D. K. Yeomans. Exploring Asteroid Interiors: The Deep Interior Mission Concept. *Lunar and Planetary Science Conference*. Ed. by S. Mackwell and E. Stansbery. Vol. 34. Lunar and Planetary Inst. Technical Report. Mar. 2003.
- [5] P. Bambach, J. Deller, E. Vilenius, Ö. Karatekin, F. da Silva Pais Cabral, S. Pursiainen, L.-I. Sorsa, K. Wada, T. Kohout, H. Goldberg and P. Tortora. ESA F-Class mission candidate AI3: A mothership/daughters concept to deliver CubeSats to an asteroid. Vol. May 28-29. 8th Interplanetary CubeSat Workshop, Milan, Italy. 2019, A.3.5.
- [6] P. Bambach, J. Deller, E. Vilenius, S. Pursiainen, M. Takala, H. M. Braun, H. Lentz and M. Wittig. DISCUS – The Deep Interior Scanning CubeSat mission to a rubble pile near-Earth asteroid. *Advances in Space Research* 62.12 (2018).

Advances in Technologies, Missions and Applications of Small Satellites, 3357–3368. ISSN: 0273-1177. DOI: 10.1016/j.asr.2018.06.016.

- [7] J.-P. Barriot, W. Kofman, A. Herique, S. Leblanc and A. Portal. A two dimensional simulation of the CONSERT experiment (Radio tomography of comet Wirtanen). *Advances in Space Research* 24.9 (1999), 1127–1138. DOI: 10.1016/S0273-1177(99)80206-3.
- [8] M. Benna, J.-P. Barriot, W. Kofman and Y. Barbin. Generation of 3-D synthetic data for the modeling of the CONSERT experiment (the radiotomography of Comet 67P/Churyumov-Gerasimenko). *IEEE Transactions on Antennas and Propagation* 52.3 (2004), 709–716. DOI: 10.1109/TAP.2004.825564.
- [9] M. Benna, A. Piot, J.-P. Barriot and W. Kofman. Data set generation and inversion simulation of radio waves propagating through a two-dimensional comet nucleus (CONSERT experiment). *Radio Science* 37.6 (2002), 1091. DOI: 10.1029/2002RS002713.
- [10] Y. Berquin, A. Herique, W. Kofman and E. Heggy. Computing low-frequency radar surface echoes for planetary radar using Huygens-Fresnel’s principle. *Radio Science* 50.10 (2015), 1097–1109. DOI: 10.1002/2015RS005714.
- [11] R. P. Binzel, A. S. Rivkin, S. J. Bus, J. M. Sunshine and T. H. Burbine. MUSES-C target asteroid (25143) 1998 SF36: A reddened ordinary chondrite. *Meteoritics & Planetary Science* 36.8 (2001), 1167–1172. DOI: 10.1111/j.1945-5100.2001.tb01950.x.
- [12] R. P. Binzel and W. Kofman. Internal structure of Near-Earth Objects. *Comptes Rendus Physique* 6.3 (2005), 321–326. DOI: 10.1016/j.crhy.2005.01.001.
- [13] J. R. Birchak, C. G. Gardner, J. E. Hipp and J. M. Victor. High dielectric constant microwave probes for sensing soil moisture. *Proceedings of the IEEE* 62.1 (1974), 93–98. DOI: 10.1109/PROC.1974.9388.
- [14] D. M. Blair, L. Chappaz, R. Sood, C. Milbury, A. Bobet, H. J. Melosh, K. C. Howell and A. M. Freed. The structural stability of lunar lava tubes. *Icarus* 282 (2017), 47–55. DOI: 10.1016/j.icarus.2016.10.008.
- [15] D. Braess. *Finite elements: theory, fast solvers, and applications in elasticity theory*. English. 3rd. Cambridge: Cambridge University Press, 2007. ISBN: 05217 05185; 9780521705189;

- [16] D. Britt, D. Yeomans, K. Housen and G. Consolmagno. Asteroid Density, Porosity, and Structure. *Asteroids III*. Ed. by W. F. Bottke, A. Cellino, P. Paolicchi and R. P. Binzel. The University of Arizona Press, 2002, 485–500.
- [17] L. Bruzzone, J. Plaut, G. Alberti, D. Blankenship, F. Bovolo, B. Campbell, A. Ferro, Y. Gim, W. Kofman, G. Komatsu, W. McKinnon, G. Mitri, R. Orosei, G. Patterson, D. Plettemeier and R. Seu. RIME: Radar for Icy Moon Exploration. *2013 IEEE International Geoscience and Remote Sensing Symposium - IGARSS*. 2013, 3907–3910. DOI: 10.1109/IGARSS.2013.6723686.
- [18] R. Carley and E. Heggy. Finite difference time domain simulation of radar wave propagation through comet nuclei models. *Meteoritics & Planetary Science* 43 (June 2008), 1085–1095. DOI: 10.1111/j.1945-5100.2008.tb00695.x.
- [19] K. Carroll and D. Faber. Tidal Acceleration Gravity Gradiometry for Measuring Asteroid Gravity Field From Orbit. Oct. 2018. DOI: 10.13140/RG.2.2.36134.98886.
- [20] B. Carry. Density of asteroids. *Planetary and Space Science* 73.1 (2012), 98–118. DOI: 10.1016/j.pss.2012.03.009.
- [21] W. C. Chew and Y. M. Wang. Reconstruction of two-dimensional permittivity distribution using the distorted Born iterative method. *IEEE Transactions on Medical Imaging* 9.2 (June 1990), 218–225. ISSN: 0278-0062. DOI: 10.1109/42.56334.
- [22] V. Ciarletti, A. C. Levasseur-Regourd, J. Lasue, C. Statz, D. Plettemeier, A. Hérique, Y. Rogez and K. W. CONSERT suggests a change in local properties of 67P/Churyumov-Gerasimenko’s nucleus at depth. *A&A* 583 (2015), A40. DOI: 10.1051/0004-6361/201526337.
- [23] R. Courant, K. Friedrichs and H. Lewy. *On the Partial Difference Equations of Mathematical Physics*. English. California University Los Angeles, 1959.
- [24] J. F. Deller. Hyper-Velocity Impacts on Rubble Pile Asteroids. PhD thesis. School of Physical Sciences University of Kent Canterbury U.K. and International Max Planck Research School for Solar System Science Göttingen Germany, 2017.

- [25] J. Deng, W. Kofman, P. Zhu, A. Hérique, R. Liu and S. Zheng. EI + FWI Method for Reconstructing Interior Structure of Asteroid Using Lander-to-Orbiter Bistatic Radar System. *IEEE Transactions on Geoscience and Remote Sensing* (2021), 1–16. DOI: 10.1109/TGRS.2021.3079240.
- [26] *CDF study report: Small Planetary Platforms (SPP) in NEO and MAB*. <http://sci.esa.int/future-missions-department/60411-cdf-study-report-small-planetary-platforms-spp/>. Accessed 10 October 2018. 2018.
- [27] L. C. Evans. *Partial Differential Equations (Graduate Studies in Mathematics)*. English. Providence, RI: American Mathematical Society, 1998.
- [28] C. Eyraud, J.-M. Geffrin, A. Litman and H. Tortel. Complex Permittivity Determination From Far-Field Scattering Patterns. *IEEE Antennas and Wireless Propagation Letters* 14 (2015), 309–311. DOI: 10.1109/LAWP.2014.2362995.
- [29] C. Eyraud, J.-M. Geffrin, P. Sabouroux, P. Chaumet, H. Tortel, H. Giovannini and A. Litman. Validation of a 3D bistatic microwave scattering measurement setup. *Radio Science* 43 (2008), RS4018. DOI: 10.1029/2008RS003836.
- [30] C. Eyraud, A. Herique, J.-M. Geffrin and W. Kofman. Imaging the interior of a comet from bistatic microwave measurements: case of a scale comet model. *Advances in Space Research* 62 (2018), 1977–1986. DOI: 10.1016/j.asr.2017.10.012.
- [31] C. Eyraud, H. Saleh and J.-M. Geffrin. Influence of the description of the scattering matrix on permittivity reconstruction with a quantitative imaging procedure: polarization effects. *JOSA A* 36 (2019), 234–244. DOI: 10.1364/JOSAA.36.000234.
- [32] R. L. Forward. Asteroid Mass Distribution Measurement with Gravity Gradiometers. *NASA Special Publication*. Ed. by T. Gehrels. Vol. 267. 1971, 585.
- [33] A. Fujiwara, J. Kawaguchi, D. K. Yeomans, M. Abe, T. Mukai, T. Okada, J. Saito, H. Yano, M. Yoshikawa, D. J. Scheeres, O. Barnouin-Jha, A. F. Cheng, H. Demura, R. W. Gaskell, N. Hirata, H. Ikeda, T. Kominato, H. Miyamoto, A. M. Nakamura, R. Nakamura, S. Sasaki and K. Uesugi. The Rubble-Pile Asteroid Itokawa as Observed by Hayabusa. *Science* 312.5778 (2006), 1330–1334. ISSN: 0036-8075. DOI: 10.1126/science.1125841.

- [34] C. Grima, W. Kofman, J. Mouginot, R. J. Phillips, A. Hérique, D. Biccari, R. Seu and M. Cutigni. North polar deposits of Mars: Extreme purity of the water ice. *Geophysical Research Letters* 36.3 (2009). DOI: 10.1029/2008GL036326.
- [35] O. S. Haddadin and E. S. Ebbini. Adaptive regularization of a distorted Born iterative algorithm for diffraction tomography. *Proceedings of 3rd IEEE International Conference on Image Processing*. Vol. 2. IEEE. 1996, 725–728. DOI: 10.1109/ICIP.1996.560985.
- [36] J. Haruyama, T. Kaku, R. Shinoda, W. Miyake, A. Kumamoto, K. Ishiyama, T. Nishibori, K. Yamamoto, K. Kurosawa, A. Suzuki et al. Detection of lunar lava tubes by lunar radar sounder onboard SELENE (Kaguya). *Lunar and Planetary Science Conference*. Vol. 48. 2017.
- [37] *Itokawa shape model*. <https://darts.isas.jaxa.jp/planet/project/hayabusa/shape.pl>. Accessed 4 November, 2019. 2007.
- [38] A. Hérique, B. Agnus, E. Asphaug, A. Barucci, P. Beck, J. Bellerose, J. Biele, L. Bonal, P. Bousquet, L. Bruzzone, C. Buck, I. Carnelli, A. Cheng, V. Ciarelli, M. Delbo, J. Du, X. Du, C. Eyraud, W. Fa, J. G. Fernandez, O. Gassot, R. Granados-Alfaro, S. Green, B. Grieger, J. Grundmann, J. Grygorczuk, R. Hahnel, E. Heggy, T.-M. Ho, O. Karatekin, Y. Kasaba, T. Kobayashi, W. Kofman, C. Krause, A. Kumamoto, M. Küppers, M. Laabs, C. Lange, J. Lasue, A. Levasseur-Regourd, A. Mallet, P. Michel, S. Mottola, N. Murdoch, M. Mütze, J. Oberst, R. Orosei, D. Plettemeier, S. Rochat, R. RodriguezSuquet, Y. Rogez, P. Schaffer, C. Snodgrass, J.-C. Souyris, M. Tokarz, S. Ulamec, J.-E. Wahlund and S. Zine. Direct observations of asteroid interior and regolith structure: Science measurement requirements. *Advances in Space Research* 62 (2018), 2141–2162. DOI: 10.1016/j.asr.2017.10.020.
- [39] A. Herique, W. Kofman, P. Beck, L. Bonal, I. Buttarazzi, E. Heggy, J. Lasue, A. C. Levasseur-Regourd, E. Quirico and S. Zine. Cosmochemical implications of CONSERT permittivity characterization of 67P/CG. *Monthly Notices of the Royal Astronomical Society* 462.Suppl_1 (Mar. 2017), S516–S532. ISSN: 0035-8711. DOI: 10.1093/mnras/stx040.
- [40] A. Herique, D. Plettemeier, H. Goldberg and W. Kofman. JuRa: the Juventas Radar on Hera to fathom Didymoon. *European Planetary Science Congress*. Sept. 2020, EPSC2020–595.

- [41] M. Jutzi and W. Benz. Formation of bi-lobed shapes by sub-catastrophic collisions A late origin of comet 67P's structure. *Astronomy & Astrophysics* 597 (2017), A62. DOI: 10.1051/0004-6361/201628964.
- [42] T. Kaku, J. Haruyama, W. Miyake, A. Kumamoto, K. Ishiyama, T. Nishibori, K. Yamamoto, S. T. Crites, T. Michikami, Y. Yokota et al. Detection of intact lava tubes at Marius Hills on the Moon by SELENE (Kaguya) Lunar Radar Sounder. *Geophysical Research Letters* 44.20 (2017), 10–155. DOI: 10.1002/2017GL074998.
- [43] W. Kofman. Radar techniques to study subsurfaces and interiors of the solar system objects. *2012 19th International Conference on Microwaves, Radar Wireless Communications*. Vol. 2. May 2012, 409–412. DOI: 10.1109/MIKON.2012.6233605.
- [44] W. Kofman, Y. Barbin, J. Klinger, A.-C. Levasseur-Regourd, J.-P. Barriot, A. Herique, T. Hagfors, E. Nielsen, E. Grün, P. Edenhofer, H. Kochan, G. Picardi, R. Seu, J. van Zyl, C. Elachi, J. Melosh, J. Veverka, P. Weissman, L. Svedhem, S. Hamran and I. Williams. Comet nucleus sounding experiment by radiowave transmission. *Advances in Space Research* 21.11 (1998), 1589–1598. ISSN: 0273-1177. DOI: 10.1016/S0273-1177(97)00952-6.
- [45] W. Kofman, A. Herique, J.-P. Goutail, T. Hagfors, I. Williams, E. Nielsen, J.-P. Barriot, Y. Barbin, C. Elachi, P. Edenhofer, A.-C. Levasseur-Regourd, D. Plettemeier, G. Picardi, R. Seu and V. Svedhem. The Comet Nucleus Sounding Experiment by Radiowave Transmission (CONSERT): A short description of the instrument and of the commissioning stages. *Space Science REviews* 128.413-432 (2007). DOI: 10.1007/s11214-006-9034-9.
- [46] W. Kofman, A. Herique, Y. Barbin, J.-P. Barriot, V. Ciarletti, S. Clifford, P. Edenhofer, C. Elachi, C. Eyraud, J.-P. Goutail, E. Heggy, L. Jorda, J. Lasue, A.-C. Levasseur-Regourd, E. Nielsen, P. Pasquero, F. Preusker, P. Puget, D. Plettemeier, Y. Rogez, H. Sierks, C. Statz, H. Svedhem, I. Williams, S. Zine and J. Van Zyl. Properties of the 67P/Churyumov-Gerasimenko interior revealed by CONSERT radar. *Science* 349.6247 (July 2015), aab0639-1 - aab0639-6. DOI: 10.1126/science.aab0639.
- [47] A. S. Konopliv, R. S. Park, D.-N. Yuan, S. W. Asmar, M. M. Watkins, J. G. Williams, E. Fahnstock, G. Kruizinga, M. Paik, D. Strelakov et al. The JPL

- lunar gravity field to spherical harmonic degree 660 from the GRAIL primary mission. *Journal of Geophysical Research: Planets* 118.7 (2013), 1415–1434. DOI: 10.1002/jgre.20097.
- [48] J. D. Kraus. Radio Astronomy. *American Journal of Physics* 35.5 (1967), 450–450. DOI: 10.1119/1.1974133.
- [49] R. Lavarello and M. Oelze. A study on the reconstruction of moderate contrast targets using the distorted Born iterative method. *IEEE Transactions on Ultrasonics, Ferroelectrics, and Frequency Control* 55.1 (2008), 112–124. DOI: 10.1109/TUFFC.2008.621.
- [50] G. Leone, R. Persico and R. Pierri. Inverse scattering under the distorted Born approximation for cylindrical geometries. *JOSA A* 16.7 (1999), 1779–1787. DOI: 10.1364/JOSAA.16.001779.
- [51] O. Levy and D. Stroud. Maxwell Garnett theory for mixtures of anisotropic inclusions: Application to conducting polymers. *Phys. Rev. B* 56 (13 Oct. 1997), 8035–8046. DOI: 10.1103/PhysRevB.56.8035.
- [52] B. R. Mahafza. *Radar systems analysis and design using MATLAB*. eng. 3rd ed. Boca Raton, [Florida] ; CRC Press, 2013. ISBN: 0-429-10932-6.
- [53] P. Michel, M. Kueppers, H. Sierks, I. Carnelli, A. F. Cheng, K. Mellab, M. Granvik, A. Kestilä, T. Kohout, K. Muinonen et al. European component of the AIDA mission to a binary asteroid: Characterization and interpretation of the impact of the DART mission. *Advances in Space Research* 62.8 (2018), 2261–2272. DOI: 10.1016/j.asr.2017.12.020.
- [54] A. Moussessian, D. D. Blankenship, J. J. Plaut, G. W. Patterson, Y. Gim, D. M. Schroeder, K. M. Soderlund, C. Grima, D. A. Young and E. Chapin. REASON for Europa. *AGU Fall Meeting Abstracts*. Vol. 2015. Dec. 2015, P13E–05.
- [55] T. Nakamura, T. Noguchi, M. Tanaka, M. E. Zolensky, M. Kimura, A. Tsuchiyama, A. Nakato, T. Ogami, H. Ishida, M. Uesugi, T. Yada, K. Shirai, A. Fujimura, R. Okazaki, S. A. Sandford, Y. Ishibashi, M. Abe, T. Okada, M. Ueno, T. Mukai, M. Yoshikawa and J. Kawaguchi. Itokawa Dust Particles: A Direct Link Between S-Type Asteroids and Ordinary Chondrites. *Science* 333.6046 (2011), 1113–1116. ISSN: 0036-8075. DOI: 10.1126/science.1207758.

- [56] T. Ono and H. Oya. Lunar Radar Sounder (LRS) experiment on-board the SELENE spacecraft. *Earth, Planets and Space* 52 (2000), 629–637. DOI: 10.1186/BF03351671.
- [57] R. Orosei, S. E. Lauro, E. Pettinelli, A. Cicchetti, M. Coradini, B. Cosciotti, F. Di Paolo, E. Flamini, E. Mattei, M. Pajola, F. Soldovieri, M. Cartacci, F. Cassenti, A. Frigeri, S. Giuppi, R. Martufi, A. Masdea, G. Mitri, C. Nenna, R. Noschese, M. Restano and R. Seu. Radar evidence of subglacial liquid water on Mars. *Science* (2018). ISSN: 0036-8075. DOI: 10.1126/science.aar7268.
- [58] G. Picardi, J. J. Plaut, D. Biccari, O. Bombaci, D. Calabrese, M. Cartacci, A. Cicchetti, S. M. Clifford, P. Edenhofer, W. M. Farrell, C. Federico, A. Frigeri, D. A. Gurnett, T. Hagfors, E. Heggy, A. Herique, R. L. Huff, A. B. Ivanov, W. T. K. Johnson, R. L. Jordan, D. L. Kirchner, W. Kofman, C. J. Leuschen, E. Nielsen, R. Orosei, E. Pettinelli, R. J. Phillips, D. Plettemeier, A. Safaeinili, R. Seu, E. R. Stofan, G. Vannaroni, T. R. Watters and E. Zampolini. Radar Soundings of the Subsurface of Mars. *Science* 310.5756 (2005), 1925–1928. ISSN: 0036-8075. DOI: 10.1126/science.1122165.
- [59] L. J. Porcello, R. L. Jordan, J. S. Zelenka, G. F. Adams, R. J. Phillips, W. E. Brown, S. H. Ward and P. L. Jackson. The Apollo lunar sounder radar system. *Proceedings of the IEEE* 62.6 (June 1974), 769–783. ISSN: 0018-9219. DOI: 10.1109/PROC.1974.9517.
- [60] *Preperm®3D ABS450 filament 1.75 mm 750 g*. <https://www.preperm.com/webshop/product/preperm-3d-abs-%c9%9br-4-5-filament/>. Accessed 24 October 2019.
- [61] S. Pursiainen and M. Kaasalainen. Detection of anomalies in radio tomography of asteroids: Source count and forward errors. *Planetary and Space Science* (2014), 36–47.
- [62] S. Pursiainen. *GPU-Torre*. 2020. URL: <https://github.com/sampsapursiainen/GPU-Torre>.
- [63] S. Pursiainen. *GPU-Torre-3D*. 2020. URL: <https://github.com/sampsapursiainen/GPU-Torre-3D>.
- [64] S. Pursiainen and M. Kaasalainen. Orbiter-to-orbiter tomography: a potential approach for small solar system bodies. *IEEE Transactions on Aerospace and Electronic Systems* 52.6 (2016), 2747–2759. DOI: 10.1109/TAES.2016.150638.

- [65] S. Pursiainen, L.-I. Sorsa, C. Eyraud and J.-M. Geffrin. *Asteroid Wireframe Package*. Version 1.0. May 2020. DOI: 10.5281/zenodo.3838480.
- [66] J. Saito, H. Miyamoto, R. Nakamura, M. Ishiguro, T. Michikami, A. M. Nakamura, H. Demura, S. Sasaki, N. Hirata, C. Honda, A. Yamamoto, Y. Yokota, T. Fuse, F. Yoshida, D. J. Tholen, R. W. Gaskell, T. Hashimoto, T. Kubota, Y. Higuchi, T. Nakamura, P. Smith, K. Hiraoka, T. Honda, S. Kobayashi, M. Furuya, N. Matsumoto, E. Nemoto, A. Yukishita, K. Kitazato, B. Dermawan, A. Sogame, J. Terazono, C. Shinohara and H. Akiyama. Detailed Images of Asteroid 25143 Itokawa from Hayabusa. *Science (AAAS)* 312.5778 (2006), 1341–1344. ISSN: 0036-8075. DOI: 10.1126/science.1125722.
- [67] H. Saleh, H. Tortel, C. Leroux, A. Coudreuse, A. Litman and J.-M. Geffrin. Approach to Control Permittivity and Shape of Centimeter-Sized Additive Manufactured Objects: Application to Microwave Scattering Experiments. *IEEE Transactions on Antennas and Propagation* 69.2 (2021), 983–991. DOI: 10.1109/TAP.2020.3016159.
- [68] P. Sava and E. Asphaug. 3D radar wavefield tomography of comet interiors. *Advances in Space Research* 61.8 (2018), 2198–2213. ISSN: 0273-1177. DOI: 10.1016/j.asr.2018.01.040.
- [69] P. Sava and E. Asphaug. Seismology on small planetary bodies by orbital laser Doppler vibrometry. *Advances in Space Research* 64.2 (2019), 527–544. ISSN: 0273-1177. DOI: 10.1016/j.asr.2019.04.017.
- [70] R. Seu, D. Biccari, R. Orosei, L. Lorenzoni, R. Phillips, L. Marinangeli, G. Picardi, A. Masdea and E. Zampolini. SHARAD: The MRO 2005 shallow radar. *Planetary and Space Science* 52.1 (2004). Exploring Mars Surface and its Earth Analogues, 157–166. ISSN: 0032-0633. DOI: 10.1016/j.pss.2003.08.024.
- [71] A. Sihvola, E. Nyfors and M. Tiuri. Mixing formulae and experimental results for the dielectric constant of snow. *Journal of Glaciology* 31.108 (1985), 163–170.
- [72] W. Stiles and F. Ulaby. Dielectric properties of snow. The University of Kansas. *Center for Research, Inc., RSL Technical Report* (1981), 527–1.
- [73] S. Sugita et al. The geomorphology, color, and thermal properties of Ryugu: Implications for parent-body processes. *Science* (2019). ISSN: 0036-8075. DOI: 10.1126/science.aaw0422.

- [74] M. Takala, P. Bambach, J. Deller, E. Vilenius, M. Wittig, H. Lentz, H. M. Braun, M. Kaasalainen and S. Pursiainen. Far-Field Inversion for the Deep Interior Scanning CubeSat. *IEEE Transactions on Aerospace and Electronic Systems* 55.4 (2019), 1683–1697. DOI: 10.1109/TAES.2018.2874755.
- [75] M. Takala, D. Us and S. Pursiainen. Multigrid-Based Inversion for Volumetric Radar Imaging With Asteroid Interior Reconstruction as a Potential Application. *IEEE Transactions on Computational Imaging* 4.2 (2018), 228–240. DOI: 10.1109/TCI.2018.2811908.
- [76] K. J. Walsh, E. Jawin, R. Ballouz, O. S. Barnouin, E. B. Bierhaus, H. C. Connolly Jr., J. L. Molaro, T. J. McCoy, M. Delbo, M. Hartzell C. M. and Pajola, S. R. Schwartz, D. Trang, E. Asphaug, K. J. Becker, C. B. Beddingfield, C. A. Bennett, W. F. Bottke, K. N. Burke, B. C. Clark, M. G. Daly, D. N. DellaGiustina, J. P. Dworkin, C. M. Elder, D. R. Golish, A. R. Hildebrand, R. Malhotra, J. Marshall, P. Michel, M. C. Nolan, M. E. Perry, B. Rizk, A. Ryan, S. A. Sandford, D. J. Scheeres, H. C. M. Susorney, F. Thuillet, D. S. Lauretta and The OSIRIS-REx Team. Craters, boulders and regolith of (101955) Bennu indicative of an old and dynamic surface. *Nature Geoscience* 12 (2019), 242–246. DOI: 10.1038/s41561-019-0326-6.
- [77] S. H. Ward and G. W. Hohmann. Electromagnetic theory for geophysical applications. *Electromagnetic Methods in Applied Geophysics: Voume 1, Theory*. Society of Exploration Geophysicists, 1988, 130–311.
- [78] M. T. Zuber, D. E. Smith, M. M. Watkins, S. W. Asmar, A. S. Konopliv, F. G. Lemoine, H. J. Melosh, G. A. Neumann, R. J. Phillips, S. C. Solomon, M. A. Wieczorek, J. G. Williams, S. J. Goossens, G. Kruizinga, E. Mazarico, R. S. Park and D.-N. Yuan. Gravity Field of the Moon from the Gravity Recovery and Interior Laboratory (GRAIL) Mission. *Science* 339.6120 (2013), 668–671. ISSN: 0036-8075. DOI: 10.1126/science.1231507.

PUBLICATIONS

PUBLICATION

I

Bistatic full-wave radar tomography detects deep interior voids, cracks and boulders in a rubble-pile asteroid model

L.-I. Sorsa, M. Takala, P. Bambach, J. Deller, E. Vilenius and S. Poursiainen


The Astrophysical Journal 872.1 (2019), 44

DOI: 10.3847/1538-4357/aafba2

Publication reprinted with the permission of the copyright holders



Bistatic Full-wave Radar Tomography Detects Deep Interior Voids, Cracks, and Boulders in a Rubble-pile Asteroid Model

Liisa-Ida Sorsa¹ , Mika Takala¹, Patrick Bambach², Jakob Deller², Esa Vilenius², and Sampsa Pursiainen¹

¹Laboratory of Mathematics, Tampere University, P.O. Box 553, FI-33101 Tampere, Finland; liisa-ida.sorsa@uni.fi

²Max Planck Institute for Solar System Research, Justus-von-Liebig-Weg 3, D-37077 Göttingen, Germany

Received 2018 November 2; revised 2018 December 17; accepted 2018 December 31; published 2019 February 8

Abstract

In this paper, we investigate full-wave computed radar tomography (CRT) using a rubble-pile asteroid model in which a realistic shape (Itokawa) is coupled with a synthetic material composition and structure model. The aim is to show that sparse bistatic radar measurements can distinguish details inside a complex-structured rubble-pile asteroid. The results obtained suggest that distinct local permittivity distribution changes such as surface layers, voids, low-permittivity anomalies, high-permittivity boulders, and cracks can be detected with bistatic CRT, when the total noise level in the data is around -10 dB with respect to the signal amplitude. Moreover, the bistatic measurement setup improves the robustness of the inversion compared to the monostatic case. Reconstructing the smooth Gaussian background distribution was found to be difficult with the present approach, suggesting that complementary techniques, such as gravimetry, might be needed to improve the reliability of the inference in practice.

Key words: minor planets, asteroids: general – planets and satellites: interiors – techniques: radar astronomy

1. Introduction

This paper investigates spaceborne computed radar tomography (CRT) applied to a rubble-pile asteroid model. Spaceborne CRT inherits its principles from the airborne ground penetrating radar (GPR) that was originally developed to provide cost-effective underground surveys in applications that entail working with an antenna that is not in contact with the surveyed structure (Catapano et al. 2012a, 2012b; Soldovieri et al. 2017). Such airborne GPR systems have been validated by airborne measurement data and numerical experiments (Fu et al. 2014). Space mission concepts to perform radio tomography of small asteroids have been proposed by, for example, Asphaug et al. (2001), Safaenili et al. (2002), Snodgrass et al. (2018), and Bambach et al. (2018).

The first attempt to reconstruct the deep interior of a small solar system body (SSSB) was the Comet Nucleus Sounding Experiment by Radio-wave Transmission, a part of the European Space Agency's (ESA) *Rosetta* mission to explore the comet 67P/Churyumov–Gerasimenko, in which a radio signal was transmitted between the orbiter *Rosetta* and the lander *Philae* (Kofman et al. 1998, 2007, 2015). Many more missions aiming to explore the structure and composition of SSSBs are currently ongoing or being planned. In 2018 August, the *Osiris-REx* mission by NASA (Berry et al. 2013) began its rendezvous with the asteroid 101955 Bennu to measure its physical, geological, and chemical properties and collect a sample of the asteroid surface regolith (Lauretta et al. 2017). The *Hayabusa* mission by the Japanese Aerospace Exploration Agency (JAXA) explored the asteroid Itokawa in 2005 (Japan Aerospace Exploration Agency 2003; Okada et al. 2006; Nakamura et al. 2011; Tsuchiyama et al. 2011) and retrieved surface regolith for analysis on Earth (Fujiwara et al. 2006), confirming the Itokawa's Earth-based classification as an S-type asteroid. The images taken by *Hayabusa* on Itokawa have been used to analyze the size distribution of boulders on its surface. The results indicate that the boulders cannot solely be the product of cratering but that many of them originated

from the disruption of a larger body (Saito et al. 2006; Michikami et al. 2008). JAXA's mission *Hayabusa2* arrived at the asteroid 16173 Ryugu in 2018 June. It will survey its target for a year and a half, returning back to Earth in 2020 December (Tsuda et al. 2013). These missions by NASA and JAXA concentrate on the surface properties of the target asteroids and do not carry instruments that could be used to explore the deep interior structures.

The next candidate to deploy a CRT system to explore the deep interior of a SSSB is ESA's asteroid mission *Hera*, which targets the binary near-Earth asteroid system Didymos and is due to launch in 2023 (Michel et al. 2016). The current plan allows deployment of a 6U CubeSat form factor payload (Carnelli 2018), which has been recently proposed for the radar-carrying spacecraft concept DISCUS (Deep Interior Scanning CUBEsat) (Bambach et al. 2018). Furthermore, ESA's recent Concurrent Design Facility (CDF) study report (European Space Agency 2018) suggests that small planetary platforms involving CubeSats can provide future opportunities for CRT.

In this paper, CRT is applied to a rubble-pile asteroid model utilizing the mathematical approach proposed in Pursiainen & Kaasalainen (2016) and Takala et al. (2018b). We investigate a synthetic framework featuring the radar specifications of the DISCUS concept, and a target with a complex shape, structure, and material composition. The shape of the asteroid Itokawa is coupled with a Gaussian random field model for the relative dielectric permittivity distribution together with added structural details. We base our model on the recent observations and impact simulations that suggest that the internal porosity of the asteroid body varies, increasing toward the center, and that it may have a detailed structure (Carry 2012; Deller 2017; Jutzi & Benz 2017).

The aim is to validate numerically the mathematical approach of Pursiainen & Kaasalainen (2016) and Takala et al. (2018b) and also to explore whether sparse bistatic radar measurements can distinguish details inside a complex-structured rubble-pile asteroid.

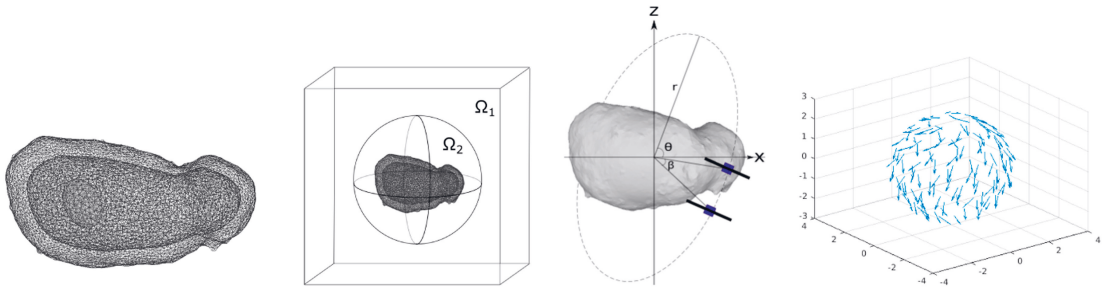


Figure 1. Left: FE model of Itokawa including a single deep interior void in the body of the asteroid. The detailed model includes surface and interior compartments and an ellipsoidal deep interior detail. Second from the left: computation domain Ω of this study comprising two nested subdomains Ω_1 and Ω_2 . The outer subdomain, Ω_1 , contains a split-field perfectly matched layer to simulate open field scattering. The asteroid model is contained in Ω_2 . The spherical boundary between the subdomains was applied in simulating the far-field signal transmission and measurements as described in Takala et al. (2018b). Third from the left: schematic illustration of the bistatic measurement approach. The angle θ depicts the limiting angle between the satellite orbiting plane normal and the asteroid spin. The angle β is the angle between the orbiters in their orbiting plane. The two satellites orbit at distance r from the center of the asteroid. Right: quiver plot of the 64 orbiter points and orientations around the asteroid.

2. Materials and Methods

In this study, we utilize the finite element time-domain (FETD) approach (Pursiainen & Kaasalainen 2016) equipped with a far-field model proposed in Takala et al. (2018b). In FETD, the radar signal is propagated over a suitably chosen time interval within a volumetric finite element (FE) mesh that can be adapted accurately to a given set of surface features. The permittivity structure can be found via a multigrid approach (Takala et al. 2018a). That is, the signal is inverted using a coarser grid that is a nested structure with respect to the more refined FE mesh.

2.1. Model of the Asteroid Itokawa

The FE mesh was constructed based on the detailed shape model of the asteroid Itokawa (Figure 1, left) which is openly available as a triangular stereolithography (STL) mesh (Hayabusa Project Science Data Archive 2007). The scaling of the asteroid was assumed to match with the actual size of Itokawa, whose longest diameter is 535 m (Fujiwara et al. 2006). The unstructured triangulated asteroid surface was imported to Meshlab (Cignoni et al. 2008) and resampled with a Poisson-disk sampling algorithm to obtain a uniform mesh with a desired resolution of 5762 nodes and 11,520 faces. The volumetric asteroid model was divided into a surface and interior compartment. The boundary between these two parts was obtained by scaling a resampled and smoothed-out version of the outer surface by a factor of 0.9. An additional ellipsoidal compartment was utilized as a void detail when simulating the measurement data.

2.2. The Structure and the 3D Domain Structure

The computation domain Ω , depicted in Figure 1 (second from the left) was constructed in the Gmsh software (Geuzaine & Remacle 2009), in which the structure of the computation domain Ω can be described within a geometry (GEO) file and the compartments of the asteroid model can be obtained via their STL surface grids. Two coarse FE meshes with 38k nodes and 212k tetrahedra were generated using Gmsh. One of these was employed for simulating the measurements, and the other one, not including any interior details, was used in the inversion stage. The reason to apply two different grids was to

avoid the so-called *inverse crime*, i.e., an overly good match between the actual permittivity distribution and its reconstruction. The permittivity was modeled as a piecewise constant function within the coarse grid. A nested, uniformly and twice-refined grid was utilized, when simulating the signal propagation, in order to achieve a sufficient resolution with respect to the wavelength.

2.3. The Set of Measurement Points

The measurement point set was modeled after the DISCUS mission concept (Takala et al. 2018b) in which a master and slave CubeSat both equipped with a half-wavelength dipole antenna orbit the target asteroid at a 5 km distance. The angle between the orbiters is 25° with respect to the asteroid's center of mass (Figure 1, third from the left). The measurement configuration is bistatic: the master CubeSat both transmits and records the signal, and the slave provides an additional receiver. The angle θ between the measurement plane normal and the asteroid spin, determining the angular coverage of the measurements, is assumed to be 70° . Optimally, a full coverage could be obtained with $\theta = 90^\circ$. A practically obtainable orbiting direction may be expected to have a somewhat but not very much lower value, as the target asteroid will likely have a close-to-retrograde spin (La Spina et al. 2004). In total, 64 measurement points were included in the point cloud. The resulting bistatic set of measurement points and antenna orientations has a sparse and limited-angle spatial coverage with an aperture around the z -axis (Figure 1, right).

2.4. Radar Specifications

Drawing from the DISCUS concept (Bambach et al. 2018), the radar is assumed to have a transmission power of 10 W, a 2 MHz total signal bandwidth, and a relatively low 20 MHz center frequency. In practice, ≤ 100 MHz will be necessary in order to achieve appropriate signal penetration and to minimize solar noise (Kofman 2012). The maximal range (imaging) resolution following from these parameters is about 35–40 m inside an asteroid with a relative permittivity of ~ 4 .

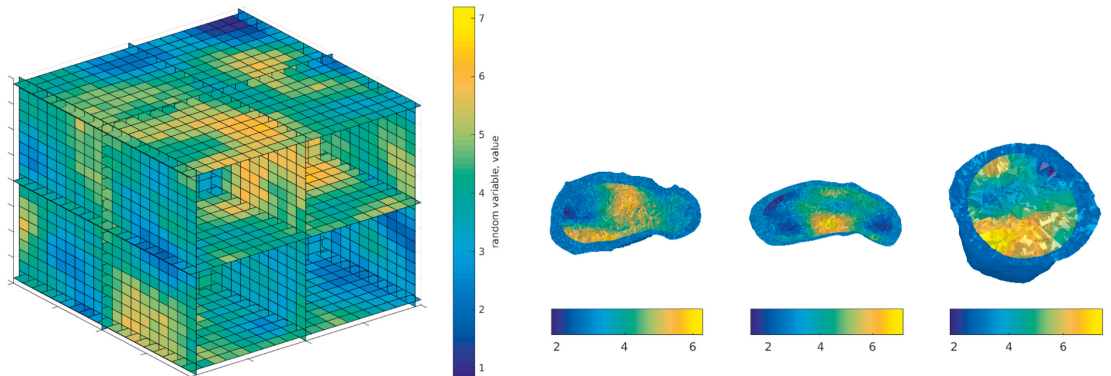


Figure 2. Left: Gaussian random field within a regular 20-by-20-by-20 grid. Right: in each model (A)–(E), the smooth interior part corresponds to a Gaussian random field. The surface layer is associated with a constant and comparably lower permittivity value $\epsilon_r = 3$. The figures from left to right, show a slice cut-view of the permittivity distribution in the xy -, yz -, and zx -planes, respectively.

Table 1
Details in the Asteroid Models (A)–(E)

Model	Description	Detail	ϵ_r	Detail Size ^a		
				Length	Width	Depth
(A)	Single void	Ellipsoid	1	120 m	120 m	55 m
				8.0λ	8.0λ	3.7λ
(B)	Highly porous inclusion	Ellipsoid	2	0.8λ	0.8λ	0.4λ
				120 m	120 m	55 m
(C)	High-permittivity boulder	Ellipsoid	15	11.3λ	11.3λ	5.2λ
				120 m	120 m	55 m
(D)	Deep crack	Crack	1	1.1λ	1.1λ	0.5λ
				185 m	10–55 m	10–50 m
(E)	Shallow crack	Crack	1	3.1λ	3.1λ	1.4λ
				185 m	10–55 m	10–50 m
				12.3λ	$0.7\text{--}3.7\lambda$	$0.7\text{--}3.3\lambda$
				1.2λ	$0.07\text{--}0.4\lambda$	$0.07\text{--}0.3\lambda$

Notes. The respective center wavelengths of the 20 MHz signal are $\lambda = \{15.0, 10.6, 3.9\}$ m in each of the relative permittivities $\epsilon_r = \{1, 2, 15\}$. The wavelengths of the 2 MHz bandwidth signal in the respective ϵ_r values are $\lambda = \{150, 106, 39\}$ m.

^a Sizes are indicated in meters, with respect to the wavelengths of a 20 MHz center frequency signal, and with respect to the wavelengths of a 2 MHz bandwidth signal.

2.5. Computing a Gaussian Random Field inside a Given Asteroid Geometry

A Gaussian random field for the dielectric relative permittivity, ϵ_r , was first generated in a regular 20-by-20-by-20 lattice (Figure 2, left). The mean of the random field was set to $\epsilon_r = 4$, assuming a standard deviation equal to one. The correlation value between the adjacent lattice points, was set to 0.2 based on visual examination. The correlation was chosen to be isotropic. These choices were thought to roughly account for the recent impact simulation results in which large pieces of porous rubble, bound together by gravity, are concentrated in the interior (Jutzi & Benz 2017), yet allowing some clear randomness of the distribution due to the fact that the exact interior structure is mainly unknown (Carry 2012).

Implementation of the Gaussian random field algorithm was retrieved from Constantine (2012). The asteroid interior geometry was then fitted inside the cubic mesh and the values

were assigned to the FE mesh nodes via the nearest-neighbor interpolation principle. Each FE mesh tetrahedron was assigned a value that is the average of the electrical permittivities of each node constituting the element. Finally, the random field was restricted to permittivity values greater or equal to one, which is the dielectric permittivity of vacuum and therefore the physical minimum of relative permittivity.

2.6. Structural Details

This section describes the details of the five asteroid models (A)–(E) applied in this study. The details of these have also been given in Table 1. In each model, the permittivity distribution in the interior part is determined by a Gaussian random field with values approximately between two and six (Figure 2, right). Furthermore, each one includes a surface layer with a lower permittivity to model the higher porosity near the surface predicted in the impact simulations (Jutzi & Benz 2017).

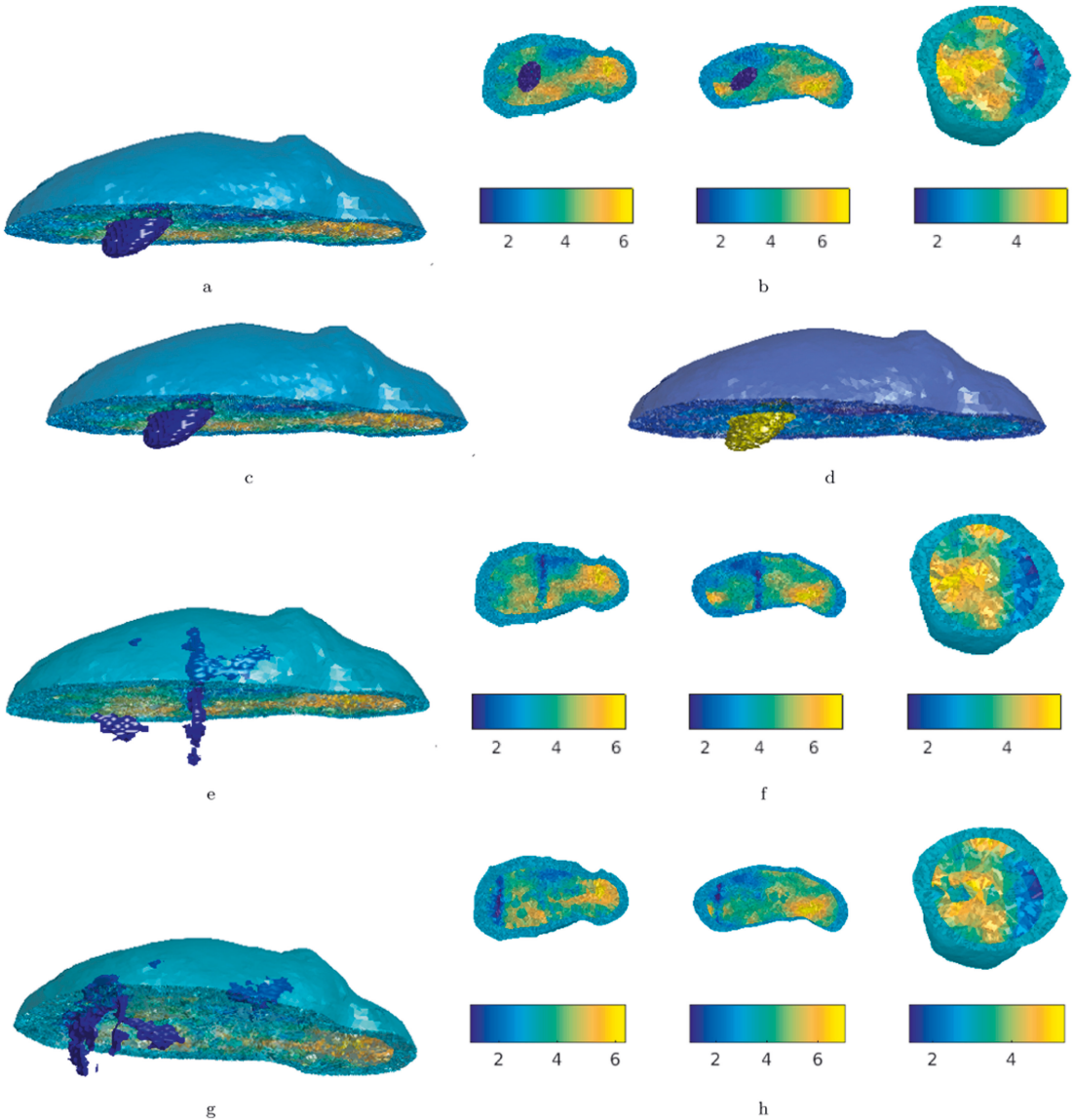


Figure 3. Top row: (a) Model (A) with a deep interior vacuum void. The 3D model shows the ellipsoid shape of the anomaly. The crosscut view (b) of the model on the right details the surface layer with $\varepsilon_r = 3$ and the Gaussian random field enclosing the ellipsoidal void with $\varepsilon_r = 1$. Second row: 3D models of the models (B) and (C) in (c) and (d), respectively. The structures of these models are the same as the one in the top row (A), but the relative permittivities of the ellipsoids are different. Third row: illustration of the deep crack model (D) with the 3D model (e) and the crosscut view (f). Bottom row: illustration of the shallow crack model in 3D (g) and crosscut view (h) showing the complicated shape of the crack.

In each case, a different random realization of the Gaussian random field is used.

2.6.1. Model (A): A Single Void

In (A), to investigate anomaly detection, a single ellipsoid with a relative permittivity value $\varepsilon_r = 1$ (vacuum) was placed deep in the interior (Figures 3(a) and (b)). This anomaly could

be, for example, a void between two large boulders constituting a part of the body of the asteroid.

2.6.2. Model (B): A Highly Porous Inclusion

In (B), we study a situation in which the anomaly is not as distinct from the surroundings as a void space (Figure 3(c)). That is, the interior may include areas that are occupied by very

porous or otherwise low-permittivity material. Therefore, we also investigate an ellipsoid whose relative dielectric permittivity is adjusted to $\varepsilon_r = 2$ instead of that of the vacuum, $\varepsilon_r = 1$.

2.6.3. Model (C): A High-permittivity Boulder

An asteroid may also be formed around a single large boulder with dielectric permittivity that is significantly higher than that of its surroundings. One such system is investigated with model (C), in which the dielectric permittivity of the enclosed ellipsoid is assigned the value $\varepsilon_r = 15$, which is significantly higher than the surrounding material (Figure 3(d)). This value corresponds, e.g., to solid basalt (Hansen et al. 1973), and was included in the study to investigate whether such permittivity structures can be reconstructed and to provide a more complete view of the capabilities of radar tomography.

2.6.4. Model (D): A Deep Crack

In (D), to model a random crack inside the asteroid, a simple nearest-neighbor walking algorithm was applied within the set of FE mesh nodes. Each node included in the path created by the random walk was assigned a permittivity value of one (vacuum), and the permittivity of each tetrahedron in the FE mesh was determined by the average permittivity of its nodes.

The resulting crack is irregularly shaped and small in comparison to the void (Figures 3(e) and (f)). The width of the crack is of the order of 10–50 m, depending on the location within the asteroid.

2.6.5. Model (E): A Shallow Crack

In (E), the random walk approach was utilized to create a shallow crack. This crack was also allowed to bifurcate to form a two-branched structure (Figures 3(g) and (h)).

2.7. Conductivity Distribution

The conductivity distribution causing signal attenuation was assumed to be a latent parameter, i.e., an uninteresting nuisance parameter, depending on the permittivity according to $\sigma = 5\xi\varepsilon_r$, where $\xi = (\mu_0/\varepsilon_0)^{-1/2} s^{-1}$ with spatial scaling parameter $s = 2100$ m (Takala et al. 2018b). If $\varepsilon_r = 4$, this results in a conductivity of around $2.5 \times 10^{-5} \text{ S m}^{-1}$, which matches roughly with an attenuation rate of 25 dB km⁻¹, approximating a low-frequency signal decay within a porous body (Kofman 2012).

2.8. Forward Model

The inversion process requires a reference permittivity $\varepsilon_r^{(\text{bg})}$, a background model. This model is constructed similar to the detailed structural models, the difference being that the interior permittivity is constant, $\varepsilon_r^{(\text{bg})} = 4$. We utilize a linearized forward model given by Pursiainen & Kaasalainen (2016):

$$\mathbf{y} = \mathbf{L}\mathbf{x} + \mathbf{y}^{(\text{bg})} + \mathbf{n}. \quad (1)$$

Here, the vectors \mathbf{y} and $\mathbf{y}^{(\text{bg})}$ contain the measured and simulated data for the actual permittivity distribution ε_r and its constant-valued approximation $\varepsilon_r^{(\text{bg})}$, respectively. The vector \mathbf{x} determines the discretized permittivity distribution, \mathbf{L} denotes the Jacobian matrix resulting from the linearization at

$\varepsilon_r^{(\text{bg})}$, and \mathbf{n} contains both the measurement and forward-modeling errors.

The noise vector \mathbf{n} is here assumed to be a zero-mean Gaussian random variable due to the various potential and unknown noise formation processes, e.g., signal attenuation due to latent factors. Following from the rough estimates for the cosmic background noise level with the present radar and mission specifications (Takala et al. 2018b), the standard deviation was chosen to be -15 dB with respect to the maximal entry of the difference $|\mathbf{y} - \mathbf{y}^{(\text{bg})}|$ between the measured and simulated signal.

2.9. Inversion Approach

We use the simple total variation (TV) based iterative regularization approach presented in Pursiainen & Kaasalainen (2016). An estimate of \mathbf{x} in Equation (1) can be produced via the iterative regularization procedure

$$\mathbf{x}_t = (\mathbf{L}^T\mathbf{L} + \alpha\mathbf{D}\mathbf{\Gamma}_t\mathbf{D})^{-1}\mathbf{L}^T\mathbf{y}, \quad \mathbf{\Gamma}_t = \text{diag}(|\mathbf{D}\mathbf{x}_t|)^{-1}, \quad (2)$$

in which $\mathbf{\Gamma}_0 = \mathbf{I}$ and \mathbf{D} is of the form:

$$D_{i,j} = \beta\delta_{i,j} + \frac{\ell^{(i,j)}}{\max_{i,j}\ell^{(i,j)}}(2\delta_{i,j} - 1),$$

$$\delta_{i,j} = \begin{cases} 1, & \text{if } j = i, \\ 0 & \text{otherwise.} \end{cases} \quad (3)$$

The first term is a weighed identity operator limiting the total magnitude of \mathbf{x} , whereas the second term penalizes the jumps of \mathbf{x} over the edges of the mesh, the $\ell^{(i,j)}$ being the edge length.

The inversion process in Equation (2) minimizes the function $F(\mathbf{x}) = \|\mathbf{L}\mathbf{x} - \mathbf{y}_{\text{bg}} - \mathbf{y}\|_2^2 + 2\sqrt{\alpha}\|\mathbf{D}\mathbf{x}\|_1$, in which the second term equals the TV of \mathbf{x} if $\beta = 0$. The coefficients α and β are the regularization parameters.

The TV penalty function is evaluated with respect to the tetrahedral inversion mesh as shown in Takala et al. (2018b). The inversion computation was run with regularization parameters values $\alpha = 0.01$ and $\beta = \{0.005, 0.0075\}$ depending on the model. The parameters were adjusted based on preliminary experiments, with the goal of maximizing the distinguishability of the interior details and to obtain an appropriate range of permittivity values with respect to the actual distribution.

3. Results

The full-wave CRT simulation was performed for five different model structures (A)–(E) covering the following features: (A) a void space, (B) a highly porous inclusion, (C) a high-permittivity boulder, (D) a deep crack, and (E) a shallow crack inside the asteroid. The results of the simulations can be found in Figures 4–7 and Table 2. The results suggest that deep interior permittivity anomalies can be detected inside a rubble-pile asteroid with a limited-angle set of bistatic full-wave data. Nevertheless, detecting smooth structures was found to be difficult in comparison to how the void, boulder, and crack details were distinguished. The model-specific results for (A)–(E) are described in the following subsections.

3.1. Simulated Measurement Data

A time series of the normalized data at a single measurement point is shown in Figure 4. The shown time interval 1.3–4.3 μs shows signal propagation within the asteroid. Extending the

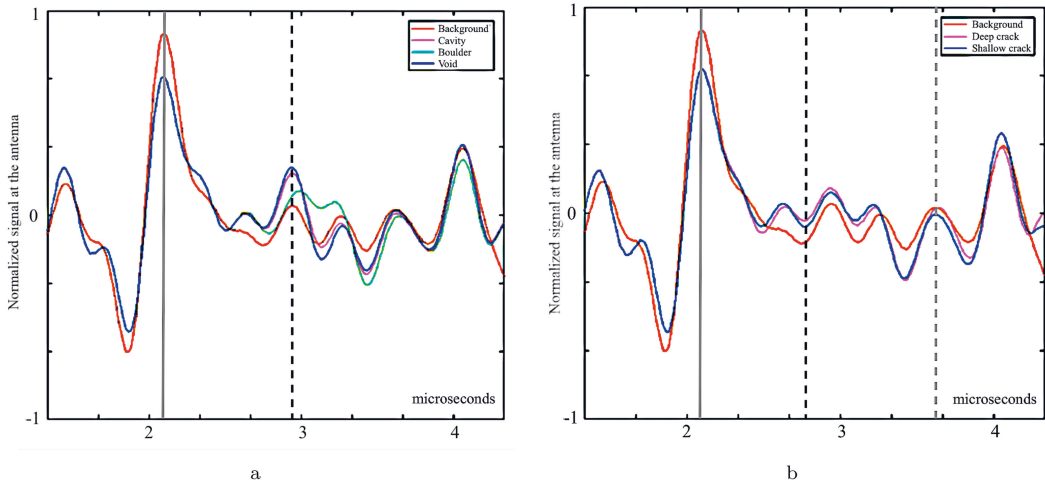


Figure 4. Time series of the normalized data at a single measurement point showing how the noiseless data of the models (A)–(E) differ in comparison to the simulated background signal (red). The effect of the surface layer on the data is marked by the solid vertical gray line. The dashed vertical black and gray lines on the right mark the effects of the shallow and the deep crack in the signal, respectively.

duration beyond $4.3 \mu\text{s}$ was found to be unfeasible due to the noise effects caused by the inward-directed reflection peak from the outer surface facing away from the measurement position. The first echo at time point $2 \mu\text{s}$ originates from the surface of the asteroid. In the background model (red line), the permittivity of the asteroid interior is constant $\varepsilon_r = 4$ across the whole asteroid interior, hence a more distinct echo is recorded in comparison to each detailed model (blue line), including a surface layer with a lower permittivity value ($\varepsilon_r = 3$). Hence, the amplitude of the reflected signal is also lower in the latter case.

Figures 4(a) and (b) show how ellipsoids and cracks, respectively, can be distinguished in the raw signal at a single measurement point. The differences in the curves are due to the differences in how the signal propagates through the asteroid. The nonlinearity of the radar signal propagation is revealed by a mutual comparison between the amplitudes of the signals for models (A)–(C). The geometrical models of these are identical, but the signal curves, however, also regarding the shape of the measured signal. The differences between the signals for the deep and shallow cracks (D) and (E) (Figure 4(b)) are minor but discernible. The shallow crack produces a more distinct echo that can be observed at the time point of approximately $2.7 \mu\text{s}$.

3.2. Model (A): Void Detection

A comparison between the reconstructed permittivity and the exact 3D distribution for model (A) is shown in Figures 5(a) and (b), respectively. It is evident that the (vacuum) void space of (A) is detectable. The quality of the radial (depth) accuracy with respect to the asteroid’s body was observed to be better than that in the tangential one. This is due to the sparse spatial distribution of the measurement points compared to the relatively dense time resolution of the data, which results in reliable localization capability.

3.3. Model (B): Detection of a Highly Porous Inclusion

The task of detecting highly porous materials ($\varepsilon_r = 2$), case (B), was also found to be feasible. However, the reconstruction quality obtained for (B) was weaker compared to that of (A) (Figure 5(e)). The exact shape of the inclusion found for (B) is not as obvious as that in the case of (A), but the location of the anomaly is evident, as shown by the Figures 5(e) and (h).

3.4. Model (C): Boulder Detection

The Figures 5(g) and (i) show that a high-permittivity boulder can be detected. Similar to the void detection, the best detection accuracy was also obtained in the transversal direction. The surface layer in the reconstruction (Figure 5(ii)) is less obvious than that for cases (A) and (B).

3.5. Model (D): Deep Crack Detection

The reconstruction for model (D) shown in the left panel of Figure 6 suggests that the deep crack is practically invisible for the radar. Obviously, its location in the deep interior, and the limited-angle data, i.e., the absence of the measurement points around the z -axis, are potential factors limiting the detectability of the crack.

3.6. Model (E): Shallow Crack Detection

In contrast to the deep crack, a moderately clear echo was detected for the shallow crack in case (E), as shown in the right panel of Figure 6. Based on the reconstruction (Figure 6(d)), a complex shape can also be discerned. However, the exact shape, especially, the branches of the crack, cannot be accurately distinguished.

3.7. Goodness of Reconstructions

A qualitative assessment of the goodness of the reconstructions presented in Figures 5 and 6 is shown in Table 2. The quantitative goodness of a reconstruction is measured by the

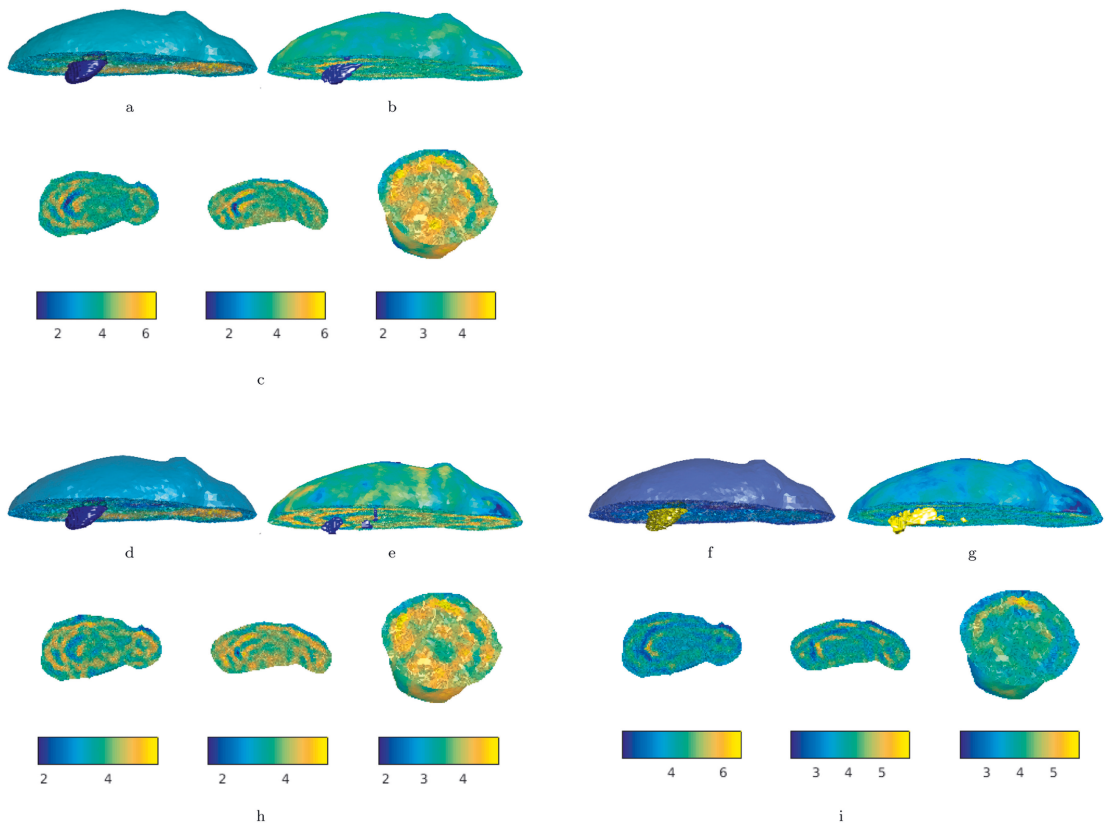


Figure 5. Top left: the void of model (A) in (a) can be detected by full-wave computed radio tomography. A 3D reconstruction of the detected void is shown in (b). The crosscut view of the reconstruction in (c) shows a reconstruction that corresponds to a very realistic radargram in which the surface layer and the deep internal void can be detected. Bottom left: for model (B), a highly porous inclusion (d) is moderately visible in 3D (e) and crosscut view reconstructions (h). Bottom right: for model (C), the boulder with a high relative permittivity value in (f) ($\epsilon_r = 15$) can be detected inside the asteroid in both the 3D (g) and crosscut view (i) reconstructions.

mean square error (MSE) and the mean absolute error (MAE) computed separately for the anomaly detail and the surface layer, in addition to the global reconstruction containing the detail, the surface layer, and the remaining asteroid interior of the asteroid model. The relative mean absolute error (MAE-R) is computed for the details only to compare the goodness of the detail reconstruction between models (A)–(E).

The computed mean and absolute error values (Table 3) reflect the qualitative reconstructions. The errors are greatest in the detail areas and smallest in the surface layer. As is evident in the reconstruction images in Figures 5 and 6, the majority of the volumes in the ellipsoids and the cracks are not captured by the reconstruction, hence the permittivity values of these areas differ from the exact model very clearly. This is especially the case with boulder model (C), in which the difference between the permittivity values in the exact model and the reconstruction varies greatly.

3.8. Comparison of Bistatic to Monostatic Measurement

Model (A) was used to compare reconstructions obtained with monostatic (single-satellite) and bistatic measurement

data. The results show (Figures 7(a) and (b)) that both satellite configurations enable the detection of the void. The bistatic measurement appears to show a slightly more prominent shape of the anomaly, but this may not be significant in practical applications. Overall, the bistatic measurement approach appears to provide robustness to the reconstruction process. The same finding was previously reported and quantified in Takala et al. (2018b) and can be accounted for by the fact that, in addition to the second receiver, the bistatic measurement setup also includes the monostatic transmitter-receiver data collection. Hence, the bistatic measurement includes more information on the object.

3.9. Effect of Noise

Finally, noise levels between -25 and 0 dB were investigated to determine the effect of noise on the reconstruction accuracy. Based on the results (Figures 7(c)–(h)), the artifacts appear at the -8 dB level, after which they increase rapidly along with the noise.

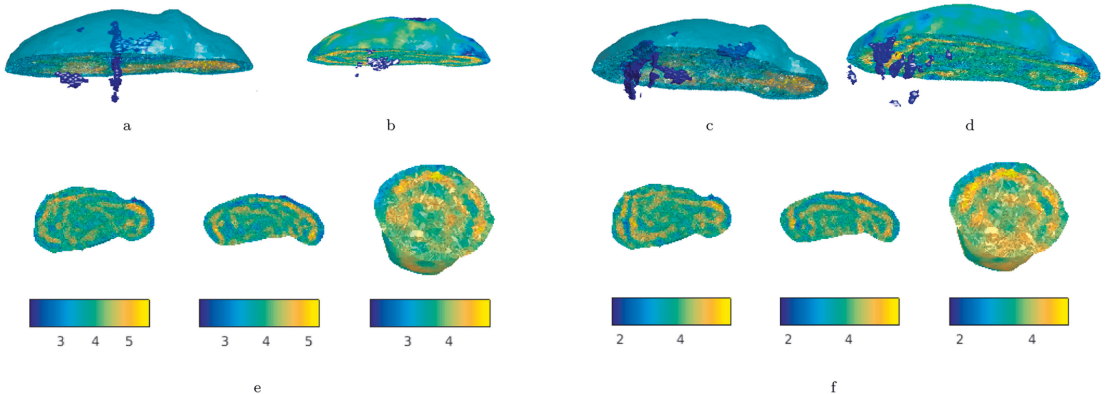


Figure 6. Left: for model (D), the deep crack running across the asteroid in the vertical direction (a) is practically absent in the 3D (b) and crosscut view (e) reconstruction. Right: for model (E), the shallow crack with two branches and a complex shape (c) can be detected in the 3D (d) and crosscut view (f) reconstructions.

4. Discussion

The aim of this paper was to numerically validate the full-wave CRT model developed by Pursiainen & Kaasalainen (2016) and Takala et al. (2018b) for complex-structured asteroid models, especially to estimate the reconstruction capability of the CRT for rubble-pile asteroids. The surface model of the asteroid Itokawa was used because it is one of the few asteroids for which the surface and bulk properties are known (Abe et al. 2006; Fujiwara et al. 2006; Okada et al. 2006; Barnouin-Jha et al. 2008; Nakamura et al. 2011; Tsuchiyama et al. 2011), and for which a high-resolution surface model is available (Hayabusa Project Science Data Archive 2007). The structural models (A)–(E) of this study were generated by combining the data and knowledge available on the physical properties of small solar system bodies and on how electromagnetic waves behave in such media (Kofman 2012; Kofman et al. 2015; Herique et al. 2018).

To create a complex model for the deep interior part, roughly matching with the mass-concentration estimates obtained from the asteroid impact evolution studies (Jutzi & Benz 2017), the dielectric properties of the asteroid were modeled by a Gaussian random field, which is a well-established approach to modeling random spatial structures in geostatistics and earth sciences (Lantuéjoul 2002; Christakos 2005; Chilès & Delfiner 2012). Gaussian random fields are also used to generate random 3D porous structures (Roberts & Garboczi 2002) and to model concrete (Bićanić et al. 2010) in civil engineering applications. Models (A)–(E) were obtained by adding a surface layer together with deep interior details to a Gaussian random field. Special interest was paid to modeling the inhomogeneous deep interior permittivity and void space accounting for bulk macroporosity of the body, which can be expected to be, for example, as high as 41% in the rubble-pile of Itokawa (Fujiwara et al. 2006).

The results suggest that permittivity anomaly details can be detected using CRT within a complex-structured asteroid, excluding the deep areas around the center of mass, which are challenging due to signal attenuation and the limited-angle measurement point distribution with an aperture around the z -axis. However, it also appears that the smooth Gaussian random field structure is difficult to reconstruct accurately. Compared to earlier work (Pursiainen & Kaasalainen 2016;

Takala et al. 2018b), the present inversion scheme is more realistic, showing that the practically achievable reconstruction quality will largely depend on the shape and the dielectric properties of the asteroid body. Moreover, it is obvious that the structures closer to the surface are detected more clearly than those lying deep inside the body.

Reconstructing the interior details was shown to be feasible up to approximately -10 dB of noise. For a carrier frequency of 20 MHz, the galactic noise can be estimated to be around $5 \times 10^{-20} \text{ W m}^{-2} \text{ Hz}^{-1}$. At a distance of 1 au, the dominating measurement noise is likely to originate from the Sun, which radiates with a magnitude of $5 \times 10^{-19} \text{ W m}^{-2} \text{ Hz}^{-1}$ and $4 \times 10^{-23} \text{ W m}^{-2} \text{ Hz}^{-1}$ for its active and inactive (quiet) phase of sunspot activity, that is, for surface temperatures 10^6 and 10^{10} K, respectively (Kraus 1967; Barron et al. 1985). During the active phase there are radio emissions on timescales varying from seconds to hours. This noise can be diminished, by some amount, via orienting the antenna in an optimal way. When moving away from the Sun, the radiation, in general, decreases proportionally to the inverse square of the radius. This means that at 3 and 30 au, the radiation levels due to the Sun will be -19 and -59 dB, respectively, with respect to those experienced at 1 au. The latter value is a rough estimate for the Kuiper Belt.

The imaging resolution was found to be higher in the radial direction than in the tangential one. The details recovered also seem to be elongated in the tangential direction, exhibiting similar wave-front properties as conventional radargrams (Daniels 2004). The elongation can be interpreted to be due to the sparsity of the spatial measurement points. It is also present in other full-wave applications of CRT (Gueting et al. 2015, 2017), suggesting that enhancing the results significantly without changing the radar specifications might be difficult. Consequently, it seems that exact shapes cannot be accurately reconstructed for, e.g., structures oriented toward the center of the asteroid. This is also reflected in the MSEs and MAEs computed for the reconstructions. However, based on the crack detection results it also seems reasonable to assume that even complex structures near the surface can be detected. The quality of reconstruction and the exact permittivity values may also be assumed to depend on the applied inversion technique and regularization parameters. In the present study, some of the

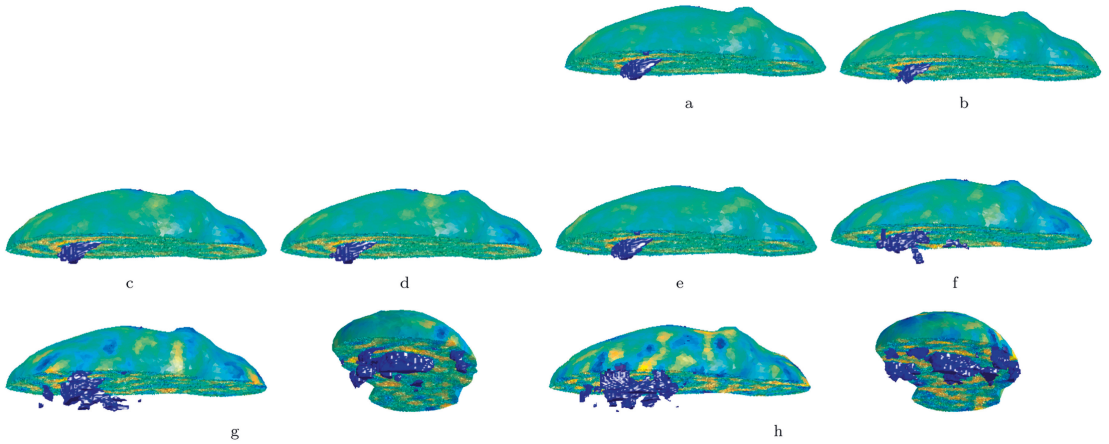


Figure 7. Top row: comparison of the bistatic (a, left) and monostatic (b, right) measurement configurations for the reconstruction of deep interior void. The bistatic setup provides slightly better reconstruction. Second and third rows: detection of void (A) with different noise levels between -25 and 0 dB (c)–(h). The critical noise level losing the shape of the void is between -15 (e) and -8 dB (f). Above -8 dB, the void can be moderately detected, but artifacts appear around the void area.

Table 2
Distinguishability of Model Details

Model	Surface Layer		Interior	
	Data ^a	Reconst. ^b	Data ^a	Reconst. ^b
(A)	Clear	Moderate	Clear	Clear
(B)	Clear	Moderate	Clear	Moderate
(C)	Clear	Moderate	Moderate	Moderate
(D)	Clear	Moderate	Weak	Weak
(E)	Clear	Moderate	Weak	Moderate

Notes.

^a Based on the data curve in Figure 4(a).

^b Based on the reconstructions in Figures 5 and 6.

Table 3

Mean Square Errors (MSEs), Mean Absolute Errors (MAEs), and Relative Mean Absolute Errors (MAE-Rs)

Model	Error	Detail	Surface Layer	Global
(A)	MSE	8.21	0.99	1.19
	MAE	2.80	0.89	0.93
	MAE-R ^a	0.93
(B)	MSE	3.65	0.89	0.98
	MAE	1.90	0.92	0.91
	MAE-R ^a	0.95
(C)	MSE	124.67	0.92	3.53
	MAE	11.12	0.87	1.08
	MAE-R ^a	1.01
(D)	MSE	7.10	0.93	1.05
	MAE	2.49	0.89	0.90
	MAE-R ^a	0.83
(E)	MSE	6.86	0.90	1.04
	MAE	2.38	0.87	0.89
	MAE-R ^a	0.79

Notes. The category “Detail” refers to the ellipsoidal anomaly in models (A)–(C) and to the deep and shallow cracks in models (D) and (E), respectively. The category “Global” refers to the complete asteroid model.

^a Normalized relative to the difference between the detail permittivity and the global mean of the Gaussian random field (4).

details, most prominently the surface layer, are more obvious in the data (Figure 4) than in the final reconstructions (Figures 5 and 6), suggesting that the inversion quality might be improved by, for example, depth weighting or noise-robust techniques such as multigrid, Markov chain Monte Carlo sampling, or expectation maximization (Liu 2008; Tilley et al. 2017; Takala et al. 2018a).

Future work on this topic could investigate methods to utilize complementary data in the inversion process. One approach would be to use multiple radar frequencies as suggested by Herique et al. (2018). For example, frequency ranges of 25, 50, and 100 MHz can be considered to provide optimization of radar penetration depth. However, because the radar signal attenuation is directly proportional to signal frequency (Kofman 2012), the scattering and attenuation effects are stronger at the higher end of such frequency ranges. In the present Itokawa model, extra signal attenuation in the deep part at the ellipsoidal void detail is 10–30 dB in the center frequency range of 50–100 MHz (Kofman 2012), respectively. Therefore, due to the lower penetration capability, it is possible that 50 and 100 MHz frequencies are suitable to exploring only the surface layer of asteroids and the deep interior details can only be recovered by low-frequency waves. The analysis in this work involved only inversion of the modulated signal across the whole bandwidth. By combining the data from the modulated signal and the envelope, the accuracy of the method might be further improved. Moreover, gravimetry combined with radar sensing might help to improve the visibility of smooth structures or layers (Fregoso & Gallardo 2009; Park et al. 2014). Resolving the effect of surface scattering from anomalies such as large boulders, steep hills, or crevasses on the quality of the inversion, and enhancing the noise model to distinguish different error sources, will also be important future directions.

5. Conclusion

The results of this paper show that bistatic CRT can detect deep interior voids, cracks and high-permittivity boulders inside a complex rubble-pile asteroid model when the total

noise level in the data is around -10 dB with respect to the signal amplitude. The results suggest that permittivity anomaly details can be detected within a complex-structured asteroid by using CRT, excluding the deep areas around the center of mass, which are challenging due to signal attenuation and the limited-angle measurement point distribution with an aperture around the z -axis.

Furthermore, the bistatic measurement setup improves the robustness of the inversion compared to the monostatic case. However, recovering the smooth Gaussian background distribution was found to be difficult with the present approach, suggesting that complementary techniques, such as gravimetry, might be needed to improve the reliability of the inference in practice. The inversion quality might be improved via method development and/or analyzing complementary data, such as a higher-frequency signal, carrier wave envelope, or gravity field measurements.

L.-I.S., M.T., and S.P. were supported by the Academy of Finland Centre of Excellence in Inverse Modelling and Imaging.

Appendix Computational Framework and Performance

For inverting the data, we used the computational full-wave radar tomography approach developed in Pursiainen & Kaasalainen (2016), Takala et al. (2018a), and Takala et al. (2018b). The computationally intensive part of the simulation was run in the GPU partition of Tampere Center for Scientific Computing (TCSC) Narvi cluster, which consists of 8 GPU nodes with 20 CPU cores, 4 GPU each, totaling 32 NVIDIA Tesla P100 16 GB GPUs. The inversion reconstruction procedures were run on a Lenovo P910 workstation equipped with two Intel Xeon E5 2697A 2.6 GHz 16-core processors and 128 GB RAM.


The creation of the system from node and tetrahedra data, including all parts of the asteroid geometry, orbiter points and interpolation of the FE mesh required approximately 11 GB of memory space and 6700 s (approximately 1 hr 52 minutes). Out of this, the actual system creation took 652 s (approximately 10 minutes) and creating the spatial interpolation matrix accounted for the rest of the computational time.

The minimum computation time of one transmitted signal was 11,400 s (approximately 3 hr 10 minutes). The system size was approximately 4.8 GB. Because the forward simulation was parallelized into 16 processes, the total computation time of the entire simulation, 64 transmitter points, took a minimum of 45,400 s (approximately 12 hr 37 minutes). A typical expected computation time for the entire forward simulation was approximately 13.5 hr.

The present study shows that full-wave (full-bandwidth) data can be computed and inverted for a rubble-pile asteroid with a realistic size and shape using a state-of-the-art computing cluster. GPU acceleration was observed to be necessary in the forward simulation stage in order to achieve feasible computation times and a speed-up by at least a factor of 10. In radar applications, similar experiences have recently been reported, for example in Cordua et al. (2013). While the GPU-based forward simulation approach performs well regarding the speed, it is at the moment restricted with respect to the system size. In our case, doubling the asteroid diameter would not have been possible due to the limited GPU RAM, which in our

cluster is currently 12 GB. Since GPUs are a rapidly progressing field of technology, the available memory capacity may be expected to be significantly larger within a few years. Further development of the present computation framework may involve a pipeline for simulating realistic asteroid interiors based on a FE mesh structural model.

ORCID iDs

Liisa-Ida Sorsa  <https://orcid.org/0000-0001-5663-0958>

References

- Abe, M., Takagi, Y., Kitazato, K., et al. 2006, *Sci*, 312, 1334
 Asphaug, E., Belton, M. J. S., & Kakuda, R. Y. 2001, *LPI*, 32, 1867
 Bambach, P., Deller, J., Vilenius, E., et al. 2018, *AdSpR*, 62, 3357
 Barnouin-Jha, O. S., Cheng, A. F., Mukai, T., et al. 2008, *Icar*, 198, 108
 Barron, W., Cliver, E., Cronin, J., & Guidice, D. 1985, in *Handbook of Geophysics and the Space Environment*, ed. A. S. Jursa (4th ed.; Springfield, VA: Air Force Geophysics Laboratory)
 Berry, K., Sutter, B., May, A., et al. 2013, *AdAnS*, 149, 667
 Bićanić, N., de Borst, R., Mang, H., & Gunther, M. (ed.) 2010, *Computational Modelling of Concrete Structures, EURO-C (Leiden: CRC)*
 Carnelli, I. 2018, *Hera Mission*, https://www.cosmos.esa.int/documents/336356/1601091/SMPAG_HERA_Carnelli
 Carry, B. 2012, *P&SS*, 73, 98
 Catapano, I., Crocco, L., Krellmann, Y., Tritltsch, G., & Soldovieri, F. 2012a, *IGRSL*, 9, 378
 Catapano, I., Crocco, L., Soldovieri, F., et al. 2012b, in *2012 14th Int. Conf. Ground Penetrating Radar (GPR)*, 310
 Chilès, J.-P., & Delfiner, P. 2012, *Geostatistics: Modeling Spatial Uncertainty (2nd ed.; Hoboken, NJ: Wiley)*
 Christakos, G. 2005, *Random Field Models in Earth Sciences (Mineola, NY: Dover)*
 Cignoni, P., Callieri, M., Corsini, M., et al. 2008, in *Eurographics Italian Chapter Conf.*, ed. V. Scarano, R. D. Chiara, & U. Erra (The Eurographics Association), 129
 Constantine, P. 2012, *Random Field Simulation*, <https://se.mathworks.com/matlabcentral/fileexchange/27613-random-field-simulation>
 Cordua, K. S., Hansen, T. M., & Mosegaard, K. 2013, *Geop*, 77, H19
 Daniels, D. J. 2004, *Ground Penetrating Radar (London: Institution of Electrical Engineers)*
 Deller, J. F. 2017, PhD thesis, Univ. Kent Canterbury U.K. and International Max Planck Research School for Solar System Science Göttingen Germany
 European Space Agency, 2018, *CDF Study Report: Small Planetary Platforms (SPP) in NEO and MAB*, <http://sci.esa.int/future-missions-department/60411-cdf-study-report-small-planetary-platforms-spp/>
 Fregoso, E., & Gallardo, L. A. 2009, *Geop*, 74, L31
 Fu, L., Liu, S., Liu, L., & Lei, L. 2014, *IJSTA*, 7, 761
 Fujiwara, A., Kawaguchi, J., Yeomans, D. K., et al. 2006, *Sci*, 312, 1330
 Geuzaine, C., & Remacle, J.-F. 2009, *IJNME*, 79, 1309
 Gueting, N., Klotzsche, A., van der Kruk, J., et al. 2015, *JHyd*, 524, 680
 Gueting, N., Vienken, T., Klotzsche, A., et al. 2017, *WRR*, 53, 49
 Hansen, W., Sill, W., & Ward, S. 1973, *Geop*, 38, 135
 Hayabusa Project Science Data Archive, 2007, *Itokawa Shape Model*, <https://darts.isas.jaxa.jp/planet/project/hayabusa/shape>
 Herique, A., Agnus, B., Asphaug, E., et al. 2018, *ApSpR*, 62, 2141
 Japan Aerospace Exploration Agency, 2003, *Hayabusa Project*, http://global.jaxa.jp/projects/sat/muses_c/index.html
 Jutzi, M., & Benz, W. 2017, *A&A*, 597, A62
 Kofman, W. 2012, in *19th Int. Conf. Microwaves, Radar Wireless Communications*, 409
 Kofman, W., Barbin, Y., Klinger, J., et al. 1998, *AdSpR*, 21, 1589
 Kofman, W., Herique, A., Barbin, Y., et al. 2015, *Sci*, 349, aab0639
 Kofman, W., Herique, A., Goutail, J.-P., et al. 2007, *SSRv*, 128, 413
 Kraus, J. D. 1967, *AmJPh*, 35, 450
 Lantuéjoul, C. 2002, *Geostatistical Simulation, Models and Algorithms (Heidelberg, Germany: Springer)*
 La Spina, A., Paolicchi, P., Kryszyńska, A., & Pravec, P. 2004, *Natur*, 428, 400
 Lauretta, D. S., Balram-Knutson, S. S., Beshore, E., et al. 2017, *SSRv*, 212, 925
 Liu, J. S. 2008, *Monte Carlo Strategies in Scientific Computing (Springer Science & Business Media)*

- Michel, P., Cheng, A., Kuppers, M., et al. 2016, *AdSpR*, 57, 2529
- Michikami, T., Nakamura, A. M., Hirata, N., et al. 2008, *EP&S*, 60, 13
- Nakamura, T., Noguchi, T., Tanaka, M., et al. 2011, *Sci*, 333, 1113
- Okada, T., Shirai, K., Yamamoto, Y., et al. 2006, *Sci*, 312, 1338
- Park, R., Konopliv, A., Asmar, S., et al. 2014, *Icar*, 240, 118
- Pursiainen, S., & Kaasalainen, M. 2016, *ITAES*, 52, 2747
- Roberts, A. P., & Garboczi, E. J. 2002, *RSPSA*, 458, 1033
- Safaeinili, A., Gulkis, S., Hofstadter, M. D., & Jordan, R. L. 2002, *M&PS*, 37, 1953
- Saito, J., Miyamoto, H., Nakamura, R., et al. 2006, *Sci*, 312, 1341
- Snodgrass, C., Jones, G., Boehnhardt, H., et al. 2018, *AdSpR*, 62, 1947
- Soldovieri, F., Catapano, I., & Ludeno, G. 2017, in *EGU General Assembly Conf. Abstracts* 19, 12415
- Takala, M., Bambach, P., Deller, J., et al. 2018b, *ITAES*, in press
- Takala, M., Us, D., & Pursiainen, S. 2018a, *IEEE Transactions on Computational Imaging*, 4, 228
- Tilley, R. S., Sadjadpour, H., & Dowla, F. 2017, *Extending Ground Penetrating Radar Imaging Capabilities through Signal Processing.*, Tech. Rep. 1458247 (Albuquerque, NM: Sandia National Lab)
- Tsuchiyama, A., Uesugi, M., Matsushima, T., et al. 2011, *Sci*, 333, 1125
- Tsuda, Y., Yoshikawa, M., Abe, M., Minamino, H., & Nakazawa, S. 2013, *AcAau*, 91, 356

PUBLICATION

II

Tomographic inversion of gravity gradient field for a synthetic Itokawa model

L.-I. Sorsa, M. Takala, P. Bambach, J. Deller, E. Vilenius, J. Agarwal, K. Carroll,
Ö. Karatekin and S. Pursiainen

Icarus 336.(2020), 113425

DOI: 10.1016/j.icarus.2019.113425

Publication reprinted with the permission of the copyright holders



Tomographic inversion of gravity gradient field for a synthetic Itokawa model

Liisa-Ida Sorsa^{a,*}, Mika Takala^a, Patrick Bambach^b, Jakob Deller^b, Esa Vilenius^b,
Jessica Agarwal^b, Kieran A. Carroll^c, Özgür Karatekin^d, Sampsa Pursiainen^a

^a Tampere University, Faculty of Information Technology and Communication Sciences, PO Box 1001, 33014 Tampere University, Finland

^b Max Planck Institute for Solar System Research, Justus-von-Liebig-Weg 3, 37077 Göttingen, Germany

^c Gedex Systems Inc., 407 Matheson Blvd. East, Mississauga, Ontario L4Z 2H2, Canada

^d Royal Observatory of Belgium (ROB), Avenue Circulaire 3, Brussels 1180, Belgium

ARTICLE INFO

Keywords:

Asteroid Itokawa
Interiors
Geophysical techniques

ABSTRACT

This article investigates reconstructing the internal mass density of a numerical asteroid model using the gradient of a simulated gravity field as synthetic measurement data. Our goal is to advance the mathematical inversion methodology and find feasibility constraints for the resolution, noise and orbit selection for future space missions. We base our model on the shape of the asteroid Itokawa as well as on the recent observations and simulation studies which suggest that the internal density varies, increasing towards the center, and that the asteroid may have a detailed structure. We introduce randomized multiresolution scan algorithm which might provide a robust way to cancel out bias and artifact effects related to the measurement noise and numerical discretization. In this scheme, the inverse algorithm can reconstruct details of various sizes without fixing the exact resolution *a priori*, and the randomization minimizes the effect of discretization on the solution. We show that the adopted methodology provides an advantageous way to diminish the surface bias of the inverse solution. The results also suggest that a noise level below 80 Eotvos will be sufficient for the detection of internal voids and high density anomalies, if a sparse set of measurements can be obtained from a close-enough distance to the target.

1. Introduction

Geophysical investigations into the subsurface of the Earth are nowadays based on combining information of multiple geophysical fields, leading to more reliable models of the subsurface structures (Erkan and Jekeli, 2011). For example, subsurface cavities have been successfully detected by combining gravity field and ground penetrating radar measurements (Chromk et al., 2016; Mochales et al., 2008; Panisova et al., 2013). Furthermore, gravity gradiometry has been shown to detect local mass or density anomalies (Erkan and Jekeli, 2011; Jekeli and Lian Abt, 2011; McKenna et al., 2016). These investigations commonly have a low signal-to-noise ratio, hence the need to combine data from various measurement techniques. Such multi-modal approach is used to maximize the probability of anomaly detection and minimize that of a false alarm (McKenna et al., 2016).

The first attempt to investigate the deep interior structure of a small solar system body (SSSB) was the Comet Nucleus Sounding Experiment

by Radio-wave Transmission (CONSERT), a part of European Space Agency's (ESA) Rosetta mission to the comet 67P/Churyumov-Gerasimenko, in which a radio signal was transmitted between the orbiter Rosetta and the lander Philae (Kofman et al., 1998, 2015, 2007). Other missions to asteroids have concentrated on the structure and composition of the surface of the target SSSBs. The Hayabusa mission (Japan Aerospace Exploration Agency, 2003) by the Japanese Aerospace Exploration Agency (JAXA) explored the asteroid Itokawa extensively and measured the physical, chemical and geological properties of the body from orbit (Fujiwara et al., 2006; Okada et al., 2006). Furthermore, the Hayabusa mission returned a sample of the asteroid surface regolith for analysis on earth, confirming the classification of the asteroid to S-type (Fujiwara et al., 2006; Nakamura et al., 2011), as was originally reported by the earth-based visible and near-infrared spectroscopy observations (Binzel et al., 2001). Analysis of the collected dust particles suggests that Itokawa is an asteroid made of reassembled pieces of the inner portions of a once larger asteroid (Nakamura et al.,

* Corresponding author.

E-mail address: liisa-ida.sorsa@tuni.fi (L.-I. Sorsa).

2011; Tsuchiyama et al., 2011).

The currently ongoing missions, Hayabusa2 to the asteroid 16173 Ruygu by JAXA (Tsuda et al., 2013) and OSIRIS-REx to the asteroid 101955 Bennu by NASA (Lauretta et al., 2017) have been designed to measure the physical, chemical and geological properties of the target asteroids.

Based on the experience obtained in terrestrial applications (Chromk et al., 2016; Erkan and Jekeli, 2011; Mochales et al., 2008), the future missions to explore the interior structure of SSSBs would benefit from combining measurements from more than one geophysical field. Our recently published simulation studies of equipping CubeSats with a low-frequency stepped-frequency radar (Sorsa et al., in press; Takala et al., in press) suggest that tomographic reconstruction of the full electromagnetic wavefield can reveal internal structural anomalies in an SSSB. Therefore, augmenting such radar measurements with gravity field measurements by gradiometry presents an interesting opportunity to obtain complementary information on the structure of the target. Such a gravity gradiometer instrument has been suggested, for example, by the recent studies (Carroll and Faber, 2018; Carroll et al., 2018). A combined gravity and radar measurement for interior investigation of an SSSB is, for example, a part of ESA's future mission plan HERA (Karatekin and Goldberg, 2018). The gravity field can be sensed via a direct measurement by a gravity gradiometer (Carroll and Faber, 2018) or indirectly by observing the Doppler shift of a radio signal transmitted by a spacecraft (Andrews-Hanna et al., 2013; Konopliv et al., 2013). The recent Moon Gravity Recovery and Internal Laboratory (GRAIL) mission used the latter method to measure the change in the distance between two co-orbiting spacecrafts as they flew above the lunar surface to calculate the gravitational potential from the spherical harmonics data set (Zuber et al., 2013).

In this paper, we investigate inversion of simulated gravity measurements obtained for a synthetic asteroid model which is based on the shape of the asteroid Itokawa and augmented with interior density anomalies. Our model relies on the recent observations and impact simulations which suggest that the internal density of asteroids varies, increasing towards the center, and that the interior may have a detailed structure in which void cavities and cracks have been formed in between rubble or larger boulders (Carry, 2012; Deller, 2017; Jutzi and Benz, 2017). Our goal is to advance the mathematical inversion methodology and find feasibility constraints for the resolution of the reconstruction, noise and orbit selection to guide the design of future space missions. We introduce and investigate a randomized multiresolution scan algorithm which might provide a robust way to cancel out bias and artifact effects related to the measurement noise and numerical discretization. In this scheme, the inverse algorithm can reconstruct details of various sizes without fixing the exact resolution *a priori*, and the randomization minimizes the effect of discretization on the solution. We show that the adopted methodology provides an advantageous way to diminish the surface bias of the inverse solution. The results also suggest that a noise level below 80 Eotvos will be sufficient for the detection of internal voids and high density anomalies, if a sparse set of measurements can be obtained from a close-enough distance to the target.

2. Materials and methods

We use the gradient of the scalar gravity field strength as input data for our inversion procedure and study how the quality of the reconstruction depends on various parameters. We focus on the field strength for simplicity, assuming that the gravitational torsion field, which is omitted here, might involve more uncertainty, if the actual *in-situ* measurement is done under a rotational motion.

The two synthetic asteroid interior structure models have been created from the shape model of the asteroid Itokawa. The forward simulation of the field strength gradient is carried out in a uniformly regular tetrahedral finite element mesh (Braess, 2007). The mesh is generated with respect to a uniform point (vertex) lattice by subdividing

each cube in the lattice into six tetrahedra. The synthetic measurements are investigated for two orbit radii. Sections 2.1–2.4 describe the model and procedure used to create the simulated measurements.

In the inversion stage described in Section 2.5, we use a hierarchical Bayesian model which allows adjusting the hyperprior parameter for finding a well-localized reconstruction. The inverse estimate is found through a randomized multiresolution scanning technique in which the inversion mesh is decomposed to multiple, nested levels. Using this randomized scanning algorithm with Iterative Alternating Sequential (IAS) inversion algorithm, it is possible to average out discretization errors and hence the final inverse solution is less dependent on the discretization of the computation domain than it would otherwise be.

2.1. Asteroid models

The asteroid models used in this work are based on the triangular stereolithography (STL) surface mesh (Hayabusa Project Science Data Archive, 2007) of the asteroid Itokawa (Saito et al., 2006). The unstructured triangulated asteroid surface model was imported to Meshlab (Cignoni et al., 2008) and resampled with Poisson-disk sampling algorithm Bridson which produces a uniformly distributed set of points fulfilling a given minimum distance condition. This was done to obtain a regular surface mesh with a resolution comparable to that of the eventual volumetric mesh applied in the numerical simulations.

The asteroid model consists of a surface layer and an interior compartment in which the deep interior anomalies are located. The surface of the interior compartment was created by further down-sampling the shape model and rescaling it by the factor of 0.9. The same asteroid model structure was also used in radar simulations in Sorsa et al. (in press).

The bulk density of Itokawa as measured during the Hayabusa mission is $1.9 \pm 0.13 \text{ g/cm}^3$ and its orthogonal axes are 535, 294, and 209 m (Fujiwara et al., 2006). A careful analysis of the rotational lightcurve observations and thermophysical analysis suggest that Itokawa is composed of two bodies with different bulk densities (Lowry, S. C. et al., 2014). A recent study on asteroid mass-concentration estimates obtained by asteroid impact simulations (Jutzi and Benz, 2017) suggests that the bulk density of the deep interior part is higher than that of the surface. To simulate these features and test tomographic inversion, we created two interior models (A) and (B) depicted in the Fig. 1.

In the Model(A), the surface and the deep interior densities were adjusted to 1.8 g/cm^3 and 2.0 g/cm^3 , respectively. This way, we could keep the bulk density close to the measured one while accounting for density variation between the surface and the deep interior structures. Two spherical void cavities of 40 and 30 m radii and zero density were inserted into the asteroid body and the head, respectively. Based on the actual measurements of Itokawa by Hayabusa mission (Fujiwara et al., 2006) a rubble-pile asteroid may contain significant void space in the deep interior and these cavities model such anomalies. The locations were chosen so that one is in the body of the asteroid, in the deep interior part, and the other in the head, enclosed closer to the surface while being moderate in size. The center of mass of the Model(A) is in $x = 64, y = 0, z = 0 \text{ m}$, assuming the center of the coordinate system is in the geometrical center of the asteroid.

In the Model(B), the densities of the surface and the interior compartments were adjusted to 1.6 g/cm^3 and 1.8 g/cm^3 , respectively. A spherical high-density anomaly with a density of 8 g/cm^3 , and 45 m radius was located in the head of the asteroid, covering approximately 55 % of the total radius of the head and resulting in a total bulk density distribution similar to the findings in Lowry, S. C. et al. (2014), and a total bulk density equal to that of Model (A), 1.9 g/cm^3 . An internal high-density anomaly within a rubble-pile asteroid could result for example from an impact event. The center of mass of the Model(B) is in the coordinates $x = 122, y = 0, z = -16 \text{ m}$.

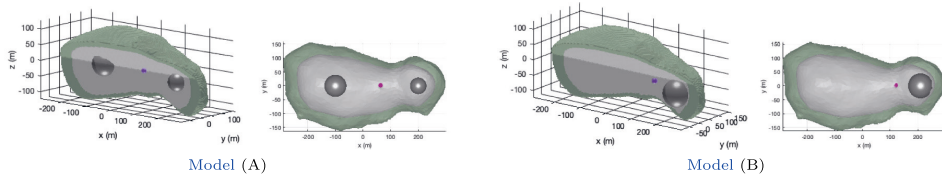


Fig. 1. 3D cut views showing the structures of the exact models (A) and (B) with their centers of mass indicated by magenta. **Left:** Model (A), the double void structure. **Right:** Model (B), the high density spherical anomaly in the head of the asteroid.

2.2. Measurement points

The measurement point sets were modelled similar to our earlier work (Sorsa et al., in press; Takala et al., in press) in which two CubeSats orbit an asteroid at a defined radius measured from the geometrical center of the asteroid. Two circular orbits with radii of 305 m and 500 m were investigated. These orbits were selected to provide initial results on the quality of reconstructions that can be achieved when performing measurements and analysis with state-of-the-art instruments and tomographic inversion methods. While the lower orbit (305 m) is not realistic for performing satellite-based measurements, it was included to provide a reference for close-proximity measurements. The angular coverage between the measurement plane and the asteroid spin axis (here: spin around the z axis in the xy plane) was set to 70 or 30°, resulting in the limited-angle spatial coverage of measurement points depicted in the Fig. 2, with apertures around the z -axis.

In practice, the gravity field measurements take time to carry out, resulting in measurement arcs rather than points. The effect of measurement arcs on the reconstructions was analyzed by introducing positional uncertainty in the model via rotating the measurement point set in comparison to the background model. Two rotation angles, 5° and 10°, corresponding to realistic measurement times in the 500 m radius orbit (Table 1) were investigated. The orbit velocity was assumed to follow the equation $v = \sqrt{GM/r}$, in which G is Newton's gravitational constant, M the bulk mass of the asteroid and r the orbit radius. The difference between the spacecraft orbit period and the spin rate of Ito-kawa (12.1 h, Fujiwara et al., 2006) resulted in approximately 5% positional uncertainty in the 500 m orbit radius case. The difference between the spacecraft orbit velocity and the asteroid spin rate in the lower orbit is too large (99%) for a meaningful examination of reconstruction effects.

2.3. Measurement noise

We apply the recent noise estimate (Carroll and Faber, 2018) obtained for the VEGA space gravimeter, when it is assumedly held by a 2.5 m boom attached to the mothership of the proposed HERA mission. Akin to Carroll and Faber (2018), the measurement noise distribution is assumed to be a Gaussian zero-mean random variable to account for

Table 1

The rotation angles and measurement durations resulting from realistic measurement arcs for the investigated orbits. The rotation angles are used in investigating the effect of measurement positional uncertainty in the inversion stage.

Rotation angle	305 m orbit Duration (s)	500 m orbit Duration (s)
5°	610 s	11,814 s
10°	1220 s	23,628 s

several independent, identically distributed sources of noise. The root mean square (RMS) error estimate relating to the standard deviation σ of a Gaussian random variable obtained in the study (Carroll and Faber, 2018) is of the form

$$\sigma \approx \frac{1}{\sqrt{\tau}} 300 \text{ E.} \quad (1)$$

Here, τ refers to the duration of the measurement in seconds. The unit E is eotvos ($1 \text{ E} = 1 \text{ e-}9 \text{ s}^{-2}$). The RMS values of this study and the required measurement times calculated according to Eq. (1) can be found in Table 2. The measurement durations for the higher noise levels shown in the Table 2 are unrealistically short from a measurement time perspective, as the shortest measurement time for the instrument is 30 s (Carroll and Faber, 2018). Therefore, they have been marked in parenthesis and are included for consistency.

The RMS noise level of the VEGA instrument is 55 E resulting in a

Table 2

The measurement noise levels investigated in this study. The level of the noise and the duration required by the measurement have been estimated according to Carroll and Faber (2018). The measurement times in (c) and (d) are unrealistically short and have therefore been marked in parenthesis only for consistency.

Item	RMS (E)	Duration (s)
(a)	2	2.3E4
(b)	8	1400
(c)	80	(14)
(d)	800	(0.14)

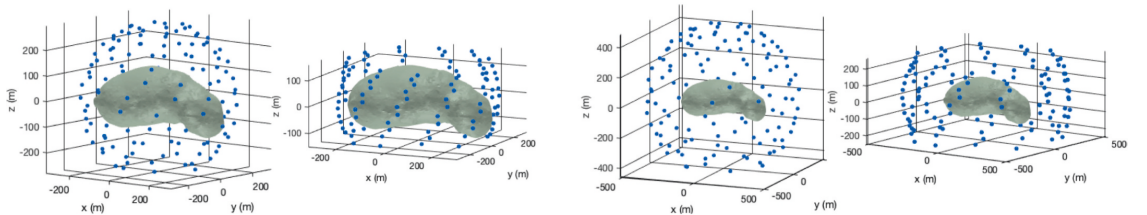


Fig. 2. **Left:** Measurement radius 305 m from the geometrical center of the asteroid, resulting in a subset of points which are very close to the surface in the long axis, limiting angle (the angle between the) 70° on the left, and 30° on the right. **Right:** Measurement radius 500 m from the center of the asteroid. Limiting angles 70° on the left, and 30° on the right.

measurement time of 27.4 s (Carroll and Faber, 2018). These finite measurement times follow from the repetitive measurement process required to measure the gradient of the gravitational field strength with a given accuracy.

From the inversion viewpoint, the measurement noise constitutes one significant error source, the other one being the modelling uncertainty related to, e.g., the position and orientation of the measurement instrument as well as the discretization of the computation domain. The methods for treating the positional error in this work are discussed more in the Section 2.5.2 which shows that the errors relating to the positional uncertainty can be decreased by a randomization and averaging procedure in the inversion stage.

2.4. Forward model

The relationship between a given mass density and the measurement data can be presented via a linear forward model of the form

$$\mathbf{y} = \mathbf{L}\mathbf{x} + \mathbf{n}, \tag{2}$$

in which $\mathbf{x} \in \mathbb{R}^N$ is the difference between the actual mass density, i.e., the unknown of the inverse problem, and an initial guess; $\mathbf{y} \in \mathbb{R}^M$ represents the difference between the actual measurements and numerically simulated data obtained for the initial mass density; \mathbf{L} is the system matrix representing the forward map; and $\mathbf{n} \in \mathbb{R}^M$ is the noise vector.

We assume that the target has been decomposed into a finite number of disjoint elements T_1, T_2, \dots, T_m (here: tetrahedra), and that the mass density is a piecewise constant distribution with respect to a set of disjoint subsets denoted by R_1, R_2, \dots, R_N consisting of $K_{j_1}, K_{j_2}, \dots, K_{j_N}$ elements, respectively, with $m = \sum_{j=1}^N K_j$. The subset R_j is defined as the union of the elements with center of mass closest to the point \vec{z}_j in the set $\vec{z}_1, \vec{z}_2, \dots, \vec{z}_N$ of randomly generated points.

The characteristic function of the element T_j , which is equal to one within the set j and zero elsewhere, is denoted by χ_j . The resulting mass difference density, $\Delta\rho$, is of the form

$$\Delta\rho = \sum_{j=1}^N x_j \psi_j \quad \text{with} \quad \psi_j = \sum_{k_j=1}^{K_j} \chi_{j,k_j}. \tag{3}$$

The $\psi_1, \psi_2, \dots, \psi_N$ is the function basis of the mass difference density, which is assumed to have a piecewise constant distribution inside the target asteroid. It is also the function basis for the inversion process.

Our data corresponds to the gradient of the scalar gravity field strength, i.e., the Euclidean norm of the three-component gravity field at a given point. The measurements are assumed to contain additive zero-mean Gaussian noise. Furthermore, the noise entries are assumed to be independent and identically distributed. The resulting forward model is of the form

$$\begin{aligned} y_i &= G \int_{\Omega} \Delta\rho(\vec{z}) \nabla_{\vec{r}_i} \frac{1}{\|\vec{z} - \vec{r}_i\|^2} d\vec{z} + n \\ &= 2G \int_{\Omega} \Delta\rho(\vec{z}) \frac{\vec{z} - \vec{r}_i}{\|\vec{z} - \vec{r}_i\|^4} d\vec{z} + n_i, \end{aligned} \tag{4}$$

where y_i with $i = 1, 2, \dots, M$ represents the difference data at the point \vec{r}_i ; n_i is a noise vector; and G is Newton's gravitational constant.

Substituting Eq. (3) into Eq. (4) and evaluating the gradient results in the equation

$$\begin{aligned} y_i &= 2G \sum_{j=1}^N x_j \int_{\Omega} \psi_j \frac{\vec{z} - \vec{r}_i}{\|\vec{z} - \vec{r}_i\|^4} d\vec{z} + n_i \\ &= 2G \sum_{j=1}^N x_j \sum_{k_j=1}^{K_j} \frac{\vec{z}_{k_j} - \vec{r}_i}{\|\vec{z}_{k_j} - \vec{r}_i\|^4} \int_{T_{j,k_j}} d\vec{z} + n_i, \end{aligned} \tag{5}$$

where \vec{z}_{k_j} is the center of mass and $\int_{T_j} d\vec{z}$ the volume of T_j . The resulting matrix equation is of the form Eq. (2) with the matrix $\mathbf{L} \in \mathbb{R}^{M \times N}$ given by

$$L_{i,j} = 2G \sum_{k_j=1}^{K_j} \frac{\mathbf{z}_{k_j} - \mathbf{r}_i}{\|\mathbf{z}_{k_j} - \mathbf{r}_i\|^4} \int_{T_j} d\mathbf{z}. \tag{6}$$

2.5. Inversion process

We approach the inverse problem via the hierarchical Bayesian model (HBM) in which the unknown parameter \mathbf{x} obeys a posterior probability density determined by the product $p(\mathbf{x}, \theta | \mathbf{y}) \propto p(\mathbf{x}, \theta) p(\mathbf{y} | \mathbf{x})$ between the prior density $p(\mathbf{x}, \theta)$, and the likelihood function $p(\mathbf{y} | \mathbf{x})$. The prior is a joint density of the form $p(\mathbf{x}, \theta) \propto p(\theta) p(\mathbf{x} | \theta)$, where the conditional part $p(\mathbf{x} | \theta)$ is a zero mean Gaussian density with a diagonal covariance matrix predicted by the hyperprior $p(\theta)$. The hyperprior is long-tailed, meaning that \mathbf{x} is likely to be a sparse vector with only few entries differing from zero. For this prior structure, HBM is advantageous for finding a well-localized reconstruction. As a hyperprior, one can use either the gamma or inverse gamma density (Calvetti et al., 2009), whose shape and scale are controlled by the parameters β and θ_0 , respectively. The likelihood follows directly from the measurement noise density via $\mathbf{n} = \mathbf{y} - \mathbf{L}\mathbf{x}$ with independent entries.

2.5.1. IAS inversion

The inverse estimate is found using the IAS *maximum a posteriori* (MAP) estimation method (Calvetti et al., 2009; Calvetti and Somersalo, 2008; Pursiainen and Kaasalainen, 2013). The gamma density is applied as the hyperprior. The IAS algorithm finds the MAP estimate via alternating the conditional posteriors $p(\mathbf{x} | \theta, \mathbf{y})$ and $p(\theta | \mathbf{x}, \mathbf{y})$ as the objective function. This is advantageous, since the maximizer for the first one can be found by solving a regularized least-squares optimization problem, and for the second one via an explicit analytical formula. When IAS inversion is applied with gamma density as the hyperprior, the outcome of the algorithm can be shown to correspond to the classical ℓ^2 -norm regularized solution of the inverse problem.

2.5.2. Randomized multiresolution scan

In order to minimize the effect of the selected function basis $\psi_1, \psi_2, \dots, \psi_N$ on the final reconstruction, we use a randomized multiresolution scan algorithm which finds the final reconstruction $\bar{\mathbf{x}}$ as an average \mathbf{x} -component of MAP estimates for $\zeta = (\mathbf{x}, \theta)$ obtained for multiple different resolution levels (Fig. 3) and randomized decompositions of the parameter space. Each decomposition is formed by selecting uniformly distributed number of points other than the selected mesh points with a nearest neighbor interpolation. Fig. 3 shows schematically one possible randomized decomposition for two resolution levels.

A decomposition D_ℓ refers to a surjective mapping $\mathbb{R}^N \rightarrow \mathbb{R}_\ell^K$ which is obtained by associating each basis function of the parameter space with the closest point in a set of K_ℓ random uniformly distributed points $\vec{p}_1, \vec{p}_2, \dots, \vec{p}_{K_\ell}$. Each decomposition is organized into a sequence of subsets $S = \{B_1, B_2, \dots, B_L\}$ in which the resolution, i.e., the number of randomized points grows along with ℓ as given by $K_\ell = Ks^{(\ell-L)}$, where s is a user-

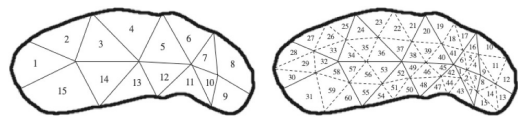


Fig. 3. A schematic illustration of subdivision of the asteroid shape into coarse (left) and fine (right) resolution subdomains. In this case the sparsity factor s , the ratio between the number of subdomains for two consecutive resolution levels, is four (4). An example of a surjective mapping from the coarse to fine resolution, $\mathbb{R}^N \rightarrow \mathbb{R}_\ell^K$, is given by $\{2\} \rightarrow \{25, 26, 27, 33\}$.

defined sparsity factor. Such a sequence is referred here to as a randomized multiresolution decomposition (Fig. 3). For optimizing the performance of the MAP estimation process, it is essential to begin with a coarse resolution and gradually proceed towards a finer one, since the distinguishability of the coarse density fluctuations which are realistic in asteroids is generally superior to that of other details such as small and well-localized density changes. The MAP estimate for $B_\ell + 1$ is obtained by using the one for B_ℓ as the initial guess (Fig. 4). Analogously, the estimate obtained for a single subset sequence is used as the initial guess for the next one. The initial guess of the whole procedure is set to be $\mathbf{x}^{(0)} = (0, 0, \dots, 0)$ and $\boldsymbol{\theta}^{(0)} = (\theta_0, \theta_0, \dots, \theta_0)$.

The algorithm proceeds as follows:

1. Choose the desired number of the resolution levels L and the sparsity factor s , i.e., the ratio of source counts between the levels.
2. For each resolution level $\ell = 1, 2, \dots, L$, create a random uniformly distributed set of center points $\bar{p}_1, \bar{p}_2, \dots, \bar{p}_{K_\ell}$. Find the sequence of subsets $B_1, B_2, \dots, B_{K_\ell}$ by applying the nearest interpolation scheme with respect to the center points.
3. Repeat the first two steps to generate a desired number D of independent randomized multiresolution decompositions S_1, S_2, \dots, S_D .
4. Start the reconstruction process with the decomposition S_1 and an initial guess $\zeta^{(0)}$ corresponding to $\mathbf{x}^{(0)} = (0, 0, \dots, 0)$ and $\boldsymbol{\theta}^{(0)} = (\theta_0, \theta_0, \dots, \theta_0)$.
5. For decomposition S_k , find a reconstruction $\mathbf{x}^{(\ell)}$ with an inversion technique chosen by the user, here the IAS method, and the initial guess $\zeta^{(\ell-1)}$ for the resolution levels $\ell = 1, 2, \dots, L$.
6. For level L , obtain the final estimate for the decomposition (basis) k as the normalized mean

$$\bar{\zeta}^{(k)} = \frac{\sum_{\ell=1}^L \zeta^{(\ell)}}{\sum_{\ell=1}^L s^{(L-\ell)}} \quad (7)$$

Here, the denominator follows from balancing out the effect of the multiplied source count which follows from the interpolation of a coarse level estimate to a denser resolution level.

7. If $k < D$ update $k \rightarrow k + 1$, i.e. move to the next decomposition, and repeat the 5-th and 6-th step with the initial guess $\bar{\zeta}^{(k-1)}$ for the resolution level $\ell = 1$.
8. Obtain the final reconstruction $\bar{\mathbf{x}}$ as the \mathbf{x} -component of the mean:

$$\bar{\zeta}^{(k)} = \frac{1}{D} \sum_{k=1}^D \bar{\zeta}^{(k)} \quad (8)$$

This procedure ensures that the ℓ^2 solution converges to the solution which is independent of the discretization of the computation domain and makes the solution to converge into the ℓ^2 -norm regularized solution. Assuming that the possible density fluctuations due to the basis selection are random and identically distributed, the average should converge towards a reconstruction which is invariant with respect to the applied basis. Hence, the randomized multiresolution decomposition enables localization of density fluctuations of various sizes within the deep interior part of the domain. Using simply the fine mesh shows any



Fig. 4. A schematic visualization of the data flow in the randomized multiresolution scan. The average of the MAP estimates obtained for the k -th multiresolution decomposition is used as the initial guess for the $k + 1$ -th one.

density anomalies only on the surface of the reconstruction. The coarser mesh decomposition and randomized scanning algorithm average out errors due to discretization arising in the decomposition process.

2.6. Numerical implementation with Geocetes interface

The present forward and inverse algorithms can be found implemented in the open Geocetes software package (Geocetes interface, 2018) for the Matlab (Mathworks, Inc.) platform. The software was developed over the course of this study and was applied in the numerical experiments. Geocetes creates a regular tetrahedral mesh conforming to the segmentation determined by the closed triangular surfaces. It applies graphics processing unit (GPU) acceleration which is essential in order to reduce computation time with reasonably high tetrahedral mesh resolution.

2.7. Numerical experiments

In the numerical experiments, we investigated the effects of the (i) noise, (ii) measurement distance, (iii) point distribution (angular coverage), (iv) number of IAS iteration steps, (v) the resolution (sparsity factor), (vi) number of the multiresolution decompositions and (vii) resolution levels, as well as (viii) anomaly density. The specifications of the features (i)–(vii) can be found in Table 3. The numerical experiments were organized into four entities devoted to (1) orbit, (2) noise, (3) number of multiresolution decompositions, as well as (4) resolution and estimate type. These focused on different features as described in Table 4.

The likelihood standard deviation was selected to match with that of the relative standard deviation of the gravity gradient field magnitude. Gamma distribution was used as the hyperprior in the inversion process. The shape parameter β was set to 1.5 based on preliminary experimentation with the prior in these types of inversion tasks, and the scaling parameter θ_0 was chosen based on the visual inspection of reconstruction quality (location and size of the detected anomaly in the reconstruction). The values were normalized with respect to the maximum entry. The workable values of θ_0 at the lower noise levels were found to be 10^5 and 10^8 for the 305 and 500 m radii orbits, respectively. These values produced an appropriate reconstruction quality in comparison to the exact model. The higher value was required for the high noise and low resolution cases. For the very low resolution, high noise, and higher orbit cases the scaling parameter had to be adjusted to 10^{10} in order to obtain a reasonable reconstruction showing the anomaly. The value of θ_0 affects the shape of the prior and, consequently, also the MAP estimates. The higher values enhanced the reconstruction and, therefore, they were used in the inversion process.

3. Results

3.1. Measurement data

The magnitude and direction of the simulated scalar gravity field

Table 3
Specifications of the features (i)–(viii) compared in the numerical experiments.

Item	Parameter	Values			
(i)	Noise	(a): 2 E	(b): 8 E	(c): 80 E	(d): 800 E
(ii)	Orbit radius	500 m	305 m		
(iii)	Angular coverage	70°	30°		
(iv)	IAS iterations n_{IAS} (Estimate type)	1	5	10	
(v)	Sparsity factor s	8	4	0	
(vi)	Number of decompositions	100	10	1	
(vii)	Number of resolutions	3	1		
(viii)	Anomaly density	Low (0 g/cm ³)		High (8.0 g/cm ³)	
(ix)	Positional uncertainty			5°	10°

Table 4
Numerical experiments (1)–(4).

Experiment	Title	Features investigated
(1)	Measurement configuration	(ii), (iii), (viii)
(2)	Noise level	(i), (ii)
(3)	Multiresolution scanning	(ii), (vi)
(4)	Estimate type	(iv), (v), (vii)

gradient is shown in the Fig. 5 for both measurement distances. The data shows clearly, how the strength of the field varies between the two models and the orbit distances, and that the difference is generally tangential. The high-density anomaly in the Model (B) causes more than five times higher field strengths in comparison to the Model (A) which contained two voids inside the asteroid. The measurement distance has an effect on, not just the magnitude of the field strength, but also on the localization of the anomalies. While there is clear localization of the signal in the lower orbit, similar effect is not seen as clearly in the more distant one, suggesting that a field originating from a distant source is averaged over the distance. The effect of the high-density anomaly in the Model (B) is clear in the 305 m orbit case. The field strength for Model (A) is generally more evenly distributed than for (B). However, that is to be expected as the mass distribution of (A) is more symmetric in comparison to (B).

Fig. 6 shows the projected data, which follows from multiplying the reconstruction with the system matrix, and also the residual, i.e., the difference between the actual and projected data, for the measurement distance of 500 m. The residual is obviously more random than the original data, which is in agreement with the current forward model in which the residual coincides with the noise term. The location of the largest amplitude is similar in each case, suggesting that the residual includes a model-driven component, which is not predicted by the present white noise error model.

3.2. Quality of reconstructions

The quality of reconstructions was inspected visually by examining how well the different parts of the exact models (A) and (B) (Fig. 1) were visible in the reconstructions. The size, shape and location of any density

anomalies indicated by the reconstructions were compared with the exact model. The good quality reconstructions showed clear, spherical anomalies of the size of the exact model, in the correct locations. The surface layer was not clearly distinguishable in any of the reconstructions.

3.3. Measurement configuration

In the experiment (1), the visually assessed quality of the reconstruction was affected more by the distance between the target and the measurement points than the point coverage of the measurements, as shown by the Fig. 7 depicting the orbits with 305 and 500 m radii. Distinguishing both low and high density anomalies, i.e., voids and boulders in the models (A) and (B), respectively, was found to be feasible at both distances. The closer, 305 m, orbit was observed to provide a superior depth localization capability, as the reconstructions obtained at 500 m distance were somewhat biased towards the surface of the target domain, which is shown by the greater spread of the anomaly detected.

3.4. Noise level

The signal-to-noise ratio (SNR) for Model (A) varied from poor 12 dB to appropriate 24 dB, and for Model (B) it was generally appropriate, ranging from 20 to 29 dB. The SNR for each case can be found in the Table 5

The effect of the noise level was investigated for the 500 m orbit in the experiment (2) the results of which can be found in Fig. 9. Anomaly detection was found to be feasible with the lowest noise level (a) for Models(A) and (B). Above that, the voids found for Model (A) were barely distinguished as such. Detection of the high density anomaly in Model (B) was less affected by the noise. However, the noise level (d) was too large for finding an appropriate reconstruction also in the case of (B).

3.5. Measurement arc

Realistic gravity gradient field measurements result in measurement arcs instead of points, causing positional uncertainty in the inversion stage. The effect of such uncertainty on the reconstruction is presented

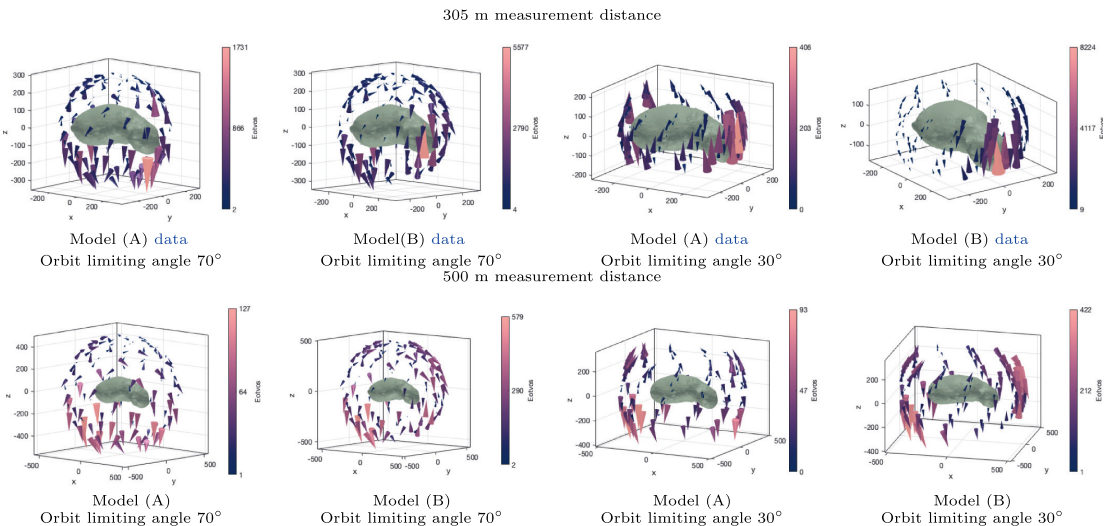


Fig. 5. The magnitude and direction of the scalar gravity field gradient at the measurement points depicted for each measurement configuration and both measurement distances.

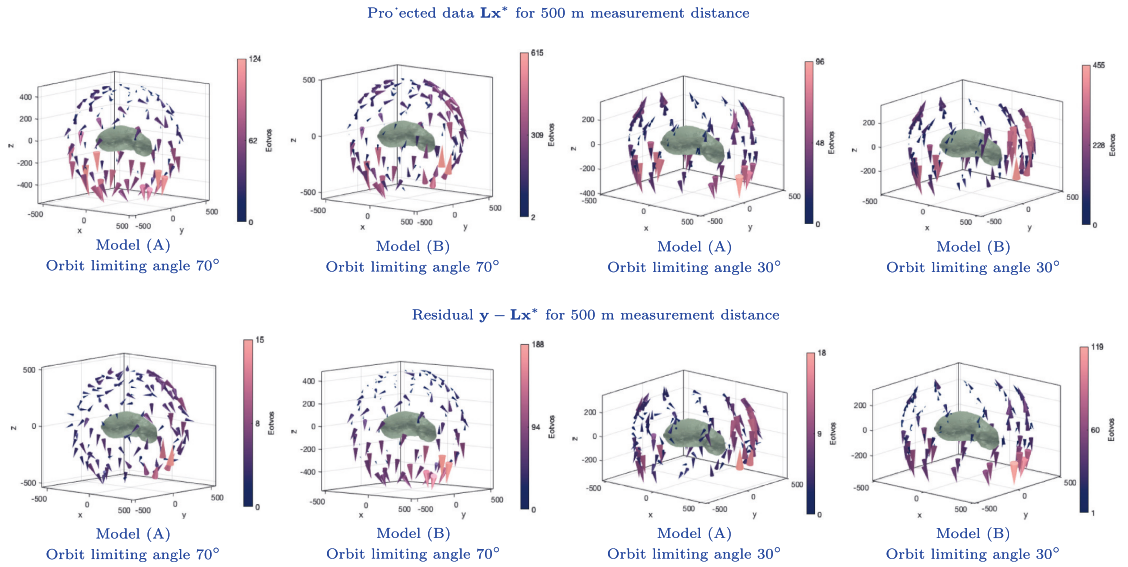


Fig. 6. The projected data Lx^* and the residual $y - Lx^*$ for the 500 m measurement distance. Here the reconstruction has been normalized so that the 2-norm of the actual and projected data coincide.

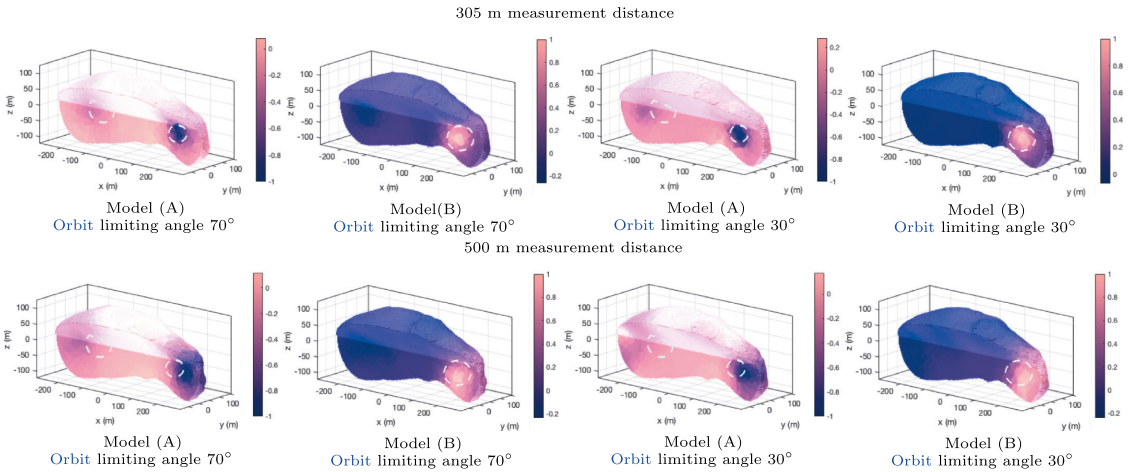


Fig. 7. 3D cut-in views of the reconstructions at 305 and 500 m measurement distances and two different angular coverages with the corresponding measurement points shown in the Fig. 2. The higher coverage of points around the asteroid (limiting angle 70°) results in better localization of the perturbation at the higher orbit radius. With the smaller radius the effect on the reconstructions is not significant. The exact locations of the density anomalies are indicated with dashed white circles.

Table 5

Signal-to-noise ratios (SNR) for the investigated models. The SNR for the Model (A) varies from poor to acceptable, whereas for the Model (B) it is generally appropriate.

θ	r (m)	Model (A)	Model (B)
70°	305	24 dB	28 dB
	500	14 dB	21 dB
30°	305	21 dB	29 dB
	500	12 dB	20 dB

in the Fig. 8 for the 500 m measurement radius. The reconstruction quality for Model (A) was found to suffer from the positional uncertainty more than that found for Model (B).

3.6. Multiresolution scanning

The effects related to the number and sparsity factor of the multi-resolution decompositions were explored in the experiment (3) and are illustrated in the Fig. 9. The smoothest results were obtained using 100 decompositions and the sparsity factor $s = 8$. With a lower value $s = 4$, i.

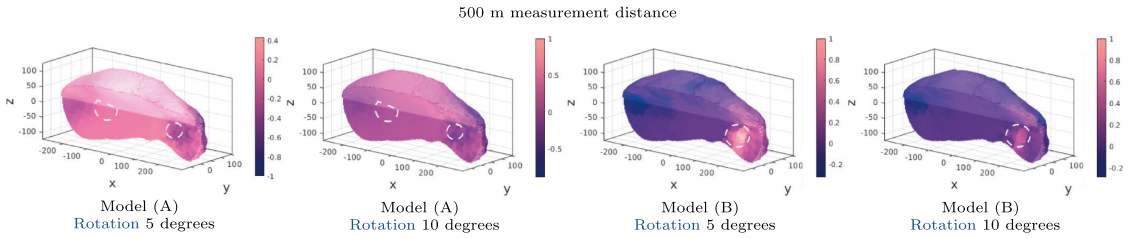


Fig. 8. The effect of positional uncertainty on the reconstructions. Such uncertainty results from measurements being carried out on a measurement arc instead of points. The exact locations of the density anomalies are indicated with dashed white circles.

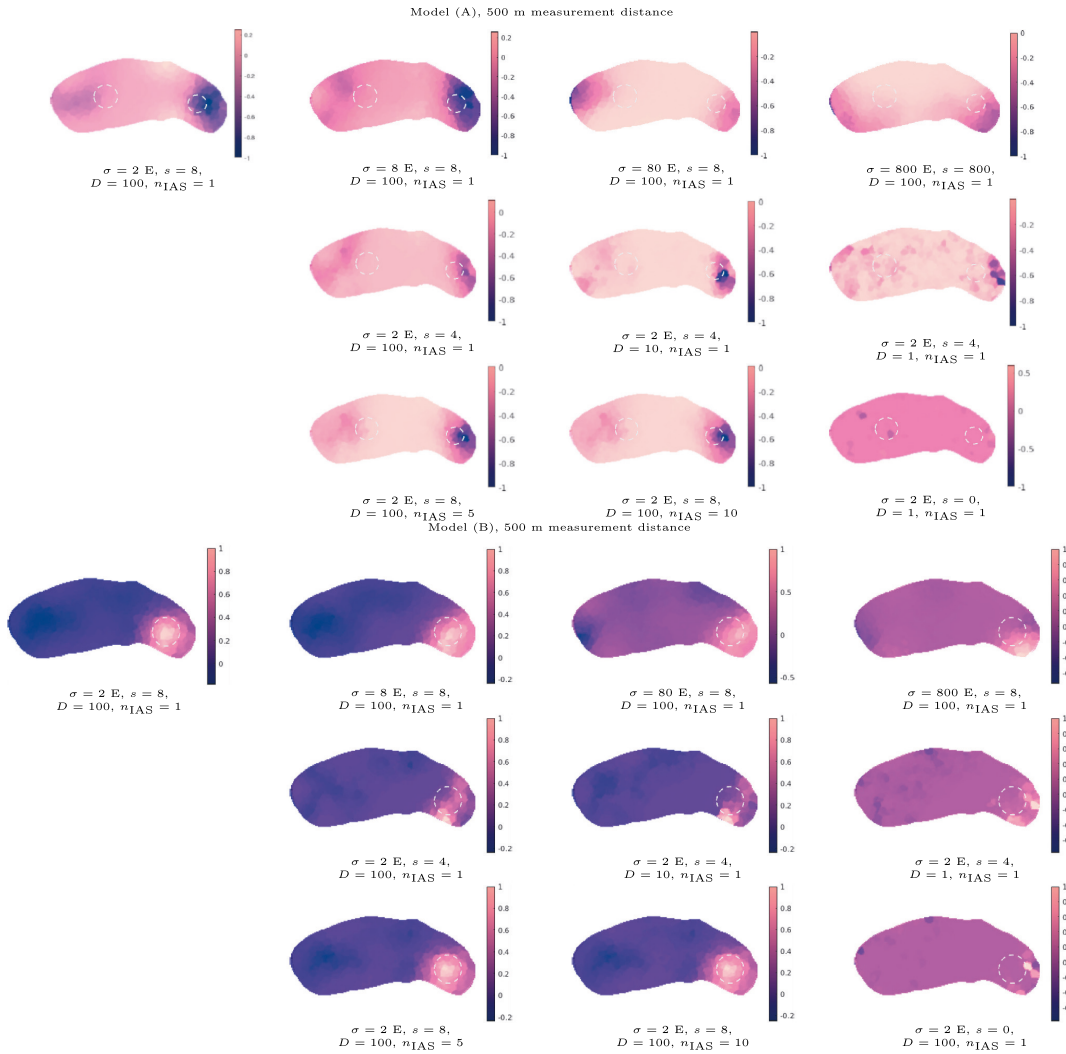


Fig. 9. The xz -plane crosscut views of the effects of noise level, sparsity factor, and IAS MAP iteration rounds n_{IAS} on the Model (A) and (B) reconstructions at 500 m measurement distance. The white dashed lines indicate the locations of the density anomalies. Parameters σ , s and D denote the standard deviation of the noise, the sparsity factor and the number of the multiresolution decompositions, respectively. The number of resolution levels is $L = 3$ in each case, and the number of IAS MAP iterations n_{IAS} performed for each level is identical. Sparsity 0 refers to a case in which the multiresolution decomposition was absent in the reconstruction process.

e., with a smaller difference between the coarse and fine resolution levels, the reconstructions became biased towards the surface, losing depth-resolution, and regularity regarding the shape of the detected anomalies. The irregularity and bias were found to be further exaggerated, when a lower number of decompositions (10 and 1) were used. The reconstructions obtained with a single decomposition also included some visible high-frequency artifact patterns which, otherwise, were essentially absent.

3.7. Estimate type

A comparison between ℓ^2 and ℓ^1 estimate types (4) can also be found in Fig. 9. The ℓ^2 estimate, obtained with $n_{IAS} = 1$, provided, overall, the most regular (smooth) outcome. Increasing the number of IAS iterations, i.e., finding an ℓ^1 type reconstruction, was observed to result in a sharper localization of the anomalies, sharpening also the other structures. The difference between the iteration counts of $n_{IAS} = 5$ and $n_{IAS} = 10$ was found to be a minor one. The essence of the multi-resolution approach for the reconstruction quality is reflected by the single-resolution ℓ^2 -reconstruction ($n_{IAS} = 1$ with a single resolution level) which suffers from an extreme surface bias and artifacts.

4. Discussion

Direct measurements of asteroid interiors have yet not been carried out (Herique et al., 2017) and, therefore, our understanding of the internal structures are based on bulk properties, asteroid spin rates, as well as on impact and other simulation studies suggesting candidate examples of structures fitting to the parameters. For example, the asteroid Itokawa is known to have a 40 % bulk porosity (Saito et al., 2006; Sanchez and Scheeres, 2014) and a potential aggregate structure (Barnouin-Jha et al., 2008). The distribution of mass inside an asteroid is yet still mainly unknown. Our study suggests that the gradient of the gravity field can provide meaningful data of the internal distribution of mass, and that the data can be used for tomographic inversion.

The two synthetic models developed for this study were selected based on the confirmed bulk parameters for the asteroid Itokawa, and on possible scenarios how these properties can be achieved, to provide baseline information on the kinds of deep interior structures that can be observed from the orbit. The results obtained in Lowry, S. C. et al. (2014) suggest that Itokawa is composed of the merger of two separate bodies with bulk densities of $1.750 \pm 0.110 \text{ g/cm}^3$ and $2.850 \pm 0.500 \text{ g/cm}^3$. They used the shape model of Gaskell et al. (2008) which was based on rotational light curve analysis and applied detailed thermophysical analysis to the shape determined by the Hayabusa spacecraft (Saito et al., 2006).

The double-void synthetic Model (A) corresponds to a low-density asteroid with significant void space in the interior. The high-density anomaly contained by the Model (B) corresponds to one possible formation scenario of Lowry, S. C. et al. (2014), a catastrophic collision on a differentiated large object which contained a high-density metallic fragment (e.g. iron) in this formation process. This fragment could then have been subsumed by the silicate material in the “head” region. Although it is unlikely that two unrelated objects would have a sufficiently low-velocity encounter to ensure the survival of both lobes and still have uniform surface composition and structure on the two lobes, and assumption of the existence of such iron-containing lobe has not been verified by direct measurements, the suggested model was included in this study to examine the reconstruction of such a high-density anomaly by gravity gradient field inversion.

The insensitivity of the depth localization for the measurement distance in this study is a well-known feature in ground based gravity inversion applications (Erkan and Jekeli, 2011; Madej, 2017). An obvious reason for this finding is the inherent ambiguity of depth information in gravity field data. Consequently, a nearby low-intensity anomaly can result in almost identical measurements with an outcome

following from a higher-intensity and more distant obstacle. As a result, fluctuations in the depth (radial) direction are difficult to be reconstructed. That is, when a vector corresponding to such a fluctuation is multiplied with the governing matrix \mathbf{L} of the forward model, the resulting vector is likely to belong into the numerical null-space of \mathbf{L} (Liu et al., 1995; Pursiainen, 2008), meaning that it can have a norm very close to zero and making it weakly distinguishable based on the measurements. In the inversion stage, the weak depth-localization capability of the gravity data causes a strong bias of the reconstructions towards the surface of the target body which is why surface projections are used in presenting the results of gravity measurements, for example, the gravity acceleration on the surface of Mars in Gorski et al. (2018). The surface bias of a reconstruction is also a general phenomenon in inverse problems involving weak depth data, such as the biomedical imaging applications based on quasi-static electric field measurements (Calvetti et al., 2009; Kaipio and Somersalo, 2004).

The essence of the proposed randomized multiresolution scan inversion approach is that the coarse density fluctuations are likely to be the clearest distinguishable components of the candidate solution set. Therefore, separating the coarse and fine details during the inversion process can provide an enhanced robustness of the final reconstruction compared to the approaches using all components at once. Here this is, especially, the case with correcting the bias in the depth direction. However, inverting measurements with a coarse discretization instead of a fine one might introduce other biases or artifacts relating to spatial location which in the present scanning approach are tackled by averaging the estimates produced by the IAS iteration over the set of randomized decompositions. The eventual inversion process can detect density details of various sizes as it can operate over a wide range of resolutions, and does not necessitate fixing the resolution *a priori* based on the deemed anomaly size.

Obtaining data from a close enough distance will obviously require a special mission design. A close approach for gravity measurement has been suggested, e.g., for Juventas CubeSat in Karatekin and Goldberg (2018). Maneuvering in the close proximity of the target will be difficult due to the inhomogeneities of the gravity field and, therefore, performing effective gravity field or gravity gradient measurements in the close proximity to a target SSSB will be challenging. Investigating realistic stable orbits around small bodies for gravimetric measurements will, therefore, be an important future research topic. A measurement duration of 5000 s resulting in a noise RMS of 4 E has been suggested to be feasible in Carroll and Faber (2018). Also incorporating the measurement arc instead of the point-approximation of the measurement used in this study and finding ways to incorporate model-driven components in the error model will be studied in the future. Obtaining a sufficiently low noise might be also possible via a radio-scientific Doppler shift measurement. Such approach was utilized, for example, in the high-precision measurements of the recent lunar science mission GRAIL (Gravity Recovery and Interior Laboratory) with two spacecraft configuration (Andrews-Hanna et al., 2013; Konopliv et al., 2013; Zuber et al., 2013). In addition to the signal specifications, the accuracy of a Doppler measurement will be limited also by external factors such as the solar wind pressure which presents a challenge with SSSBs of the size such as Itokawa and other asteroids with a few hundred meter diameters.

Another important direction for the future work will be to investigate parallel radar and gravity inversion. Akin to the ground-based geointerferometry applications (Erkan and Jekeli, 2011; Hausmann et al., 2007; Mochales et al., 2008), a radar-based reconstruction of the interior structure may be expected to provide a superior depth-resolution compared to gravimetry, since the electromagnetic wave of the radar signal carries time-domain information which enables depth-inference of the scattering obstacle. Hence, a radar observation will be also less dependent on the observation distance in comparison to gravity measurements. Our recent findings suggest that radar inversion emphasizes high-contrast details with the cost of smooth variations such as large

areas of denser or more porous regolith which might be detected by a gravimeter (Sorsa et al., in press). Therefore, it will also be vital to analyze the interconnection and correlation between the electric permittivity and mass density distributions observed by the radar and gravimeter, respectively (Trabelsi et al., 2001). Validating the gravity gradiometry inversion approach proposed in this paper with measurements in a terrestrial application such as suggested by Kirkendall, Barry et al. (2007) is also a potential future work topic.

5. Conclusion

This article concentrated on the mathematical methodology, resolution, noise and orbit radius selection with tomographic gravity field investigation performed for an asteroid as the potential application. The results obtained with simulated data suggest that the randomized multiresolution scanning technique combined with the iterative alternating sequential (IAS) inversion algorithm provides an advantageous way to enable depth localization of density anomalies, a feature not inherent in other inversion methods.

Void localization in an asteroid would require the measurement noise to be below 8 E at 500 m orbit. The reconstruction of a high-density anomaly is less sensitive to noise, and it can be achieved with noise levels up to 80 E. This is also reflected in the signal-to-noise ratios obtained for the models. The reconstruction method was shown to be robust with respect to the positional uncertainty of the measurement for up to 5% error, confirming long enough measurement times to be able to reduce the measurement noise in real measurement scenarios.

Acknowledgments

L.-I.S., M.T. and S.P. were supported by the Academy of Finland Centre of Excellence in Inverse Modelling and Imaging 2018-2025.

References

- Andrews-Hanna, J.C., Asmar, S.W., Head, J.W., Kiefer, W.S., Konopliv, A.S., Lemoine, F. G., Matsuyama, I., Mazarico, E., McGovern, P.J., Melosh, H.J., et al., 2013. Ancient igneous intrusions and early expansion of the moon revealed by grail gravity gradiometry. *Science* 339, 675–678.
- Barnouin-Jha, O.S., Cheng, A.F., Mukai, T., Abe, S., Hirata, N., Nakamura, R., Gaskell, R. W., Saito, J., Clark, B.E., 2008. Small-scale topography of 25143 Itokawa from the Hayabusa laser altimeter. *Icarus* 198, 108–124.
- Binzel, R.P., Rivkin, A.S., Bus, S.J., Sunshine, J.M., Burbine, T.H., 2001. Muses-c target asteroid (25143) 1998 sf36: a reddened ordinary chondrite. *Meteorit. Planet. Sci.* 36, 1167–1172.
- Braess, D., 2007. *Finite Elements: Theory, Fast Solvers, and Applications in Solid Mechanics*. Cambridge University Press.
- Bridson, R. Fast poisson disk sampling in arbitrary dimensions. Please supply the year of publication in "Bridson". <http://www.cs.ubc.ca/rbridson/docs/bridson-siggraph07-poissondisk.pdf>. Accessed: 17 May 2019.
- Calvetti, D., Hakula, H., Pursiainen, S., Somersalo, E., 2009. Conditionally Gaussian hypermodels for cerebral source localization. *SIAM J. Imag. Sci.* 2, 879–909.
- Calvetti, D., Somersalo, E., 2008. Hypermodels in the Bayesian imaging framework. *Inverse Prob.* 24, 034013.
- Carroll, K., Faber, D., 2018. Tidal Acceleration Gravity Gradiometry for Measuring Asteroid Gravity Field from Orbit. https://www.researchgate.net/publication/328828084_Tidal_Acceleration_Gravity_Gradiometry_for_Measuring_Asteroid_Gravity_Field_From_Orbit.
- Carroll, K., Zee, R., Spencer, H., Connors, M., 2018. Geophysical Reconnaissance Asteroid Surface Probe (GRASP). https://www.researchgate.net/publication/328828150_Geophysical_Reconnaissance_Asteroid_Surface_Probe_GRASP.
- Carry, B., 2012. Density of asteroids. *Planet. Space Sci.* 73, 98–118.
- Chromk, J., Grin, M., Panisova, J., Vajda, P., Kubov, A., 2016. Validation of sensitivity and reliability of gpr and microgravity detection of underground cavities in complex urban settings: test case of a cellar. *Contributions to Geophysics and Geodesy* 46.
- Cignoni, P., Callieri, M., Corsini, M., Dellepiane, M., Ganovelli, F., Ranzuglia, G., 2008. MeshLab: An Open-Source Mesh Processing Tool. In: Scarano, V., Chiara, R.D., Erra, U. (Eds.), *Eurographics Italian Chapter Conference*. The Eurographics Association.
- Deller, J.F., 2017. *Hyper-Velocity Impacts on Rubble Pile Asteroids*. Ph.D. thesis. School of Physical Sciences University of Kent Canterbury U.K. and International Max Planck Research School for Solar System Science Göttingen Germany.
- Erkan, K., Jekeli, C., 2011. A comparative analysis of geophysical fields for multi-sensor applications. *J. Appl. Geophys.* 74, 142–150.
- Fujiwara, A., Kawaguchi, J., Yeomans, D.K., Abe, M., Mukai, T., Okada, T., Saito, J., Yano, H., Yoshikawa, M., Scheeres, D.J., Barnouin-Jha, O., Cheng, A.F., Demura, H., Gaskell, R.W., Hirata, N., Ikeda, H., Kominato, T., Miyamoto, H., Nakamura, A.M., Nakamura, R., Sasaki, S., Usugi, K., 2006. The rubble-pile asteroid Itokawa as observed by Hayabusa. *Science* 312 (5778), 1330–1334.
- Gaskell, R., Saito, J., Ishiguro, M., Kubota, T., Hashimoto, T., Hirata, N., Abe, S., Barnouin-Jha, O., Scheeres, D., 2008. Gaskell Itokawa Shape Model v1.0. HAY-A-AMICA-5-ITOKAWASHAPE-V1.0. NASA Planetary Data System.
- Geocoles interface, 2018. Geomapping Tool for Small Celestial Bodies. <https://github.com/sampsapursiainen/Geocoles> [Accessed 5 December 2018].
- Gorski, K.M., Bills, B.G., Konopliv, A.S., 2018. A high resolution mars surface gravity grid. *Planet. Space Sci.* 160, 84–106.
- Hausmann, H., Krainer, K., Brckl, E., Mostler, W., 2007. Internal structure and ice content of Reichenkar rock glacier (Stubai Alps, Austria) assessed by geophysical investigations. *Permafrost. Periglacial Process.* 18, 351–367.
- Hayabusa Project Science Data Archive, 2007. Itokawa Shape Model. <https://darts.isas.jaxa.jp/planet/project/hayabusa/shape.pl>. Accessed 18 December 2017.
- Herique, A., Agnus, B., Asphaug, E., Barucci, A., Beck, P., Bellerose, J., Biele, J., Bonal, L., Bousquet, P., Bruzzone, L., Buck, C., Carnelli, L., Cheng, A., Ciarletti, V., Delbo, M., Du, J., Du, X., Eyraud, C., Fa, W., Fernandez, J.G., Gassot, O., Granados-Alfaro, R., Green, S., Grieger, B., Grundmann, J., Grygorczuk, J., Hahnell, R., Heggy, E., Ho, T.-M., Karatekin, O., Kasaba, Y., Kobayashi, T., Kofman, W., Krause, C., Kumamoto, A., Kuppers, M., Laabs, M., Lange, C., Lasue, J., Levasseur-Regourd, A., Mallet, A., Michel, P., Mottola, S., Murdoch, N., Mutze, M., Oberst, J., Orosei, R., Plettemeier, D., Rochat, S., Rodriguez-Suquet, R., Rogez, Y., Schaffer, P., Snodgrass, C., Souyris, J.-C., Tokarz, M., Ulamec, S., Wahlund, J.-E., Zine, S., 2017. Direct observations of asteroid interior and regolith structure: Science measurement requirements. *Adv. Space Res.*
- Japan Aerospace Exploration Agency, 2003. Hayabusa Project. http://global.jaxa.jp/projects/sat/muses_c/index.html [Accessed 18 January 2018].
- Jekeli, C., Lian, A.T., 2011. Locating anomalies by gravity gradiometry using the matched filter with a probabilistic assessment. *Stud. Geophys. Geod.* 55, 1–19.
- Jutzi, M., Benz, W., 2017. Formation of bi-lobed shapes by sub-catastrophic collisions. A late origin of comet 67P's structure. *Astron. Astrophys.* 597, A62.
- Kaipio, J., Somersalo, E., 2004. *Statistical and Computational Inverse Problems*. Springer-Verlag New York.
- Karatekin, Ö., Goldberg, H., 2018, November. Juventas cubesat. In: Hera community workshop 15-16 November 2018. https://www.cosmos.esa.int/documents/1786001/18460917.+juventas-overview_v3.pdf/b548e67a-9243-9263-96d7-60d643f8f8e1.
- Kirkendall, Barry, Li, Yaoguo, Oldenburg, Douglas, 2007. Imaging cargo containers using gravity gradiometry. *IEEE Trans. Geosci. Remote Sens.* 45, 1786–1797.
- Kofman, W., Barbin, Y., Klingner, J., Levasseur-Regourd, A.-C., Barriot, J.-P., Herique, A., Hagfors, T., Nielsen, E., Grn, E., Edenhofer, P., Kochan, H., Picardi, G., Seu, R., van Zyl, J., Elachi, C., Melosh, J., Veverka, J., Weissman, P., Svedhem, L., Hamran, S., Williams, L., 1998. Comet nucleus sounding experiment by radiowave transmission. *Adv. Space Res.* 21, 1589–1598.
- Kofman, W., Herique, A., Barbin, Y., Barriot, J.-P., Ciarletti, V., Clifford, S., Edenhofer, P., Elachi, C., Eyraud, C., Goutail, J.-P., Heggy, E., Jorda, L., Lasue, J., Levasseur-Regourd, A.-C., Nielsen, E., Pasquero, P., Preusker, F., Puget, P., Plettemeier, D., Rogez, Y., Sierks, H., Stutz, C., Svedhem, H., Williams, L., Zine, S., Van Zyl, J., 2015. Properties of the 67p/Churyumov-Gerasimenko interior revealed by consert radar. *Science* 349.
- Kofman, W., Herique, A., Goutail, J.-P., Hagfors, T., Williams, L.P., Nielsen, E., Barriot, J.-P., Barbin, Y., Elachi, C., Edenhofer, P., Levasseur-Regourd, A.-C., Plettemeier, D., Picardi, G., Seu, R., Svedhem, J., 2007. The comet nucleus sounding experiment by radiowave transmission (consert): a short description of the instrument and of the commissioning stages. *Space Sci. Rev.* 128, 413–432.
- Konopliv, A.S., Park, R.S., Yuan, D.-N., Asmar, S.W., Watkins, M.M., Williams, J.G., Fahnestock, E., Kruizinga, G., Paik, M., Strelakov, D., et al., 2013. The jpl lunar gravity field to spherical harmonic degree 660 from the grail primary mission. *J. Geophys. Res. Planets* 118, 1415–1434.
- Lauretta, D.S., Balram-Knutson, S.S., Beshore, E., Boynton, W.V., Drouet d'Aubigny, C., DellaGiustina, D.N., Enos, H.L., Golish, D.R., Hergenrother, C.W., Howell, E.S., Bennett, C.A., Morton, E.T., Nolan, M.C., Rizk, B., Roper, H.L., Bartels, A.E., Bos, B. J., Dworkin, J.P., Highsmith, D.E., Lorenz, D.A., Lim, L.F., Mink, R., Moreau, M.C., Nuth, J.A., Reuter, D.C., Simon, A.A., Bierhaus, E.B., Bryan, B.H., Ballouz, R., Barnouin, O.S., Binzel, R.P., Botke, W.F., Hamilton, V.E., Walsh, K.J., Chesley, S.R., Christensen, P.R., Clark, B.E., Connolly, H.C., Crombie, M.K., Daly, M.G., Emery, J. P., McCoy, T.J., McMahon, J.W., Scheeres, D.J., Messenger, S., Nakamura-Messenger, K., Righter, K., Sandford, S.A., 2017. Osiris-rex: sample return from asteroid (101955) bennu. *Space Sci. Rev.* 212, 925–984.
- Liu, J., Guenier, B., Benard, C., 1995, Dec. A sensitivity decomposition for the regularized solution of inverse heat conduction problems by wavelets. *Inverse Prob.* 11, 1177–1187.
- Lowry, S.C., Weissman, P.R., Duddy, S.R., Rozitis, B., Fitzsimmons, A., Green, S.F., Hicks, M.D., Snodgrass, C., Wolters, S.D., Chesley, S.R., Pittichová, J., van Oers, P., 2014. The internal structure of asteroid (25143) Itokawa as revealed by detection of yorp spin-up. *A&A* 562, A48.
- Madej, J., 2017. Gravimetric surveys for assessing rock mass condition around a mine shaft. *Acta Geophys.* 65, 465–479.
- McKenna, J.R., Rim, H., Li, Y., 2016. Feasibility and limitations of void detection using gravity gradiometry. *IEEE Trans. Geosci. Remote Sens.* 54, 881–891.
- Mochales, T., Casas, A.M., Pueyo, E.L., Pueyo, O., Román, M.T., Poció, A., Soriano, M. A., Anson, D., 2008. Detection of underground cavities by combining gravity,

- magnetic and ground penetrating radar surveys: a case study from the Zaragoza area, NE Spain. *Environ. Geol.* 53, 1067–1077.
- Nakamura, T., Noguchi, T., Tanaka, M., Zolensky, M.E., Kimura, M., Tsuchiyama, A., Nakato, A., Ogami, T., Ishida, H., Uesugi, M., Yada, T., Shirai, K., Fujimura, A., Okazaki, R., Sandford, S.A., Ishibashi, Y., Abe, M., Okada, T., Ueno, M., Mukai, T., Yoshikawa, M., Kawaguchi, J., 2011. Itokawa dust particles: a direct link between s-type asteroids and ordinary chondrites. *Science* 333, 1113–1116.
- Okada, T., Shirai, K., Yamamoto, Y., Arai, T., Ogawa, K., Hosono, K., Kato, M., 2006. X-ray fluorescence spectrometry of asteroid Itokawa by Hayabusa. *Science* 312, 1338–1341.
- Panisova, J., Fratia, M., Wunderlich, T., Pateka, R., Kunirk, D., 2013. Microgravity and ground-penetrating radar investigations of subsurface features at the St Catherine's Monastery, Slovakia. *Archaeol. Prospect.* 20, 163–174.
- Pursiainen, S., 2008, 12. Coarse-to-fine reconstruction in linear inverse problems with application to limited-angle computerized tomography. *Journal of Inverse and Ill-posed Problems* 16, 873–886.
- Pursiainen, S., Kaasalainen, M., 2013. Iterative alternating sequential (ias) method for radio tomography of asteroids in 3d. *Planet. Space Sci.* 82, 84–98.
- Saito, J., Miyamoto, H., Nakamura, R., Ishiguro, M., Michikami, T., Nakamura, A.M., Demura, H., Sasaki, S., Hirata, N., Honda, C., Yamamoto, A., Yokota, Y., Fuse, T., Yoshida, F., Tholen, D.J., Gaskell, R.W., Hashimoto, T., Kubota, T., Higuchi, Y., Nakamura, T., Smith, P., Hiraoka, K., Honda, T., Kobayashi, S., Furuya, M., Matsumoto, N., Nemoto, E., Yukishita, A., Kitazato, K., Dermawan, B., Sogame, A., Terazono, J., Shinohara, C., Akiyama, H., 2006. Detailed Images of Asteroid 25143 Itokawa from Hayabusa. *Science* 312, 1341–1344.
- Sorsa, L.-I., Takala, M., Bambach, P., Deller, J., Vilenus, E., Pursiainen, S., 2019. Bistatic full-wave radar tomography detects deep interior voids, cracks and boulders in a rubble-pile asteroid model. *The Astrophysical Journal* 872 (1), 44.
- Sanchez, P., Scheeres, D.J., 2014. The strength of regolith and rubble pile asteroids. *Meteorit. Planet. Sci.* 49, 788–811.
- Takala, M., Bambach, P., Deller, J., Vilenus, E., Wittig, M., Lentz, H., Braun, H., Kaasalainen, M., Pursiainen, S., 2018. Far-field inversion for the deep interior scanning cubesat. *IEEE Trans. Aerosp. Electron. Syst.* 55 (4), 1683–1697.
- Trabelsi, S., Kraszewski, A.W., Nelson, S.O., 2001. Microwave dielectric sensing of bulk density of granular materials. *Meas. Sci. Technol.* 12, 2192–2197.
- Tsuchiyama, A., Uesugi, M., Matsushima, T., Michikami, T., Kadono, T., Nakamura, T., Uesugi, K., Nakano, T., Sandford, S.A., Noguchi, R., Matsumoto, T., Matsuno, J., Nagano, T., Imai, Y., Takeuchi, A., Suzuki, Y., Ogami, T., Katagiri, J., Ebihara, M., Ireland, T.R., Kitajima, F., Nagao, K., Naraoka, H., Noguchi, T., Okazaki, R., Yurimoto, H., Zolensky, M.E., Mukai, T., Abe, M., Yada, T., Fujimura, A., Yoshikawa, M., 2011. Three-dimensional structure of Hayabusa samples: origin and evolution of Itokawa regolith. *Science* 333, 1125–1128.
- Tsuda, Y., Yoshikawa, M., Abe, M., Minamino, H., Nakazawa, S., 2013. System design of the Hayabusa 2 — asteroid sample return mission to 1999 ju3. *Acta Astronaut.* 91, 356–362.
- Zuber, M.T., Smith, D.E., Watkins, M.M., Asmar, S.W., Konopliv, A.S., Lemoine, F.G., Melosh, H.J., Neumann, G.A., Phillips, R.J., Solomon, S.C., Wiczorek, M.A., Williams, J.G., Goossens, S.J., Kruizinga, G., Mazarico, E., Park, R.S., Yuan, D.-N., 2013. Gravity field of the moon from the gravity recovery and interior laboratory (grail) mission. *Science* 339, 668–671.

PUBLICATION

III

A Time-Domain Multigrid Solver with Higher-Order Born Approximation for Full-Wave Radar Tomography of a Complex-Shaped Target

L.-I. Sorsa, M. Takala, C. Eyraud and S. Pursiainen

IEEE Transactions on Computational Imaging 6.(2020), 579–590

DOI: 10.1109/TCI.2020.2964252

Publication reprinted with the permission of the copyright holders

A Time-Domain Multigrid Solver with Higher-Order Born Approximation for Full-Wave Radar Tomography of a Complex-Shaped Target

Liisa-Ida Sorsa, Mika Takala, Christelle Eyraud, Sampsa Pursiainen

Abstract—This paper introduces and evaluates numerically a multigrid solver for non-linear tomographic radar imaging. Our goal is to enable the fast and robust inversion of sparse time-domain data with a mathematical full-wave approach utilizing a higher-order Born approximation (BA). Full-wave inversion is computationally expensive, hence techniques to speed up the numerical procedures are needed. To model the wave propagation effectively, we use the finite element time-domain (FETD) method, which is equipped with a multigrid scheme to enable the rapid evaluation of the higher-order BA. As a potential application, we consider the tomography of small solar system bodies (SSSBs) and asteroid interiors particular, the latter of which can contain internal details observable by radar, e.g., layers, voids and cracks. In the numerical experiments, we investigated monostatic, bistatic and multistatic measurement configurations. The results obtained suggest that, with a relevant noise level, the tomographic reconstruction quality can be improved by applying the higher-order BA in comparison to the first-order case, which we interpret as a linearization of the inverse problem. Our open multigrid-FETD solver for Matlab (The Mathworks Inc.) is available online. It applies Matlab’s features for graphics computing unit acceleration to enhance computational performance.

Index Terms—Radar Tomography, Small Solar System Bodies, Finite Element Time-Domain (FETD), Multigrid, Graphics Computing Unit (GPU)

I. INTRODUCTION

This paper concerns tomographic full-wave radar imaging in which the internal permittivity distribution of a given domain is to be reconstructed via transmitting and measuring electromagnetic waves penetrating through a domain [1], [2], [3], [4]. We consider inverting a wave equation in the time domain for a sparse set of measurements to reconstruct the interior structure of a complex target object, for example, a small solar system body (SSSB), which can be sounded by radar in a planetary space mission [5], [6], [7], [8]. The first attempt aiming at tomographic reconstruction of the interior of a SSSB was the Comet Nucleus Sounding Experiment by Radio-wave Transmission (CONCERT) [9], [8], [10], a part of the European Space Agency’s (ESA) Rosetta mission, which visited the comet 67P/Churyumov-Gerasimenko in 2014. The density estimates available today [11] suggest that SSSBs

can be highly porous and contain a significant amount of void space, which might be detectable via tomographic radar imaging.

In this study, we aim at developing a mathematical and numerical higher-order Born approximation (BA) [12], [13] for the effective modeling and inversion of non-linear full-wave scattering in the time-domain for a complex-shaped or structured target object. Data processing in the time domain has been applied, e.g., in CONCERT [10], [8], as it is beneficial in the presence of complex scattering; the noisy parts of the signal can be filtered out of the data based on their travel time, including, e.g., the effects of anisotropic structures or highly uncertain scattering. As of other studies concentrating on the present theoretical context, analytical and computational approaches to solve scattering problems [14], [15] utilizing BA have been previously introduced for various different cases including, among other things, special domain structures such as the cylindrical geometry [16], [17], [18], [19]; advanced inversion of spectral information, e.g., via multiple signal classification (MUSIC) or other methods in the time-reversal of signals [20], [21], [22], [23]; and non-linear processes, e.g., distorted Born iterative (DBI) techniques [16], [24], [25], [26], [27], [28]. Moreover, regularization techniques such as TV constraints can be used in reconstructing structural distributions based on electromagnetic measurements [29].

Differing from the aforementioned studies, we approach the tomography of a *per se* complex—e.g., non-convex and irregular—target applying a multigrid version of the finite element time-domain (FETD) method [30], [31]. Multigrid-FETD enables the accurate modeling of an arbitrary target, maintaining its actual shape with various different finite element (FE) mesh resolutions. It also allows one to speed up the inversion process, which can be performed using a coarse mesh resolution determined by the size of the smallest detectable details. We have previously introduced a multigrid-FETD inversion approach [32] in which the first-order BA of the wave scattering is used. It has been successfully applied in linearized and iterative TV regularization to reconstruct a synthetic permittivity distribution within a real 3D asteroid shape in [5], [33]. Here, building on our previous work, we introduce an iterative and *fully* non-linear inverse solver in which the unknown permittivity is updated via subsequent linearized approximations akin to the DBI approach and the numerical wave-field can be updated through a higher-order BA. This update requires performing a computationally intensive deconvolution routine. The multigrid-FETD provides the

Liisa-Ida Sorsa is with the Faculty of Information Technology and Communication Sciences, Tampere University, Tampere, Finland.

Mika Takala is with the Faculty of Information Technology and Communication Sciences, Tampere University, Tampere, Finland.

Christelle Eyraud is Aix Marseille University, CNRS, Centrale Marseille, Institut Fresnel, Marseille, France.

Sampsa Pursiainen is with the Faculty of Information Technology and Communication Sciences, Tampere University, Tampere, Finland.

TABLE I
LIST OF ESSENTIAL MATHEMATICAL SYMBOLS.

Symbol	Description
ε_r	Relative electric permittivity
ε_{bg}	Background permittivity
ρ_ε	Local permittivity perturbation
σ	Conductivity distribution
$\mathcal{G}[\varepsilon_r]_{\vec{p}_1, \vec{p}_2}$	Green's function between \vec{p}_1 and \vec{p}_2 w.r.t. ε_r
\vec{f}	Signal transmitted at \vec{p}_1
\vec{d}	Signal received at \vec{p}_2 .
\vec{h}	The total wave-field at \vec{r} .
\mathbf{p}_ℓ	The discretized wave-field at ℓ -th time point
$\mathbf{q}_{\ell-\frac{1}{2}}^{(k)}$	k -th component of integrated gradient at ℓ -th time point
$\mathbf{a}_{\ell-\frac{1}{2}}^{(k)}$	time-evolution of $\mathbf{q}_\ell^{(k)}$ at ℓ -th time point
$\mathbf{b}_{\ell+\frac{1}{2}}^{(k)}$	time-evolution of \mathbf{p}_ℓ at ℓ -th time point
\mathbf{h}_ℓ	Discretized total wave-field at \vec{r} at ℓ -th time point
$\tilde{\mathbf{h}}_{BA,n}^\ell$	n -order Born approximation of \mathbf{h}_ℓ
$\mathbf{h}_{\ell}^{(i,j)}$	$\tilde{\mathbf{h}}_{BA,1}^\ell$ w.r.t. j -th element and i -th node in a coarse mesh
$\mathbf{d}_{\ell}^{(i,j)}$	\mathbf{p}_ℓ w.r.t. j -th element and i -th node in a coarse mesh
$\mathbf{h}_{\ell}^{\text{diff}}$	$\tilde{\mathbf{h}}_{BA,1}^\ell$ obtained as a differential
$\mathbf{C}, \mathbf{C}_1, \mathbf{C}_2$	Mass matrices weighted w.r.t. $\varepsilon_r, \varepsilon_{bg}$ and ρ_ε , resp.
\mathbf{R}	Mass matrix weighted w.r.t. σ
$\mathbf{S}, \mathbf{T}^{(k)}$	Scalar and gradient perfectly matched layer matrix
$\mathbf{A}, \mathbf{B}^{(k)}$	Diagonal weight and gradient evaluation matrix, resp.
$\tilde{\mathbf{Q}}^{(i)}$	Restriction matrix with a single non-zero entry $Q_{i,i}^{(i)} = 1$
u, \vec{g}	Electric field and its gradient integrated over time
v, \vec{w}	Scalar and vector valued test function, resp.
$\mathcal{T}, \mathcal{T}_j$	Finite element mesh and its j -th element, resp.
φ_i	i -th nodal FE basis function
χ_j	Characteristic function of the j -th element

essential means to tackle the computational cost of this update. Our implementation is available online as an open toolbox for Matlab (The Mathworks Inc.). To enhance the computational performance, Matlab's features for graphics processing unit (GPU) acceleration are applied in both the forward modeling and inversion stage.

The numerical experiments involve a two-dimensional test domain and simulated data. The parameter selection in the numerical experiments was made regarding the radar tomography of an SSSB—a small asteroid in particular—as a potential application. The results suggest that, using the present approach, a candidate solution for the full non-linear inverse problem can be found in a sufficiently short time with improved accuracy when compared to solving a linearized inverse problem. Furthermore, it seems that maximizing the benefit of the potential future bistatic [34], [35] and multistatic measurements [36] yielding a sparse set of data might necessitate applying a higher-order BA.

This article is organized as follows. Section II describes mathematically the BA, forward simulation and inversion process. Additionally, the underlying wave propagation model is briefly reviewed in Appendix A. Section III includes the numerical results, and Section IV discusses the outcome. Table I lists the essential mathematical symbols of this study.

II. METHODS

A. Sparse full-wave tomography in time-domain

We aim at resolving the relationship between the relative electrical permittivity distribution ε_r , and the full time-dependence of the wave defined in domain Ω and received at a given set of measurement points. For reconstructing ε_r , the ability to model full-wave measurements is essential, since it allows distinguishing signal fluctuations arriving from different parts of the tomography target \mathcal{D} , e.g., from the surface or the deep interior. It is necessary to tackle the potential modeling errors arising from the complexity, for example, the effects related to anisotropic structures or scattering effects with high uncertainty. In particular, to optimize the reconstruction quality in a backscattering measurement, it is necessary to filter out the signal peak arising from the wave scattered by the rear wall of \mathcal{D} [5], [33]. Namely, the amplitude of such a peak can be larger compared to the earlier arriving peaks which are essential for detecting the scatterers in the interior structure. Time-domain full-wave modeling allows this via restricting the investigated signal length as depicted in Fig. 1.

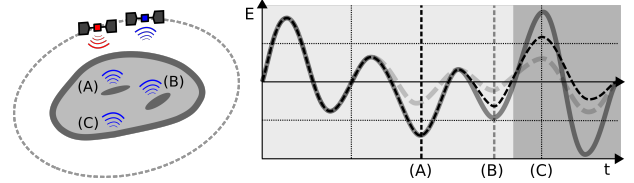


Fig. 1. **Left:** A schematic picture of a tomography target \mathcal{D} , e.g. an asteroid, in which the electromagnetic wave transmitted by an antenna (e.g. an orbiting spacecraft) is scattered at different locations denoted by (A), (B) and (C). **Right:** The signal (solid grey wave), i.e., the electric field E , corresponding to the measurement configuration on the right has peaks at time (t) points corresponding to the locations (A), (B) and (C). The intense and potentially noisy peak (C) arriving from the rear wall of \mathcal{D} needs to be excluded from the final data in order to improve the signal-to-noise ratio of the measurement. The first-order BA takes into account the scattered wave-front which originates at (A) and interacts with the domain (dashed grey wave). The second-order BA takes into account also the two times scattered part of the wave-field, thereby leading to a further correction and an improved approximation for the later arriving peak (dashed black wave) scattered from (B).

B. Green's functions

Assuming that the signal \vec{f} is transmitted at the point \vec{p}_1 and \vec{d} is received at \vec{p}_2 , the problem of modeling the full wave can be associated with the task of finding the Green's function [37] $\mathcal{G}_{\vec{p}_1, \vec{p}_2}$ predicting the wave received according to the equation $\vec{d} = \mathcal{G}_{\vec{p}_1, \vec{p}_2} * \vec{f}$. The Green's function is a functional of the relative permittivity ε_r and a nuisance parameter θ , i.e., $\mathcal{G} = \mathcal{G}[\varepsilon_r, \theta]$. That is, the Green's function is not exactly known because of the different uncertainties in the mathematical model. The unknown exact effect of θ on the outcome is related to (numerical) modeling errors, for example, to ambiguities arising from signal attenuation effects which can be related to various factors, e.g., to the conductivity σ and its indirect relationship to ε_r [38], propagation losses, reflections, and refractions. For simplicity, it is modeled here with additive random effects by assuming that

$$\mathcal{G}[\varepsilon_r, \theta] = \mathcal{G}[\varepsilon_r] + \mathfrak{E}, \quad (1)$$

where \mathfrak{E} is an unknown modeling error.

In this study, the numerical approximation of the Green's function is first obtained in a forward simulation process after which it is used in the inversion stage. In the latter case it is significant that the dependence of \mathcal{G} on ε_r is non-linear. Consequently, in order to optimize the modeling accuracy, the approximation for $\mathcal{G}[\varepsilon_r]$ needs to be updated during an iterative inversion process in which ε_r is gradually updated.

C. Higher-order Born approximation of wave scattering

Assume that the Green's function $\mathcal{G}[\varepsilon_{bg}]$ of a background permittivity distribution ε_{bg} is given and the task is to approximate $\mathcal{G}[\varepsilon_r]$, where $\varepsilon_r = \varepsilon_{bg} + \rho_\varepsilon$ with ρ_ε denoting a local perturbation of the relative permittivity at \vec{r} . That is, a small scattering obstacle at \vec{r} acts as a point source, whose amplitude is proportional to the local wave-field $\tilde{\mathbf{h}}$. Since the wave-field is altered only at \vec{r} , Green's function equals to $\mathcal{G}[\varepsilon_{bg}]$ elsewhere. The perturbed wave-field is, consequently, of the form (Fig. 2)

$$\tilde{\mathbf{d}} = \mathcal{G}[\varepsilon_{bg}]_{\vec{p}_1, \vec{p}_2} * \tilde{\mathbf{f}} + c \mathcal{G}[\varepsilon_{bg}]_{\vec{r}, \vec{p}_2} * \tilde{\mathbf{h}}, \quad (2)$$

where c is a constant contrast factor, whose numerical dependence on the perturbation ε_2 is to be determined in the following sections, and

$$\tilde{\mathbf{h}} = \mathcal{G}[\varepsilon_r]_{\vec{p}_1, \vec{r}} * \tilde{\mathbf{f}}. \quad (3)$$

The n -th order Born approximation (BA) of $\tilde{\mathbf{h}}$ is to assume that $\tilde{\mathbf{h}}$ is an n -th degree polynomial with respect to the first term of (2). The first-order BA follows from substituting $\mathcal{G}[\varepsilon_r]$ with $\mathcal{G}[\varepsilon_{bg}]$, i.e.,

$$\tilde{\mathbf{h}}^{\text{BA},1} = \mathcal{G}[\varepsilon_{bg}]_{\vec{p}_1, \vec{r}} * \tilde{\mathbf{f}}. \quad (4)$$

The higher-order (n -th order) approximation can be derived from the following recursive equation:

$$\tilde{\mathbf{h}}^{\text{BA},n} = \mathcal{G}[\varepsilon_{bg}]_{\vec{p}_1, \vec{r}} * \tilde{\mathbf{f}} + c \mathcal{G}[\varepsilon_{bg}]_{\vec{r}, \vec{r}} * \tilde{\mathbf{h}}^{\text{BA},n-1}. \quad (5)$$

As depicted in Fig. 2, the first-order BA is based on $\mathcal{G}[\varepsilon_{bg}]$ and, therefore, it cannot reproduce the non-linear propagation effects in which the path of the altered wave crosses the point \vec{r} two or more times. Taking such effects into account necessitates a second or higher-order BA which can improve the accuracy of the signal tail, i.e., later arriving peaks, as illustrated in Fig. 1.

D. Evaluation of Green's function via regularized deconvolution

Evaluation of Green's function for any complex-structured ε_r necessitates advanced computations which cannot be performed exactly within a feasible time for each scattering point \vec{r} . Therefore, it is approximated by the following regularized deconvolution process [39] (Fig. 2):

- 1) Evaluate the terms $\tilde{\mathbf{h}} = \mathcal{G}[\varepsilon_r]_{\vec{p}_1, \vec{r}} * \tilde{\mathbf{f}}$ and $\tilde{\mathbf{p}} = \mathcal{G}[\varepsilon_r]_{\vec{p}_2, \vec{r}} * \tilde{\mathbf{f}}$ for each scattering point \vec{r} by propagating a single wave from both \vec{p}_1 and \vec{p}_2 .

2) Estimate the Green's function

$$\tilde{\mathbf{g}} = \mathcal{G}[\varepsilon_r]_{\vec{r}, \vec{p}_2} = \mathcal{G}[\varepsilon_r]_{\vec{p}_2, \vec{r}} \quad (6)$$

by using Tikhonov regularized deconvolution with a suitably chosen regularization parameter δ .

The reciprocity of the wave propagation ensures that the equation (6) holds. The estimate obtained for $\tilde{\mathbf{g}}$ can be then applied to estimate the wave $\tilde{\mathbf{d}} = \tilde{\mathbf{g}} * \tilde{\mathbf{f}}$ originating at the scattering point \vec{r} .

E. Numerical higher-order Born approximation

We assume that an incident wave-field \mathbf{p}_ℓ for time points $\ell = 1, 2, \dots, n_T$ has been modeled numerically for a given distribution ε_{bg} and the task is to obtain it for $\varepsilon_r = \varepsilon_{bg} + \rho_\varepsilon$, where ρ_ε corresponds to a small scattering obstacle. The time-evolution of the wave-field obeys the following so-called leap-frog formulae derived in Appendix A:

$$\begin{aligned} \mathbf{q}_{\ell+\frac{1}{2}}^{(k)} &= \mathbf{q}_{\ell-\frac{1}{2}}^{(k)} + \Delta t \mathbf{a}_{\ell-\frac{1}{2}}^{(k)} \\ \mathbf{p}_{\ell+1} &= \mathbf{p}_\ell + \Delta t \mathbf{C}^{-1} (\mathbf{f}_\ell + \mathbf{b}_{\ell+\frac{1}{2}}). \end{aligned} \quad (7)$$

Here $\mathbf{q}_{\ell-\frac{1}{2}}^{(k)}$ is the gradient of \mathbf{p}_ℓ integrated over time and $\mathbf{a}_{\ell-\frac{1}{2}}^{(k)}$ and $\mathbf{b}_{\ell+\frac{1}{2}}$ are auxiliary time-evolution vectors (Appendix A). Matrix \mathbf{C} is a permittivity-weighted positive definite mass matrix [40] with entries of the form $C_{i,j} = \int_\Omega \varepsilon_r \varphi_i \varphi_j d\Omega$, where φ_i and φ_j denote FE basis functions (Appendix A). It can be decomposed as

$$\mathbf{C} = \mathbf{C}_1 + \mathbf{C}_2, \quad (8)$$

where \mathbf{C}_1 and \mathbf{C}_2 correspond to ε_{bg} and ρ_ε , respectively. If ρ_ε is small enough so that $\|\mathbf{C}_1^{-1} \mathbf{C}_2\| < 1$, the inverse of \mathbf{C} can be expanded via the geometric Born series expression for $(\mathbf{I} + \mathbf{C}_1^{-1} \mathbf{C}_2)^{-1}$ as given by

$$\begin{aligned} \mathbf{C}^{-1} &= (\mathbf{C}_1 + \mathbf{C}_2)^{-1} = (\mathbf{I} + \mathbf{C}_1^{-1} \mathbf{C}_2)^{-1} \mathbf{C}_1^{-1} \\ &= (\mathbf{I} + \mathbf{C}_1^{-1} \mathbf{C}_2 + \mathbf{C}_1^{-2} \mathbf{C}_2^2 + \dots) \mathbf{C}_1^{-1}. \end{aligned} \quad (9)$$

The first-degree polynomial approximation of this identity is of the form $\mathbf{C}^{-1} \approx (\mathbf{I} + \mathbf{C}_1^{-1} \mathbf{C}_2) \mathbf{C}_1^{-1}$. When substituted into the leap-frog formulae (7), this results in the following expression:

$$\begin{aligned} \mathbf{q}_{\ell+\frac{1}{2}}^{(k)} &= \mathbf{q}_{\ell-\frac{1}{2}}^{(k)} + \Delta t \mathbf{a}_{\ell-\frac{1}{2}}^{(k)} \\ \mathbf{p}_{\ell+1} &= \mathbf{p}_\ell + \Delta t \mathbf{C}_1^{-1} (\mathbf{h}_\ell + \mathbf{f}_\ell + \mathbf{b}_{\ell+\frac{1}{2}}), \end{aligned} \quad (10)$$

where $\mathbf{h}_\ell = \mathbf{C}_2 \mathbf{C}_1^{-1} (\mathbf{f}_\ell + \mathbf{b}_{\ell+\frac{1}{2}})$ denotes an auxiliary source vector. We denote

$$\mathbf{h}_\ell^{\text{BA},1} = \mathbf{C}_2 \mathbf{C}_1^{-1} (\mathbf{f}_\ell + \mathbf{b}_{\ell+\frac{1}{2}}) \quad (11)$$

to emphasize that this particular choice for the auxiliary source results in the first-order BA. That is, at each order, the change of the total field $\mathbf{C}^{-1} (\mathbf{f}_\ell + \mathbf{b}_{\ell+\frac{1}{2}})$ is approximated with that of the incident field $\mathbf{C}_1^{-1} (\mathbf{f}_\ell + \mathbf{b}_{\ell+\frac{1}{2}})$.

Formula (10) can be applied recursively n times to obtain the n -th order BA. The auxiliary source corresponding to the result of the recursion is:

$$\mathbf{h}_\ell^{\text{BA},n} = \mathbf{C}_2 P_n (\mathbf{C}_1^{-1} \mathbf{C}_2) \mathbf{C}_1^{-1} (\mathbf{f}_\ell + \mathbf{b}_{\ell+\frac{1}{2}}), \quad (12)$$

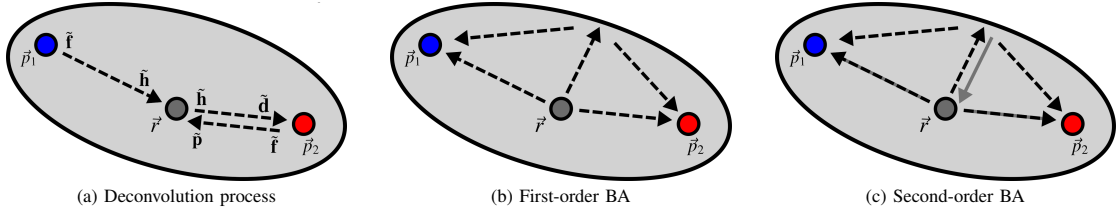


Fig. 2. (a) A schematic picture depicting the principle of the Tikhonov-regularized deconvolution process which is applied in the Born approximation (BA) of the wave scattering and in forming the Jacobian matrix (as first-order BA). (b) The first-order BA takes into account the scattering wavefronts (black dashed arrows) originating from a single point and its interaction \vec{r} w.r.t. the existing details in the computation geometry, including the internal part and the surface of the target \mathcal{D} . (c) The second-order BA, takes into account, additionally, the wavefronts which have scattered two-times at \vec{r} (solid gray arrows). Generally, the order of BA determines the maximal number of times the wave can be scattered at \vec{r} in the model.

where P_n is a matrix-valued polynomial of the form

$$P_n(\mathbf{C}_1^{-1}\mathbf{C}_2) = \mathbf{I} + \mathbf{C}_1^{-1}\mathbf{C}_2 + \dots + \mathbf{C}_1^{-n+1}\mathbf{C}_2^{n-1}. \quad (13)$$

The formula (12) can be derived inductively as follows. Using the first-order formula two times recursively results in the second order form:

$$\begin{aligned} \mathbf{h}_\ell^{\text{BA},2} &= \mathbf{C}_2\mathbf{C}_1^{-1}(\mathbf{h}_\ell^{\text{BA},1} + \mathbf{f}_\ell + \mathbf{b}_{\ell+\frac{1}{2}}) \\ &= \mathbf{C}_2\mathbf{C}_1^{-1}(\mathbf{C}_2\mathbf{C}_1^{-1}(\mathbf{f}_\ell + \mathbf{b}_{\ell+\frac{1}{2}}) + \mathbf{f}_\ell + \mathbf{b}_{\ell+\frac{1}{2}}) \\ &= \mathbf{C}_2(\mathbf{I} + \mathbf{C}_1^{-1}\mathbf{C}_2)\mathbf{C}_1^{-1}(\mathbf{f}_\ell + \mathbf{b}_{\ell+\frac{1}{2}}) \\ &= \mathbf{C}_2P_2(\mathbf{C}_1^{-1}\mathbf{C}_2)\mathbf{C}_1^{-1}(\mathbf{f}_\ell + \mathbf{b}_{\ell+\frac{1}{2}}). \end{aligned} \quad (14)$$

Further, the assumption that the formula

$$\mathbf{h}_\ell^{\text{BA},n} = \mathbf{C}_2P_n(\mathbf{C}_1^{-1}\mathbf{C}_2)\mathbf{C}_1^{-1}(\mathbf{f}_\ell + \mathbf{b}_{\ell+\frac{1}{2}}) \quad (15)$$

holds for an arbitrary natural number n , is verified by the induction step:

$$\begin{aligned} \mathbf{h}_\ell^{\text{BA},n+1} &= \mathbf{C}_2\mathbf{C}_1^{-1}(\mathbf{h}_\ell^{\text{BA},n} + \mathbf{f}_\ell + \mathbf{b}_{\ell+\frac{1}{2}}) \\ &= \mathbf{C}_2\mathbf{C}_1^{-1}(\mathbf{C}_2P_n(\mathbf{C}_1^{-1}\mathbf{C}_2)\mathbf{C}_1^{-1}(\mathbf{f}_\ell + \mathbf{b}_{\ell+\frac{1}{2}}) \\ &\quad + \mathbf{f}_\ell + \mathbf{b}_{\ell+\frac{1}{2}}) \\ &= \mathbf{C}_2P_{n+1}(\mathbf{C}_1^{-1}\mathbf{C}_2)\mathbf{C}_1^{-1}(\mathbf{f}_\ell + \mathbf{b}_{\ell+\frac{1}{2}}). \end{aligned} \quad (16)$$

The n -th order approximation (12) tends to the exact solution as $n \rightarrow \infty$. This can be shown as follows:

$$\begin{aligned} \mathbf{C}_1^{-1}(\mathbf{h}_\ell^{\text{BA},\infty} + \mathbf{f}_\ell + \mathbf{b}_{\ell+\frac{1}{2}}) &= (\mathbf{C}_1^{-1}\mathbf{C}_2P_\infty(\mathbf{C}_1^{-1}\mathbf{C}_2) + \mathbf{I}) \\ &\quad \cdot \mathbf{C}_1^{-1}(\mathbf{f}_\ell + \mathbf{b}_{\ell+\frac{1}{2}}) \\ &= P_\infty(\mathbf{C}_1^{-1}\mathbf{C}_2)\mathbf{C}_1^{-1}(\mathbf{f}_\ell + \mathbf{b}_{\ell+\frac{1}{2}}) \\ &= \mathbf{C}^{-1}(\mathbf{f}_\ell + \mathbf{b}_{\ell+\frac{1}{2}}), \end{aligned} \quad (17)$$

where the last identity follows from the fact that $\mathbf{C}^{-1} = P_\infty(\mathbf{C}_1^{-1}\mathbf{C}_2)\mathbf{C}_1^{-1}$.

1) *Convergence of the higher-order Born approximation:* The condition number κ of an unweighted mass matrix is independent of the mesh size within a quasi-uniform FE mesh, i.e., a mesh in which the ratio between the maximum and minimum element size is uniformly bounded [41]. That is, for a quasi-uniform mesh, $\kappa = \|\mathbf{C}^{-1}\| \|\mathbf{C}\| = \text{constant}$, if ε_r is constant. It follows that the weighted mass matrices \mathbf{C}_1 and \mathbf{C}_2 arising from the same FE discretization satisfy the following inequality:

$$\|\mathbf{C}_1^{-1}\mathbf{C}_2\| \leq \|\mathbf{C}_1^{-1}\| \|\mathbf{C}_2\| \leq \text{constant} \times \frac{\max_{\mathbf{x}} |\rho_\varepsilon|}{\min_{\mathbf{x}} \varepsilon_{bg}}, \quad (18)$$



Fig. 3. A schematic illustration of the nested mesh structure. The fine mesh \mathcal{T} (left) is used in the forward simulation and the coarse mesh, \mathcal{T}' (right) in the inversion.

showing that the condition $\|\mathbf{C}_1^{-1}\mathbf{C}_2\| < 1$ for the convergence of the Born series (9) and, thereby, the higher-order Born approximation, can be satisfied only if the magnitude of the perturbation ρ_ε is moderate compared to the background ε_{bg} . The minimum $\min_{\mathbf{x}} \varepsilon_{bg}$ can be considered in the local neighborhood of the perturbation, since any vector multiplied by $\mathbf{C}_1^{-1}\mathbf{C}_2$ is negligible far from the perturbation. Namely, first multiplication by \mathbf{C}_2 restricts any vector to the perturbed neighborhood which is, then, spread by some amount, when multiplied by \mathbf{C}_1^{-1} , since the solution of the linear system defined by a mass matrix decays, when moving away from the source.

As the BA is here found through the Tikhonov regularized deconvolution process (Section II-D) and the source $\mathbf{h}_\ell^{\text{BA},n}$ of BA is linear respect to \mathbf{C}_2 , selecting the magnitude of ρ_ε can be associated with choosing an appropriate regularization parameter value δ . Namely, an update of the form $\rho_\varepsilon \rightarrow \gamma\rho_\varepsilon$ with scaling $\gamma > 0$ corresponds to $\mathbf{h}_\ell^{\text{BA},n} \rightarrow \gamma\mathbf{h}_\ell^{\text{BA},n}$ and alternatively to $\delta \rightarrow \gamma^{-1}\delta$, if the estimate \mathbf{p}_ℓ obtained for the wave is updated as $\mathbf{p}_\ell \rightarrow \gamma\mathbf{p}_\ell$. That is, the same effect which follows by decreasing the perturbation can be generated via increasing the regularization parameter. Therefore, in the numerical implementation, it suffices to assume that $\rho_\varepsilon = 1$ in the numerical evaluation of the BA, and to select an appropriate regularization parameter with respect to that.

2) *Multigrid formulation of the permittivity:* We define the permittivity distribution with respect to a coarse and nested d-simplex mesh \mathcal{T}' (Fig. 3), i.e., $\varepsilon_r = \sum_{j=1}^M c_j\chi'_j$ and assume that the permittivity distribution is piecewise constant as given by $\varepsilon_r = \sum_{j=1}^m c_j\chi_j$. The multigrid formulation, i.e., the use of a coarse inversion mesh, is applied to set the resolution of the unknown permittivity distribution on a suitable level. Namely, the maximal theoretical reconstruction accuracy obtainable with full data is generally lower than what is needed for propagating the wave.

In order to obtain a feasible performance with the deconvolution approach presented in II-D, it is assumed that ε_r is

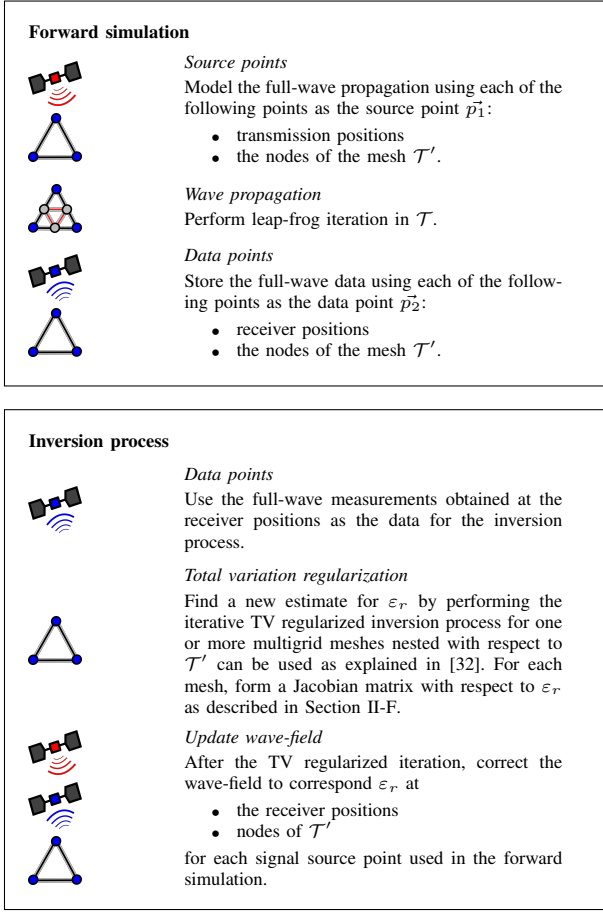


Fig. 4. Graphical description of the forward and inversion stages of the present multigrid solver. The unknown permittivity ε_r is updated sequentially via a linearized approximation akin to the DBI method [28]. The left column visualizes the point sets involved and the right one includes the descriptions.

updated in a single element $T'_j \in \mathcal{T}'$. Denoting by $\tilde{\mathbf{C}}_2^{(j)}$ an update restricted to T'_j , we define the following element-wise auxiliary source vector which is used in the deconvolution process:

$$\mathbf{h}_\ell^{(i,j)} = \tilde{\mathbf{C}}_2^{(j)} \mathbf{Q}^{(i)} \mathbf{C}_1^{-1} (\mathbf{f}_\ell + \mathbf{b}_{\ell+\frac{1}{2}}). \quad (19)$$

Here, the matrix $\mathbf{Q}^{(i)} \in \mathbb{R}^{n \times n}$ has one nonzero entry $Q_{i,i}^{(i)} = 1$ and the vector $\mathbf{h}^{(i,j)}$ differs from zero only if the i -th node belongs to T'_j . The solution of the system (10) with respect to $\mathbf{h}^{(i,j)}$ can be obtained as

$$\mathbf{p}_\ell \approx \sum_{\tilde{r}_i \in T'_j, i \leq N} \mathbf{d}'_\ell^{(i,j)} = \sum_{k=1}^{d+1} \mathbf{d}'_\ell^{(i_k,j)}, \quad (20)$$

where the number of terms is $d+1$, that is, the number of nodes in T'_j , and $\mathbf{d}'_\ell^{(i,j)}$ is the regularized deconvolution-based solution of the following auxiliary system:

$$\begin{aligned} \mathbf{r}_{\ell+\frac{1}{2}}^{(i,j,k)} &= \mathbf{r}_{\ell-\frac{1}{2}}^{(i,j,k)} + \Delta t \mathbf{a}_{\ell-\frac{1}{2}}^{(i,j,k)}, \\ \mathbf{d}_{\ell+1}^{(i,j)} &= \mathbf{d}_\ell^{(i,j)} + \Delta t \mathbf{C}^{-1} (\mathbf{h}_\ell^{(i,j)} + \mathbf{b}_{\ell+\frac{1}{2}}^{(i,j)}). \end{aligned} \quad (21)$$

This system can be derived from (10) simply by substituting $\mathbf{h}_\ell^{(i,j)}$ as the source. The definition for the auxiliary vectors

$\mathbf{a}_{\ell-\frac{1}{2}}^{(i,j,k)}$ and $\mathbf{b}_{\ell+\frac{1}{2}}^{(i,j)}$ follow directly by substituting \mathbf{p}_ℓ and $\mathbf{d}_{\ell-\frac{1}{2}}^{(k)}$ with $\mathbf{d}_\ell^{(i,j)}$ and $\mathbf{r}_{\ell-\frac{1}{2}}^{(i,j,k)}$, respectively, in Equation (28) and (29) (Appendix A).

Note that only $\mathbf{d}_{\ell+1}^{(i,j)}$ out of the auxiliary variables $\mathbf{r}_{\ell+\frac{1}{2}}^{(i,j,k)}$ and $\mathbf{d}_{\ell+1}^{(i,j)}$ needs to be evaluated. This is approximated via the regularized deconvolution process. Hence, with the multigrid approach, one can perform the deconvolution process with respect to the coarse system (21) by applying the wave data obtained with the dense one. A graphical description of the multigrid solver is shown in the Fig. 4.

F. Jacobian matrix

As shown in [32], the wave equation can be linearized with respect to the permittivity distribution as follows:

$$\begin{aligned} \frac{\partial \mathbf{q}_{\ell+\frac{1}{2}}^{(k)}}{\partial c_j} &= \frac{\partial \mathbf{q}_{\ell-\frac{1}{2}}^{(k)}}{\partial c_j} + \Delta t \frac{\partial \mathbf{a}_{\ell-\frac{1}{2}}^{(k)}}{\partial c_j} \\ \frac{\partial \mathbf{p}_{\ell+1}}{\partial c_j} &= \frac{\partial \mathbf{p}_\ell}{\partial c_j} + \Delta t \mathbf{C}^{-1} (\mathbf{h}_\ell^{\text{diff}} + \frac{\partial \mathbf{b}_{\ell+\frac{1}{2}}}{\partial c_j}), \end{aligned} \quad (22)$$

where

$$\mathbf{h}_\ell^{\text{diff}} = \frac{\partial \mathbf{C}}{\partial c_j} \mathbf{C}^{-1} (\mathbf{f}_\ell + \mathbf{b}_{\ell+\frac{1}{2}}) \quad (23)$$

is an auxiliary source function implied by the identities $(\partial \mathbf{C}^{-1} / \partial c_j) (\mathbf{f}_\ell + \mathbf{b}_{\ell+\frac{1}{2}})$ and $\partial \mathbf{C}^{-1} / \partial c_j = \mathbf{C}^{-1} (\partial \mathbf{C} / \partial c_j) \mathbf{C}^{-1}$ the latter one of which can be obtained via differentiating both sides of $\mathbf{C} \mathbf{C}^{-1} = \mathbf{I}$ which gives $\partial \mathbf{C}^{-1} / \partial c_j = \mathbf{C}^{-1} \partial \mathbf{C} / \partial c_j \mathbf{C}^{-1}$. Based on the definition of the permittivity distribution and the matrix \mathbf{C} , it holds that $(\partial \mathbf{C} / \partial c_j)_{k,\ell} = \int_{T_j} \varphi_k \varphi_\ell d\Omega$. That is, the entry $(\partial \mathbf{C} / \partial c_j)_{k,\ell}$ is non-zero only if for which φ_k and φ_ℓ are supported on T_j .

When interpreted in terms of Section II-E, $\mathbf{h}_\ell^{\text{diff}}$ can be interpreted as a special case of the first-order BA (11). Moreover, the multigrid formulation presented in Section II-E2 is valid, since the update $(\partial \mathbf{C} / \partial c_j)$ differs from zero only in the element $T'_j \in \mathcal{T}'$.

G. Non-linear inversion process

The data was inverted using the following fully non-linear inversion process (Figure 4):

- 1) Choose a constant initial guess $\mathbf{x}^{(0)}$ for the unknown permittivity distribution, a desired number of iterations N , and set $\ell = 1$.
- 2) Find an estimate $\mathbf{x}^{(\ell)}$ for the permittivity distribution using the iterative total variation (TV) regularization algorithm described in [32] with one or more multigrid meshes nested with respect to \mathcal{T}' . For each mesh, evaluate a Jacobian matrix with $\mathbf{x}^{(\ell-1)}$ as the linearization point.
- 3) If $\ell < N$, update the wave-field via BA with $\mathbf{x}^{(\ell)}$ as the reference permittivity distribution, set $\ell \rightarrow \ell + 1$ and repeat the second step. Perform the update sequentially element-by-element with the element-wise strategy described in Section II-E2.
- 4) Associate the final estimate with the reconstruction of the permittivity distribution.

This algorithm is a fully non-linear generalization of the reconstruction method presented in the study [32] which is restricted to the linearized case $N = 1$. Note that the iterative TV regularization process of the second step can be non-linear also when $N = 1$. It also allows using an arbitrary number of multigrid hierarchy levels in a straightforward manner as explained in [32]. Here, for simplicity without losing the generality, the investigation is restricted to two hierarchy levels \mathcal{T} and \mathcal{T}' .

H. Computational complexity

1) *Forward approach:* The computational complexity of the forward solver follows from the signal's shortest wavelength which determines the mesh size, h . The number of spatial degrees of freedom n in the FE mesh is proportional to h^{-d} , in which d is the dimension of the mesh. That is, the number of non-zeros in the system matrices grow as $\mathcal{O}(n)$. Hence, the complexity of each time step is $\mathcal{O}(n)$, including the multiplication by \mathbf{C}^{-1} . Namely, the complexity of the solution of the linear system determined by \mathbf{C} by preconditioned conjugate gradient method [42], applied in inverting the mass matrix \mathbf{C} , is $\mathcal{O}(n\sqrt{\kappa})$ and the condition number κ of \mathbf{C} is independent of n in a quasi-uniform mesh (Section II-E1). The total complexity of the forward solution is, thus, $\mathcal{O}(n^{1+1/d})$ since the number of time steps is depends on the degrees of freedom along a single dimension, i.e. it is of the complexity of $\mathcal{O}(n^{1/d})$. [43].

2) *Inverse approach:* In the present multigrid scheme, the resolution of the mesh \mathcal{T}' is not bound by that of the forward simulation but rather by that of the desired imaging resolution. Following from the radar range resolution, the maximal imaging resolution is determined by the signal bandwidth [44]. Evaluation of the first-order BA for a given signal transmission requires performing the regularized deconvolution process (Section II-D), i.e., accounting the effect of the signal propagating through the target object \mathcal{D} for each of the M elements in \mathcal{T}' at each of the K measurement points, resulting in the complexity of $\mathcal{O}(KM)$. Since the number of elements is comparable to that of the nodes, this can be expressed also as $\mathcal{O}(KN)$, where N refers to the number of nodes. When evaluating a higher-order transform, the regularized deconvolution is evaluated for the combined set of nodes and measurement points. That is, the complexity is $\mathcal{O}(KN^2)$ with respect to the spatial degrees of freedom. The computational cost is also directly proportional to the order of the transform. The evaluation of a BA essentially determines the computational complexity of the inversion process (Section II-G).

I. Numerical implementation with the GPU-accelerated Tomographic Radar Reconstruction (GPU-ToRR) toolbox

Numerical forward and inverse methods were implemented for the MATLAB (The MathWorks Inc.) programming environment which natively allows using GPU accelerated algorithms as a part of the code. The GPU-accelerated Tomographic Radar Reconstruction (GPU-ToRR) toolbox¹ de-

TABLE II
THE PROPERTIES OF THE TEST DOMAIN Ω CORRESPONDING TO THE FOLLOWING VALUES OF THE SCALING PARAMETER: $s = 1$, $s = 500$ M AND $s = 0.5$ M. THE FIRST SI-UNIT VALUE MATCHES WITH A RADIO FREQUENCY MEASUREMENT PERFORMED FOR A SMALL SOLAR SYSTEM BODY [46], AND THE LAST ONE TO A MICROWAVE-RANGE LABORATORY MEASUREMENT (TABLE III).

Scaling	s	\mathcal{D}	Surface layer	Voids
1	Diameter	0.28	0.02	0.01– 0.09 m
		58λ	4λ	$2-18\lambda$
	Value of ε_r	4	3	1
	Value of σ	20	15	5
500 m	Diameter	140 m	10 m	5 – 45 m
	Value of ε_r	4	3	1
	Value of σ	11.0	8.0E-5 S/m	2.8E-5 S/m
0.5 m	Diameter	14 cm	1 cm	0.5 – 4.5 cm
	ε_r	4	3	1
	σ	0.11 S/m	0.80 S/m	0.028 S/m

TABLE III
SIGNAL PROPERTIES AND CLASSIFICATION FOR THE SCALING PARAMETER VALUES $s = 1$, $s = 500$ M AND $s = 0.5$ M.

s	Center freq.	Bandwidth	T	λ in \mathcal{D}	Class.
1	15.5	15.5	0.1	0.03	Unitless
500 m	10 MHz	10 MHz	2.2 μ s	15 m	Radio wave
0.5 m	10 GHz	10 GHz	2.2 ns	15 mm	Microwave

veloped in this study is available online in GitHub. The documentation can be found therein. The numerical results of this study have been computed using this toolbox.

J. Domain

Numerical experiments were performed in a two-dimensional origin-centric square Ω including the tomography target \mathcal{D} (Figure 5) in the center part and a perfectly matched layer (PML) [45] near the boundaries. The PML was embedded in the model as shown in Appendix to simulate an open-field wave propagation, i.e., to dampen echoes from the boundaries back to the center. For the generality of the results, we used a unitless set of parameters $t, \vec{x}, \varepsilon_r, \sigma$ and $c = \varepsilon_r^{-1/2}$ (velocity) which can be scaled to SI-units via the expressions $(\mu_0\varepsilon_0)^{1/2}st, s\vec{x}, \varepsilon_0\varepsilon_r, (\varepsilon_0/\mu_0)^{1/2}s^{-1}\sigma$, and $(\varepsilon_0\mu_0)^{-1/2}c$ ($c = 1$ for $\varepsilon_r = 1$), respectively, with s denoting a spatial scaling factor (meters), $\varepsilon_0 = 8.85 \cdot 10^{-12}$ F/m the electric permittivity of vacuum, and $\mu_0 = 4\pi \cdot 10^{-7}$ H/m the magnetic permeability which is assumed to be constant in Ω . By tuning s , the system can be scaled to match with different scales and applications. That is, the actual target and its analog scale model can be modeled through a single system but two different values of s . Table II shows the scaling for $s = 1$, $s = 500$ m and $s = 0.5$ m. The first one of these is the unitless representation, the second one corresponds to a radio frequency measurement performed for a SSSB, and the last one to a laboratory-scale microwave experiment. Conductivity was considered as an unknown latent nuisance parameter predicted by the equation $\sigma = 5\varepsilon_r$, as it difficult to be inverted as shown, e.g., in [38].

In the unitless coordinates, the diameter of \mathcal{D} was approximately 0.28, or in terms of wavelength, 8.7λ . The relative

¹<https://github.com/sampsapursiainen/GPU-Torre>

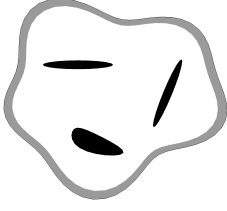


Fig. 5. The exact tomography target \mathcal{D} used in the numerical experiments. The white, gray and black area have the relative permittivity value of 4 (solid layer), 3 (porous layer) and 1 (vacuum), respectively.

permittivity distribution of \mathcal{D} included a surface layer with the thickness around 0.02 (0.6λ) and three inclusions (voids) with maximum diameter of 0.01 – 0.09 (0.3 – 2.8λ) (Figure 5). The values of ε_r for the interior part, the surface layer and the voids were chosen to be 4, 3 and 1, respectively. Outside \mathcal{D} , ε_r was set to be one, i.e., that of air or vacuum. Inside \mathcal{D} , conductivity causing signal energy loss was assumed to be a nuisance parameter of the form $\sigma = 5\varepsilon_r$, and vanish elsewhere, i.e., $\sigma = 0$.

1) *Numerical discretization:* To avoid the *inverse crime*, i.e., the overly good data fit in the inversion process, the exact and background wave data were simulated using two different triangular (shape-regular and unstructured) FE meshes consisting of 93 475 and 40 715 nodes together with 186 544 and 81 040 triangles. The time increment Δt in the leap-frog iteration was set to be $6.25E-5$ and $2.5E-4$, respectively.

Each triangular mesh applied in the wave propagation process (forward simulation) was obtained by refining a coarse one uniformly two times. The permittivity distribution was reconstructed for an original coarse mesh (996 triangular elements, 552 nodes) which was nested with respect to the one corresponding to the background data.

2) *Signal pulse and measurement:* The Blackman-Harris window [47], [48], [49] with the duration T_0 was used as the shape of the source function $\tilde{f}(t)$ for $t \leq T_0$ (0.67 ns), and $\tilde{f}(t) = 0$, otherwise. The duration of the pulse was chosen to be $T_0 = 0.1$ and the duration of the measurement $T = 1.1$. The time interval between each data sampling point was set to be 0.005 corresponding to a 2.5 oversampling rate relative to the Nyquist criterion. The signal properties and classification can be found in Table III.

The signal was transmitted and received at 0.32 diameter circular path centered at the origin and enclosing \mathcal{D} . We investigated the following four different spatial measurement configurations depicted in Figure 6:

- 1) The *monostatic* configuration is constituted by a single spacecraft.
- 2) The *bistatic I* configuration includes two spacecraft with a constant 22.5 degree angle in between them.
- 3) In the *bistatic II* configuration, the separating angle is 90 degrees.
- 4) In the *multistatic* configuration, a 90 degrees angle is covered by altogether five equally spaced spacecraft, each two separated by a 22.5 angle.

In each one of these, the red one both transmits and receives the signal while the other spacecraft are used as additional

receivers. The dataset included a total number of 16 transmission points equally distributed around the target \mathcal{D} . This sparse distribution not satisfying the Nyquist criterion is used in order to take into account the *in-situ* restrictions of a radar measurement performed during a planetary space mission. Achieving a full spatial measurement coverage would necessitate using a point density which would oversample the Nyquist criterion by factor two in the vicinity of \mathcal{D} . The corresponding number of points can be obtained dividing the wavelength of the highest frequency signal component in vacuum (here 0.03) by four times the circumference of the circumcircle containing \mathcal{D} (here 0.9), resulting here to about 120 equally spaced points [50].

3) *Noise:* Zero-mean Gaussian white noise with a fixed standard deviation (STD) was added to the measurements. To investigate the effect of the noise on the signal, the peak-to-peak signal-to-noise ratio (PPSNR) was evaluated for each measurement configuration. It was defined as the decibel value of the relative noise peak level with respect to the amplitude of the initial data vector, i.e., the difference between the exact signal and the background data. The noise peak level was defined to be the 95 % quantile of the Gaussian noise distribution. When selecting the noise STD, the targeted level of PPSNR was between 10 and 20 dB (with 0 dB referring to the level of the signal peak) which is known to allow finding a tomographic reconstruction and also seems a potential range for measurements performed for an SSSB based on the CONSERT data [5], [8]. The motivation to use Gaussian noise is the significance of the modeling errors, whose net effect approach a Gaussian random variable under the additive uncertainty model, assuming that the errors are, additionally, independent and identically distributed.

4) *Inverse estimates:* The final reconstruction of the permittivity distribution was obtained via three steps of the non-linear inversion algorithm in which, on each step, a regularized permittivity estimate was found through a single step of the iterative TV regularization scheme presented in [32]. In this algorithm, the regularizing function is a sum of TV and L2-norm penalty term. The TV term corresponds to the Euclidean norm of the permittivity gradient integrated over \mathcal{D} . It regularizes the jumps between adjacent elements, while the L2-norm penalizes the total magnitude of the distribution. These terms were scaled by the parameter values $\alpha = 2E-1$ and $\beta = 1E-3$, respectively. The predominating parameter α affects the reconstruction quality and the role of β is mainly to ensure the numerical stability of the inversion process, i.e., the boundedness of the reconstruction. The value of the Tikhonov regularization parameter for the deconvolution process was set to be $\delta = 1E-4$. Each parameter value was selected based on preliminary tests. The reconstructions were produced and analyzed separately for the first, second and third-order Born approximation.

5) *Inverse error measures:* The quality of the inverse estimates was measured by evaluating the structural similarity (SSIM) [51] between the exact and the reconstructed permittivity distribution denoted here by ε_r and ε_r^* . To analyze the value accuracy and localization of the permittivity details, we evaluated also the mean squared error (MSE) and the relative overlap error (ROE). The latter one of these is defined as the

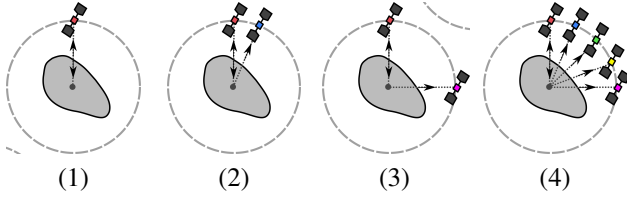


Fig. 6. The signal configurations of the numerical experiments. In each one of these, the red one both transmits and receives the signal while the other spacecraft are used as additional receivers. The dataset included a total number of 16 transmission points equally distributed around the target \mathcal{D} . 1) The *Monostatic* configuration is constituted by a single spacecraft. 2) The *Bistatic I* configuration includes two spacecraft with a constant 22.5 degree angle in between them. 3) In the *Bistatic II* configuration, the separating angle is 90 degrees. 4) In the *Multistatic* configuration, a 90 degrees angle is covered by altogether five equally spaced spacecraft, each two separated by a 22.5 angle.

relative error in overlap between ε_r and ε_r^* for the surface layer and voids. We define ROE as the percentage

$$\text{ROE}_i = 100 \left(1 - \frac{\text{Area}(A) \cap \text{Area}(S_i)}{\text{Area}(S_i)} \right) \text{ for } i = 1, 2, \quad (24)$$

where S_1 denotes the voids and S_2 the surface layer, $A = (S_1 \cup S_2) \cap R$ is the overlap between the target set $S_1 \cup S_2$ and the set R in which a given reconstruction is smaller than a limit such that $\text{Area}(R) = \text{Area}(S_1 \cup S_2)$.

III. RESULTS

The results of the numerical experiments can be found in Tables IV and V and Figure 7. Both the signal configuration and the order of the Born approximation were observed to have a significant effect on the reconstruction quality obtained in the non-linear inversion process.

A. Peak-to-peak signal-to-noise ratio

The Bistatic I and multistatic signal configuration, i.e., those including a measurement point within a 22.5-degree angle from the transmission location, produced a higher measurement PPSNR than the monostatic one. The PPSNR obtained with Bistatic II, in which the additional measurement point is at 90 degrees with respect to the transmitter, was equal to that of the monostatic case.

B. SSIM

A visual inspection of the reconstructions suggests the two and multi-point approaches provide an increased sharpness and distinguishability of the permittivity details. This observation is supported by the SSIM results, showing that the structural similarity between the reconstruction and the exact permittivity distribution increases along with the measurement point count and also with the order of the BA. Based on the SSIM, the Bistatic configurations I and II were found to improve the reconstruction quality by a somewhat similar marginal as compared to the monostatic case, while the superior results were obtained with the multistatic configuration.

C. MSE and ROE

The first-order BA was found to be advantageous with respect to the overlap (ROE), especially, in the cases of the Bistatic I and multistatic configuration, which nevertheless had a lower value-accuracy with regard to MSE as compared to the other two configurations. Increasing the order of the BA led to an enhanced global value-accuracy for each configuration, and based on a visual examination, it also led to a sharper contrast between the image details and the background. The advantage of using a higher-order BA was obvious, especially, with respect to the value of the surface layer, which generally is overly low in the first-order case. Notably, with the second and third-order BA, the Bistatic configuration I performed slightly better compared to II regarding both MSE and ROE.

D. Computing time

The performance of the numerical solver was evaluated using an NVIDIA Quadro P6000 GPU; using it computing the Jacobian took about 45 s, updating the full-wave data 75, 150 and 225 s with the first-, second-, and third-order BA, resulting in a total reconstruction process duration of about 285, 435 and 585 s, respectively. Propagating the wave for a single transmission point took about 45 and 135 s for the background and exact permittivity distribution, respectively. The wave was propagated for each node included in the regularized deconvolution process. The total number of transmission points was 16 outside the target \mathcal{D} and 552 inside, corresponding to each node of the coarse inversion mesh. Performing these processes in a standard CPU was observed to generally take 20–100 times the time required by a GPU.

IV. DISCUSSION

In this study, we have shown that the linearized full-wave inversion approach for the tomographic reconstruction of small solar system bodies (SSSBs) presented in [32] can be derived from the first-order Born approximation (BA) by associating it with the Jacobian matrix of the numerical wave-field. Here, this approach was generalized as a non-linear iteration in which the wave-field—i.e., the forward solution—can be updated via a BA of an arbitrary order. The structural similarity (SSIM) criterion shows an improvement in the reconstructions with the increase in the BA order. We have also prepared a graphics processing unit-accelerated toolbox, GPU-ToRRe for Matlab (MathWorks Inc.), to achieve a sufficiently short computation time for experimentation and further method development.

The structural similarity (SSIM) and overlap (ROE) results suggest that the quality of the reconstruction can be increased via bistatic or multistatic measurement configurations, i.e., dual- or multi-point measurement schemes. Increasing the order of the BA was found to improve the SSIM further, and its role with regard to the value-accuracy (MSE) of the reconstructions was found to be crucial. In the Bistatic I configuration, an angular separation of 22.5 degrees between the transmitter and the additional receiver was observed to result in an enhanced measurement PSNR level compared to the monostatic case, which was recently proposed in [7], whereas

TABLE IV
THE RESULTS OF THE NUMERICAL EXPERIMENTS. THE BEST VALUE OF SSIM IS 1 AND THE BEST VALUE OF MSE AND ROE IS 0.

Configuration	BA order	PPSNR (dB)	SSIM	Global MSE	Void MSE	Surface MSE	Void ROE	Surface ROE
Monostatic	1	13.9	0.896	0.344	0.147	0.102	37.1	22.6
	2	13.9	0.914	0.283	0.171	0.0485	37.3	26.0
	3	13.9	0.918	0.288	0.189	0.0495	34.2	32.0
Bistatic I	1	15.2	0.897	0.419	0.164	0.124	33.6	17.9
	2	15.2	0.916	0.302	0.173	0.0425	39.4	20.6
	3	15.2	0.922	0.285	0.185	0.0387	40.0	23.8
Bistatic II	1	13.9	0.907	0.339	0.140	0.0647	34.2	26.4
	2	13.9	0.916	0.305	0.181	0.0480	38.0	32.6
	3	13.9	0.920	0.303	0.200	0.0493	39.8	36.0
Multistatic	1	-15.2	0.908	0.489	0.232	0.0636	37.7	14.5
	2	-15.2	0.924	0.331	0.208	0.0334	36.5	18.0
	3	-15.2	0.925	0.305	0.209	0.0392	35.9	22.0

TABLE V
COMPUTING TIMES (S) FOR THE GPU-ACCELERATED ALGORITHMS.

	Process type			
	BA order			Other
	1st	2nd	3rd	
Jacobian matrix	45			
Wave-field update	75	150	225	
Reconstruction process	285	435	585	
Exact wave data				135
Background wave data				45

the larger 90-degree angle of the Bistatic II configuration did not. It seems that, whereas the Bistatic I reconstruction is superior to the Bistatic II on the surface part, there is not such a difference in the deep interior, which we interpret to follow from the longer and more "multi-way" signal propagation in comparison to the background prediction in the latter case. The findings of this study suggest that, in addition to the noise-robustness [5], [33], the reconstruction quality can be improved via a bistatic measurement with regard to both structural similarity and value accuracy, especially if a higher-order BA is used. A bistatic configuration had also been chosen for CONSERT to provide tomographic travel-time data [6], [8].

Regarding the practical aspects of a space mission design, placing the transmitter in the mothership might be convenient to guarantee its power supply. Small spacecrafts could carry the additional receivers for the chosen measurement configuration [34], [35]. Therefore, in addition to the monostatic and bistatic configurations, the multistatic one can also be considered as a potential scenario for a future space mission. In the light of the present numerical results, such a configuration should improve the reconstruction quality as shown by the SSIM, global MSE and ROE criteria.

Referring to the convergence properties, the numerical stability of the BA with the present Tikhonov regularization approach seems appropriate. It converges rapidly as a function of the approximation order, matching with our justification given in Section II-E1 for a well-chosen regularization parameter. Based on our inversion results, it seems that the third-order approximation might be applicable for wave propagation investigations, as the effect of increasing the order of the BA is

already minor when moving from the second to the third order. The practical limit for increasing the order is set by the noise, the effect of which becomes visible gradually as the order of the BA increases. Here the third-order case was selected as the limit, due to the observation of minor noise effects. Even though the highest SSIM was obtained for the third-order reconstructions, they can also be argued to be affected by the noise based on a comparison of MSE values. We deem them to be due to the inversion process, which applies the BA multiple (three) times to correct the wave-field—i.e., the Green's function. The sensitivity of such updates to noise is a well-known property of the DBI techniques [16], [24], [25], [26], [27], [28]. Our method is similar to the DBI methods, but it performs the computations in the time domain and allows for complex-shaped target domains. The noise effects could be resolved by strengthening the regularization which, however, would diminish the effect of the higher-order updates, since they would alter and decrease the terms of the Born series. In addition to the noise, another obvious factor affecting the performance of the inversion algorithm is the contrast of the permittivity details—i.e., as shown in Section II-E1, the ratio between the magnitude of the permittivity perturbation and the background permittivity distribution is the key factor determining the level of the Tikhonov regularization necessary for the convergence of the BA. Following from this, in can be challenging to reconstruct high-contrast details [24], [25].

The Born iterative method with a steady Green's function has been shown to be advantageous with respect to the noise robustness of the inversion process compared to a DBI updating method to data in the frequency domain [28]. This observation is also in agreement with our present time-domain modeling results, suggesting that the update routine necessitates finding a balance between accuracy and noise suppression. The analysis of the noise tolerance of our method with the first-order BA without updating the Green's function (corresponding to the Born iterative method) can be found in our previous work [32], [5] where a noise level above 8 to 10 dB was found to be necessary for obtaining an appropriate reconstruction quality. This compares well with the findings for microwave tomography of the breast [52], for example. For its superior magnitude, the first-order BA determines the inver-

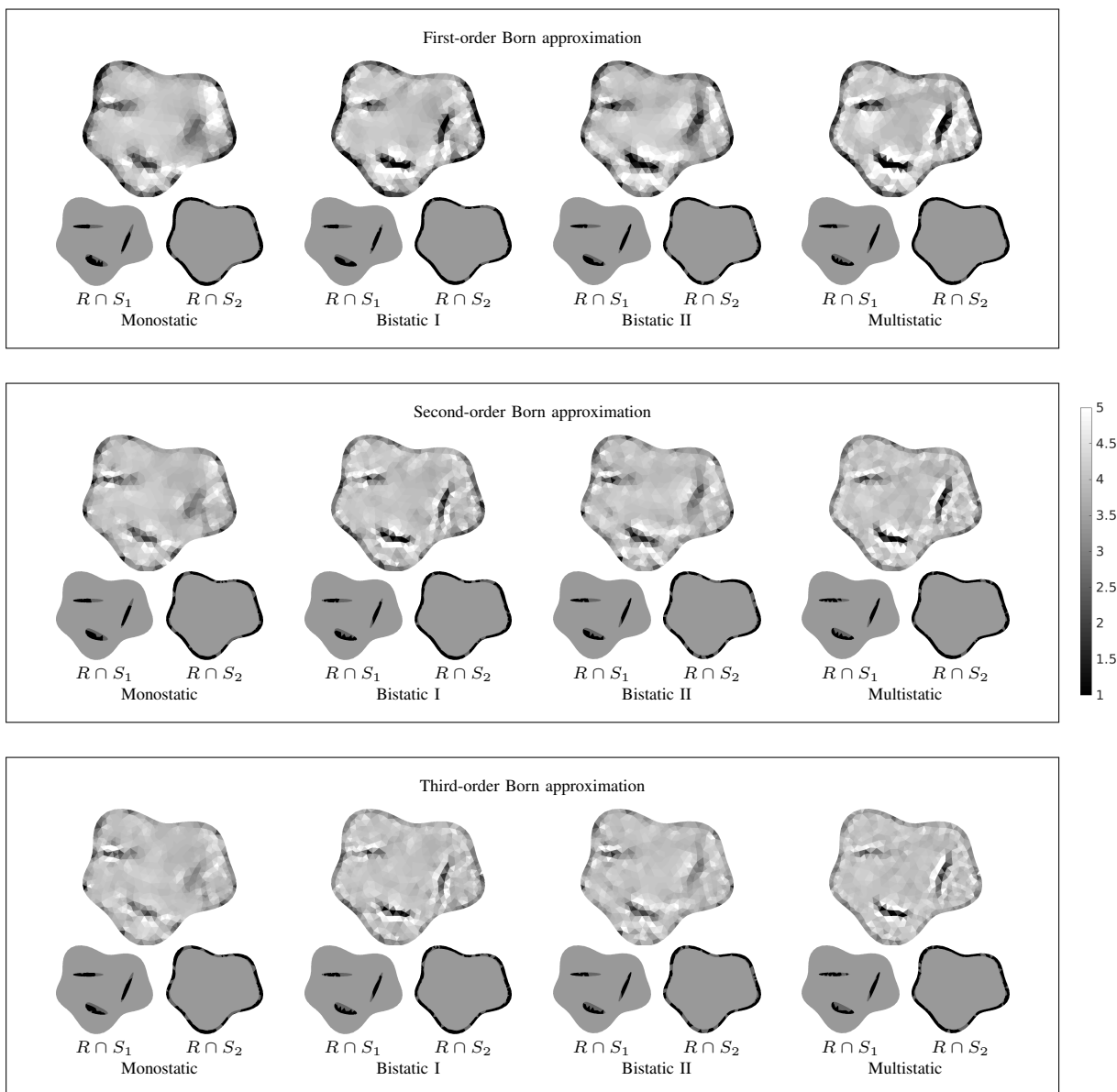


Fig. 7. The reconstructions of the two-dimensional permittivity distribution together with the overlap sets $R \cap S_1$ and $R \cap S_2$. The color scale is from 1 (black) to 5 (white).

sion performance in high-noise cases, where the minor higher-order corrections have a less significant effect in cases where the level of the Tikhonov regularization is sufficient. The first-order BA is also less demanding regarding computational complexity. Therefore, it might be preferable for dense inversion meshes. Optimizing the performance of the multigrid solver with respect to noise and regularization is a complex topic, as it depends on altogether three regularization parameters: the TV, L2-norm and Tikhonov regularization parameters. It is obvious that the optimal conditions, including the most suitable order of the BA, depend on the application-related parameters, such as the permittivity distribution, wavelength, targeted imaging resolution, and the distribution of the scattering obstacles.

Regarding the goal of reconstructing the interior structure of an asteroid, it will be important to implement and evaluate the present higher-order BA for a 3D computation geometry. This could be done by extending the linearized multigrid

solver introduced and used in our recent studies [32], [33]. Applying the multigrid approach is crucial in discretizing the unknown permittivity distribution, as the sparsity of the inversion grid enables the fast performance of the wave-field updating routine. The results of this study together with the adaptability of the multigrid mesh suggest that our approach will be sufficiently fast also in a three-dimensional case where the coarse mesh might consist of a few thousand elements. A three-dimensional inverse solver could be evaluated via microwave-range measurements on an analogue target. Recently, a multistatic inversion approach has been validated for frequency-domain data in such a way [53]. Thus, a natural next step would be to perform a validation for the time domain. Other interesting research directions would be to investigate carrier wave effects in the full-wave inversion of tomographic radar data, and sampling techniques to improve the noise-robustness of the reconstructions [54].

APPENDIX

A. Wave propagation model

Following [32], the wave equation for a transverse electric field $\vec{E} = u\vec{e}_z$ in the spatio-temporal set $[0, T] \times \Omega$ can be formulated as a first-order system

$$\varepsilon_r \frac{\partial u}{\partial t} + \sigma u - \nabla \cdot \vec{g} = f \quad \text{and} \quad \frac{\partial \vec{g}}{\partial t} - \nabla u = 0, \quad (25)$$

where ε_r and σ denote the relative permittivity and conductivity distribution, respectively, $\vec{g} = \int_0^t \nabla u(\tau, \vec{x}) d\tau$, and the boundary conditions are set by $\vec{g}|_{t=0} = \nabla u_0$ and $u|_{t=0} = u_1$. The right-hand side is the signal source, i.e., the antenna current density given by $f(t, \vec{x}) = \delta_{\vec{p}}(\vec{x})\tilde{f}(t)$ transmitted at the point \vec{p} . Here $\delta_{\vec{p}}(\vec{x})$ is Dirac's delta function with respect to \vec{p} . Integrating (25) multiplied by $v : [0, T] \rightarrow H^1(\Omega)$ and $\vec{w} : [0, T] \rightarrow L_2(\Omega)$ and applying the rule of partial integration, one can obtain the following weak form:

$$\begin{aligned} \frac{\partial}{\partial t} \int_{\Omega} \vec{g} \cdot \vec{w} d\Omega - \int_{\Omega} \vec{w} \cdot \nabla u d\Omega = 0, \\ \frac{\partial}{\partial t} \int_{\Omega} \varepsilon_r uv d\Omega + \int_{\Omega} \sigma uv d\Omega + \int_{\Omega} \vec{g} \cdot \nabla v d\Omega = \begin{cases} \tilde{f}, & \text{if } \vec{x} = \vec{p}, \\ 0, & \text{else.} \end{cases} \end{aligned} \quad (26)$$

Here, it is assumed that the domain and the parameters are regular enough, so that the weak form has a unique solution $u : [0, T] \rightarrow H^1(\Omega)$ [55].

To obtain a numerical solution, we assume that the electric and gradient field are finite sums of the form $u = \sum_{j=1}^n p_j \varphi_j$ and $\vec{g} = \sum_{k=1}^d g^{(k)} \vec{e}_k$ with $g^{(k)} = \sum_{i=1}^m q_i^{(k)} \chi_i$, respectively. Here, $\varphi_1, \varphi_2, \dots, \varphi_n$ are real-valued linear (nodal) basis functions and $\chi_1, \chi_2, \dots, \chi_n$ are piecewise (element-wise) constant element-indicator functions. Defining test functions $v : [0, T] \rightarrow \mathcal{V} \subset H^1(\Omega)$ and $\vec{w} : [0, T] \rightarrow \mathcal{W} \subset L_2(\Omega)$ with $\mathcal{V} = \text{span}\{\varphi_1, \varphi_2, \dots, \varphi_n\}$ and $\mathcal{W} = \text{span}\{\chi_1, \chi_2, \dots, \chi_m\}$ the weak form can be written in the Ritz-Galerkin discretized form [40], that is,

$$\begin{aligned} \frac{\partial}{\partial t} \mathbf{A} \mathbf{q}^{(k)} - \mathbf{B}^{(k)} \mathbf{p} + \mathbf{T}^{(k)} \mathbf{q}^{(k)} = 0, \\ \frac{\partial}{\partial t} \mathbf{C} \mathbf{p} + \mathbf{R} \mathbf{p} + \mathbf{S} \mathbf{p} + \sum_{k=1}^d \mathbf{B}^{(k)T} \mathbf{q}^{(k)} = \mathbf{f}, \end{aligned} \quad (27)$$

with $\mathbf{p} = (p_1, p_2, \dots, p_n)$ and $\mathbf{q}^{(k)} = (q_1^{(k)}, q_2^{(k)}, \dots, q_m^{(k)})$, and $\mathbf{f} \in \mathbb{R}^n$ with $f_i = \int_{\Omega} f \varphi_i d\Omega$ denoting the coordinate vectors for u , \vec{g} and the source function, respectively.

The matrices of the system are given by $\mathbf{A} \in \mathbb{R}^{m \times m}$, $\mathbf{B} \in \mathbb{R}^{m \times n}$, $\mathbf{C} \in \mathbb{R}^{n \times n}$, $\mathbf{S} \in \mathbb{R}^{n \times n}$, $\mathbf{T} \in \mathbb{R}^{m \times m}$. Matrices \mathbf{A} and $\mathbf{T}^{(k)} = \zeta^{(k)} \mathbf{A}$ are diagonal with non-zero entries determined by $A_{i,i} = \int_{T_i} d\Omega$. The matrix $\mathbf{B}^{(k)}$ is a projection matrix of the form $B_{i,j}^{(k)} = \int_{T_i} \vec{e}_k \cdot \nabla \varphi_j d\Omega$, and \mathbf{C} , \mathbf{R} and \mathbf{S} are mass matrices weighted by ε_r , σ and ξ , respectively, as given by $C_{i,j} = \int_{\Omega} \varepsilon_r \varphi_i \varphi_j d\Omega$, $R_{i,j} = \int_{\Omega} \sigma \varphi_i \varphi_j d\Omega$ and $S_{i,j} = \int_{\Omega} \xi \varphi_i \varphi_j d\Omega$. The matrices \mathbf{S} and $\mathbf{T}^{(k)}$ correspond to a split-field perfectly matched layer (PML), i.e., the set $\{\vec{x} \in \Omega \mid \varrho_1 \leq \max_k |x_k| \leq \varrho_2\}$ which eliminates reflections from the boundary $\partial\Omega$ back to the inner part of Ω [45]. For the PML parameters, $\xi(\vec{x}) = \varsigma$, if $\varrho_1 \leq \max_k |x_k| \leq \varrho_2$, and $\zeta^{(k)}(\vec{x}) = \varsigma$, if $\varrho_1 \leq |x_k| \leq \varrho_2$, and $\xi(\vec{x}) = \zeta^{(k)}(\vec{x}) = 0$, otherwise.

To discretize the time interval $[0, T]$, we utilize Δt spaced regular grid of n_T time points and the standard difference approximations for the time derivative. These substituted into (27) lead to the leap-frog formulae (7) [45], [56], [57], where the auxiliary time-evolution vectors $\mathbf{a}_{\ell-\frac{1}{2}}^{(k)}$ and $\mathbf{b}_{\ell+\frac{1}{2}}$ are defined as follows:

$$\mathbf{a}_{\ell-\frac{1}{2}}^{(k)} = \mathbf{A}^{-1} \mathbf{B}^{(k)} \mathbf{p}_{\ell} - \mathbf{A}^{-1} \mathbf{T}^{(k)} \mathbf{q}_{\ell-\frac{1}{2}}^{(k)}, \quad (28)$$

$$\mathbf{b}_{\ell+\frac{1}{2}} = -\mathbf{R} \mathbf{p}_{\ell} - \mathbf{S} \mathbf{p}_{\ell} - \sum_{k=1}^d \mathbf{B}^{(k)T} \mathbf{q}_{\ell+\frac{1}{2}}^{(k)}. \quad (29)$$

REFERENCES

- [1] C. Yu et al. Microwave imaging in layered media: 3-d image reconstruction from experimental data. *IEEE Trans. Antennas Propag.*, 58:440–448, 2010.
- [2] C. Eyraud et al. A large 3d target with small inner details: A difficult cocktail for imaging purposes without a priori knowledge on the scatterers geometry. *Radio science*, 47(05):1–9, 2012.
- [3] M. Haynes et al. “real-time microwave imaging of differential temperature for thermal therapy monitoring. *IEEE Trans. Biomed. Eng.*, 61:1787–1797, 2014.
- [4] C. Eyraud et al. Influence of the description of the scattering matrix on permittivity reconstruction with a quantitative imaging procedure: polarization effects. *JOSA A*, 36(2):234–244, 2019.
- [5] M. Takala et al. Far-field inversion for the deep interior scanning cubesat. *IEEE Transactions on Aerospace and Electronic Systems*, 55(4):1683–1697, 2018.
- [6] A. Hérique et al. Direct observations of asteroid interior and regolith structure: science measurement requirements. *Advances in Space Research*, 62(8):2141–2162, 2018.
- [7] P. Sava and E. Asphaug. 3d radar wavefield tomography of comet interiors. *Advances in Space Research*, 61(8):2198–2213, 2018.
- [8] W. Kofman et al. Properties of the 67p/churyumov-gerasimenko interior revealed by consert radar. *Science*, 349(6247), 2015.
- [9] W. Kofman et al. Comet nucleus sounding experiment by radiowave transmission. *Advances in Space Research*, 21(11):1589–1598, 1998.
- [10] W. Kofman et al. The comet nucleus sounding experiment by radiowave transmission (CONSERT): A short description of the instrument and of the commissioning stages. *Space Science Reviews*, 128(1-4):413–432, 2007.
- [11] B. Carry. Density of asteroids. *Planetary and Space Science*, 73(1):98–118, 2012.
- [12] P. Verma. *Elementary Theory of Scattering*. Atlantic Publishers and Distributors, 2005.
- [13] M. Born. Quantenmechanik der stoßvorgänge. *Zeitschrift für Physik*, 38(11-12):803–827, 1926.
- [14] D. Colton and R. Kress. *Inverse Acoustic and Electromagnetic Scattering Theory*. Applied Mathematical Sciences. Springer, 1998.
- [15] A. Tarantola. Inverse problem theory and methods for model parameter estimation, 2005.
- [16] G. Leone et al. Inverse scattering under the distorted born approximation for cylindrical geometries. *JOSA A*, 16(7):1779–1787, 1999.
- [17] A. Brancaccio et al. Information content of born scattered fields: results in the circular cylindrical case. *JOSA A*, 15(7):1909–1917, 1998.
- [18] R. Pierri et al. Dielectric profiles reconstruction via the quadratic approach in 2-d geometry from multifrequency and multifrequency/multiview data. *IEEE transactions on geoscience and remote sensing*, 40(12):2709–2718, 2002.
- [19] R. Pierri et al. Second-order iterative approach to inverse scattering: numerical results. *JOSA A*, 17(5):874–880, 2000.
- [20] A. J. Devaney. Time reversal imaging of obscured targets from multistatic data. *IEEE Transactions on Antennas and Propagation*, 53(5):1600–1610, May 2005.
- [21] D. Ciunzio. On time-reversal imaging by statistical testing. *IEEE Signal Processing Letters*, 24(7):1024–1028, July 2017.
- [22] D. Ciunzio and P. S. Rossi. Noncolocated time-reversal music: High-snr distribution of null spectrum. *IEEE Signal Processing Letters*, 24(4):397–401, April 2017.
- [23] D. Ciunzio et al. Performance analysis of time-reversal music. *IEEE Transactions on Signal Processing*, 63(10):2650–2662, May 2015.

- [24] O. S. Haddadin and E. S. Ebbini. Adaptive regularization of a distorted Born iterative algorithm for diffraction tomography. In *Proceedings of 3rd IEEE International Conference on Image Processing*, volume 2, pp. 725–728. IEEE, 1996.
- [25] R. Lavarello and M. Oelze. A study on the reconstruction of moderate contrast targets using the distorted Born iterative method. *IEEE transactions on ultrasonics, ferroelectrics, and frequency control*, 55(1):112–124, 2008.
- [26] R. J. Lavarello and M. L. Oelze. Tomographic reconstruction of three-dimensional volumes using the distorted born iterative method. *IEEE Transactions on Medical Imaging*, 28(10):1643–1653, 2009.
- [27] A. J. Hesford and W. C. Chew. Fast inverse scattering solutions using the distorted born iterative method and the multilevel fast multipole algorithm. *The Journal of the Acoustical Society of America*, 128(2):679–690, 2010.
- [28] W. C. Chew and Y. M. Wang. Reconstruction of two-dimensional permittivity distribution using the distorted born iterative method. *IEEE Transactions on Medical Imaging*, 9(2):218–225, June 1990.
- [29] A. Abubaker and P. M. Van Den Berg. Total variation as a multiplicative constraint for solving inverse problems. *IEEE Transactions on Image Processing*, 10(9):1384–1392, 2001.
- [30] J. Li and Y. Huang. *Time-domain finite element methods for Maxwell's equations in metamaterials*, volume 43. Springer Science & Business Media, 2012.
- [31] J. Jin. *The Finite Element Method in Electromagnetics*. Wiley - IEEE. Wiley, 2015.
- [32] M. Takala et al. Multigrid-based inversion for volumetric radar imaging with asteroid interior reconstruction as a potential application. *IEEE Transactions on Computational Imaging*, 4(2):228–240, 2018.
- [33] L.-I. Sorsa et al. Bistatic full-wave radar tomography detects deep interior voids, cracks and boulders in a rubble-pile asteroid model. *Astrophysical Journal*, 872(1), 2019.
- [34] A. Herique and V. Ciarletti. A Direct Observation of the Asteroid's Structure from Deep Interior to Regolith: Two Radars on the AIM Mission. In *47th Lunar and Planetary Science Conference, LPSC 2016, Conference abstract 2096, 2 pages. Topic 315: Planetary Mission Concepts: Small Bodies.*, 2016.
- [35] P. Bambach et al. DISCUS –The Deep Interior Scanning CubeSat mission to a rubble pile near-Earth asteroid. *Advances in Space Research*, 62(12):3357–3368, 2018.
- [36] J.-M. Geffrin et al. Optimization of a bistatic microwave scattering measurement setup: From high to low scattering targets. *Radio Science*, 44(02):1–12, 2009.
- [37] D. Duffy. *Green's Functions with Applications*. Applied Mathematics. CRC Press, 2001.
- [38] J.-P. Barriot et al. A two dimensional simulation of the CONSERT experiment (radio tomography of comet wirtanen). *Advances in Space Research*, 24(9):1127 – 1138, 1999.
- [39] V. Dimri. *Deconvolution and Inverse Theory: Application to Geophysical Problems*. Methods in Geochemistry and Geophysics. Elsevier Science, 2013.
- [40] D. Braess. *Finite Elements: Theory, Fast Solvers, and Applications in Solid Mechanics*. Cambridge University Press, 2007.
- [41] L. Kamenski et al. Conditioning of finite element equations with arbitrary anisotropic meshes. *Mathematics of Computation*, 83(289):2187–2211, 2014.
- [42] G. Golub and C. van Loan. *Matrix Computations*. The John Hopkins University Press, Baltimore, 1989.
- [43] A. Annan. Electromagnetic principles of ground penetrating radar. In H. M. Jol, editor, *Ground Penetrating Radar Theory and Applications*, chapter 1. Elsevier Science, 2008.
- [44] D. J. Daniels. *Ground Penetrating Radar (2nd Edition)*. Institution of Engineering and Technology, Stevenage, 2004.
- [45] J. B. Schneider. *Understanding the FDTD Method*. John B. Schneider, 2016.
- [46] W. Kofman. Radar techniques to study subsurfaces and interiors of the solar system objects. In *2012 19th International Conference on Microwaves, Radar Wireless Communications*, volume 2, pp. 409–412, May 2012.
- [47] J. Irving and R. Knight. Numerical modeling of ground-penetrating radar in 2-D using MATLAB. *Computers & Geosciences*, 32(9):1247 – 1258, 2006.
- [48] F. J. Harris. On the use of windows for harmonic analysis with the discrete fourier transform. *Proceedings of the IEEE*, 66(1):51–83, 1978.
- [49] A. H. Nuttall. Some windows with very good sidelobe behavior. *IEEE Transactions on Acoustics, Speech, Signal Processing*, ASSP-29(1):84–91, 1981.
- [50] O. Bucci and T. Isernia. Electromagnetic inverse scattering: Retrievable information and measurement strategies. *Radio Science*, 32(6):2123–2137, 1997.
- [51] Z. Wang et al. Image quality assessment: from error visibility to structural similarity. *IEEE transactions on image processing*, 13(4):600–612, 2004.
- [52] X. Zeng et al. Effects of noise on tomographic breast imaging. In *2011 XXXth URSI General Assembly and Scientific Symposium*, pp. 1–4, Aug 2011.
- [53] C. Eyraud et al. Imaging the interior of a comet from bistatic microwave measurements: case of a scale comet model. *Advances in Space Research*, 62(8):1977–1986, 2018.
- [54] C. Eyraud et al. Microwave imaging from experimental data within a bayesian framework with realistic random noise. *Inverse problems*, 25(2):024005, 2009.
- [55] L. Evans. *Partial Differential Equations*. Graduate studies in mathematics. American Mathematical Society, 1998.
- [56] A. Bossavit and L. Kettunen. Yee-like schemes on a tetrahedral mesh, with diagonal lumping. *International Journal of Numerical Modelling: Electronic Networks, Devices and Fields*, 12(1-2):129–142, 1999.
- [57] K. Yee. Numerical solution of initial boundary value problems involving Maxwell's equations in isotropic media. *Antennas and Propagation, IEEE Transactions on*, 14(3):302–307, 1966.

PUBLICATION

IV

Complex-structured 3D-printed wireframes as asteroid analogues for tomographic microwave radar measurements

L.-I. Sorsa, C. Eyraud, A. Hérique, M. Takala, S. Pursiainen and J.-M. Geffrin

Materials & Design 198.(2021), 109364

DOI: <https://doi.org/10.1016/j.matdes.2020.109364>

Publication reprinted with the permission of the copyright holders

Complex-Structured 3D-Printed Wireframes as Asteroid Analogues for Tomographic Microwave Radar Measurements

Liisa-Ida Sorsa^{a,*}, Christelle Eyraud^b, Alain Hérique^c, Mika Takala^a, Sampsa Pursiainen^a, Jean-Michel Geffrin^b

^aComputing Sciences, Tampere University, PO Box ddr, FI-33014 Tampere, Finland

^bAix Marseille Univ., CNRS, Centrale Marseille, Institut Fresnel, Marseille, France

^cUniv. Grenoble Alpes, CNRS, IPAG, F-38000 Grenoble, France

Abstract

This study introduces a fused filament fabrication (FFF) process for manufacturing complex-structured asteroid analogue objects to be applied in tomographic microwave radar measurements and inversion studies. We describe an approach to control the volume fraction of the plastic and, thereby, the effective relative permittivity within a tetrahedral wireframe which serves as metamaterial representing the actual asteroid composition. To determine the effective permittivity of the plastic–air mixture, we use an exponential model. In this study, two analogue objects based on the shape of the asteroids KY26 and Itokawa were 3D-printed in a scale suitable for microwave range laboratory measurements using ABS filament with a controlled constant relative electric permittivity. The results obtained suggest that the permittivity of solid and powdery asteroid minerals can be modelled with the proposed technique and, in particular, that the numerical structural permittivity models of the earlier numerical studies can be approximated by 3D-printed analogues.

Keywords: Asteroid Tomography, Analogue Modelling, Radar Measurements, Microwaves, Mission Design

1. Introduction

Fused filament fabrication (FFF) has recently become an important focus in electromagnetic radio frequency and microwave applications [1, 2, 3, 4, 5] as the advances made in the material technology has enabled controlling the electrical permittivity and conductivity of a plastic filament [6, 7, 8]. This study introduces an FFF process for manufacturing complex structured asteroid analogue objects to be applied in tomographic microwave radar measurements and inversion studies [9, 10, 11]. Based on [12], we describe an approach to control the volume fraction of the plastic and, thereby, the effective relative permittivity within a tetrahedral wireframe which serves as metamaterial representing the actual asteroid composition. To determine the effective permittivity of the plastic–air mixture, we use an exponential model which is commonly applied, e.g., to approximate the permittivity of snow with respect to its relative air content [13].

The motivation for this study follows from the potential future radar applications of the deep space missions investigating the structure and composition of the small Solar System bodies and, thus, providing information on the early development of the Solar System. Of such missions, Hayabusa [14] encountered asteroid Itokawa in 2005 [15] and was the first one to bring a sample of asteroid surface regolith back to Earth in 2010 [16]. In 2018–2019, JAXA’s mission Hayabusa 2 [17] investigated the asteroid Ruygu *in situ* being the first one to collect a subsurface sample from a crater caused by an

impactor. Another physical characterization and surface sample retrieval mission, OSIRIS-REx by NASA [18], is ongoing with the asteroid Bennu as its target. The first attempt to reconstruct the interior structure of a small body, Comet Nucleus Sounding Experiment with Radiowave Transmission (CONSERT), was carried out in 2014 as a part of the European Space Agency’s (ESA) mission Rosetta with the comet 67P/Churyumov-Gerasimenko as its target. The ongoing investigation of CONSERT’s data has so far shown that the internal properties of a comet can be revealed via a bistatic radar configuration [19] of radiowave transmission between an orbiter and a lander by observing the travel time of the electromagnetic wave propagating through the body [20, 21, 22, 23]. Furthermore, the recent numerical and experimental studies [10, 11, 24, 25, 26, 27, 28], have suggested that a bistatic radar can detect deep interior electrical permittivity anomalies and recover internal structural properties within an asteroid.

As such a target body is likely to be very large in comparison to the wavelength of the signal, and as the number of measurement points is limited, carrying out and modelling the tomographic radar measurements in the deep space environment from asteroid orbit involves obvious technological and methodological challenges. While the tomography can be approached via numerical experiments and simulations under some simplifications of the target geometry and measurement configuration, a more advanced analysis necessitates performing experimental radar measurements with an asteroid analogue model as a target [11]. In this study, two analogue objects based on the shape of the asteroid 1998 KY26 and 25143 Itokawa were 3D printed in a scale suitable for microwave range laboratory measure-

*Corresponding author

Email address: liisa-ida.sorsa@tuni.fi (Liisa-Ida Sorsa)

ments using acrylonitrile butadiene styrene (ABS) filament with a controlled constant relative electric permittivity. The results obtained suggest that permittivities of solid and porous asteroid minerals can be modelled with the proposed technique and, in particular, that the numerical structural permittivity models of the earlier numerical studies [26, 25] can be approximated by 3D printed analogues. In addition to the analogues themselves, a special analogue stand design was developed in order to optimize the positioning accuracy of the radar measurement.

2. Materials and methods

In this study, we concentrated on two analogue models corresponding to the detailed openly available¹ shapes found for the asteroids (I) 1998 KY26 [29] and (II) 25143 Itokawa [30] (Figure 1). In each case (I) and (II), a tetrahedral mesh based wireframe was created for a given surface segmentation decomposing the model into different compartments, whose relative filling densities were selected to approximately match given relative permittivities $\epsilon_r = \epsilon_r' + j\epsilon_r''$. The following compartments were concerned: voids ($\epsilon_r = 1$), an interior part ($\epsilon_r' = 4$), and a surface layer or mantle ($\epsilon_r' = 3$). The permittivity of the interior and mantle part follow, respectively, from the properties of typical porous and powdered asteroid minerals such as Kaolinite and Dunite [31], while the air-filled voids have the permittivity of the vacuum. This three-compartment model with the present target objects has been earlier investigated via numerical radar simulation in [32, 25] and is referred here to as the case (IA) and (IIA). As a reference case (IB) and (IIB), we consider a single-compartment model with a homogeneous density matched with the interior permittivity value $\epsilon_r' = 4$. To control and measure the relative volumetric filling and, thereby, the permittivity of the manufactured analogue objects, we investigate three spheres (III)–(V) containing different volume fractions of plastic. Of these, spheres (III) and (IV) correspond to the interior and mantle compartments of the asteroid analogues and (V) is a solid reference sphere.

2.1. Surface segmentation

In creating the surface segmentation, the unstructured, triangulated asteroid surface data files were imported to Meshlab [33], where they were processed to obtain a mesh size suitable for the volumetric tetrahedral mesh generator. The following operations were performed: (1) generating a point cloud of suitable size and close-to-uniform density via Poisson-disk sampling [34], (2) approximating the surface normals corresponding to the cloud created and (3) producing the final surface with the ball-pivoting algorithm [35]. The goal was to obtain an eventual wireframe structure with details, i.e., edge width and aperture, finer than one fourth of the planned measurement wavelength range, while at the same time maintaining the 3D printability of the resulting structure. The mantle was constructed by cloning the outer surface of the model, smoothing and re-scaling the surface and placing it inside the outer

compartment. Interior cavities (three in 1998 KY26 and one in 25143 Itokawa) were constructed by placing an ellipsoid inside the mantle surface.

2.2. Scaling

The scaling of the analogue objects was chosen considering the maximal target size and weight that can currently be robustly manufactured with a conventional 3D filament printer and also safely measured in the anechoic chamber of Centre Commun de Ressources en Microondes (CCRM), Marseille, covering the frequency band 2–18 GHz. The aim was to relate the analogue scale to *in situ* low frequency radar measurements in which the signal can penetrate hundreds of meters inside the target [36, 37]. Of the analogues manufactured, (I) corresponds to a diameter of 9–30 m at the frequencies 60–200 MHz and (II) to 132–535 m at 5–20 MHz, respectively. In both cases, the largest diameter given corresponds to that of the actual asteroid. The scaling of the analogues and the corresponding potential measurement frequencies in the real and analogue scale are summarized in Table 1.

2.3. Material

As the plastic 3D printing material, we used the commercially available Preperm ABS450 filament (diameter 1.75 mm, density 1.52 g/cm³) which has a complex permittivity of $\epsilon_r = 4.5 + j0.019$ (loss angle $\epsilon_r''/\epsilon_r' = 0.0042$) measured at 2.4 GHz by the manufacturer². In the following, we describe our approach to determine the effective relative permittivity of the wireframe in the different compartments. Using this approach, the volume fraction of the filament is selected with the aim to steer the real part ϵ_r' towards the desired $\epsilon_r' = 3$ and $\epsilon_r' = 4$ in the mantle and interior part, respectively (Table 1).

2.3.1. Permittivity

The effective permittivity of the wireframe is estimated via a classical exponential mixture model

$$\epsilon_{r,m}^a = \sum_{i=1}^M f_i \epsilon_{r,i}^a \quad (1)$$

in which M is the number of different components, $\epsilon_{r,i}$ is the permittivity of the i -th component, f_i its volumetric filling ratio, and a is an exponential constant to be determined by the application context. This model has been developed, for example, in [38] to estimate the dielectric constant of a soil-water mixture, in [39] the properties of dry snow, and in [13] a mixture of snow, air and liquid water. Of these studies, the first one suggests choosing $a = 0.5$, the second one $a = 1/3$, and the third one the mean of these two values, i.e. $a = 0.4$, to take into account the variation of both the real and imaginary part of the permittivity. For a two-component mixture formed by air

¹<https://sbn.psi.edu/pds/shape-models/>

²<https://www.preperm.com/webshop/product/preperm-3d-abs-%c9%9br-4-5-filament/>

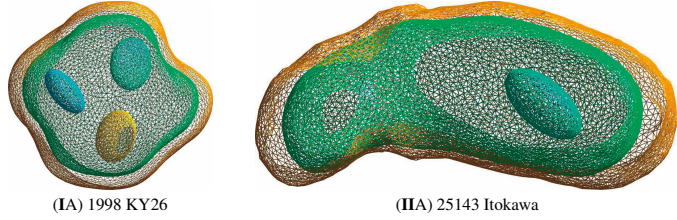


Figure 1: Asteroid models (IA) and (IIA) corresponding to the shape of 1998 KY26 and 25143 Itokawa, respectively. The ellipsoidal subdomains model empty voids. The mantle compartment is between the orange and green boundary of which the latter encloses the interior compartment.

Table 1: The sizes and scaling of the analogues with respect to the real scale measurements. The microwave radar center frequencies f and wavelengths λ of the scaled analogues are based on the potential parameters of actual tomographic radar measurements. The lowest frequency in the real scale corresponds to the largest observed diameter which is 30 and 535 m for 1998 KY26 and 25143 Itokawa, respectively.

ID	Real scale				Analogue scale (13 GHz)			Interior parameters		Scale factor
	f (MHz)	λ (m)	Size (m)	Attenuation dB/km	λ (cm)	Size (cm)	Attenuation dB/cm	ϵ_r	Part	
(I)	60	2.49	30	51.24	1.16	13.3	0.095	$4.0 + j0.016$	Interior	4.43E-3
				31.70	1.34		0.069	$3.0 + j0.010$	Mantle	
	100	1.49	18	73.20					Interior	7.39E-3
				52.83					Mantle	
	200	0.75	9	146.40					Interior	1.48E-2
		0.86		105.66					Mantle	
(II)	5	29.8	535	3.66	1.16	20.5	0.095	$4.0 + j0.016$	Interior	3.83E-4
		34.4		2.64	1.34		0.069	$3.0 + j0.010$	Mantle	
	10	14.9	265	7.32					Interior	7.74E-4
		17.2		5.28					Mantle	
	20	7.46	132	14.64					Interior	1.60E-3
		8.61		10.56					Mantle	

with the relative permittivity of one and dielectric plastic with a close-to-constant permittivity $\epsilon_{r,p}$, one can write

$$\epsilon_{r,m} = \left(1 + (\epsilon_{r,p}^a - 1)f_p\right)^{1/a}, \quad (2)$$

where f_p denotes the volume fraction (filling ratio) of the plastic. In the case of the ABS450 filament, i.e., $\epsilon_{r,p} = 4.5 + j0.019$, the effective mixture permittivity, as predicted by this model, is $\epsilon_{r,m} = 4.0 + j0.016$ and $\epsilon_{r,m} = 3.0 + j0.010$ for the filling ratios of $f_p = 0.90$ and $f_p = 0.66$, respectively (Table 1), if $a = 0.4$.

2.3.2. Attenuation effects

Attenuation effects are caused by absorption as well as multiple diffuse Rayleigh and Mie scattering phenomena within the unstructured tetrahedral mesh of the wireframe. A thorough analysis of the scattering losses is omitted here as any structural details in the mesh are smaller than one fourth of the wavelength and, thereby, the interaction of the wave with the mesh resembles its interaction within solid material.

The absorption rate can be approximated based on the skin depth [40], i.e., the distance where the field intensity drops by the factor e^{-1} , which is determined by

$$\delta = \frac{1}{2\pi f} \sqrt{\frac{2}{\mu_0 \epsilon_0 \epsilon_r'} \left(\sqrt{1 + \left(\frac{\epsilon_r''}{\epsilon_r'}\right)^2} - 1 \right)^{-1}}. \quad (3)$$

Here, ϵ_0 and μ_0 denote the electric and magnetic permittivity of vacuum, respectively, and f the signal frequency. The approximate loss rate in decibels is, thus, given by $-8.69 \log_{10} e = -191$

$-8.69/\delta$ which evaluated for the effective permittivity predicted by the exponential model (Table 1) matches roughly with the lower end of the attenuation range predicted for asteroids, i.e., about 10 dB/km at 10 MHz and 100 dB/km 100 MHz frequency [36].

2.4. Wireframe edges and apertures

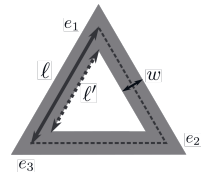


Figure 2: The side-length ℓ of a triangle (dashed) in the original mesh is shown by the solid grey line. The aperture size ℓ' within the wireframe (thick grey triangle) is determined by the width w (black) of its edges.

When the edges of the tetrahedral mesh are substituted with prisms, the structure will have complex shaped apertures. The approximate edge length for these apertures depends on the applied edge width and should be smaller than one fourth of the maximal applied wavelength so that in the measurement phase, the structure would appear as a solid having the desired effective permittivity. The width of a prism w associated with a given edge e_i is assumed to be proportional to that of the maximum edge length ℓ_{\max} in the tetrahedral mesh with respect to a constant shape factor s , i.e., $w = s\ell_{\max}$. On any triangular

192 surface mesh, including both the exterior and internal bound-
 193 aries, the size of the apertures can be estimated based on the
 194 following equation satisfied by any triangle:

$$195 \quad \frac{d_1}{h_1} + \frac{d_2}{h_2} + \frac{d_3}{h_3} = 1. \quad (4)$$

196 Here d_i and h_i denote the perpendicular distance and triangle
 197 altitude with respect to edge e_i , $i = 1, 2, 3$ [41]. After adding the
 198 prisms the edge length and height for the remaining triangular
 199 aperture are given by $\ell'_i = \alpha \ell_i$ and $h'_i = \alpha h_i$ for $i = 1, 2, 3$,
 200 respectively, as the shape of the aperture coincides that of the
 201 original triangle. Consequently, it holds that

$$202 \quad \frac{d_1 - (w/2)}{\alpha h_1} + \frac{d_2 - (w/2)}{\alpha h_2} + \frac{d_3 - (w/2)}{\alpha h_3} = 1. \quad (5)$$

203 To obtain the scale factor, this can be written in the form

$$204 \quad \alpha = 1 - \frac{w}{2} \left(\frac{1}{h_1} + \frac{1}{h_2} + \frac{1}{h_3} \right), \quad (6)$$

205 where the first right-hand side term follows from the original
 206 equation (4). It follows that the longest side of the aperture can
 207 be estimated using

$$208 \quad \ell'_i \leq \left(1 - \frac{3w}{2h_{\min}} \right) \ell_i, \quad (7)$$

209 where h_{\min} denotes the shortest side-length and altitude of the
 210 original triangle.

211 For an equilateral triangle, $\ell_i/h_i = 2/\sqrt{3}$ implying $\ell'_i =$
 212 $\ell_i - w\sqrt{3}$ which calculated for the median edge length is used
 213 here as the approximation of the effective surface mesh aperture
 214 size. In addition this triangle-based surface approach, as an al-
 215 ternative strategy to approximate the aperture size, we apply the
 216 volumetric formula $s = \sqrt[3]{(1-f_r)V}$, where V denotes the me-
 217 dian volume of a tetrahedron within a given compartment and
 218 f_r is its relative volumetric filling.

219 2.4.1. Edge inflation effect

220 The volumetric filling and, thereby, the permittivity of the
 221 analogue objects is, in this study, controlled by inflating the
 222 edges of the tetrahedral mesh [12], which also slightly affects
 223 the details of the modelled geometry: the smaller the detail the
 224 greater the effect. We examine the effect of the inflation via the
 225 following measure

$$226 \quad \nu = \frac{S_{\text{volume}}}{S_{\text{volume}} - S_{\text{surface}}/2}, \quad (8)$$

227 where $S_{\text{volume}} = \sum_{i \in I_{\text{volume}}} \ell_i$ and $S_{\text{surface}} = \sum_{i \in I_{\text{surface}}} \ell_i$ de-
 228 note the sum of the edge length over the volume I_{volume} (in-
 229 cluding the surface) and the surface I_{surface} , respectively. Since
 230 the inflated surface edges are symmetrically distributed on both
 231 sides of the surface, $S_{\text{surface}}/2$ corresponds to the proportion
 232 outside the surface. Following from the definition, ν is inde-
 233 pendent of the (inflated) edge width. When evaluated for a
 234 given meshed detail with a closed surface, ν gives the ratio
 235 $\nu = M_{\text{total}}/M_{\text{enclosed}}$ between the total amount of the inflated ma-
 236 terial M_{total} constituting the detail and the proportion M_{enclosed}

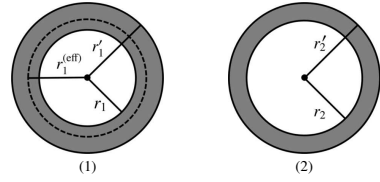


Figure 3: An example of mesh filling in the case of two spheres (1) and (2) with radii r_1 , r_2 and r'_1 , r'_2 before and after edge inflation, respectively. The effective radius r'_1 has been selected so that the effect of the inflation is equal with respect to r'_1 and r_2 , i.e., $r'_1/r_1 = r'_2/r_2$.

237 enclosed by it. For an inflated mesh the sums S_{volume} and S_{surface}
 238 can be equivalently evaluated also as the total material volume
 239 in the mesh and on the surface, respectively. If the radius of
 240 curvature for the detail is r in the original tetrahedral mesh, it
 241 will have the radius $r' = \nu^{1/3}r$ after the mesh inflation. Here the
 242 exponent $1/3$ follows from the conversion between volumetric
 243 and one dimensional scaling. Further, if ν_1 and ν_2 are the infla-
 244 tion measures of two different details (1) and (2) with radii of
 245 curvature r_1 and r_2 (see Figure 3), then

$$246 \quad r'_1 = \left(\frac{\nu_1}{\nu_2} \right)^{1/3} r_1 \quad (9)$$

247 will be an effective radius such that $r'_1 = \nu_2^{1/3} r_1$, meaning that
 248 the inflation measure of r'_1 with respect to the inflated detail
 249 (1) will be that of the detail (2), i.e., ν_2 .

250 2.5. Wireframe construction

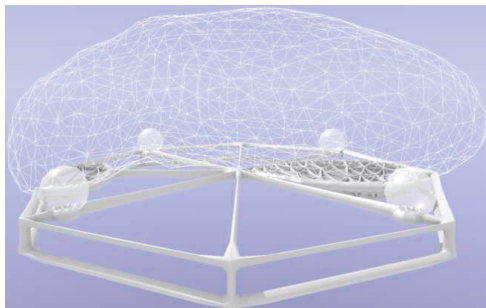
251 The tetrahedral mesh for the object containing the mantle,
 252 interior and voids was created by Gmsh software³ and then im-
 253 ported into Matlab (Mathworks, Inc.) to create the wireframe
 254 structure, i.e. to replace the edges of the tetrahedral mesh with
 255 regular prisms. The edge width w was set to match with the
 256 filling ratio $f_p = 0.66$ and $f_p = 0.90$ for the mantle and interior
 257 compartment, respectively, accounting the effect of the inflation
 258 with respect to a volume of a 35 mm diameter sphere. The edge
 259 was placed on the longitudinal symmetry axis of the prism, and
 260 the length of the prism was set to be slightly larger with respect
 261 to that of the edge to create some overlap and, thereby, ensure
 262 the printability of the structure. Each prism was constructed
 263 of eight triangles, i.e., the minimum triangular configuration
 264 required to present a regular prism, to keep the size of the fi-
 265 nal triangular mesh of the volumetric model as low as possible.
 266 The eventual model, i.e., a surface mesh describing the wire-
 267 frame, was stored as an STL (stereolithography) file which can
 268 be read by the most extensively used 3D printing software such
 269 as the Prusa Slicer⁴ application used in this study. The edge
 270 width corresponding to a given filling level f_p was sought by
 271 optimizing the slicer's estimate for the filament volume for the
 272 spherical meshes (III) and (IV).

³<http://gmsh.info>

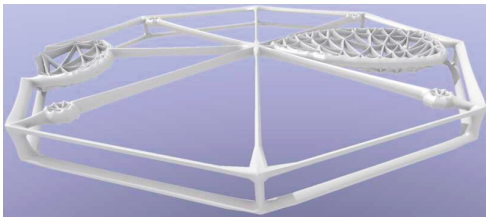
⁴<https://www.prusa3d.com/prusaslicer/>

2.6. Stand design

Developing a 3D printed stand was found to be necessary to allow accurate positioning of the model in the anechoic chamber. The Blender software⁵ was applied to configure a cylindrical wireframe stand with an octagonal cross section of 190 mm diameter and 13.7 mm height, and a triangulated cut-out part matching with a slightly expanded and coarse resolution asteroid shape model. The edge width of the stand was set to be around 2.8 mm, i.e., less than one fourth of the shortest wavelength in the planned measurement wavelength range (Section 2.2) to ensure the invisibility of the stand in the actual measurement. The standard polylactic acid (PLA) filament (diameter 1.75 mm, density 1.24 g/cm³) was used, as it has a relatively low weight and permittivity ($\epsilon_r < 3$), while providing a solid enough support for the measurement purpose. This design allows obtaining a principally arbitrary placement and orientation for the target. Additionally, it includes four supports for reflecting alignment spheres, which are used as divergent mirrors to position and align the target in the anechoic chamber. These spheres are removed after the target alignment. The stand design for 25143 Itokawa is illustrated in Figure 4.



A support plate with cut-out asteroid and sphere meshes.



The support plate design resulting from the cuts.

Figure 4: A wireframe design of a support plate with an octagonal cross-section. The edge width is smaller than the planned wavelengths (Table 1) divided by four to ensure that the plate does not interact with the radar signal. The picture on the top shows the mesh structures which are to be supported by the plate and are, therefore, cut out of the support volume via a Boolean difference. Of those meshes, the spheres are used in the optical positioning of the plate, and the asteroid surface is a coarse approximation of the actual one, in order that the eventual wireframe would be sparse. The bottom picture visualizes the final support plate as is.

3. Results

The Gmsh, Matlab, and Blender source files as well as the wireframes (STL files) created in this study can be found in the Asteroid Wireframe Package which is available via Zenodo [42]. The details of these numerical models together with a description of the FFF process and final 3D printing results can be found below.

3.1. Wireframe models

The numerical wireframe models, their relative filling ratios, edge widths, and maximal aperture sizes have been described in Table 2. The complete models are illustrated in Figure 5, and a close view of the mesh structure with the two applied filling ratios in Figure 6. The edge width was selected so that the final printable model (GCODE file) had the given relative filling ratios $f_r = 0.66$ and $f_r = 0.90$ in their respective compartments.

The results show that the aperture diameter inside the printed analogue objects does not exceed 1.4 mm. In addition to the aperture size, the overall structural accuracy of the models can be estimated to be determined by one half of the edge width, i.e., $w/2$, which is also maximally 1.4 mm. The edge length varies slightly within each wireframe as the mesh generator routine of Gmsh relates the tetrahedral grid to the slightly varying surface mesh size. The edge widths and aperture sizes can be observed to grow along with the edge length, in order that the relative filling ratio is maintained.

3.2. 3D printing

The objects were printed with single-nozzle Prusa i3 MK3S printers using a nozzle diameter of 0.4 mm and a rectilinear support pattern to stabilize the object on the build plate. When printing ABS450, the layer height was set to 0.3 mm and the temperature to 270–275 °C for the nozzle and to 110–112 °C for the plate. During the printing process, we observed that using a slightly higher nozzle temperature compared to the Prusa Slicer’s preset for generic ABS (255 °C) is advantageous to prevent the jamming of the filament. The applied value was found through a few trials and errors. While the filament would allow a nozzle temperature above 300 °C, a value above 280 °C was likely to lead to overheating of the printer, especially, for the dense $f_r = 0.90$ structure and, thereby, a disrupted printing process. Pre-heating the nozzle carefully, when loading and changing the filament was found to be necessary for the same reason. For the PLA prints the layer height of 0.15 mm and the default temperature settings 210 and 60 °C for the nozzle and bed were applied. The support material consisting of the printed filament was observed to penetrate a maximum of 0.5 cm inside the printed structure. This was deemed as a minor structural deviation based on its relatively small amount and the larger scale of the voids and the mantle.

Figure 7 illustrates the objects (IA) and (IIA) during the printing process, showing their mantle and void structures. The final objects (IA), (IB), (IIB) and (IIA) together with their stands are shown in Figure 8. The object-wise 3D printing details can be found in Table 3. The wireframes for the analogues resulted

⁵<https://www.blender.org/>

Table 2: The wireframe details for the interior and mantle compartment including the relative filling f_p , edge width w (mm), median tetrahedron edge length ℓ (mm), estimated edge length for the apertures ℓ' (mm) based on ℓ , estimated volumetric aperture diameter s (mm) based on f_p , maximum tetrahedron edge length ℓ_{\max} (mm), and minimum tetrahedron edge length ℓ_{\min} (mm). The filling f_p has been calculated accounting the effect of the inflation with respect to a volume of a 35 mm diameter sphere.

ID	Points	Tetrahedra	Compartment	Mesh parameters						
				f_p	w	ℓ	ℓ'	s	ℓ_{\max}	ℓ_{\min}
(IA)	21543	107439	Interior	0.90	2.5	4.1	0	0.9	8.7	2.1
			Mantle	0.66	1.9	4.4	1.2	1.4	7.8	1.8
(IB)	12800	62769	Whole object	0.90	2.9	5.2	0.2	1.1	8.8	2.4
(IIA)	21125	109433	Interior	0.90	2.4	4.4	0.1	0.9	8.1	2.0
			Mantle	0.66	1.8	4.4	1.2	1.4	8.2	0.9
(IIB)	13454	64625	Whole object	0.90	2.9	5.1	0.2	1.1	8.7	2.5
(III)	740	2960	Whole object	0.66	1.8	4.1	1.0	1.3	7.1	1.4
(IV)	641	2504	Whole object	0.90	2.4	4.3	0.2	0.9	7.4	1.6

Table 3: The 3D printing details: object type, file size, printing time, volume, and filament. The volume of the filament is given separately for the object and a rectilinear support structure.

ID	Type	Size		Object vol. (cm ³)	Support vol. (cm ³)	Fil.
		(MB)	Time			
(IA)	Analogue	294.6	5d 08h 17m	632.0	52.4	ABS450
(IB)	Analogue	288.7	5d 13h 23m	743.4	55.2	ABS450
(IIA)	Analogue	304.8	5d 12h 53m	627.7	71.3	ABS450
(IIB)	Analogue	296.4	5d 17h 47m	745.5	74.3	ABS450
(III)	Sphere	9.4	4h 2m	14.9	3.4	ABS450
(IV)	Sphere	10.8	4h 44m	20.3	3.6	ABS450
(I)	Stand 1	12.5	7h 29m	18.3	15.3	PLA
(II)	Stand 2	11.3	6h 54m	17.5	14.5	PLA
(I)	Stand 1	15.3	8h 48m	21.3	17.1	PLA
(II)	Stand 2	14.4	8h 12m	20.2	15.9	PLA

in GCODE files around 300 MB in size and a printing time of about 5 1/2 days. The GCODE files were prepared using Lenovo P910 workstation with two Intel Xeon 2697A V4 processors and 256 GB of RAM, as a standard laptop with Intel Core i7 I7-5650U processor and 8 GB of RAM was found to have an insufficient memory capacity and overall performance.

Printing a three-layered (category A) object required a total of about 700 cm³ of filament while a single-layered (category B) object with a constant density consumed around 800 cm³.

3.3. Sphere permittivity

The permittivity of the analogue objects was investigated via bistatic far-field electromagnetic scattering patterns of test spheres (III)–(V) with a method based on the exploitation of the scattering pattern in the far field [43, 12]. The experimental data were measured with a spherical setup in the anechoic chamber of the CCRM in Marseille. Table 4 shows the complex relative permittivity values and their averages over the measured frequency range 2–18 GHz. It also includes the measured loss angles, the attenuation (3) corresponding to the observed loss angle at 13 GHz frequency, and the 90 % confidence intervals for the relative permittivities and the loss angles. As shown in the Table 4, the average complex relative permittivity values of the spheres (III) and (IV) modelling the asteroid interior and the mantle were measured as $3.41 + j0.04$ and $2.56 + j0.02$, respectively.

The nine-point moving average measurement data for the real part permittivity ϵ'_r and the loss angle ϵ''_r/ϵ'_r of permittivity are shown in Figure 9. The real part was found to have a smooth distribution over the measured frequency range,

while the loss angle fluctuates more obviously in relation to its average value. The absolute fluctuation of the imaginary part or the loss angle, however, does not exceed that of the real part which is shown by the confidence intervals.

4. Discussion

The present study introduced an FFF process and its implementation for manufacturing a tetrahedral wireframe with a complex structured electrical permittivity distribution to be used as an analogue object in microwave range radar measurements. Our motivation to develop such objects is to investigate the tomographic imaging of small Solar System bodies [24, 20, 11]. Therefore, the exterior shape was to be matched with a given asteroid shape model, and the volumetric structure with the existing knowledge of potential asteroid interior composition. We showed the feasibility of manufacturing a wireframe which consists of around 100 000 tetrahedra divided into a mantle, denser interior part, and voids. The mantle and interior part were given the relative filling ratios which, based on the exponential mixture model [13, 38], correspond approximately to the effective complex relative permittivity of $3.0 + j0.010$ and $4.0 + j0.016$ and according to a radar measurement to $2.56 + j0.02$ and $3.41 + j0.04$, respectively. Both the estimated and measured permittivity values match roughly with the current knowledge about the mineral composition and structure of asteroids [31, 36].

The overall accuracy of the manufactured objects was found to be roughly 1.4 mm regarding both the apertures and edges of the wireframe, suggesting that the analogues might consti-

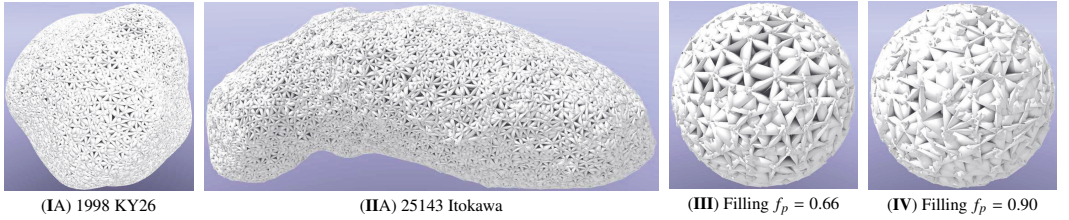


Figure 5: The volumetric wireframe models obtained by generating a tetrahedral finite element mesh for the models (IA) and (IIA) and replacing the edges of the mesh with triangular prisms. The level of filling and, thereby, the relative permittivity is varied by controlling the width to length ratio of the prisms. The spheres (III) and (IV) have been designed to match with the relative permittivity $\epsilon_r = 3.0 + j0.010$ and $\epsilon_r = 4.0 + j0.016$, respectively.

Table 4: The measured ϵ_r and loss angle (ϵ_r''/ϵ_r') values and their 90 % confidence intervals modelling the different compartments in asteroid analogues. The attenuation values have been determined with respect to a 13 GHz signal frequency.

ID	ϵ_r	90% conf. of ϵ_r	Attenuation (dB/cm)	Loss angle (ϵ_r''/ϵ_r')	90% conf. of loss angle
(III)	$3.41+j0.04$	$[3.39+j0.03, 3.42+j0.05]$	0.22	0.0068	$[0.0097, 0.0153]$
(IV)	$2.56+j0.02$	$[2.56+j0.01, 2.57+j0.02]$	0.13	0.0125	$[0.0040, 0.0097]$
(V)	$4.20+j0.05$	$[4.19+j0.05, 4.21+j0.06]$	0.35	0.0130	$[0.0119, 0.0141]$

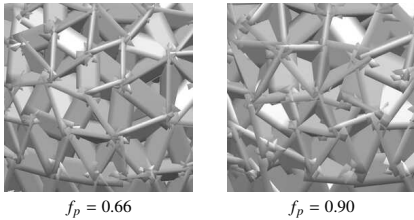
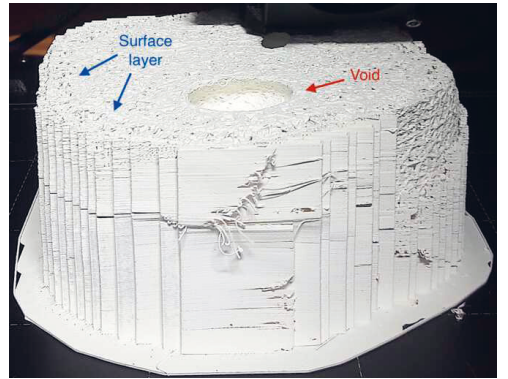
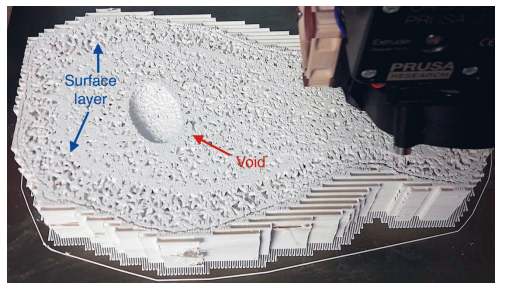


Figure 6: A close view of a mesh structure created by replacing the edges of a tetrahedral mesh with regular overlapping prisms for relative volumetric filling $f_p = 0.66$ and $f_p = 0.90$.



(IA) 1998 KY26



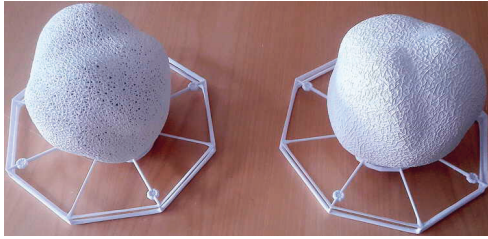
(IIA) 25143 Itokawa

Figure 7: Images of the models (IA) and (IIA) during the 3D printing process. The mantle and the void structures are visible in the interior part, i.e., on the horizontal cross-section.

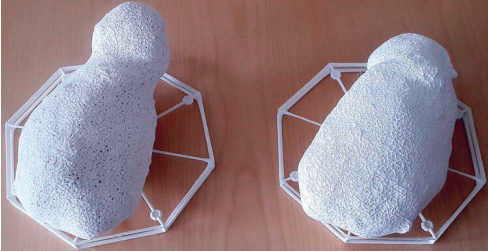
405 tute an accurate approximation of a solid structure up to 52
 406 GHz signal frequency, i.e., a wavelength of approximately four
 407 times the present structural modelling accuracy. Thus, the ana-
 408 logues developed in this study might be applied to model a to-
 409 mographic *in-situ* measurement [24] for an asteroid up to a sig-
 410 nal frequency 20 MHz and 200 MHz in the case of the models
 411 (I) 25143 Itokawa and (II) 1998 KY26, respectively. With re-
 412 spect to the real size of these asteroids, this accuracy scales to
 413 3.7 and 0.3 m, respectively. Furthermore, the maximum tetra-
 414 hedron edge length obtained suggest that the detail-size is max-
 415 imally about two times that of these median estimates, i.e., that
 416 the model should be sufficiently accurate with respect to at least
 417 the real-size frequencies 10 and 100 MHz in the case of (I) and
 418 (II), respectively. The present volumetric accuracy obtained for
 419 the mantle and voids can be regarded as sufficient for the to-
 420 mography of asteroids and comets, as due to the various limita-
 421 tions related to an *in-situ* measurement, the bandwidth of the
 422 signal determining the maximal imaging accuracy will be compar-
 423 ably small, e.g. one fifth with respect to the center (carrier)
 424 frequency [37].

425 To improve the modelling resolution, it is possible to refine
 426 the tetrahedral mesh uniformly which would lead to eight times

the number of tetrahedra compared to the present case, i.e., to
 around 0.8 M elements for the detailed analogues. According to
 our preliminary results, this would be allowed by the framework



Models (IA) and (IB) of 1998 KY26 on the left and right, respectively.



Models (IIA) and (IIB) of 25143 Itokawa on the left and right, respectively.

Figure 8: **Top row:** The final asteroid analogue models (IA) and (IB) of 1998 KY26 and (IIA) and (IIB) of 25143 Itokawa. The left and right side support plate represent two opposite orientations of the asteroid with respect to a vertical 180 degree turn.

applied including both the numerical model and the printing process, while approximately doubling the size of the GCODE file and increasing the printing time by a few days. The current resolution was found to be preferable, since using the finer alternative would have required halving the edge width, potentially resulting in a less robust 3D printing outcome. Enhancing the modelling precision might be interesting and even necessary with high measurement frequencies, more complex interior structures such as cracks [25], and also other applications which the structural *a priori* information is more coherent. An alternative tetrahedral mesh generation strategy would be to apply a uniform grid which would provide a constant element size over the whole structure and, thereby, might improve the accuracy of the relative filling. Nevertheless, it would also mean less accurate staircase-like external and internal boundaries between the permittivity compartments, which was here deemed to be a potential factor to diminish the surface modelling accuracy and the overall durability of the analogues. A uniform mesh might also lead to diffraction effects and hence not be appropriate in this application. Therefore, the Gmsh software which generates a well-balanced tetrahedral mesh with respect to both the geometrical accuracy and volumetric regularity, was seen advantageous in this study.

The match between targeted permittivity and the final 3D printed wireframe was verified via a radar measurement performed for the spherical objects (III) and (IV) [43] with filling levels corresponding to the mantle and interior compartment, respectively, using the solid sphere (V) as the reference. Compared to the estimates given by the exponential model, the mea-

sured values were found to be roughly 85 % of the real parts of the permittivity. We deem these deviations from the predictions acceptable in the present planetary scientific application context, as due to the large variety of the small Solar System bodies [24], the permittivity values of the 3D printed analogues will not need to be matched exactly with any *a priori* given estimate. Moreover, from the tomographic reconstruction point of view, the local contrasts between the different parts of the target structure can be considered more important than the exact permittivity values. Comparing the filament permittivity given by the manufacturer ($4.5 + j0.019$) to the measured value obtained for the solid sphere ($4.20 + j0.05$) it is obvious that a significant part of the differences between the estimated and measured permittivity values can be attributed to the 3D printing process in which different factors might affect the material properties, e.g., the air-containing microstructure of the 3D printed object.

Of the other possible factors, the effect of the edge inflation on the permittivity was found to depend on the detail size: the smaller the detail the greater the effect. Compared to the original (non-inflated) size of the detail, this effect seems to be maximally 1.5 %, concerning both the permittivity measured (here $3.41 + j0.04$ and $2.56 + j0.02$ for sphere (III) and (IV), respectively) and the effective diameter, for any detail larger than the 35 mm test sphere diameter up to the size of the analogue objects. The greatest absolute measurement fluctuation was found for the real part of the permittivity, while the measurement of the loss angle was found to involve a larger fluctuation in relation to its average value, which is in parallel with the findings of, e.g., [43], suggesting that the actual permittivity and loss angle of (III) and (IV) are contained by the the confidence intervals found in this study. Some amount of fluctuation is expected to be caused by the edge inflation effect since the surface of a 3D printed sphere is not purely convex but deviates from its intended spherical shape and also includes material outside and lacks material inside this shape.

Our FFF approach enables modelling principally any relative permittivity value between one and that of the filament. However, the 3D printable range is, in practice, bounded from below due to the finite resolution of the printer. The most challenging parts regarding the accuracy of the 3D printing process may be expected to arise from the complexity of the geometry, especially, close-to-horizontal structures which require support material to sustain the shape of the printed structure, potentially setting limitations for the printability of fine mesh edges (prisms) in the horizontal direction and, thereby, restricting the range of applicable permittivity values. With the present setup, edge widths down to at least 1.2 mm were found to be printable and separable from the support material. Extrapolating from the present results such an edge width might lead to a relative filling of 0.2–0.3, i.e., a relative permittivity of about 1.4–1.7, assuming that the edge length is maintained. With more precise 3D printers enabling stereolithography, permittivities down to 1.02 have proven to be feasible [12]. Extending the upper limit of the feasible permittivity range, e.g., to model structures containing water such as some biological tissues [44, 45], would necessitate using a filament with a higher permittivity and, thus, potentially also require a higher printing temperature

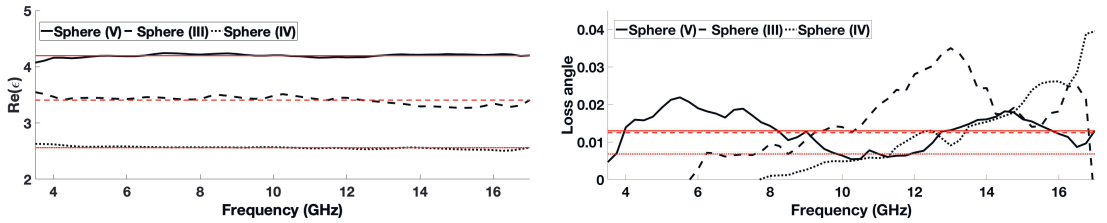


Figure 9: The nine-point moving average of the real (left) part ϵ'_r and the loss angle ϵ''_r/ϵ'_r (right) of the relative permittivity for the spheres (III)–(V). The black lines indicate the measurements and the red lines the corresponding averages.

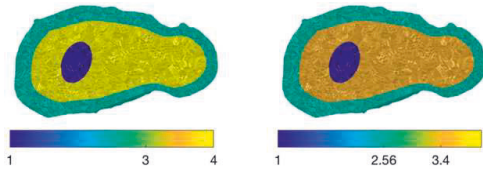


Figure 10: The expected (left) and measured (right) permittivity distribution inside the three-compartment analogue (IIA). The same structure is applied also in (IA). Analogues (IB) and (IIB) consist of a single compartment which corresponds here to the interior part (yellow). The permittivities were measured based on the test spheres (III)–(IV)

due to a greater concentration of permittivity-controlling fused components within the filament. As here the printing equipment was operated close to the upper end of its temperature range, also modelling higher-permittivity structures will likely require a more sophisticated printer.

Signal attenuation due to the multiple diffuse Rayleigh and Mie scattering events in the tetrahedral mesh structure was omitted in this study as the structural details in the mesh are smaller than one fourth of the wavelength and, thereby, the wave interacts with the mesh similarly as it would interact with solid material. However, a more detailed analysis of this effect is an important future topic, as Rayleigh scattering is strongly dependent on the wavelength (by λ^{-4}) and the shorter wavelengths are scattered more strongly than the longer ones, possibly introducing a bias in the actual measurements. This might be investigated in a future study via residual scattering, akin to [46] and [47]. Advanced numerical approximation of high-frequency scattering losses in mixtures can be found, for example, in [48]. As another potential future direction, it would be interesting to add an electrically conductive component into the analogue objects to investigate the effect and role of a stronger signal attenuation. Such an approach would probably necessitate mixing a conductive filament into the structure, e.g., by filling apertures or subdividing edges into two different parts.

5. Conclusion

This study showed that a plastic wireframe-based asteroid analogue object with a complex shape and permittivity structure can be manufactured successfully via FFF and that the per-

mittivity of the object can be controlled to create an appropriate scale model of a small Solar System body. The analogue objects manufactured in this study can be used in tomographic microwave radar measurements and to develop analysis methods for the future applications concerning the tomography of the Small Solar system bodies, whose interior structures are still largely unknown.

Acknowledgement

We acknowledge the Premix Group for their support in permittivity controlled filaments. L-IS, MT and SP were supported by the Academy of Finland Centre of Excellence in Inverse Modelling and Imaging (2018-2025). L-IS was also supported by a young researcher's research grant by Emil Aaltonen Foundation. The authors acknowledge the opportunity provided by the Centre Commun de Ressources en Microondes (CCRM) to use its fully equipped anechoic chamber.

References

- [1] C. Tomassoni, R. Bahr, M. Tentzeris, M. Bozzi, L. Perregrini, 3d printed substrate integrated waveguide filters with locally controlled dielectric permittivity, in: 2016 46th European Microwave Conference (EuMC), IEEE, 2016, pp. 253–256.
- [2] Z. Larimore, S. Jensen, P. Parsons, B. Good, K. Smith, M. Mirotznik, Use of space-filling curves for additive manufacturing of three dimensionally varying graded dielectric structures using fused deposition modeling, *Additive Manufacturing* 15 (2017) 48–56.
- [3] M. Mirzaee, S. Noghianian, L. Wiest, I. Chang, Developing flexible 3d printed antenna using conductive abs materials, in: 2015 IEEE International Symposium on Antennas and Propagation & USNC/URSI National Radio Science Meeting, IEEE, 2015, pp. 1308–1309.
- [4] S. L. Marasso, M. Cocuzza, V. Bertana, F. Perrucci, A. Tommasi, S. Ferrero, L. Scaltrito, C. F. Pirri, Pla conductive filament for 3d printed smart sensing applications, *Rapid Prototyping Journal* 24 (2018) 739–743.
- [5] Q. Mu, L. Wang, C. K. Dunn, X. Kuang, F. Duan, Z. Zhang, H. J. Qi, T. Wang, Digital light processing 3d printing of conductive complex structures, *Additive Manufacturing* 18 (2017) 74–83.
- [6] Y. Wu, D. Isakov, P. Grant, Fabrication of composite filaments with high dielectric permittivity for fused deposition 3d printing, *Materials* 10 (2017) 1218.
- [7] S. W. Kwok, K. H. H. Goh, Z. D. Tan, S. T. M. Tan, W. W. Tjui, J. Y. Soh, Z. J. G. Ng, Y. Z. Chan, H. K. Hui, K. E. J. Goh, Electrically conductive filament for 3d-printed circuits and sensors, *Applied Materials Today* 9 (2017) 167–175.
- [8] A. Dorigato, V. Moretti, S. Dul, S. Unterberger, A. Pegoretti, Electrically conductive nanocomposites for fused deposition modelling, *Synthetic Metals* 226 (2017) 7–14.

- [9] J.-M. Geffrin, C. Eyraud, A. Litman, P. Sabouroux, Optimization of bistatic microwave scattering measurement setup: From high to low scattering targets, *Radio Science* 44 (2009) 1–12.
- [10] C. Eyraud, H. Saleh, J.-M. Geffrin, Influence of the description of the scattering matrix on permittivity reconstruction with a quantitative imaging procedure: polarization effects, *JOSA A* 36 (2019) 234–244.
- [11] C. Eyraud, A. Hérique, J.-M. Geffrin, W. Kofman, Imaging the interior of a comet from bistatic microwave measurements: case of a scale comet model, *Advances in Space Research* 62 (2018) 1977–1986.
- [12] H. Saleh, H. Tortel, C. Leroux, A. Coudreuse, A. Litman, J.-M. Geffrin, Approach to control permittivity and shape of centimeter-sized additive manufactured objects: Application to microwave scattering experiments, *IEEE Transactions on Antennas and Propagation* (2020). URL: <https://doi.org/10.1109/TAP.2020.3016159>.
- [13] A. Sihvola, E. Nyfors, M. Tiuri, Mixing formulae and experimental results for the dielectric constant of snow, *Journal of Glaciology* 31 (1985) 163–170.
- [14] H. J. Kramer, Hayabusa-2, japan’s second asteroid sample return mission 2016. Available: <https://directory.eoportal.org/web/eoportal/satellite-missions/h/hayabusa-2>. Accessed November 4th, 2019.
- [15] A. Fujiwara, J. Kawaguchi, D. K. Yeomans, M. Abe, T. Mukai, T. Okada, J. Saito, H. Yano, M. Yoshikawa, D. J. Scheeres, O. Barnouin-Jha, A. F. Cheng, H. Demura, R. W. Gaskell, N. Hirata, H. Ikeda, T. Kominato, H. Miyamoto, A. M. Nakamura, R. Nakamura, S. Sasaki, K. Uesugi, The rubble-pile asteroid itokawa as observed by hayabusa, *Science* 312 (2006) 1330–1334. doi:10.1126/science.1125841.
- [16] A. Tsuchiyama, M. Uesugi, T. Matsushima, T. Michikami, T. Kadono, T. Nakamura, K. Uesugi, T. Nakano, S. A. Sandford, R. Noguchi, T. Matsumoto, J. Matsuno, T. Nagano, Y. Imai, A. Takeuchi, Y. Suzuki, T. Ogami, J. Katagiri, M. Ebihara, T. R. Ireland, F. Kitajima, K. Na-gao, H. Naraoka, T. Noguchi, R. Okazaki, H. Yurimoto, M. E. Zolensky, T. Mukai, M. Abe, T. Yada, A. Fujimura, M. Yoshikawa, J. Kawaguchi, Three-dimensional structure of hayabusa samples: Origin and evolution of itokawa regolith, *Science* 333 (2011) 1125–1128. doi:10.1126/science.1207807.
- [17] Y. Tsuda, M. Yoshikawa, M. Abe, H. Minamino, S. Nakazawa, System design of the hayabusa 2-asteroid sample return mission to 1999 JU3, *Acta Astronautica* 91 (2013) 356–362.
- [18] K. Berry, B. Sutter, A. May, K. Williams, B. Barbee, M. Beckman, B. Williams, Osiris-rex touch-and-go (tag) mission design and analysis, *Advances in the Astronautical Sciences* 149 (2013) 667–678.
- [19] W. Kofman, A. Hérique, J.-P. Goutail, T. Hagfors, I. P. Williams, E. Nielsen, J.-P. Barriot, Y. Barbin, C. Elachi, P. Edenhofer, A.-C. Levasseur-Regourd, D. Plettemeier, G. Picardi, R. Seu, V. Svethem, The comet nucleus sounding experiment by radiowave transmission (CON-SERT): A short description of the instrument and of the commissioning stages, *Space Science Reviews* 128 (2007) 413 – 432.
- [20] W. Kofman, A. Hérique, Y. Barbin, J.-P. Barriot, V. Ciarletti, S. Clifford, P. Edenhofer, C. Elachi, C. Eyraud, J.-P. Goutail, E. Heggy, L. Jorda, J. Lasue, A.-C. Levasseur-Regourd, E. Nielsen, P. Pasquero, F. Preusker, P. Puget, D. Plettemeier, Y. Rogez, H. Sierks, C. Statz, H. Svethem, I. Williams, S. Zine, J. Van Zyl, Properties of the 67p/churyumov-gerasimenko interior revealed by consort radar, *Science* 349 (2015). doi:10.1126/science.aab0639.
- [21] V. Ciarletti, A. Hérique, J. Lasue, A.-C. Levasseur-Regourd, D. Plettemeier, F. Lemmonier, C. Guiffaut, P. Pasquero, W. Kofman, Consort constrains the internal structure of 67p at a few metres size scale, *Monthly Notices of the Royal Astronomical Society* 469 (2017) S805–S817.
- [22] A. Hérique, W. Kofman, P. Beck, L. Bonal, I. Buttarazzi, E. Heggy, J. Lasue, A. C. Levasseur-Regourd, E. Quirico, S. Zine, *Cosmochemical implications of CONSERT permittivity characterization of 67P/CG.721 Monthly Notices of the Royal Astronomical Society* 462 (2017) S516–722 S532. doi:10.1093/mnras/stx040.
- [23] Hérique, A., Kofman, W., Zine, S., Blum, J., Vincent, J.-B., Ciarletti, V., Homogeneity of 67p/churyumov-gerasimenko as seen by consort: implication on composition and formation, *A&A* 630 (2019) A6. doi:10.1051/0004-6361/201834865.
- [24] A. Hérique, B. Agnus, E. Asphaug, A. Barucci, P. Beck, J. Bellerose, J. Biele, L. Bonal, P. Bousquet, L. Bruzzone, et al., Direct observations of asteroid interior and regolith structure: science measurement requirements, *Advances in Space Research* 62 (2018) 2141–2162.
- [25] L.-I. Sorsa, M. Takala, P. Bambach, J. Deller, E. Vilenius, S. Poursiainen, Bistatic full-wave radar tomography detects deep interior voids, cracks and boulders in a rubble-pile asteroid model, *Astrophysical Journal* 872 (2019).
- [26] M. Takala, P. Bambach, J. Deller, E. Vilenius, M. Wittig, H. Lentz, H. M. Braun, M. Kaasalainen, S. Poursiainen, Far-field inversion for the deep interior scanning cubesat, *IEEE Transactions on Aerospace and Electronic Systems* 55 (2018) 1683–1697.
- [27] S. Poursiainen, M. Kaasalainen, Orbiter-to-orbiter tomography: A potential approach for small solar system body, in: *IEEE Transactions on Aerospace and Electronic Systems*, volume 52, 2016, pp. 2747–2759. doi:10.1109/TAES.2016.150638.
- [28] A. Hérique, V. Ciarletti, A Direct Observation of the Asteroid’s Structure from Deep Interior to Regolith: Two Radars on the AIM Mission, in: 47th Lunar and Planetary Science Conference, LPSX 2016, Conference abstract 2096, 2 pages. Topic 315: Planetary Mission Concepts: Small Bodies., 2016.
- [29] C. Neese, Ed. Small Body Radar Shape Models V2.0., EAR-A-5-DDR-RADARSHAPE-MODELS-V2.0, NASA Planetary Data System (2004).
- [30] R. Gaskell, J. Saito, M. Ishiguro, T. Kubota, T. Hashimoto, N. Hirata, S. Abe, O. Barnouin-Jha, D. Scheeres, Gaskell Itokawa Shape Model V1.0., HAY-A-AMICA-5-ITOKAWASHAPE-V1.0. NASA Planetary Data System (2008).
- [31] A. Hérique, J. Gilchrist, W. Kofman, J. Klinger, Dielectric properties of comet analog refractory materials, *Planetary and Space Science* 50 (2002) 857–863.
- [32] M. Takala, D. Us, S. Poursiainen, Multigrid-based inversion for volumetric radar imaging with asteroid interior reconstruction as a potential application, *IEEE Transactions on Computational Imaging* 4 (2018) 228–240.
- [33] P. Cignoni, M. Callieri, M. Corsini, M. Dellepiane, F. Ganovelli, G. Ranzuglia, MeshLab: an Open-Source Mesh Processing Tool, in: V. Scarano, R. D. Chiara, U. Erra (Eds.), *Eurographics Italian Chapter Conference*, The Eurographics Association, 2008. doi:10.2312/LocalChapterEvents/ItalChap/ItalianChapConf2008/129-136.
- [34] R. L. Cook, Stochastic sampling in computer graphics, *ACM Transactions on Graphics (TOG)* 5 (1986) 51–72.
- [35] F. Bernardini, J. Mittleman, H. Rushmeier, C. Silva, G. Taubin, The ball-pivoting algorithm for surface reconstruction, *IEEE transactions on visualization and computer graphics* 5 (1999) 349–359.
- [36] W. Kofman, Radar techniques to study subsurfaces and interiors of the solar system objects, in: 2012 19th International Conference on Microwave, Radar Wireless Communications, volume 2, 2012, pp. 409–412. doi:10.1109/MIKON.2012.6233605.
- [37] R. P. Binzel, W. Kofman, Internal structure of near-earth objects, *Comptes Rendus Physique* 6 (2005) 321–326.
- [38] J. R. Birchak, C. G. Gardner, J. E. Hipp, J. M. Victor, High dielectric constant microwave probes for sensing soil moisture, *Proceedings of the IEEE* 62 (1974) 93–98.
- [39] W. Stiles, F. Ulaby, Dielectric properties of snow. The University of Kansas, Center for Research, Inc., RSL Technical Report (1981) 527–1.
- [40] S. H. Ward, G. W. Hohmann, Electromagnetic theory for geophysical applications, in: *Electromagnetic Methods in Applied Geophysics: Volume 1, Theory*, Society of Exploration Geophysicists, 1988, pp. 130–311.
- [41] R. A. Johnson, *Advanced euclidean geometry*, Courier Corporation, 2013.
- [42] S. Poursiainen, L.-I. Sorsa, C. Eyraud, J.-M. Geffrin, Asteroid wireframe package, 2020. URL: <https://doi.org/10.5281/zenodo.3838480>.
- [43] C. Eyraud, J.-M. Geffrin, A. Litman, H. Tortel, Complex permittivity determination from far-field scattering patterns, *IEEE Antennas and Wireless Propagation Letters* 14 (2015) 309–312. doi:10.1109/LAWP.2014.2362995.
- [44] A. Peyman, S. Holden, C. Gabriel, Dielectric properties of tissues at microwave frequencies, RUM3 MTHR final technical report (2005).
- [45] J. Lin, *Advances in Electromagnetic Fields in Living Systems*, number nid. 4 in *Advances in Electromagnetic Fields in Living Systems*, Springer US, 2006.
- [46] L. Liu, S. A. Arcone, Integrative GPR loss in a discrete random medium model: The effect of rough-surface and subsurface Mie scatterers, in:

- 731 2012 14th International Conference on Ground Penetrating Radar (GPR),
732 2012, pp. 981–984. doi:10.1109/ICGPR.2012.6255006.
- 733 [47] R. Grimm, E. Heggy, S. Clifford, C. Dinwiddie, R. McGinnis, D. Far-
734 rell, Absorption and scattering in ground-penetrating radar: Analysis of
735 the bishop tuff, *Journal of Geophysical Research* 111 (2006) E06S02.
736 doi:10.1029/2005JE002619.
- 737 [48] D. Boyarskii, V. Tikhonov, N. Klecorin, V. Mirovskii, Inclusion of scat-
738 tering losses in the models of the effective permittivity of dielectric mix-
739 tures and applications to wet snow, *Journal of Electromagnetic Waves*
740 and Applications 8 (1994) 1395–1410. doi:10.1163/156939394X00281.

PUBLICATION

V

Full Wavefield Simulation vs. Measurement of Microwave Scattering by a Complex 3D-Printed Asteroid Analogue

C. Eyraud, L.-I. Sorsa, J.-M. Geffrin, M. Takala, G. Henry and S. Pursiainen

Astronomy & Astrophysics 643.(2020), A68

DOI: 10.1051/0004-6361/202038510

Publication reprinted with the permission of the copyright holders

Full wavefield simulation versus measurement of microwave scattering by a complex 3D-printed asteroid analogue[★]

Christelle Eyraud¹, Liisa-Ida Sorsa², Jean-Michel Geffrin¹, Mika Takala², Gérard Henry¹, and Sampsa Pursiainen²

¹ Aix-Marseille Univ., CNRS, Centrale Marseille, Institut Fresnel, Marseille, France
e-mail: christelle.eyraud@fresnel.fr

² Computing Sciences, Tampere University (TAU), PO Box 692, 33101 Tampere, Finland

Received 27 May 2020 / Accepted 6 September 2020

ABSTRACT

Context. The small bodies of the Solar System, and especially their internal structures, are still not well-known. Studies of the interior of comets and asteroids could provide important information about their formation and also about the early Solar System.

Aims. In this paper, we investigate the possibility of obtaining information about their inner structure from their response to an incident electromagnetic field in preparation for future space radar missions. Our focus is on experimental measurements concerning two analog models with the shape of 25143 Itokawa, a small rubble pile asteroid monitored by the Japanese space agency's (JAXA) Hayabusa mission in 2005.

Methods. The analog models prepared for this study are based on the a priori knowledge of asteroid interiors of the time. The experimental data were obtained by performing microwave-range laboratory measurements. Two advanced in-house, full-wave modelling packages – one performing the calculations in the frequency domain and the other one in the time domain – were applied to calculate the wave interaction within the analog models.

Results. The electric fields calculated via both the frequency and time domain approach are found to match the measurements appropriately.

Conclusions. The present comparisons between the calculated results and laboratory measurements suggest that a high-enough correspondence between the measurement and numerical simulation can be achieved for the most significant part of the scattered signal, such that the inner structure of the analog can be observed based on these fields. Full-wave modeling that predicts direct and higher order scattering effects has been proven essential for this application.

Key words. scattering – techniques: image processing – methods: numerical – minor planets, asteroids: general – waves

1. Introduction

This study concerns radar measurement as a potential technique for detecting scattering from inside of an asteroid of a complex shape. The internal structure of the small bodies of the Solar System remains an unanswered scientific question that is central to theories on the formation and evolution of the Solar System (Gomes et al. 2005; Tsiganis et al. 2005; Morbidelli et al. 2005; Desch 2007; Herique et al. 2018) as well as to the development of planetary defense strategies and asteroid deflection (Cheng et al. 2018; Michel et al. 2018). Small bodies and their interior structures have been investigated in several recent planetary space missions, most prominently, ESA's Rosetta mission which, among other things, was aimed at reconstructing the nucleus of the comet 67P/Churyumov-Gerasimenko by its tomographic radar instrument known as CONSERT (Kofman et al. 2007, 2015). Among the most significant future missions planned in the area of low-frequency radar investigation is the HERA mission (Michel et al. 2018), the European component of Asteroid Impact and Deflection Assessment (AIDA), which is a shared effort between ESA and NASA (Hérique et al. 2019).

A radio frequency radar measurement is one of several potential approaches to obtaining direct measurement data

(Herique et al. 2018) from the subsurface structures of asteroid. Due to the absence of liquid water, a low-frequency and low-power radio wave can penetrate a significant distance from several hundred meters to a few kilometers inside an asteroid regolith (Kofman 2012). Distinguishing surface and interior scattering is, however, a challenging task which necessitates advanced mathematical modeling of the electromagnetic field.

Here, our goal is to validate this distinguishability by measuring and simulating the full-field wave propagation and to show in situ radar investigations. We compare the numerical results to experimental microwave radar data measured for a 3D-printed analog object with an exterior surface shape that follows that of the asteroid 25143 Itokawa (Fujiwara et al. 2006) and an interior structure built based on current a priori knowledge of the asteroid interiors (Jutzi & Benz 2017; Carry 2012). Itokawa is a small rubble pile asteroid, an ordinary chondrite S-type assemblage, which is supposed to contain mainly pyroxene and olivine (Abell et al. 2006; Nakamura et al. 2011). Its exact shape was obtained when it rendezvoused with the Japanese space agency's (JAXA) Hayabusa mission in 2005 (Kawaguchi et al. 2008).

We performed analyses in both the frequency and time domain. In the former case, we used the dyadic Green's function recursively in order to model the full measured spectrum and calculate the field in the time domain using the inverse Fourier transform. In the latter case, a pulse with a limited bandwidth

[★] The measurement data obtained for the asteroid analog models are freely available on this web page <https://www.fresnel.fr/3Ddirect/index.php> following a basic registration.

is propagated in the time domain using the finite element time-domain (FETD) method (Takala et al. 2018a; Sorsa et al. 2019). Our ultimate aim is to advance the development of both frequency- and time-domain full-wave tomography techniques for complex-structured targets, in particular, small bodies of the Solar System (Eyraud et al. 2018, 2019; Sorsa et al. 2020).

The results obtained show that the applied full-wave modeling approach is valid for a target with a realistic shape and a priori 3D structure and that the computational resources are sufficient. Together with our earlier numerical simulation results (Sorsa et al. 2019; Takala et al. 2018a), the present observations of the peak signal-to-noise ratio (peak S/N) between the measured and modeled signal suggest that the internal details of a target with a realistic shape and a priori 3D structure can be detected via radar observations. Also, higher order scattering wavefronts were observed to be predictable. Based on these results, the full-wave modeling approach seems necessary to distinguish the subsurface structures in a situation where the measurement point distribution is sparse, which is a likely scenario for a space mission.

This study is structured as follows: In Sect. 2, we describe our asteroid analog model and the experimental radar laboratory measurements. In Sect. 3, the frequency and time-domain full-waveform modeling approaches are described. Section 4 presents the results of the laboratory measurements and the comparisons. Finally, in Sect. 5, we discuss the results and in Sect. 6, we present our conclusions.

2. Asteroid wave interaction

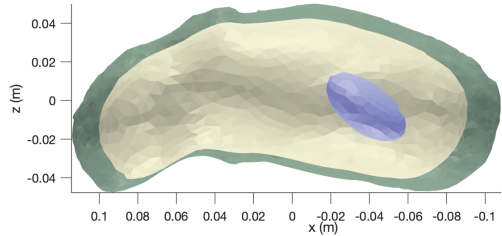
2.1. Asteroid analog model

In this study, we investigate the interior structure of two 3D-printed analog models (Fig. 1) with the largest dimension of 20.5 cm and the exterior surface shape of the 535 m diameter asteroid 25143 Itokawa (Hayabusa Project Science Data Archive 2007). These analogs are referred to as the homogeneous model (HM) and the detailed model (DM) based on their relative electric permittivity distribution, ϵ_r , which is constant in HM and has a detailed structure in DM. Following Sorsa et al. (2019, and in prep.), we know that the DM is composed of a mantle, an interior, and an ellipsoidal detail compartment. The compartment-wise constant permittivity was modeled on the basis of the a priori knowledge of typical asteroid minerals (Hérique et al. 2002, 2018) as well as on studies of asteroids' internal porosity distribution, in particular, the binary system and impact studies (Jutzi & Benz 2017; Carry 2012). The impact studies (Jutzi & Benz 2017) imply that the porosity is likely to increase towards the surface, due, for instance, to a granular mantle. The density versus volume estimates obtained for binary systems (Carry 2012) suggest that the interior structure can include inhomogeneities with a considerably higher porosity compared to its average value. The relative permittivity of HM and of the interior structure of the DM was thus assumed to be $\epsilon_r \approx 4$ at a few dozen of MHz, matching roughly with that of solid or fragmented rocky minerals, for example Kaolinite or Dunitite (Hérique et al. 2016). The mantle permittivity was approximated as $\epsilon_r \approx 3$, modeling a granular regolith with the same mineral decomposition, and the ellipsoidal detail was assumed to be a void with ($\epsilon_r = 1$).

A tetrahedral mesh consisting of 21 125 nodes and 109 433 tetrahedra was applied as a metamaterial structure. The inflated edges of the mesh were 3D-printed out of a prototyping



(a) The 3D printed DM analogue model.



(b) A cut-in view of DM along the y axis.

Fig. 1. *Top:* 3D printed detailed model (DM) analog of the relative electric permittivity ϵ_r . *Bottom:* both the analog and the numerical model include the surface layer (mantle), interior part, and the ellipsoidal deep interior void.

ABS plastic filament (PREPERM ABS450, Premix Oy) with a relative permittivity of $\epsilon_r \approx 4.5$ at 2.4 GHz¹. To obtain the sought a priori permittivity values for the interior and mantle compartments, the edge width was adjusted (Saleh et al. 2020) so that the mixture between the plastic and air would roughly match the volumetric filling levels predicted by the classical Maxwell Garnett (MG), exponential (EXP), and complex refractive index model (CRIM). Denoting by η the volume fraction of the plastic filament, the MG mixing formula is given by

$$\epsilon_r^{\text{MG}} = \frac{2\eta(\epsilon_r - 1) + \epsilon_r + 2}{2 + \epsilon_r - \eta(\epsilon_r - 1)}. \quad (1)$$

The exponential law (Birchak et al. 1974) takes the form:

$$\epsilon_{r,a}^{\text{EXP}} = (1 + (\epsilon_r^a - 1)\eta)^{1/a}, \quad (2)$$

where a is a case-specific exponential constant. As the exponential model reference, we use the value of $a = 0.4$, which has been recognized to be well-suited for mixtures of snow, air, and liquid water (Sihvola et al. 1985), where both the real and imaginary part of the permittivity vary. When $a = 1/2$, as, for example, in Birchak et al. (1974), the exponential model coincides with CRIM, that is,

$$\epsilon_r^{\text{CRIM}} = \epsilon_{r,1/2}^{\text{EXP}}. \quad (3)$$

Based on a priori estimates obtained from the mixing laws, the volume fraction of the filament was set to be 66 and 90% for the mantle and interior compartments, respectively. The median structural parameters of the 3D-printed mesh constituting the analog object are found in Table 1.

¹ <https://www.preperm.com/webshop/product/preperm-3d-abs-%c9%9br-4-5-filament/>

Table 1. Median structural parameters of the 3D-printed tetrahedral mesh constituting the analog object of this study.

Compartment	Volume fraction	edge width (mm)	edge length (mm)	Aperture (mm)
Mantle	0.66	1.8	4.4	1.4
Interior	0.90	2.4	4.4	0.9

Notes. The volume fraction has been evaluated with respect to a 35 mm diameter sphere.

2.2. Permittivity measurements

To obtain refined estimates for the permittivity in the different parts of each analog object, we investigated the bistatic far-field scattering patterns of three 3D-printed test spheres (Eyraud et al. 2015) with volume fraction levels of 66, 90, and 100%. These spheres were based on a 35 mm diameter tetrahedral mesh, whose effective diameter (due to the edge inflation) was found to be 35.5 mm with respect to the asteroid analog (Appendix A). Table 2 shows a priori and a posteriori estimates given by the mixing laws (Sect. 2.1) together with the measured values for the mantle and interior permittivity. The estimates given by the mixing laws are somewhat higher compared to the measured values, which might be partly due to the effect of the fragmented microstructures of the 3D-printed filament resulting from the printing process. The closest match is obtained with MG with a difference of 6% and <1% to the measured mantle and interior permittivity. In relating the measurements to the effective test sphere diameter 35.5 mm, the permittivity was observed to be 1.5% lower compared to the value obtained for the original 35 mm diameter. Since the effective diameter depending on the modeled detail grows along with the size, with the largest diameter being 35.5 mm, details larger than the test spheres up to the size of the asteroid analog can have 0–1.5% lower permittivity compared to the values in Table 2; the larger the size, the greater the difference (Sorsa et al., in prep.) (Appendix A).

2.3. Laboratory measurements of the wave interaction within the analog

2.3.1. Experimental procedure

The electromagnetic fields scattered by the asteroid analog model were measured using the anechoic chamber of the Centre Commun de Recherches en Microondes (CCRM) in Marseille, France (Fig. 2), which makes it possible to perform measurements at a realistic distance with respect to the diameter of the analog model. Many electromagnetic scattering problems (nm to m wavelengths) can be experimentally simulated with microwaves (cm wavelengths) on a scale of a few centimeters (Geffrin et al. 2012; Vaillon & Geffrin 2014; Barreda et al. 2017; Hettak et al. 2019). Microwave experiments allow us to make accurate measurements of the quantitative complex scattered fields in controlled conditions in order to extract relevant information about the target. Thanks to the centimeter-sized analog targets, such experimental simulations are possible, on the one hand for large objects (tens or hundreds of wavelengths) that involve complex scattering effects and, on the other hand, for nanoscale analog models, which are very difficult to handle, characterize, and control in their original size.

2.3.2. Experiment setup

The measurement distance in the laboratory was set to be 1.85 m, which scales to a 4.83 km distance (orbit), considering the actual size of 25143 Itokawa. To detect the mantle and void inside the analog object, backscattering data were recorded from a direction in which the void is closest to the surface in the horizontal plane intersecting the centre of mass (Fig. 2). The measurements were performed in the quasi-monostatic configuration described in Fig. 2. The source and the receiver were moved together over a given range with respect to both the polar angle ϕ and azimuth θ of the spherical coordinate system with the center of mass fixed to the origin (Zwillinger 2002), maintaining a constant 12° separation angle between the transmitter and receiver. In both directions, the angular range is 30° and the angular step is 3° , satisfying the Nyquist sampling criterion with respect to the information content of the scattered field (Bucci & Franceschetti 1987). Consequently, both transmitter and receiver positions form a regular 11×11 point grid distributed over the surface of the spherical measurement coordinate system. The polarization of the field is linear along the e_ϕ unit vector, with $\phi\phi$ (vertical) polarization (Fig. 2c).

The fields were measured with continuous waves between 2 and 18 GHz, with a 0.05 GHz frequency step and they were calibrated at each frequency so that the incident electric field at the origin has an amplitude of 1 S m^{-1} and a null phase. Consequently, the measurements at a given location correspond to a flat-spectrum point source, meaning that any time domain pulse shape can be synthesized based on the measurement data. In this study, we synthesize a Ricker window pulse with the center frequency of 6.00 GHz and two quadrature amplitude modulated Blackman-Harris (BH) window pulses with center frequencies of 10.1 and 12.9 GHz and bandwidths of 5.45 and 5.70 GHz, respectively. Altogether, these cover the investigated frequency range regarding the intensity range from -10 to 0 dB with respect to the pulse amplitude. The limit -10 dB has been chosen to ensure that the signal bandwidths are appropriately contained within the measured frequency range. Both the Ricker and BH windows are frequently used in the processing of the ground-penetrating radar measurements (Priska et al. 2019; Daniels & Institution of Electrical Engineers 2004).

The most significant factors limiting the accuracy of our experimental setup are the ≤ 1 mm positioning and ≤ 1 degree orientation error allowed by a specifically designed 3D-printed support plate (Fig. 2) and the >20 dB S/N of the radar measurement, which was obtained here by evaluating the difference between the measurement and analytically calculated field for a metallic reference sphere. In addition, the accuracy of the final experiment is affected by the modeling approaches utilized in analog preparation and numerical wavefield simulations.

2.3.3. Data

Figure 3 shows the 2D cuts of the radargrams obtained from the measurements considering the entire measurement domain described in Fig. 2 for the two analogs, DM and HM. The radargrams for the DM (top in the Fig. 3) and for the HM (bottom) are rather similar, but for the DM, the signal is denser than in the case of the HM, suggesting the presence of an internal structure. Based on this radargram, we deem that there are no significant hot spots in the data and thereby we choose to investigate the centermost measurement position (Fig. 2) as the primary point of interest.

Table 2. Modeled and measured relative permittivity in the DM and HM analog models.

Part	Estimate type	Analog	Percentage of material	Mixing model			Nominal	Measured
				CRIM	MG	EXP		
Filament	A priori	DM, HM	100				4.50 + j0.02	4.19 + j0.06
	A posteriori	DM, HM	100					
Interior	A priori	DM, HM	90	4.04 + j0.02	3.83 + j0.02	4.01 + j0.02		
	A posteriori	DM, HM	90	3.76 + j0.05	3.59 + j0.04	3.75 + j0.05		3.40 + j0.04
Mantle	A priori	DM	66	3.03 + j0.01	2.65 + j0.01	2.96 + j0.01		
	A posteriori	DM	66	2.86 + j0.03	2.55 + j0.02	2.80 + j0.03		2.56 + j0.02
Void	A priori	DM	0	1.00	1.00	1.00	1.00	

Notes. The a priori estimates refer to the nominal permittivity value of the ABS450 filament which has been measured by the manufacturer at 2.4 GHz frequency. The a posteriori estimates have been obtained by performing bistatic far-field scattering measurements (Eyraud et al. 2015) with the 3D-printed spheres as targets and, in the case of the mixing models, referring to the permittivity of the 100% filled sphere. The best match between a priori and a posteriori values is obtained with the MG mixing model.

Table 3. Scattering zones and time points corresponding to the analog objects' volumetric compartments and their boundaries illustrated in Fig. 4.

Zone	Range (ns)	Point ID	Time (ns)	Boundary
Mantle I	11.50–12.12	(1)	11.86	Air–Mantle
		(2)	12.05	Mantle–Interior
Void	12.12–12.71	(3)	12.22	Interior–Void
		(4)	12.48	Void–Interior
Mantle II	12.71–13.50	(5)	12.87	Interior–Mantle
		(6) ^{DM}	13.06	Mantle–Air
		(6) ^{HM}	13.33	Mantle–Air
(2nd reflection)	14.00–15.07	(7) ^{DM}	14.27	Mantle–Air
		(7) ^{HM}	14.80	Mantle–Air

Notes. Reflections (1) to (7) concern the DM; the HM is only relevant to reflections (1), (6), and (7). The times indicated are two-way travel-times.

In order to enable a comparison between the measured and the simulated signal, we divided the temporal domain into mantle I (reflections due to air–mantle and mantle–interior interfaces), void (reflections due to interior–void and void–interior interfaces), mantle II (reflections due to interior–mantle and mantle–air interfaces), and a higher order scattering zone (Fig. 4). These zones, summarized in Table 3, were determined on the basis of a plane wave propagation, as predicted by geometrical optics and considering the different paths involving a single or dual reflection. They contain the effects originating from the subdomains depicted in Fig. 4. The higher order scattering zone involves mainly multipath and multiple scattering effects. As the specific time points of interest, we consider the two-way travel-times for the scattering boundaries (1)–(7) described in Table 3. The widths of the zones determined are based on these arrival times, taking into account the duration of the pulse.

3. Modeling of the wave interaction within the asteroid

To obtain the electromagnetic field scattered by an asteroid analog, we model the electromagnetic interaction with two in-house modeling packages based on (A) frequency and (B) time domain calculations. These numerical simulations are compared with the laboratory measurements in an ideally controlled environment.

3.1. Frequency domain

The interaction between the wave and the asteroid can be modeled in a harmonic domain using the integral formulation of the Maxwell equations. The electric field scattered by an inhomogeneous structure, contained in the spatial domain Ω , is written in the integral form. The scattered field, E^s , on the receiver positions, \mathbf{r} , included in the domain, Γ , is thus obtained with the observation equation:

$$E^s(\mathbf{r}; f) = \int_{\Omega} \mathbf{G}(\mathbf{r}, \mathbf{r}'; f) \chi(\mathbf{r}'; f) \mathbf{E}(\mathbf{r}'; f) d\mathbf{r}'. \quad (4)$$

Here, \mathbf{E} represents the electric field and \mathbf{G} the free space dyadic Green's function between a point \mathbf{r}' in the Ω domain and a point \mathbf{r} in the Γ domain, $\chi(\mathbf{r}'; f) = k^2(\mathbf{r}'; f) - k_0^2$ is the contrast term where $k(\mathbf{r}'; f)$ is the wavenumber at the point \mathbf{r}' from Ω and k_0 the wave number in the vacuum. The field \mathbf{E} satisfies the following coupling equation:

$$\mathbf{E}(\mathbf{r}'; f) = \mathbf{E}_i(\mathbf{r}'; f) + \int_{\Omega} \mathbf{G}(\mathbf{r}', \mathbf{r}''; f) \chi(\mathbf{r}'') \mathbf{E}(\mathbf{r}''; f) d\mathbf{r}'', \quad (5)$$

where $\mathbf{E}_i(\mathbf{r}'; f)$ is the incident field at point \mathbf{r}' in Ω domain and $\mathbf{G}(\mathbf{r}', \mathbf{r}''; f)$ the Green's dyade of the free space between the points \mathbf{r}' and \mathbf{r}'' of the Ω area.

Equation (5) is solved numerically using the method of moments (Harrington 1987) and a biconjugated gradient stabilized method (van der Vorst 2003); for more details, see Merchiers et al. (2010). The Toeplitz structure of the dyadic Green function is exploited in this resolution (Barrowes et al. 2001). This improves the computation speed and reduces memory requirements, which is particularly necessary for large objects in relation to the wavelength. Once the scattered field is calculated in the frequency domain, the field in the time domain is obtained in response to a Ricker pulse $p(t)$ using an inverse Fourier transform \mathcal{F}^{-1} as follows:

$$p(t) = [1 - 2\pi^2 f_c^2 t^2] \exp(-\pi^2 f_c^2 t^2), \quad (6)$$

$$\mathcal{F}^{-1}[p](f) = C \frac{2}{\sqrt{\pi}} \frac{f^2}{f_c^3} \exp\left(-\frac{f^2}{f_c^2}\right). \quad (7)$$

Here, f_c is the center frequency of the pulse and $C = \pi^{3/2} f_c \exp(1)$ is the factor set to normalize the maximum of the Fourier transform of the Ricker pulse to one. In this study, the zero-time reference is taken when the wave is at the source position for all the time domain results.

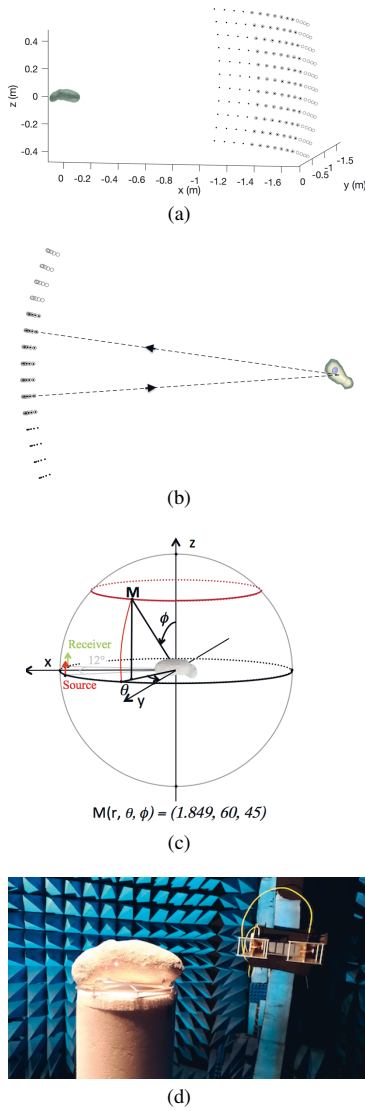


Fig. 2. Measurement configuration. (a) Complete measurement configuration depicting the transmitter points with solid, black points and the receiver positions in gray circles. (b) Signal path for the centermost transmitter-receiver pair showing a cut-in view through the target. The view is along the z -axis. The source is at the position $\phi_s = 90^\circ$, $\theta_s = 174^\circ$ and the receiver at $\phi_r = 90^\circ$, $\theta_r = 186^\circ$. (c) Experimental configuration with the angles definition. (d) Photograph of the analog object and the transmitter-receiver pair in the anechoic chamber of the CCRM in Marseille. The transmitter-receiver pair is seen in the background and the 3D-printed support plate applied for positioning is visible under the analog model.

3.2. Time domain

Given a complex-valued permittivity distribution $\epsilon_r = \epsilon_r' + j\epsilon_r''$, the wave can be modeled in the time domain by solving the wave equation for the total field, \mathbf{E} , numerically via the following

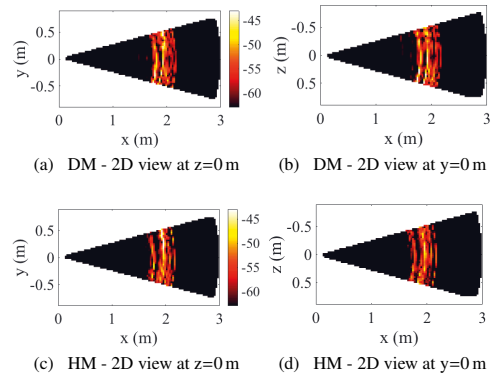


Fig. 3. 2D view of the 3D radargram obtained considering all the measurements in the configuration described in Fig. 2 for two analogs, DM and HM. The distance corresponds to the two-way travel after a time-distance conversion considering a propagation in vacuum. The entire frequency band (2–18 GHz) was used for this radargram. The magnitude of the scattered field is given in decibels.

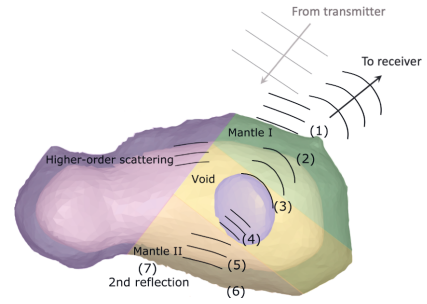


Fig. 4. Scattered signal in time domain, which can be identified to have originated from mantle I and II, a void, or higher order scattering zone based on the travel-time of the received signal. The transmitted plane wave is indicated with gray. The wavefronts (1)–(6) correspond to the values given in Table 3. The gray and black arrows indicate the directions of the transmitter and the receiver, respectively. The wavefront (7) corresponds to a round trip inside the analog, starting from reflection number (6). High-order scattering zone includes multi-path and multiple scattering contributions.

first-order system (Takala et al. 2018a; Sorsa et al. 2020):

$$\epsilon_r' \frac{\partial \mathbf{E}}{\partial t} + \sigma \mathbf{E} - \sum_{i=1}^3 \frac{\partial \mathbf{F}^{(i)}}{\partial x} + \nabla \text{Tr} [\mathbf{F}^{(1)} \mathbf{F}^{(2)} \mathbf{F}^{(3)}] = -\mathbf{J},$$

$$\frac{\partial \mathbf{F}^{(i)}}{\partial t} - \frac{\partial \mathbf{E}}{\partial x_i} = 0, \quad (8)$$

for $i = 1, 2, 3$ in the spatio-temporal set $[0, T] \times \Omega \cup \Gamma$ with Tr denoting the trace operator which evaluates the sum of the diagonal entries of its argument matrix and

$$\mathbf{F}^{(i)} = \int_0^t \frac{\partial \mathbf{E}}{\partial x_i}(\tau, \mathbf{r}') d\tau, \quad \mathbf{F}^{(i)}|_{t=0} = \mathbf{0} \quad \text{and} \quad \mathbf{E}|_{t=0} = \mathbf{0}. \quad (9)$$

Denoting the signal frequency as f , the absorption parameter (conductivity) takes the form $\sigma = 2\pi f \epsilon_r''$. The coordinates are scaled by a spatial scaling factor of s (meters), setting the

velocity of the wave in vacuum to one. With this scaling, the time, t , position, $\mathbf{r} = (x_1, x_2, x_3)$, absorption σ , and frequency, f , in SI-units can be obtained as $(\mu_0 \epsilon_0)^{1/2} st$, $s\mathbf{x}$, $(\epsilon_0/\mu_0)^{1/2} s^{-1} \sigma$, and $(\mu_0 \epsilon_0)^{-1/2} s^{-1} f$, respectively, with $\epsilon_0 = 8.85 \times 10^{-12}$ F m $^{-1}$ denoting the electric permittivity of vacuum and $\mu_0 = 4\pi \times 10^{-7}$ H m $^{-1}$ denoting the magnetic permeability, which is assumed to be constant in Ω . The right-hand side of Eq. (8) denotes the antenna current density given by $\mathbf{J}(t, \mathbf{r}') = \delta_{\mathbf{p}}(\mathbf{r}') J(t) \mathbf{e}_{\Lambda}$, transmitted at the point, \mathbf{p} , in the far-field domain Γ . The time-dependence of the current is $J(t)$. Its position, \mathbf{p} , is determined by the Dirac's delta function, $\delta_{\mathbf{p}}(\mathbf{r})$, and orientation by the vector, \mathbf{e}_{Λ} . By finding the numerical solution, Green's function, \mathbf{G} , can be approximated by $[0, T] \times \Omega \cup \Gamma$.

The numerical solution of the system (Eq. (8)) within the near-field subdomain $[0, T] \times \Omega$ can be obtained through the finite element time-domain (FETD) method (Sorsa et al. 2020). The incident and scattered field can be simulated in the far-field subdomain $[0, T] \times \Gamma$ via surface integrals defined on the boundary of Ω (Takala et al. 2018a). An iterative time-domain solver following from the FETD discretization involves sparse matrices which necessitate effective parallel processing for their large size and the need to perform a high number of iteration steps. A state-of-the-art high-performance computing cluster equipped with high-end graphics processing units (GPUs) provides an efficient platform for running such an iteration (Takala et al. 2018a). In this study, the FETD computations were performed using the 32 GB RAM GPUs of the Puhti supercomputer² (CSC – IT Center for Science Ltd., Finland).

4. Comparison of the numerical simulations both in time and frequency domains versus laboratory measurements

4.1. Cube as a reference case

Since this is the first time that a complex-shaped and comparably large (w.r.t. wavelength) target is measured in this quasi-monostatic configuration, we first validate the present full-wave approach with a cube made of polyethylene. The side length of this cube is equal to 119 mm, corresponding to 1.2λ and 11λ with respect to the longest and shortest wavelength (inside the cube) within the investigated frequency band. The permittivity of the cube was found to be equal to $\epsilon_r = 2.35$, based on the bistatic far-field scattering patterns of a sphere made of the same material (Eyraud et al. 2015). The comparison between the laboratory measurements and numerical simulations in the frequency domain, presented in Fig. 5, and the corresponding time-domain results (after a Ricker window centered at 6.00 GHz applied to the fields and an inverse Fourier transform) in Fig. 5c validate the configuration for large objects.

4.2. Asteroid analog

The numerical simulations concerning the DM and HM analog models were performed using the measured a posteriori permittivity values (Table 2). Table 4 describes the signal properties applied in these simulations for multiple different scales.

4.2.1. Results with the full-wave solver in the frequency domain

The numerical simulations in the frequency domain were performed for the HM and DM analogs. Figure 6 shows a comparison

² <https://research.csc.fi/csc-s-servers>

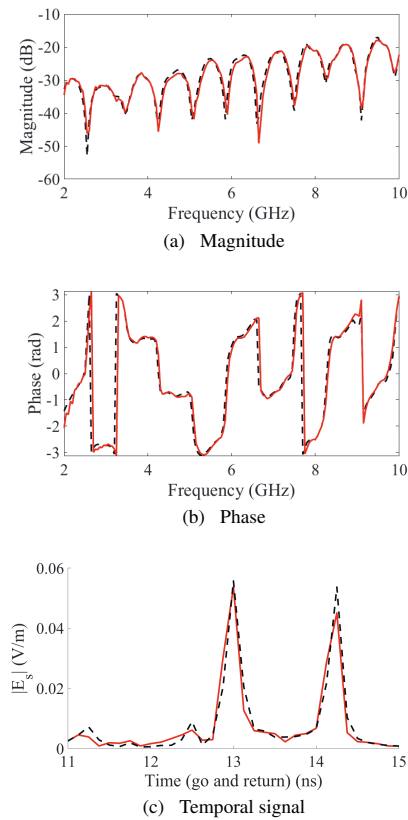


Fig. 5. Scattered field of the cube in the configuration described in Fig. 2 for $\phi\phi$ polarization and the central transmitter–receiver position. Measurement is in (–) and calculation in (–). In the case of (c), the signal in the time domain was obtained using the inverse Fourier transform (Eq. (7)) and a Ricker window centered at 6.00 GHz.

in the frequency domain between the measurement and the numerical simulations in the case of DM and the centermost point. The simulated field is very close to the experimental one below the frequency of 6.00 GHz. The differences that appear at around 6 GHz can be due to local inhomogeneities in the permittivity distribution or possible resonance effects related to the homogenization limit of the analog object. This point is detailed in the discussion (Sect. 5). Once the scattered field has been calculated in the frequency domain, it can be obtained in the time domain via the inverse Fourier transform (Eq. (7)). The scattered fields in the time domain, in response to a Ricker pulse with a center frequency of 6.00 GHz, are shown in Figs. 7a and b for DM and HM, respectively. Figure 7c presents the difference between the magnitude of the temporal field in these two cases. Figure 3 shows that disturbances due to echoes other than the analog echo are low as the signal has a significant value only in the time zone corresponding to the target's response.

In this response zone, the calculated and measured fields are close to each other for both the DM and HM. In order to analyze these in more detail, we used the temporal arrival times (Table 3) expected for a single reflection on each interface (1)–(6) and for a dual reflection on the back interface (7) (in relation to Fig. 4).

Table 4. Parameters used in simulating the electric field propagation through (A) the frequency domain approach (Sect. 3.1) and (B) the finite element time domain (FETD) approach (Sect. 3.2).

Scale	Diameter	Distance	Method	Range	Frequency domain		Time domain		
					Relative size	Pulse	Center frequency	Relative size	Bandwidth
Itokawa	535 m	4.83 km	(A)	0.766–6.90 MHz	2.53–22.8 λ	Ricker	2.30 MHz	7.6 λ	1.53 MHz
			(B)			BH	3.87 MHz	12.8 λ	2.09 MHz
			(B)			BH	4.92 MHz	16.3 λ	2.20 MHz
Analog object	20.5 cm	1.85 m	(A)	2.00–18.0 GHz		Ricker	6.00 GHz	7.6 λ	4.00 GHz
			(B)			BH	10.1 GHz	11.0 λ	5.45 GHz
			(B)			BH	12.9 GHz	14.8 λ	5.70 GHz
Center frequency 10 MHz	124 m	1.12 km	(A)	2.38–21.5 MHz		Ricker	10 MHz	7.6 λ	6.67 MHz
	207 m	1.87 km	(B)			BH	11.0 λ	5.40 MHz	
	264 m	2.38 km	(B)			BH	14.8 λ	4.42 MHz	
Center frequency 20 MHz	62 m	0.560 km	(A)	4.76–42.2 MHz		Ricker	20 MHz	7.6 λ	13.3 MHz
	104 m	0.935 km	(B)			BH	11.0 λ	10.8 MHz	
	132 m	1.19 km	(B)			BH	14.8 λ	8.84 MHz	

Notes. In the case of (A), the time domain data was obtained using the Ricker window and, in (B), the first time derivative of a quadrature amplitude modulated Blackman-Harris (BH) window. The dimensions are given in term of wavelengths, with λ , the wavelength in the medium having a permittivity of $\epsilon_r = 3.4 + j0.04$ (interior part).

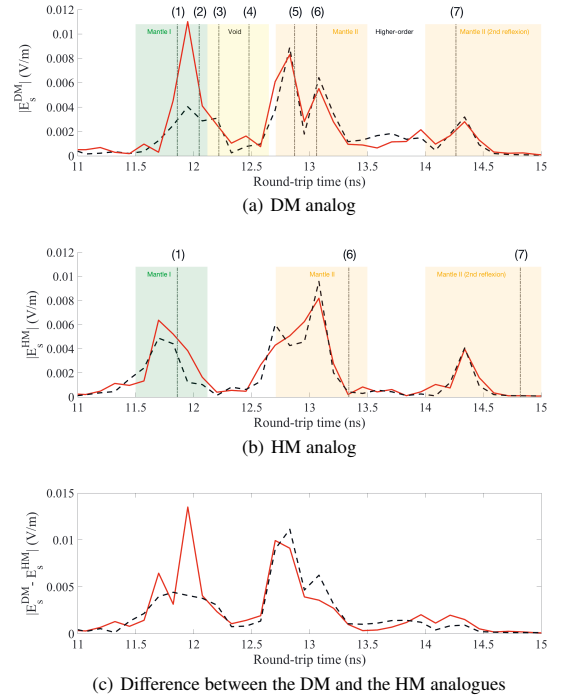
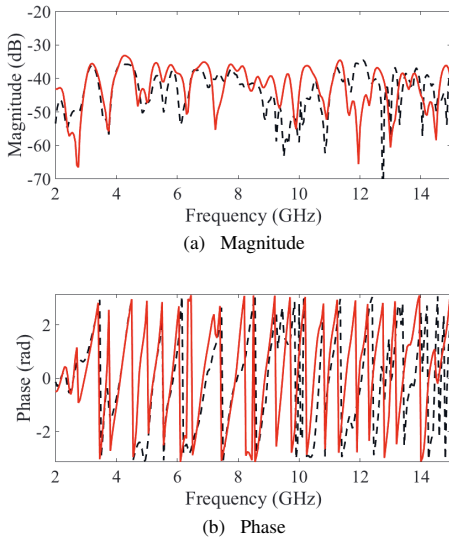


Fig. 6. Scattered field for the DM analogs in the configuration described in Fig. 2 for $\phi\phi$ polarization and the central transmitter–receiver position (Fig. 2). Measurement is in (–) and calculation in (– –). The phase shown is the phase of the field after compensating the propagation distance.

In Fig. 7, the first peak in both the measurement and the simulation correspond to the reflection between the air–mantle (1) and mantle–interior (2) interface. The ambiguity between these two responses is due to the pulse duration. The peaks corresponding to the reflections by the back of the asteroid, that is, by the interior–mantle (5) and mantle–air (6) interface, are separate and fully visible in the two curves. The distinguishability of the reflections from the void boundaries (3) and (4) is comparably weak. This somewhat counterintuitive finding suggests that the main part of the energy coming from the void does not directly propagate to the receiver. The final peak (7) corresponds to the second reflection due to the mantle–air interface,

Fig. 7. Scattered fields for the DM and the HM analogs in the configuration described in Fig. 2 for $\phi\phi$ polarization and the central transmitter–receiver position (Fig. 2). Measurement is in (–) and calculation in (– –). A Ricker window centered at 6.00 GHz is used. The vertical lines (1)–(6) shown in (a) and (b) correspond to the time points of interest, whose spatial correspondence is shown in Fig. 4 and Table 3.

that is, a doubled two-way path inside the analog; the time interval between (1) and (7) is roughly double the one between (1) and (6) for each analog and for both the measurement and simulation. In the case of the DM (Fig. 7a), the measured and the simulated

fields are relatively intense in the higher order scattering zone compared to the case of HM, where the fields are almost zero in this zone proving that the effects of multipath scattering are likely to be significant with the presence of internal heterogeneity(ies) (Fig. 7b). This is obvious when looking at the magnitude of the difference between the fields obtained in these two cases (Fig. 7c). This is expected as the target has a high contrast and has a relatively large diameter corresponding to the wavelength, suggesting that the wave interaction within this kind of target necessitates a full-wave approach akin to the one used here, which takes into account all the multiple interactions.

4.2.2. Results with the full-wave solver in time domain

Figures 8 and 9 illustrate the measurement and simulation results for the two center frequencies 10.1 and 12.9 GHz of the Blackman-Harris pulse (Table 4). The results are shown for the following three cases: (i) HM data; (ii) DM data; and (iii) the difference between DM and HM data. The approximate of the maximum observed measurement error given by the reference measurement (Sect. 2.3.2) is indicated as a shadowed region around the measurement data, reflecting the credibility of the measurement. As previously, the vertical lines (1)–(7) in the figures indicate the a priori estimated travel-times of the wavefronts scattering from the external and internal boundaries. The measured signal (solid red line) exhibits distinct peaks which localize at the areas where scattering is expected. This effect is clearly visible with the 12.9 GHz center frequency data (the right panel in the Fig. 8), while being somewhat less prominent in the case of the lower center frequency 10.1 GHz (the left panel). Of the two center frequencies, the superior distinguishability of the interior details is obtained with 12.9 GHz which yields clear electrical field amplitude peaks observed in the scattering interfaces in both the measured and the simulated data. For the DM data (the right middle panel), these peaks are localized appropriately in the air-mantle and interior-void-interior interfaces, as expected based on the estimated travel-times (the right panel in the Fig. 8), suggesting that the detail structure inside the asteroid has been detected. The difference curves (the right bottom panel) indicate that the simulated and measured amplitude peaks coincide approximately providing evidence on the detail detection via both the experimental and computational methods.

The comparison between the simulated and measured HM data shows that there are no interior details in HM as the curve lacks most of the peaks observed in the case of the DM. The deviations between the measurement and simulated data can be observed to increase along with the time, which is highlighted in the higher order scattering (strongly non-linear) zone, where the best match corresponds to the DM and 12.9 GHz center frequency.

Figure 9 presents a moving peak S/N between the measurement and FETD simulation for the DM, HM, and DM–HM difference signals. This peak S/N includes the effect of both the measurement and modeling accuracy of which the former is determined by the radar instrument performance ($S/N > 20$ dB), positioning and orientation errors (≤ 1 mm and ≤ 1 degree, respectively), and the latter one by the accuracy of the numerical FETD simulation and of the modeled permittivity, which can involve deviations of $\leq 1.5\%$ due to the variation of the edge inflation effect for different surface curvatures (see Appendix A).

Of the two center frequencies, the superior peak S/N is obtained in the case of 12.9 GHz, where the peak S/N for the DM is maintained at or above 10 dB on an interval 11.95–13.4 ns, starting from the mantle I zone, covering the void zone, and

the major part of the mantle II zone. Additionally, this level is reached and surpassed in the beginning of the higher order scattering zone. The corresponding peak S/N for the HM is above this level in the mantle II zone, which is obviously due to the backscattering from the exterior surface opposed to the antenna position, but lower in the mantle I and void zones, which can be understood as the mantle and void structure being absent in the HM and, thus, the scattering signal has a lower amplitude over those zones. The peak S/N of the DM–HM difference corresponding to a 12.9 GHz center frequency is above 0 dB otherwise except in the higher order scattering zone. That is, the simulated difference peaks correspond roughly to the measured ones. Because of a lower amplitude, the peak S/N of the difference is lower overall than for either of the DM and HM signals alone.

5. Discussion

This study concerns two asteroid analog models, a homogeneous model (HM) and a detailed model (DM), with the surface shape of the asteroid 25143 Itokawa. DM and HM were investigated through experimental radar measurements and numerical modeling. The permittivity of the interior and mantle were evaluated via an electromagnetic measurement of spherical sample objects. The results we obtained are in a good agreement with the estimates given by the classical mixing models, in particular, the Maxwell Garnett formula. The frequency modeling results show that there is an appropriate match between the measured and simulated fields electric fields in the frequency domain, in both amplitude and phase, up to a frequency of 6.00 GHz (Fig. 6). Above that, the differences observed between the measured and simulated fields may be due to the local inhomogeneities of the 3D-printed mesh and to the resonances related to the metamaterial structure. Based on a visual inspection of the analog object during the 3D printing process, the tetrahedral mesh structure might deviate slightly in vicinity of the compartment boundaries, which might be reflected in the laboratory measurements. At a 6 GHz frequency, the wavelength in the metamaterial and air (2.7 and 5.0 cm, respectively) correspond to about ten times the average edge width and edge length in the interior compartment of the 3D-printed mesh (2.4 and 4.4 mm, respectively), which might be a potential cause of a resonance. These effects are, nevertheless, not very significant in the analysis of time signals, which confirms that the permittivity values measured for the test spheres match with the direct-path travel-times of the wave within the analog. Namely, by setting the permittivity to the measured value, the measured two-way travel-time of the wave, that is, the arrival time of the signal peaks, can be observed to match with the outcome of the numerical simulation. Similarly, when comparing the simulated and measured signals, the observed total attenuation rate, that is, the total effect of absorption and multiple scattering, matches roughly with the expectation given by the permittivity measurement. Moreover, the loss tangent (ϵ''/ϵ') of the 3D-printed structures is about 0.01 which, based on the present knowledge of asteroid materials and minerals, is close to the expected range for a real asteroid corresponding to around 10–20 dB km⁻¹ attenuation at 10 MHz center frequency (Kofman 2012).

The simulated fields are appropriately matched by the laboratory measurements, verifying that it is possible to distinguish the structural details as separate reflections dominated by the ones from the surface facing and opposing the radar antennae. With respect to frequency-domain modeling (6 GHz center

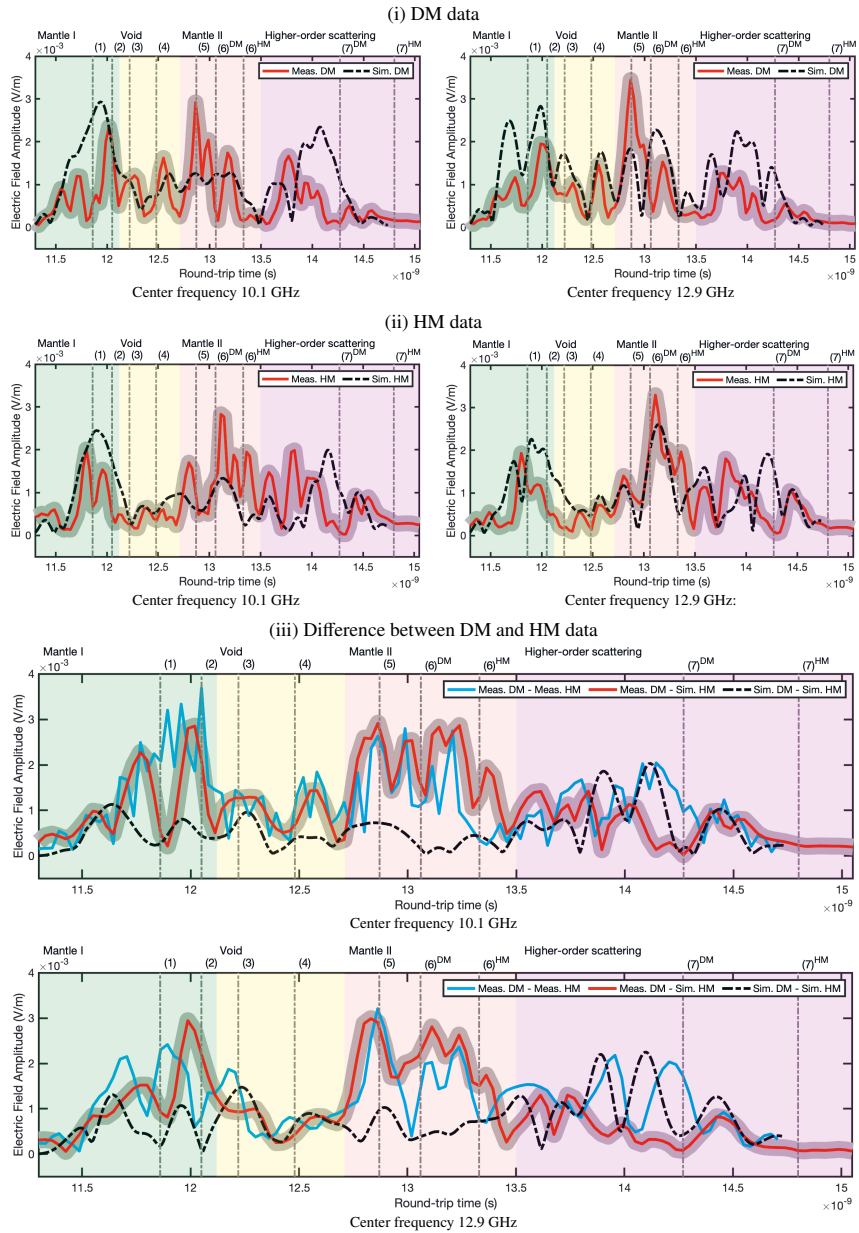


Fig. 8. Comparison of the between the measurements and finite element time-domain (FETD) simulation data for the center frequency of 10.1 and 12.9 GHz and $\phi\phi$ polarization at the central transmitter–receiver position. The solid red and dashed black curve depict the measured and simulated signals, respectively. The shadowed region around the measured signal (red) shows the approximate of the maximum observed error in the reference measurement (Sect. 2.3.2) indicating the credibility of the measurement. The results for the (i) HM and (ii) DM analogs are shown in the *top and middle panels*, respectively. *Bottom panel:* (iii) difference between the DM and HM data (Sim. = Simulated, Meas. = Measured). The vertical lines (1)–(7) depict the a priori estimated travel-times (Table 3) of the wavefronts scattering from the surface, mantle, and void matching roughly with the peaks of the measured field and the simulated DM data. These peaks are emphasized in the difference data. Of the center frequencies 10.1 and 12.9 GHz, the latter one yields a superior match between the measured and simulated data.

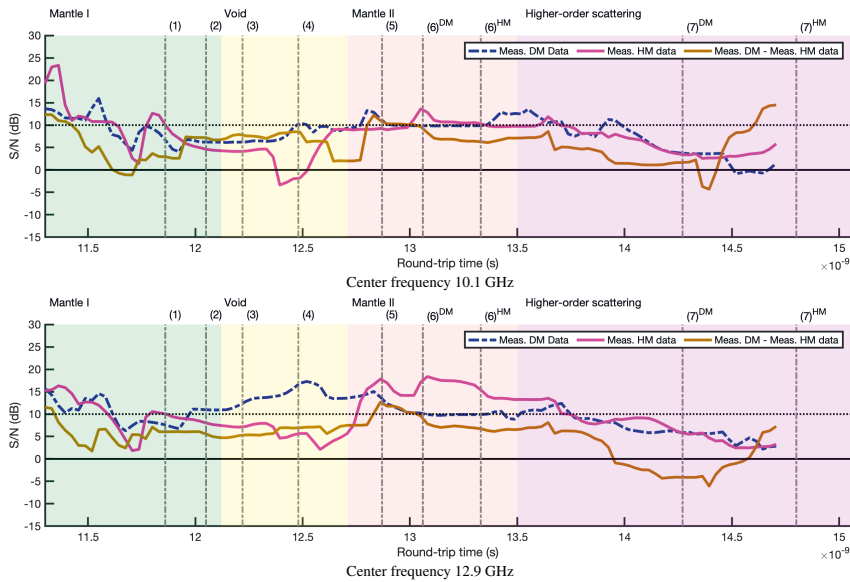


Fig. 9. Moving peak S/N between the measurement and FETD simulation for the DM (dashed blue), HM (solid purple), and DM–HM difference (solid brown) signal. Here, the mean power of the simulated signal is normalized to that of the measured one and the length of the moving window is 0.5 ns. Of the center frequencies, 10.1 and 12.9 GHz, the superior overall level is obtained in the latter case, where the peak S/N for DM is maintained over 10 dB (horizontal dashed line) on the interval 11.95–13.4 ns starting in the Mantle I zone, continuing through the void zone almost to the end of the mantle II zone.

frequency), the time domain results match very well with the laboratory measurements even in the high-order scattering zone. We find a clear difference between the DM and HM analogs in both numerical simulations and laboratory measurements in this high-order scattering zone and also in the mantle I and mantle II zones. With regard to the modeling in the time domain and with a higher center frequency (10.1 and 12.9 GHz), this difference also appears in the void zone, where direct scattering by the void is observed in the case of the DM. It is obvious that the temporal resolution increases with the bandwidth but also that the scattered field depends on the parameters of the applied signal. We regard this as an expected result because of the complexity and non-linearity of the scattering phenomena. For the complexity of the current wave propagation problem, the present frequency and time domain approach constitute two alternative strategies to simulating the signal. We leave a more profound comparison of these methods to a future work.

Full-wave approaches complement other methods developed to calculate the interaction of waves with a target of this size and which are based on optical physics, such as the ray-tracing technique (Ciarletti et al. 2015) and solvers based on physical optics (Berquin et al. 2015). The latter methods do not require the solution of the rigorous diffraction problem and are generally less expensive in terms of computational requirements but, on the other hand, they do not allow for a full reconstruction of the signal. The present strategy for modeling the full wavefield is all the more important since the higher order scattering effects, that is, multi-path and multiple scattering effects are likely to be significant (see for example Fig. 7). In addition, depending on the target geometry and pulse duration, the scattered wavefronts are likely to overlap and involve indirect propagation effects, implying that the full-wave approaches, which take these effects into

account appropriately, are fully justified and may even be necessary in order to optimize the outcome of the structural analysis, in particular, as the interior details were observed to affect the higher order scattering wavefronts in this study.

In our earlier studies which focused on simulated measurements (Sorsa et al. 2019; Takala et al. 2018a), a peak S/N of around 10 dB has been found sufficient for finding a reconstruction of the interior structures. The peak S/N analysis of the present experimental study shows that in the case of the DM analog with internal details, this accuracy can be reached and even surpassed in mantle I, void and mantle II zone which correspond to the direct scattering originating from the mantle and void compartment. Together these results suggest that the structural details inside the DM analog object, that is, the surface layer and void, can be distinguished based on the experimental measurement data. Achieving a comparable accuracy with in situ measurements might be possible when assuming that the positioning accuracy is similar, that is, with a ≤ 1 degree angle error (for the potential effect of the orientation inaccuracy, see Takala et al. 2018b) and ≤ 1 mm position error in the analog scale (≤ 2.6 m scaled to the actual size of 25143 Itokawa). Namely, comparing the S/N of the laboratory measurement (Sect. 2.3.2) to the peak S/Ns observed, it is obvious that the measurement noise is low compared to the errors related to the experimental setup and modeling. Furthermore, our earlier estimates for 1 AU distance from the Sun suggest that the possible measurement errors due to the Galactic noise and the radiation by the Sun will remain at a sufficiently low level with respect to observing the interior structures (Takala et al. 2018a; Sorsa et al. 2019). In particular, their effect can be shrunk via repetitive measurements. Regarding the literature about the signal quality and noise, our present assumptions match also with the general knowledge of

the ground-penetrating radar (Daniels & Institution of Electrical Engineers 2004), and by the successful CONSERT measurement (Kofman et al. 2015).

Since the required density of the spatial discretization and, thereby, the computational cost of the simulation increases along with the signal frequency, the applicability of actual target sizes and signal frequencies might still be a computational challenge regarding real in-situ planetary radar measurements. With the current model parameters and asteroid model, we are able to simulate the wave propagation at least up to a target diameter of 264 m at 10 MHz center frequency a bandwidth of 4.42 MHz, which might be sufficient for a real mission configuration (Binzel & Kofman 2005; Kofman 2012; Herique et al. 2018). Furthermore, based on our preliminary numerical experiments, the computing platforms utilized in this study, that is, the 32 GB RAM GPUs of the Puhti supercomputer and the 128 2 TB RAM symmetrical multiprocessing CPU cores of the Mesocentre AMU, will allow us to expand the target diameter to at least to 480 m or, alternatively, the center frequency to 20 MHz. Considering the potential mission relevance of these numbers, for example, the 163-m moon of the asteroid 65803 Didymos which is the target of the HERA mission falls into these limits (Michel et al. 2018). Also, larger asteroids can be considered, the maximum size being dependent on the computing platform's performance. Targets that do not fit into the memory available can be modeled by restricting the wave simulation process into a subdomain. If needed, such a restriction could be done based on the present principles to divide the scattering processes into lower and higher order scattering zones.

6. Conclusion

The results of this study, obtained in microwave-range laboratory experiments and computer simulations with an analog model based on the shape of the asteroid 25143 Itokawa as a target, suggest that full-wave modeling is a valid approach for investigating the interior structure of asteroids based on radar measurements in both the frequency and time domains. Comparing the present results to earlier numerical simulation studies suggests that a high enough peak S/N can be obtained for the direct scattering from the mantle and void structures, that is, in mantle I, void and mantle II zones. Our results underline that due to the complexity of the scattered wavefield, full-wave modeling might be essential for optimizing the outcome of in situ measurements which are potentially sparse in space missions. Namely, it distinguishes the overlapping direct and indirect wavefronts scattering from different parts of the target and, thereby, allows for the detection of otherwise weakly detectable internal details. For this capability, we are also able to predict multiple scattered and multi-path wavefronts (i.e., data corresponding to higher order scattering zone) which can potentially be utilized in the observation of the interior structures. As the present experiment setup and permittivity modeling approach are applicable with various measurement configurations, asteroid shapes, and interior structures, they can potentially be applied in the examination of subsequent asteroid models in the future.

Acknowledgement. The authors acknowledge the opportunity provided by the Centre Commun de Ressources en Microonde to use its fully equipped anechoic chamber and the Mesocentre of Aix-Marseille University for its support for these numerical simulations. L.-I.S., M.T. and S.P. were supported by the Centre of Excellence in Inverse Modelling and Imaging (Academy of Finland 2018-2025).

L.-I.S. was also supported by an Emil Aaltonen Foundation research grant for young researchers. L.-I.S. and S.P. acknowledge CSC – IT Center for Science Ltd., for providing computing services on the Puhti supercomputer. Premix Oy is acknowledged for providing support for the permittivity-controlled 3D printable filament materials.

References

- Abell, P., Vilas, F., Jarvis, K., Gaffey, M., & Kelley, M. 2006, *Lunar and Planetary Science XXXVII*
- Barreda, A., Saleh, H., Litman, A., Gonzalez, F., & Geffrin, J.-M. 2017, *Nat. Commun.*, 8, 13910
- Barrowes, B. E., Teixeira, L. F., & Kong, J. A. 2001, *Microw. Opt. Technol. Lett.*, 31, 28
- Berquin, Y., Herique, A., Kofman, W., & Heggy, E. 2015, *Radio Sci.*, 50, 1097
- Binzel, R. P., & Kofman, W. 2005, *CR Phys.*, 6, 321
- Birchak, J. R., Gardner, C. G., Hipp, J. E., & Victor, J. M. 1974, *Proc. IEEE*, 62, 93
- Bucci, O., & Franceschetti, G. 1987, *IEEE Trans. Antennas Propag.*, 35, 1445
- Carry, B. 2012, *Planet. Space Sci.*, 73, 98
- Cheng, A. F., Rivkin, A. S., Michel, P., et al. 2018, *Planet. Space Sci.*, 157, 104
- Ciarletti, V., Levasseur-Regourd, A. C., Lasue, J., et al. 2015, *A&A*, 583, A40
- Daniels, D., & Institution of Electrical Engineers. 2004, *Ground Penetrating Radar, Ground Penetrating Radar No. nid. 1* (Institution of Engineering and Technology)
- Desch, S. 2007, *ApJ*, 671, 878
- Eyraud, C., Geffrin, J.-M., Litman, A., & Tortel, H. 2015, *IEEE Antennas Wirel. Propag. Lett.*, 14, 309
- Eyraud, C., Herique, A., Geffrin, J.-M., & Kofman, W. 2018, *Adv. Space Res.*, 62, 1977
- Eyraud, C., Saleh, H., & Geffrin, J.-M. 2019, *J. Opt. Soc. Am. A*, 36, 234
- Fujiwara, A., Kawaguchi, J., Yeomans, D., et al. 2006, *Science*, 312, 1330
- Geffrin, J., Garcia-Camara, B., Gomez-Medina, R., et al. 2012, *Nat. Commun.*, 3, 171
- Gomes, R., Levison, H. F., Tsiganis, K., & Morbidelli, A. 2005, *Nature*, 435, 466
- Harrington, R. 1987, *J. Electromagn. Waves Appl.*, 3, 1
- Hayabusa Project Science Data Archive. 2007, *Itokawa shape model*, <https://darts.isas.jaxa.jp/planet/project/hayabusa/shape.pl>, accessed 4 November, 2019
- Herique, A., Gilchrist, J., Kofman, W., & Klinger, J. 2002, *Planet. Space Sci.*, 50, 857
- Hérique, A., Kofman, W., Beck, P., et al. 2016, *MNRAS*, 462
- Hérique, A., Agnès, B., Asphaug, E., et al. 2018, *Adv. Space Res.*, 62, 2141
- Hérique, A., Plettemeier, D., Lange, C., et al. 2019, *Acta Astron.*, 156, 317
- Hettak, L., Saleh, H., Dahon, C., et al. 2019, *IEEE Geosci. Remote Sens. Lett.*, 17, 933
- Jutzi, M., & Benz, W. 2017, *A&A*, 597, A62
- Kawaguchi, J., Fujiwara, A., & Uesugi, T. 2008, *Acta Astron.*, 62, 639
- Kofman, W. 2012, in *2012 19th IEEE International Conference on Microwaves, Radar & Wireless Communications*, 2, 409
- Kofman, W., Herique, A., Goutail, J.-P., et al. 2007, *Space Sci. Rev.*, 128, 413
- Kofman, W., Herique, A., Barbin, Y., et al. 2015, *Science*, 349, aab0639
- Merchiers, O., Eyraud, C., Geffrin, J.-M., et al. 2010, *Opt. Express*, 18, 2056
- Michel, P., Kueppers, M., Sierks, H., et al. 2018, *Ad. Space Res.*, 62, 2261
- Morbidelli, A., Levison, H. F., Tsiganis, K., & Gomes, R. 2005, *Nature*, 435, 462
- Nakamura, T., Noguchi, T., Tanaka, M., et al. 2011, *Science*, 333, 1121
- Priska, A., Parnadi, W. W., & Parnadi, R. G. 2016 2019 in, *IOP Conf. Ser. Earth Environ. Sci.*, 318, 012028
- Saleh, H., Tortel, H., Leroux, C., et al. 2020, *IEEE Trans. Antennas Propag.*, in press
- Sihvola, A., Nyfors, E., & Tiuri, M. 1985, *J. Glaciol.*, 31, 163
- Sorsa, L.-I., Takala, M., Bambach, P., et al. 2019, *ApJ*, 872, 44
- Sorsa, L.-I., Takala, M., Eyraud, C., & Pursiainen, S. 2020, *IEEE Trans. Comput. Imag.*, 6, 579
- Takala, M., Bambach, P., Deller, J., et al. 2018a, *IEEE Trans. Aerospace Electron. Syst.*, 55, 1683
- Takala, M., Us, D., & Pursiainen, S. 2018b, *IEEE Trans. Comput. Imag.*, 4, 228
- Tsiganis, K., Gomes, R., Morbidelli, A., & Levison, H. F. 2005, *Nature*, 435, 459
- Vaillon, R., & Geffrin, J.-M. 2014, *J. Quant. Spectr. Rad. Transf.*, 146, 100
- van der Vorst, H. A. 2003, *Iterative Krylov Methods for Large Linear Systems* (Cambridge University Press)
- Zwillinger, D. 2002, *CRC Standard Mathematical Tables and Formulae*, Chapman and Hall/CRC: 31st revised edition

Appendix A: Effect of edge inflation

The volumetric filling and permittivity of the analog objects is controlled by inflating the edges of the tetrahedral mesh. This edge inflation process slightly affects the details of the modeled geometry. Given a meshed detail with a closed surface, this effect can be measured through the ratio ν of the total material M_{total} forming the detail and the proportion enclosed by it M_{enclosed} . This ratio depends on the mesh properties, but is independent of the inflated edge width, which can be observed based on the following definition:

$$\nu = \frac{M_{\text{total}}}{M_{\text{enclosed}}} = \frac{S_{\text{volume}}}{S_{\text{volume}} - S_{\text{surface}}/2}. \quad (\text{A.1})$$

Here, $S_{\text{volume}} = \sum_{i \in I_{\text{volume}}} \ell_i$ and $S_{\text{surface}} = \sum_{i \in I_{\text{surface}}} \ell_i$ denote the total sum of the edge length, or equivalently that of the inflated edge volume evaluated over the volume of the detail I_{volume} , including the surface, and over its surface I_{surface} , respectively. As the inflated surface edges are symmetrically distributed on both sides of the surface, $S_{\text{surface}}/2$ gives the proportion outside the surface. Assuming that the radius of curvature for the detail is r in the original mesh, it will have the radius $r' = \nu^{1/3} r$ in the inflated one inflation with 1/3 following from the conversion

between volumetric and one-dimensional scaling. If ν_1 and ν_2 correspond to some details (1) and (2) with non-inflated and inflated radii of curvature r_1 , r_2 and r'_1 , r'_2 , respectively, then the imaginary effective radius $r_1^{(\text{eff})}$ for which level of inflation with respect to r'_1 is that of r_2 with respect to r'_2 detail (2) is defined by:

$$r_1^{(\text{eff})} = \left(\frac{\nu_1}{\nu_2} \right)^{1/3} r_1 \quad \text{that is,} \quad r'_1 = \nu_2^{1/3} r_1^{(\text{eff})}. \quad (\text{A.2})$$

Here, detail (1) can be interpreted as a test sphere which we utilize to measure the reference permittivity value of a permittivity layer and (2) as a detail within the asteroid analog model, whose permittivity is to be modeled. Since the tetrahedron size is kept constant, ν decreases as the volume of the detail grows. Namely, the total number of tetrahedra grows compared to the number on the surface. Therefore, the larger the detail (2) compared to the test sphere (1) the greater the effective radius $r_1^{(\text{eff})}$. This means that larger details, that is, those parts of the asteroid analog model with a relatively low surface curvature, will correspond to a slightly larger size, less dense structure, and a lower permittivity value compared to the actual sphere.

PUBLICATION

VI

Analysis of full microwave propagation and backpropagation for a complex asteroid analogue via single-point quasi-monostatic data

L.-I. Sorsa, S. Pursiainen and C. Eyraud

Astronomy & Astrophysics 645.(2021), A73

DOI: 10.1051/0004-6361/202039380

Publication reprinted with the permission of the copyright holders

Analysis of full microwave propagation and backpropagation for a complex asteroid analogue via single-point quasi-monostatic data

Liisa-Ida Sorsa^{*1}, Sampsa Pursiainen^{*1}, and Christelle Eyraud^{*2}

¹ Computing Sciences, Tampere University (TAU), P.O. Box 692, 33101, Tampere, Finland

² Aix Marseille Univ, CNRS, Centrale Marseille, Institut Fresnel, Marseille, France

November 30, 2020

ABSTRACT

Context. Information carried by the full wave field is particularly important in applications involving wave propagation, backpropagation, and a sparse distribution of measurement points, such as in tomographic imaging of a small Solar System body.

Aims. With this study, our aim is to support the future mission and experiment design, such as for example ESA's HERA, by providing a complete mathematical and computational framework for the analysis of structural full-wave radar data obtained for an asteroid analogue model. We analyse the direct propagation and backpropagation of microwaves within a 3D printed analogue in order to distinguish its internal relative permittivity structure.

Methods. We simulate the full-wave interaction between an electromagnetic field and a three-dimensional scattering target with an arbitrary shape and structure. We apply the Born approximation and its backprojection (the adjoint operation) to evaluate and backpropagate the wave interaction at a given point within the target body. As the data modality can have a significant effect on the distinguishability of the internal details, we examine the demodulated wave and the wave amplitude as two alternative data modalities and perform full-wave simulations in frequency and time domain.

Results. The results obtained for a single-point quasi-monostatic measurement configuration show the effect of the direct and higher-order scattering phenomena on both the demodulated and amplitude data. The internal mantle and void of the analogue were found to be detectable based on backpropagated radar fields from this single spatial point, both in the time domain and in the frequency domain approaches, with minor differences due to the applied signal modality.

Conclusions. Our present findings reveal that it is feasible to observe and reconstruct the internal structure of an asteroid via scarce experimental data, and open up new possibilities for the development of advanced space radar applications such as tomography.

Key words. Physical data and processes: Scattering– Astronomical instrumentation, methods and techniques: Techniques: image processing – Planetary systems: Minor planets, asteroids: general

1. Introduction

This article concerns the modelling of full-wave propagation and backpropagation with an asteroid analogue model as the target. The possibilities provided by these techniques continue to expand thanks to the rapidly increasing computing resources which enable modelling of the full wave propagation in an arbitrary domain and at high frequency. Information carried by the full wave field is particularly useful in applications based on sparse distribution of wave transmission and/or measurement points in order to maximise the information content of the eventual measurements. Here, our focus is on potential radar investigations of future space missions (Hérique et al. 2018; Takala et al. 2018; Sorsa et al. 2019; Hérique et al. 2019; Sorsa et al. 2020; Eyraud et al. 2020). Our objective is to provide a complete mathematical and computational framework for the analysis of structural full-wave radar measurements obtained for a structurally complex asteroid analogue model, thereby supporting the related future space mission and laboratory experimental design. In particular, we consider the 3D printed analogue of Eyraud et al. (2020) which is based on the optical high-resolution shape model of asteroid 25143 Itokawa (Fujiwara et al. 2006; Hayabusa Project Science Data Archive 2007). In Eyraud et al. (2020), we investigated this analogue using state-of-the-art laboratory experi-

ments, showing that full wave modelling, which can predict both the direct and higher order scattering effects caused by its complex shape and structure, is needed for this analogue. The analysis presented here constitutes an important feasibility study for the observation of the internal structure of this analogue using data obtained in laboratory-based experiments. Finding a back-propagated reconstruction based on radar data is an ill-posed and ill-conditioned inverse problem (M. Bertero & Boccacci 1998) meaning that slight errors in the measurement, the numerical model, or the choice of the data modality can have a significant effect on the result. For this reason, we compare several different approaches.

In planetary science (Picardi et al. 2005; Kofman et al. 2007; Grima et al. 2009; Kofman et al. 2015; Blair et al. 2017; Haruyama et al. 2017; Kaku et al. 2017), there is a need to detect radiowave scattering from different obstacles and interior structures to maximise the scientific outcome of a space mission. Important goals in this regard are, for example, to distinguish scattering from surface and subsurface obstacles and to determine their relative permittivity in order to infer the structure of the investigated domain. Planetary radar investigations have so far led to important scientific discoveries, such as for example in the exploration of the Moon and Mars in which the mapping of the Lunar lava tubes (Haruyama et al. 2017; Kaku et al. 2017; Blair et al. 2017) and the detection of the Martian water ice (Picardi

* The authors contributed equally

et al. 2005; Grima et al. 2009) are among the most significant recent findings.

In small-body research, the interior structure of the comet 67P/Churyumov-Gerasimenko was recently investigated by the CONSERT instrument (Kofman et al. 2007, 2015) during ESA’s Rosetta mission. Significant future plans to perform surface-penetrating radar measurements include, for example, the HERA mission which is the European component of the Asteroid Impact and Deflection Assessment (AIDA) mission, a joint effort between ESA and NASA. The primary target of HERA will be the asteroid moon of the binary system of 65803 Didymos. Such future radar investigations will be crucial, as current knowledge of small-body interiors still relies on indirect data, such as for example the outcome of impact simulations and density estimates obtained for binary systems (Vernazza et al. 2020). From the modelling perspective, the planned *in situ* investigations pose a special challenge because the complex shape and surface structure of a small Solar System body results in various interlaced scattering phenomena which require the application of advanced numerical methodology to achieve the scientific goals. The complexity of the modelling and inversion task is further emphasised by the large size of the target and therefore the large wave field as compared to the wavelength, the restricted bandwidth of the measurement, and the limited number of measurement points.

In this article, we perform a numerical analysis of the full wave interaction between an electromagnetic field transmitted by a microwave radar and a 3D-printed asteroid analogue in both the time and the frequency domain. We analyse the direct and higher-order scattering effects numerically by examining the effect of the signal frequency and bandwidth on the wave propagation, and the sensitivity of the radar to detect obstacles in different parts of the analogue model. We apply the Born approximation (BA) and its adjoint operation (backprojection) to evaluate and backpropagate the wave interaction at a given point within the target body. As the data modality can have a significant effect on the distinguishability of the internal details, we examine the demodulated wave and the wave amplitude as two different alternative, linearly independent, and complementary signal modalities.

The results obtained for a single-point quasi-monostatic measurement configuration show the effect of the direct and higher-order scattering phenomena on both the demodulated and amplitude data. The internal mantle and void of the analogue were found to be detectable based on backpropagated radar fields from this single spatial point, which is the minimum signal configuration in the case of a radar space mission, in both the time and the frequency domain approaches, with minor differences due to the applied signal modality. The methodology and findings presented here are crucial for observing and reconstructing the internal structure of an asteroid via experimental data, as suggested earlier in Eyraud et al. (2020), and open up new possibilities for the development of space radar applications, such as for example tomography, where the interior structure of the target is reconstructed using a large set of multi-directional measurements.

This article is structured as follows: In Section 2, we briefly review the frequency and time-domain-based approaches to model wave propagation within the analogue. In Section 3, we describe the methods for the analysis of the fields, including time–frequency domain analysis, and BA and its backprojection. In section 4, both the asteroid analogue and the radar configuration are detailed. The results are presented in Section 5 and discussed in Section 6, and our conclusions are presented in Section 7.

2. Wave propagation models

We apply two in-house software implementations to obtain the full wave (forward) interaction of an electromagnetic wave with an asteroid analogue. One of these implementations is based on the integral formulation of the Maxwell’s equations with the solution in the frequency domain, and the other one on a local formulation solved in the time domain. The mathematical methodology applied in these forward solvers is briefly described in this section.

2.1. Solution in the frequency domain

2.1.1. Formulation

The volume integral formulation allows us to compute the scattered electric field by an inhomogeneous structure included in the spatial domain Ω , i.e. a structure with a spatially variable relative permittivity ε_r . At each point \mathbf{r}' in Ω , the relative permittivity can be written as

$$\varepsilon_r(\mathbf{r}'; f) = \varepsilon_r'(\mathbf{r}'; f) + j \varepsilon_r''(\mathbf{r}'; f), \quad (1)$$

with $\varepsilon_r'(\mathbf{r}'; f)$ and $\varepsilon_r''(\mathbf{r}'; f)$ denoting, respectively, the real and the imaginary part of the relative electrical permittivity in Ω domain at the point \mathbf{r}' . The scattered field \mathbf{E}_s on the receiver position \mathbf{r} in the Γ domain is obtained via the observation equation

$$\mathbf{E}_s(\mathbf{r}; f) = \iiint_{\Omega} \mathbf{G}(\mathbf{r}, \mathbf{r}'; f) \chi(\mathbf{r}'; \mathbf{f}) \mathbf{E}(\mathbf{r}'; f) d\mathbf{r}', \quad (2)$$

with \mathbf{E} representing the total electric field, that is $\mathbf{E} = \mathbf{E}_i + \mathbf{E}_s$, which is the sum of the incident (illuminating) field \mathbf{E}_i and the scattered one \mathbf{E}_s , and \mathbf{G} representing the Green’s dyadic function between an \mathbf{r}' point in the Ω domain and an \mathbf{r} point in the Γ domain. Here, $\chi(\mathbf{r}'; f) = k^2(\mathbf{r}'; f) - k_o^2(f)$ is the contrast term with $k(\mathbf{r}')$ denoting the wave number at the point \mathbf{r}' from the Ω zone and k_o is the wave number in the vacuum.

The field \mathbf{E} satisfies the following coupling equation:

$$\mathbf{E}(\mathbf{r}'; f) = \mathbf{E}_i(\mathbf{r}'; f) + \iiint_{\Omega} \mathbf{G}(\mathbf{r}', \mathbf{r}''; f) \chi(\mathbf{r}''; \mathbf{f}) \mathbf{E}(\mathbf{r}''; f) d\mathbf{r}'', \quad (3)$$

which we evaluate numerically using the method of moments (Harrington 1987). The linear system is solved using a stabilised biconjugate gradient method (van der Vorst 2003); for more details see Merchiers et al. (2010). The properties of the dyadic Green’s function are exploited in this resolution as explained below.

2.1.2. Computational considerations

The dyadic Green’s function used in these equations corresponds to the free space. This function has a multilevel block-Toeplitz structure. The exploitation of this structure, which is explained in (Barrowes et al. 2001), allows one to store only non-redundant elements. This considerably reduces the memory requirement which is particularly necessary for the present application with objects that are very large compared to the wavelength. The use of this multi-level Toeplitz block structure also accelerates matrix-vector multiplications containing the matrix of Green’s dyadic function. It is based on one-dimensional (1D) FFT implementations directly as opposed to 2D and 3D FFTs.

2.2. Solution in the time domain

The wave can be modelled via the following locally defined first-order system of partial differential equations for the total field (Takala et al. 2018; Sorsa et al. 2020):

$$\varepsilon_r \frac{\partial \mathbf{E}}{\partial t} + \sigma \mathbf{E} - \sum_{i=1}^3 \frac{\partial \mathbf{F}^{(i)}}{\partial x_i} + \nabla \text{Tr}[\mathbf{F}^{(1)} \mathbf{F}^{(2)} \mathbf{F}^{(3)}] = -\mathbf{J},$$

$$\frac{\partial \mathbf{F}^{(i)}}{\partial t} - \frac{\partial \mathbf{E}}{\partial x_i} = 0, \quad (4)$$

where $i = 1, 2, 3$ in the spatio-temporal set $[0, T] \times \Omega \cup \Gamma$, where T denotes the length of the investigated time interval and Tr the trace operator which evaluates the sum of the diagonal entries for its argument matrix. The absorption parameter (conductivity) is of the form $\sigma = 2\pi f \varepsilon_r''$. The right-hand side of Equation (4) denotes the current density of the antenna given by $\mathbf{J}(t, \mathbf{r}') = \delta_{\mathbf{p}}(\mathbf{r}) J(t) \mathbf{e}_A$ and transmitted at $\mathbf{p} \in \Gamma$. The time-dependence of the current is $J(t)$, its position \mathbf{p} is determined by the Dirac's delta function $\delta_{\mathbf{p}}(\mathbf{r})$ and orientation is \mathbf{e}_A . The near-field numerical solution of the system (4) in $[0, T] \times \Omega$ is obtained here using the finite element time-domain (FETD) method (Sorsa et al. 2020). The incident and scattered far-field field in $[0, T] \times \Gamma$ follow from Kirchhoff's surface integrals defined on the boundary of Ω (Takala et al. 2018).

The coordinates are scaled by a spatial scaling factor s (metres). When $s = 1$ m, the velocity of the wave in vacuum is equal to one. Given s , the time t , position $\mathbf{r} = (x_1, x_2, x_3)$, absorption σ , and frequency f in SI-units can be obtained as $(\mu_0 \varepsilon_0)^{1/2} s t$, $s \mathbf{r}$, $(\varepsilon_0 / \mu_0)^{1/2} s^{-1} \sigma$, and $(\varepsilon_0)^{-1/2} s^{-1} f$ respectively, with the electric permittivity of vacuum being $\varepsilon_0 = 8.85 \cdot 10^{-12}$ F/m and the magnetic permeability which is assumed to be constant in Ω being $\mu_0 = 4\pi \cdot 10^{-7}$ H/m.

2.2.1. Quadratic amplitude modulation

In our FETD simulation, the signal propagated is assumed to be a quadrature amplitude modulated (QAM) Blackman-Harris (BH) window function. Quadrature amplitude modulation allows amplitude-preserving modulation and demodulation of the signal and is therefore suitable for the radar signal transmission and measurement. In QAM, a two-component signal $s_f = [s_{f,I}, s_{f,Q}]$ with an amplitude of $A_s = \sqrt{s_{f,I}^2 + s_{f,Q}^2}$ is carried by an in-phase and quadrature component $s_{f,I}$ and $s_{f,Q}$, which are modulated by a carrier wave with a frequency f and have a mutual phase difference of $\pi/2$. Here these components are defined as

$$\begin{aligned} s_{f,I} &= \frac{1}{2\pi f} \frac{d}{dt} (s_Q \cos(2\pi f t)) \\ &= s_I \cos(2\pi f t) - s_Q \sin(2\pi f t) \\ s_{f,Q} &= \frac{1}{2\pi f} \frac{d}{dt} (s_Q \sin(2\pi f t)) \\ &= s_I \sin(2\pi f t) + s_Q \cos(2\pi f t), \end{aligned} \quad (5)$$

where s_I defines the in-phase component and

$$s_Q = 2\pi f \int_0^t s_I(\tau) d\tau \quad \text{with} \quad \max_t |s_Q(t)| \geq \max_t |s_I(t)|, \quad (6)$$

the quadrature component of the original unmodulated signal $s = [s_I, s_Q]$. In this study, s_Q is set to be the BH window and s_I its

time derivative according to (6). The amplitude of s is equal to that of s_f , i.e.

$$A_s = \sqrt{s_I^2 + s_Q^2} = \sqrt{s_{f,I}^2 + s_{f,Q}^2}. \quad (7)$$

Given the modulated signal components $s_{f,I}$, the original signal $s = [s_I, s_Q] = [s_I, s_Q]$ can be obtained via a demodulation process, where the phase ϕ of the carrier is sought by maximising the function

$$\begin{aligned} \tilde{s}(t, \psi) &= s_{f,I} \cos(2\pi f t + \psi - \phi) \\ &\quad + s_{f,Q} \sin(2\pi f t + \psi - \phi) \\ &= s_I \cos(\psi - \phi) + s_Q \sin(\psi - \phi), \end{aligned} \quad (8)$$

at the point $t_{\max} = \text{argmax}_t |s_Q(t)|$ with respect to the phase of the demodulation ψ , that is, $\phi = \text{argmax}_\psi |\tilde{s}(t_{\max}, \psi)|$. The in-phase and quadrature component of s can be obtained as $s_I = \tilde{s}(t, \phi - \pi/2)$ and $s_Q = \tilde{s}(t, \phi)$. Namely, the equation $s_I(t_{\max}) = 0$, which follows from the definition (6) of $s_Q(t)$, implies that ϕ maximises the second (sinus) term of (8). In other words, the amplitude A_s and $|s_Q|$ are maximised at the same time point, where $A_s = |s_Q|$ and s_I vanishes.

2.2.2. Computational considerations

An iterative time-domain solver following from the FETD discretisation necessitates effective parallel processing, as each iteration step involves large, sparse matrices following from the spatial finite element discretisation. A sufficiently efficient platform for running such an iteration is provided by a state-of-the-art high-performance computing cluster equipped with high-end graphics computing units (GPUs) (Takala et al. 2018). In this study, the FETD computations were performed using the 32 GB RAM GPUs of the Puhti supercomputer¹, CSC – IT Center for Science, Finland.

3. Numerical analysis of the wave interaction

3.1. Time–frequency analysis

To perform a time–frequency analysis, that is, a multi-band analysis over a wide frequency range, the scattered field in the time domain in response to a signal pulse s can be expressed as

$$\mathbf{E}_s(\mathbf{r}; t) = \mathcal{F}^{-1}[\mathbf{E}_s(\mathbf{r}; f) \mathcal{F}[s](f)](t), \quad (9)$$

with \mathcal{F} and \mathcal{F}^{-1} denoting the Fourier transform and its inverse. Here, we use the Ricker pulse

$$s(t) = [1 - 2\pi^2 f_c^2 t^2] \exp(-\pi^2 f_c^2 t^2), \quad (10)$$

$$\mathcal{F}[s](f) = \frac{2\pi f^2}{f_c^2} \exp\left(1 - \frac{f^2}{f_c^2}\right), \quad (11)$$

where f_c is the centre frequency of the pulse. Once the scattered field has been calculated in the frequency domain, it can be obtained in the time domain using an inverse Fourier transform.

$$\mathbf{E}_s(\mathbf{r}; t) = \int_{f_{\min}}^{f_{\max}} \mathcal{F}[s](f) \mathbf{E}_s(\mathbf{r}; f) \exp(j 2\pi f t) df, \quad (12)$$

with f_{\min} and f_{\max} denoting the minimum and maximum frequencies of the band.

¹ <https://research.csc.fi/csc-s-servers>

3.2. Born approximation

To analyse the point-wise scattering effects, we apply the BA presented in Takala et al. (2018) and Sorsa et al. (2020), which gives an estimate for the effect of a single-point permittivity perturbation on the wave propagation within the target object. A BA can be formed via Tikhonov regularised deconvolution between (1) a wave $u(t)$ originating from the transmission antenna and (2) a reciprocal of a wave $h(t)$ emitted by the receiving antenna. The Tikhonov regularised deconvolution (Sorsa et al. 2020) can be evaluated at the point of scattering as given by

$$d(t) = \mathcal{F}^{-1} \left[\frac{\mathcal{F}[h](f) \mathcal{F}[u](f)}{\mathcal{F}[s](f) + \nu} \right] (t), \quad (13)$$

where BA is denoted by d , the signal transmitted by s , and the constant regularisation parameter by ν . For a given time point, BA approximates the distribution of the perturbation effect over the target body. Thus, the time evolution of this distribution reflects the balance between the direct and higher-order scattering effects due to the body. We consider the BA of the following two different signal modalities: (i) the demodulated wave and (ii) the wave amplitude with respect to a QAM modulated two-component signal.

3.2.1. Born approximation as a differential

The BA can be interpreted as a differential of the full wave signal with respect to a perturbed permittivity distribution $\varepsilon_r = \varepsilon_r^{(bg)} + \Delta\varepsilon_r$, where $\Delta\varepsilon_r = \sum_{j=1}^N c_j \delta_j$ where δ_j is a normalised local permittivity perturbation at a given point \mathbf{r}_j , and $\varepsilon_r^{(bg)}$ denotes a homogeneous permittivity distribution (Sorsa et al. 2020; Takala et al. 2018). BA of a given signal s at \mathbf{r}_j can be expressed as a partial derivative d of the form

$$d = \left. \frac{\partial s}{\partial c_j} \right|_{c=0}. \quad (14)$$

This partial derivative d can be evaluated through the regularized deconvolution process (13). Consequently, for each measurement point, BA can be associated with an array of the form $\mathbf{B} = [d_1, d_2, \dots, d_N]$ with \mathbf{d}_j denoting BA evaluated at \mathbf{r}_j . By defining $\Delta\mathbf{c} = [\Delta c_1, \Delta c_2, \dots, \Delta c_N]^T$, the signal perturbation Δs corresponding to $\Delta\varepsilon_r$ can be approximated via the product

$$\Delta s = \mathbf{B} \Delta\mathbf{c}. \quad (15)$$

In the case of the demodulated signal $s = [s_I, s_Q]$ (Section 2.2.1), the process can be performed by substituting s in (14). Again, when BA is formed with respect to the amplitude $A_{\Delta s}$ of the difference signal Δs , it is of the form

$$\begin{aligned} d_{A_{\Delta s}} &= \frac{\partial A_{\Delta s}}{\partial c} = \left. \frac{\partial}{\partial c} \right|_{c=0} \sqrt{(\Delta s_I)^2 + (\Delta s_Q)^2} \\ &= \frac{1}{A_{\Delta s} + \xi} \left((\Delta s_I) \left. \frac{\partial s_I}{\partial c} \right|_{c=0} + (\Delta s_Q) \left. \frac{\partial s_Q}{\partial c} \right|_{c=0} \right), \end{aligned} \quad (16)$$

where ξ denotes an additional small regularisation parameter which prevents numerical instability following division by zero or a small number at points where $A_{\Delta s}$ is very small or equal to zero.

3.2.2. Backpropagation via adjoint operation

In time domain, the adjoint operation of BA, that is, the multiplication $\mathbf{B}^T \Delta s$, is obtained from the equation

$$\Delta s^T (\mathbf{B} \Delta\mathbf{c}) = \Delta\mathbf{c}^T (\mathbf{B}^T \Delta s). \quad (17)$$

It can be interpreted as a tomographic backprojection, a rough backpropagated reconstruction, whose non-zero entries correspond to those locations at which a permittivity perturbation can contribute Δs in a given time interval.

In the frequency domain, the measured scattered field and reconstructed one are compared at the receiving point in the form of a quadratic standard, without taking into account *a priori* information on the noise or on the permittivity map (Eyraud et al. 2019a). Considering Born approximation in both the direct and the adjoint problem, for each frequency f , the gradient of the backpropagated real part of the permittivity ε_r' at the iteration 0 can be written as follows:

$$g^{(0)}(\mathbf{r}; f) = -k_0^2(f) \text{Re}[\mathbf{G}(\mathbf{r}, \mathbf{r}_s; f) \mathbf{E}_i(\mathbf{r}; f) (E_s^m(\mathbf{r}_r; f) - E_s^{(0)}(\mathbf{r}_r; f))^*], \quad (18)$$

where \mathbf{G} is the dyadic Green function in the free space, \mathbf{E}_i is the incident field generated by the antenna source at position \mathbf{r}_s , considering the wave propagate in vacuum ($\varepsilon_r = 1$), and E_s^m and $E_s^{(0)}$ are respectively the scattered field measured by the receiver and the scattered field calculated via the Born approximation. Finally, \mathbf{r}_r is the receiver antenna position. In order to take into account the information for all frequencies, these gradients are added together as given by

$$\mathcal{G}^{(0)}(\mathbf{r}) = \frac{1}{N_f} \sum_{f=1}^{N_f} g^{(0)}(\mathbf{r}; f). \quad (19)$$

4. Numerical experiments with the asteroid analogue

We perform numerical experiments on the wave interaction using both numerical and laboratory measurement data obtained for the asteroid analogue model of Eyraud et al. (2020) (Fig. 1) which is based on the current knowledge of asteroid interiors (Asphaug et al. 2002; Jutzi & Benz 2017; Carry 2012) and has the exterior shape model of 25143 Itokawa (Fujiwara et al. 2006; Hayabusa Project Science Data Archive 2007). We consider the setup of the quasi-monostatic laboratory experiment performed using this analogue (Eyraud et al. 2020). The system parameters (Table 1) have been scaled to laboratory, real, and two hypothetical sizes, in which the signal centre frequency applied corresponds to 10 MHz and 20 MHz. We consider two interior structures: (1) Homogeneous Model (HM) and (2) Detailed Model (DM). Of these, HM constitutes a numerical reference model and DM the actual analogue. The relative permittivity in HM has a constant value $\varepsilon_r = 3.4 + j0.04$ whereas in DM, it is piecewise constant with the values $\varepsilon_r = 1.0$, $\varepsilon_r = 2.56 + j0.02$, and $\varepsilon_r = 3.4 + j0.04$ inside an internal void, in a mantle layer and elsewhere within the asteroid body, respectively. These values are based on the dielectric materials found in asteroids (Herique et al. 2002) as well as on our results obtained for the 3D-printed analogue object (Eyraud et al. 2020). The 3D shape and the internal permittivity structure of DM are illustrated in Fig. 1 for three directions and 3D views.

Figure 1 also shows the single-point quasi-monostatic measurement configuration, the same as in Eyraud et al. (2020),

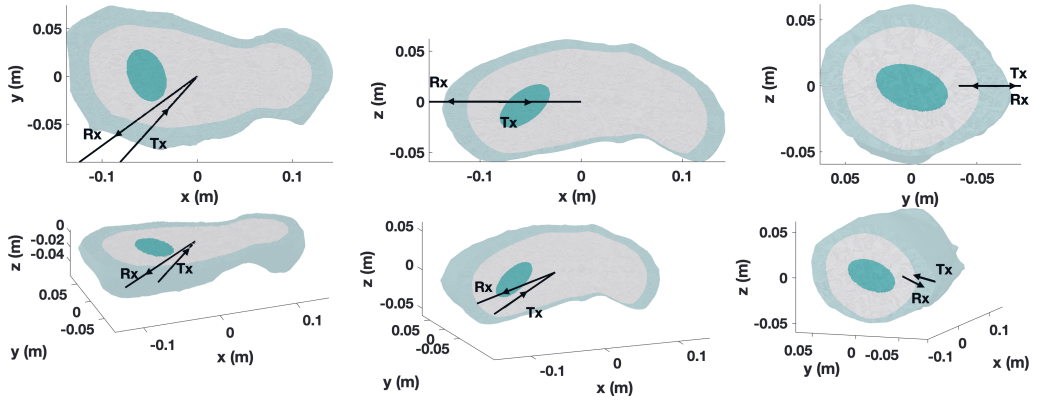


Fig. 1. Cut-views of the 3D numerical model with the exterior shape corresponding to that of the asteroid 25143 Itokawa (Fujiwara et al. 2006). The signal paths between the transmitter (Tx) and the receiver (Rx) are also shown in various cut-views through the model. The real part of the exact relative permittivity distribution for the DM is piecewise constant with the values $\epsilon_r = 1$, $\epsilon_r = 2.56 + j0.02$, and $\epsilon_r = 3.4 + j0.04$ inside the ellipsoidal internal void, in the mantle layer, and elsewhere within the asteroid body, respectively.

where the signal transmitter and receiver antennae are separated by 12° and placed at a 1.85 m distance from the target. The scattered field simulated via the frequency and time domain method has successfully confronted with lab measurements (Eyraud et al. 2020), which, along with the earlier numerical simulation studies, such as for example those by Sava & Asphaug (2018a); Sorsa et al. (2019), suggests that the internal structure of the analogue can be observed. Here, we use numerically simulated data to investigate (a) the wavefield propagation inside the DM analogue model, (b) the signal propagation effects in the time–frequency domain, (c) BA, and (d) backpropagation. The backpropagated estimates for the permittivity structure are evaluated both numerically and with the actual quasi-monostatic measurement data obtained in Eyraud et al. (2020).

5. Results

5.1. Electric field inside the analogue

Figure 2 depicts a simulated electric field \mathbf{E} propagation inside the DM analogue at two frequencies 2 GHz and 10 GHz. This total field differs significantly from the incident field and the influence of multiple scattering is clearly visible at 10 GHz, while it is present already at 2 GHz. This is due to the size of the target and its contrast, and suggests the inadequacy of linear propagation (single scattering, i.e., scattering under Born approximation) models as they omit the effects of multiple scattering or multiple coupling including multiple reflections and refractions, which are also referred to as multi-path effects determined by the second term on the right-hand side of equation (3). At 2 GHz, the main dimension of the analogue is equal to $2.5 \lambda_m$ with λ_m denoting the wavelength in the medium. The amplitude of the field is almost constant within the analogue and that is why the outline of the mantle and the void can be clearly distinguished. At 10 GHz, the target is larger in terms of the wavelength, that is, the main dimension of the analogue is equal to $12.6 \lambda_m$, and the field inside includes fine ripples which correspond to multiple paths and scattering effects due to the high contrast between the permittivity of the analogue and that of the vacuum.

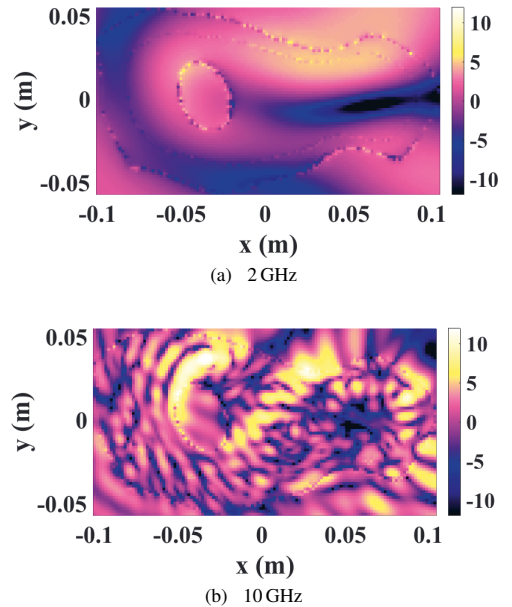


Fig. 2. Magnitude (in dB) of the calculated field inside the DM analogue.

5.2. Time–frequency analysis

Figure 3 includes the time–frequency analysis of the scattered field corresponding to DM and HM. The temporal zones corresponding to travel-times scattering from the different parts of the analogues are distinguished (Table 2) according to Eyraud et al. (2020), that is, Mantle I (the first mantle reflection), Void (scattering by the void), Mantle II (the reflection on the opposite side of the asteroid with respect to the first one), Higher-order (multiple scattering), and second-order reflection zones. The travel times can be seen as annotations for linking the time axis to the

Table 1. Signal parameters used in simulating the electric field propagation. The dimensions are given in terms of wavelengths, with λ_m as the wavelength in a medium of permittivity $\epsilon_r = 3.4$.

Scale	Diameter Distance		Frequency Domain		Time Domain		
			Range	Relative size	Centre frequency	Relative size	Bandwidth
Itokawa	535 m	4.83 km	0.766–6.90 MHz	2.53–22.8 λ_m	4.48 MHz	14.8 λ_m	2.00 MHz
Analogue object	20.5 cm	1.85 m	2.00–18.0 GHz		11.7 GHz		5.20 GHz
Centre freq. 10 MHz	124 m	1.12 km	2.38–21.5 MHz		10 MHz		4.44 MHz
Centre freq. 20 MHz	62 m	0.560 km	4.76–42.2 MHz		20 MHz		8.88 MHz

Table 2. We distinguish the following scattering zones and time points t_1 – t_5 for evaluating the BA.

ID	Zone	Range (ns)	Time point (ns)
t_1	Mantle I	11.50–12.12	12.10
t_2	Void	12.12–12.71	12.50
t_3	Mantle II	12.71–13.50	12.93
t_4	Higher-order scattering	13.50–14.00	13.50
t_5	2nd order reflections	14.00–	14.05

space and they provide guidance as to which peaks in the data correspond to which space in the object. These are based on our previous careful analysis (Eyraud et al. 2020) and are included here to help the reader to understand the time–space correspondence. The scattering signatures of the two analogues are relatively similar. The major signatures are in the frequency band 2.6–9.1 GHz. A weaker signal is visible also in the frequency 11.1–12.4 GHz. For the other frequencies, the signature is comparably weak, ≤ -20 dB with respect to the maximal amplitude of the scattered signal.

Figure 3 also compares the cases of 32 and 8 frequency bands of width ≈ 0.4 GHz and ≈ 1.6 GHz, respectively, of which the latter allows a better temporal resolution. Based on the results, it is obvious that while the ≈ 0.4 GHz bandwidth essentially corresponds to a single scattered wavefront (between 12 ns and 13.7 ns) caused by the asteroid body as a whole, the greater bandwidth ≈ 1.6 GHz enables us to distinguish between the wavefronts originating from the Mantle I and Mantle II zones, that is, from the two opposite sides of the analogue model, and can therefore be considered as a minimal bandwidth for detecting interior details in the time domain.

Notably, the scattered signal corresponding to the DM has a greater intensity not only in the direct scattering zone but also in the higher-order zone (between 2 GHz and 9 GHz) as compared to the HM analogue, which is visible in the difference between the two signatures. In summary, this analysis shows not only that it is possible to detect the interior structures of asteroids by considering direct reflections, but also that these structures can be deduced by analysing the higher-order zone when the temporal resolution is sufficient to separate this zone from the others which seems the case at ≥ 1.6 GHz bandwidth.

5.3. Born approximation

The spatial distribution of the BA was analysed for the time points t_1 – t_5 described in Table 2. The spatial plots are shown in Fig. 4 for the demodulated BA (Eq. 15) with three different regularisation parameter values, $\nu = 2E-2$ (optimised via bracketing), $\nu = 2E-4$ (underregularised), and $\nu = 2$ (overregularised), and for the amplitude-based BA (Eq. 16) with just the first of these, $\nu = 2E-2$. In relation to the maximum absolute value of the denominator in equation (13), these values are $1E-3$, $1E-5$, and $1E-1$, respectively.

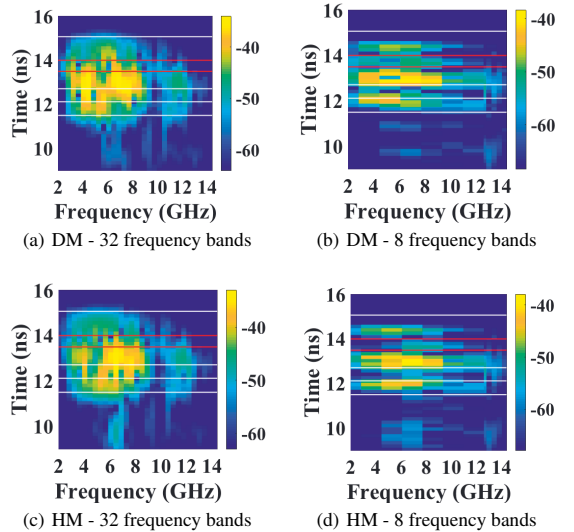


Fig. 3. Time–frequency analysis for the two analogues with a variation of the frequency bands. The horizontal lines correspond to the temporal zones indicated by Table 2.

Table 3. Volumetric compartments of different analogue objects and their boundaries illustrated in Figs. 9 and 10. The distances correspond to the $\|\vec{OM}\|$ with 0 centre of the coordinate system and M the point belonging to the considered interface, \vec{OM} being collinear with the wave vector.

Reflections	$\ \vec{OM}\ $	$\ \vec{OM}\ $ with Born compensation
air/mantle	-0.069 m	-0.069 m
mantle/interior	-0.051 m	-0.040 m
interior/void	-0.038 m	-0.016 m
void/interior	-0.003 m	0.048 m
interior/mantle	0.034 m	0.087 m
mantle/air	0.043 m	0.102 m

The full temporal wave was analysed for the five different locations \mathbf{p}_1 – \mathbf{p}_5 as indicated by circled dots in the top row of Fig. 4. These locations correspond to the spatial maximiser of the BA for the time points t_1 – t_5 , respectively. In Fig. 5, the first and second rows from the top show the full demodulated wave and its amplitude for the locations \mathbf{p}_1 – \mathbf{p}_5 , respectively. The third to sixth rows illustrate the complete normalised BA at \mathbf{p}_1 – \mathbf{p}_5 , revealing the effect of the parameter choice on the regularised deconvolution process (Takala et al. 2018; Sorsa et al. 2020). Overall, the most regular outcome can be observed to result with the value $\nu = 2E-2$ (third row). Oscillation artifacts were found to occur when the regularisation parameter is either larger or smaller than

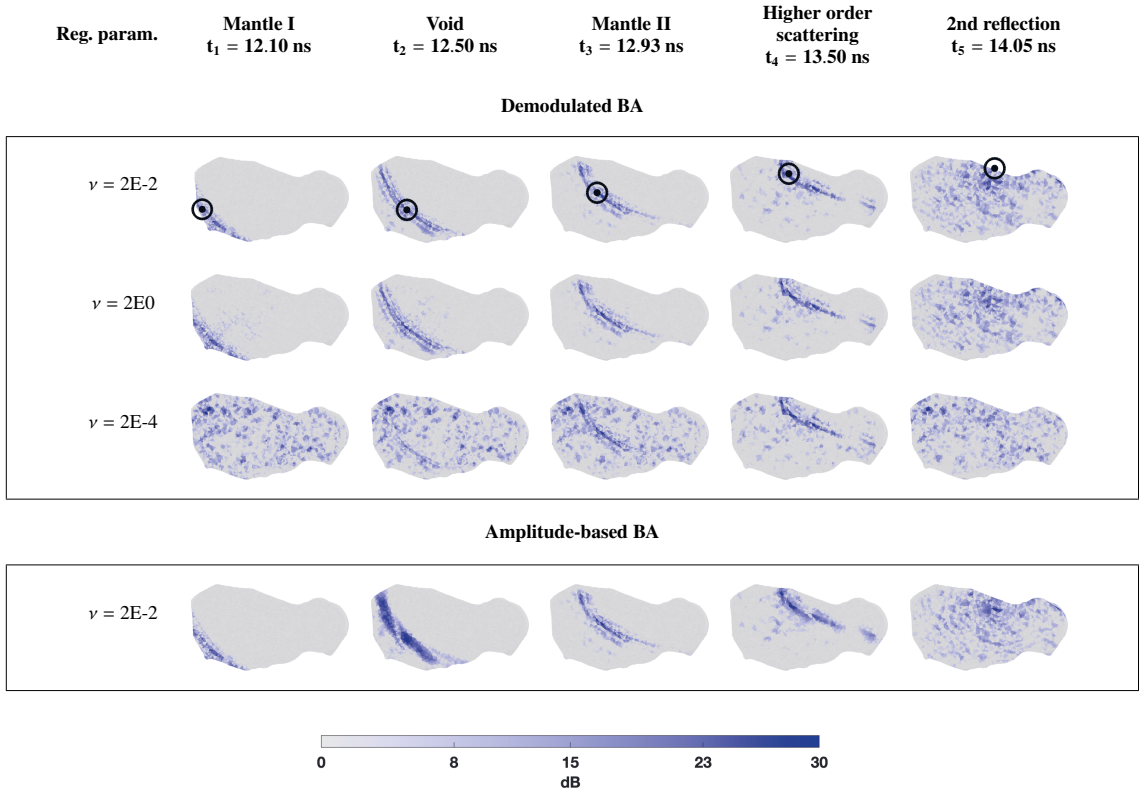


Fig. 4. The effect of the deconvolution regularisation parameter on the volume-normalised BA of the QAM signal "Demodulated BA", d in equation (15), and the BA of the amplitude-based signal "Amplitude-based BA", $d_{A_{AS}}$ in equation (16), at five different time points t_1 – t_5 showing the propagation of the wave through the object body. The circled dot in the top row figures indicates the maximum absolute value of the wavefield at the time point and these are the maximiser points for which time-domain data curves are shown in Fig. 5. The close-to-optimal regularisation parameter $\nu = 2E-2$ is shown for the both BAs. The overregularised (reg. param. $\nu = 2E0$) and the underregularised (reg. param. $\nu = 2E-4$) are shown for the demodulated BA.

this value; their frequency increases when the parameter is decreased. In the case of overregularisation $\nu = 2$ (fourth row), the deconvoluted signal has pre-ringing artifacts. That is, the fluctuations start before the actual pulse response occurs. The underregularised outcome obtained with $\nu = 2E-4$ (fifth row) is corrupted by high-frequency noise. The sixth row of Fig. 5 shows the optimal regularisation parameter for the amplitude-based BA.

5.4. Backpropagation

5.4.1. In time domain

From the scattered field obtained in a quasi-monostatic configuration at a single point, structural imaging maps were obtained by backpropagation using two algorithms, one in the time domain and the other in the frequency domain. The time domain fields corresponding to the simulation and measurement are visualised in Fig. 6. Backpropagation was carried out first from calculations and then from experimental data measured in the anechoic chamber of the Centre Commun de Ressources en Microondes (CCRM) in Marseille Eyraud et al. (2020).

Figure 7 shows the backpropagated reconstructions obtained via the demodulation and amplitude-based BA and visualised for an increasing amount of simulated time-domain data. By visual

comparison to the exact DM structure, which is shown in the background of each reconstruction, the superior outcome is obtained, when Mantle I to Mantle II, and Mantle I to Higher order scattering zones are included in the data. These reconstructions, shown framed in the middle of the figure, account for the best localisation of the void area and suggest that the mantle is also detectable in Mantle I zone, that is, on the side corresponding to the signal transmission and measurement.

The laboratory measurement data of Eyraud et al. (2020) obtained with the 3D-printed DM was applied to calculate back-projection reconstructions shown in Fig. 8. Also, in this case, the superior reconstructions are obtained when the zones from Mantle I to Mantle II and up to the Higher order scattering zone are included in the data (centre frame). Although generally similar in comparison to the simulated data in Fig. 7, the measured data yield more focused reconstruction around the void area especially in the cut-view along the z-axis.

Common to the reconstructions shown in Figs. 7 and 8 is a slight deviation of the observed void location away from the receiver which might be due to the absence of the mantle in HM which is applied as the point of linearisation for the BA. Moreover, comparison between the results obtained with the demodulation and amplitude-based BA shows that the reconstruction

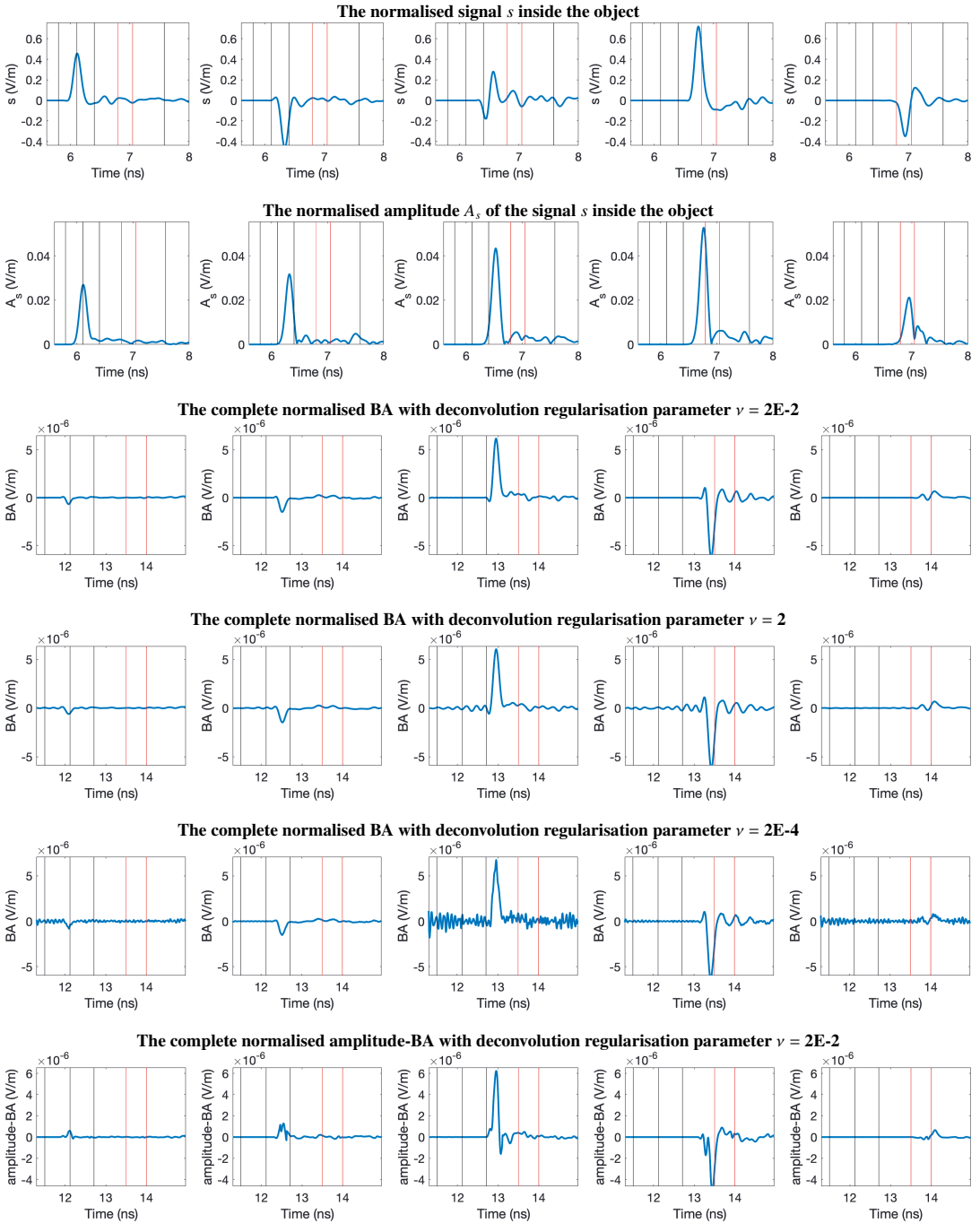


Fig. 5. Numerical data at the five spatial points \mathbf{p}_1 – \mathbf{p}_5 , indicated by circled dots in Fig. 4, showing the wave propagation in the time domain. The vertical lines show the zone interfaces in Table (2) with the red lines outlining the higher order zone. The two top rows show the BA and its amplitude at the fixed point along the time domain as it propagates through the object. The row ordering follows that of Fig. 4 and clearly illustrates the effect of the Tikhonov regularisation parameter ν on the deconvolution. The data in each plot have been normalised spatially with respect to the transmitter distance.

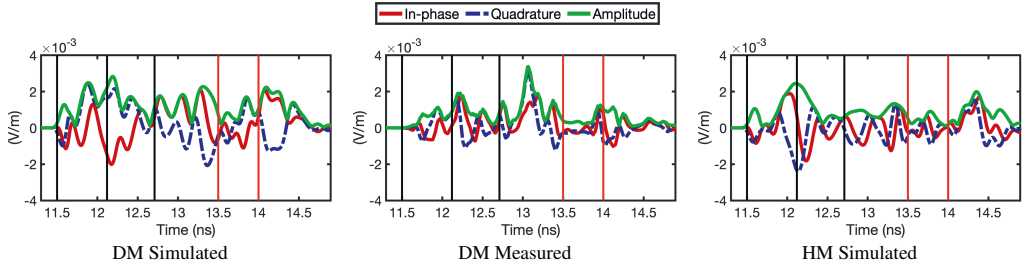


Fig. 6. Time domain data obtained via QAM. **Two left columns:** Demodulated in-phase (solid red), quadrature component (dashed blue), and amplitude (solid light green) obtained for the DM analogue via simulation and measurement, respectively. **Right column:** Simulated data obtained for HM analogue. The vertical lines illustrate the temporal zones of Table 2. The red vertical lines indicate the higher order scattering zone.

of the void appears more distinct in the former case, while the mantle appears more pronounced in the latter.

5.4.2. In frequency domain

The maps reconstructed with backpropagation using the simulated and measured field data are plotted in Figs. 9 and 10, respectively. These maps correspond to the sum of the gradients for the different frequencies at the first iteration according to (19). For the results from calculations the frequency band 2–10 GHz is used and for the results from measurements, the frequency band 4–18 GHz is used. In the measurements, the low frequencies (2–4 GHz) are eliminated because these measuring points are more noisy because the antenna pattern is not very directional at these frequencies.

In these figures, the positions of the different boundaries (air/mantle, mantle/interior, interior/void, void/interior, interior/mantle, mantle/air) are plotted with different colours. For interfaces air/mantle, mantle/interior, interior/mantle, and mantle/air, the coloured area correspond to the calculated position with $\pm 15\%$ accuracy considering that Born approximation is used (including a distance compensation). The void area is the size of the void in the direction orthogonal to the wave propagation with Born distance compensation. The corresponding values are given in Table 3.

Firstly, it can be noted that the reconstructed areas are, as expected, orthogonal to the direction of wave propagation. Looking to the maps reconstructed from the calculations (Fig. 9), the two boundaries between the air and the target are visible for both DM and HM objects. For the DM analogue, an additional signature is reconstructed inside the target which corresponds to the void. We note that the two air/object and object/air interfaces are in the correct areas for both analogues and that the interface inside the object (for the DM analogue) is appropriately within the void area. The mantle/interior and interior/mantle interfaces (for DM analogue) are not visible.

Considering the maps reconstructed from the measurements (Fig. 10), it is still possible to see the two air/target and target/air boundaries for the HM analogue. We note that the target/air boundary is somewhat shifted. For the DM analogue, the air/target boundary is visible (but slightly shifted), and the target/air boundary is missing. The void signature (shifted) is also visible in the reconstruction.

6. Discussion

Here we analyse full microwave propagation and backpropagation with a structurally complex asteroid analogue model as a

target. This analogue was first 3D printed as a plastic wire-frame structure applying the recently introduced permittivity control method of Saleh et al. (2020) after which quasi-monostatic laboratory experiments were performed (Eyraud et al. 2020). The thorough analysis performed for a single measurement point, which is the worst-case scenario for a space radar, constitutes an important feasibility study for observing the interior structure of the analogue based on the experimental measurement data of Eyraud et al. (2020).

Our results obtained in both the frequency and time domains show that the internal void and mantle compartments of the analogue can be reconstructed by backpropagating the full wave field. We find that the properties of the BA applied in the backpropagation process affect the reconstruction quality. In particular, the temporal coverage of the data used in computing the BA is found to have a significant effect on the performance. The most detailed description of the interior structure of the asteroid is obtained when Mantle I, Void, Mantle II, and Higher-order scattering zone are covered by the data, and excluding the second-order reflection zone is found to be necessary. An optimised regularisation parameter was applied in calculating the BA to ensure that the results are of the best quality possible.

Our results demonstrate the feasibility of revealing the details of the interior an asteroid analogue with a realistic shape and complex structure via full wave-field modelling. Our findings support the previous observation that a peak signal-to-noise ratio of 10 dB between the measured and simulated wave field might be sufficient for observing the interior structures, as suggested by Sorsa et al. (2019) who rely on numerical simulations in their study. In the present measurement dataset, this limit is achieved for the Mantle I, Void, and Mantle II zones described by Eyraud et al. (2020). Moreover, parallel to the previous findings of Sorsa et al. (2020); Eyraud et al. (2020), we find higher order scattering effects to be significant with respect to the quality of the BA and therefore the reconstruction.

While the present implementation of BA in the time domain takes into account both direct and indirect (higher order) scattering effects, its accuracy decreases as time elapses. Modelling the second-order reflections corresponding to long (double side-to-side) signal propagation paths was found to lead to a noisy outcome and to corrupt the backpropagated reconstructions, and therefore we found it necessary to limit the temporal range of the data. The present frequency domain approach to backpropagation shows that the interior structures can be distinguished based on the full data set without any information about the surface shape or mean permittivity inside the asteroid. In this case, the wavefield considered in BA is that of vacuum.

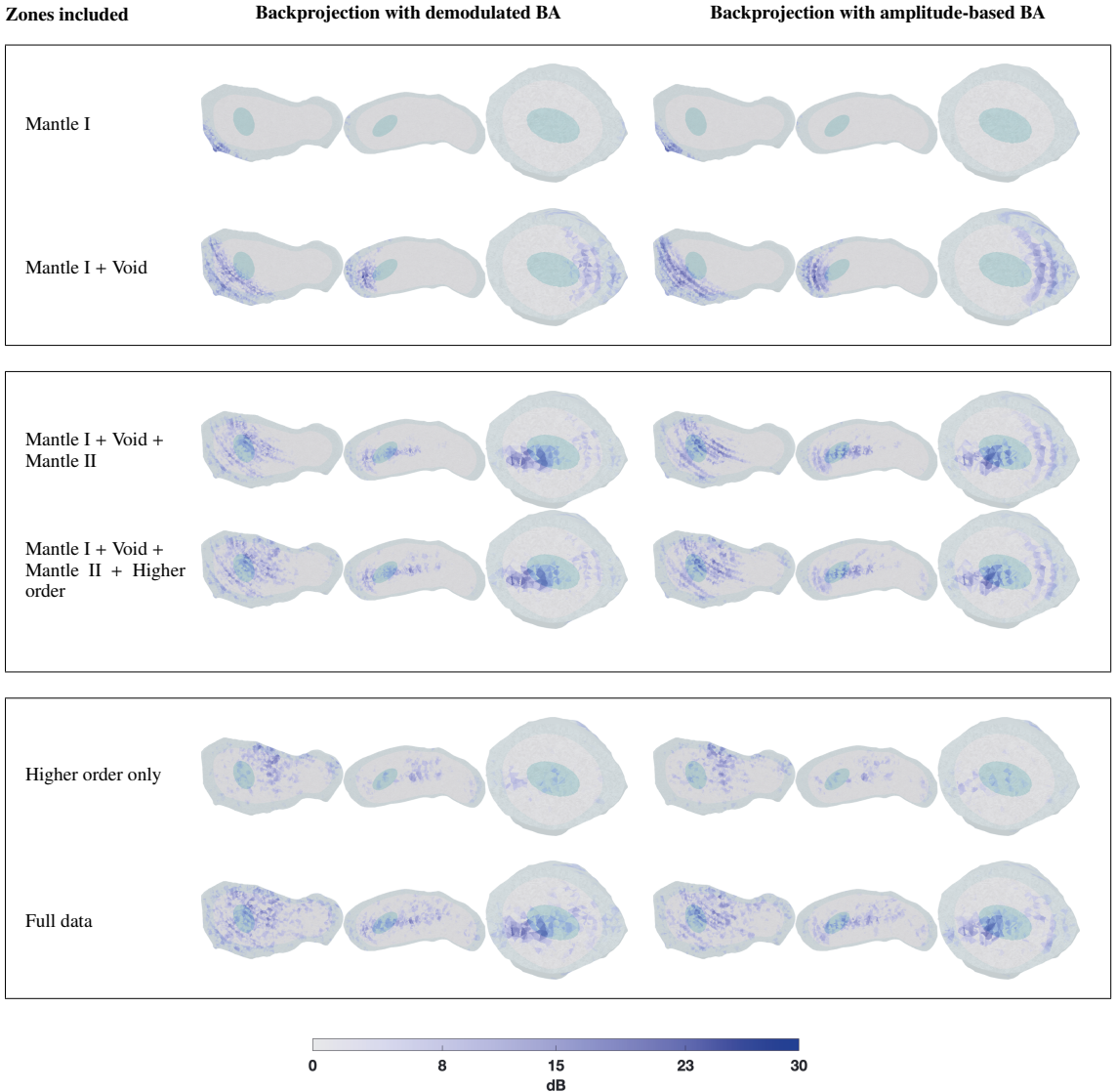


Fig. 7. Tomographic backprojection (adjoint operation of BA) obtained with the simulated data with the signal path shown in Fig. 1. Reconstructions are shown in blue for both the demodulated BA (**left**) and the amplitude-based BA (**right**) and for the temporal ranges of data as specified by zones in Table 2. The exact DM model structure with the surface layer and the void is shown in the reconstruction background.

The backpropagation approaches of this study are relatively simple and may therefore be expected to lead to slight mispositioning of the interior structures: firstly, in the frequency domain, no permittivity approximation for the interior part of the asteroid model is made (so it is vacuum), and in the time domain, the permittivity estimate relies on an *a priori* measurement performed for a test sphere (Eyraud et al. 2020), but is not optimised using the dataset obtained for the analogue. Secondly, the first-order BA is applied on the direct and adjoint problem, meaning that the multiple scattering or coupling effects are omitted. Thus, it is immediately clear that the reconstruction quality might be improved by applying more advanced backpropagation techniques

which we regard as a challenging future work topic. For instance, the higher order BA developed in Sorsa et al. (2020) or the wave-field tomography proposed in Sava & Asphaug (2018b), both in the time domain, as well as full-wave inversion developed in the frequency domain (Eyraud et al. 2012, 2019b), constitute potential approaches to take into account the high-order scattering effects. Namely, the slightly biased void location in the reconstructions obtained in this study might be corrected if the non-linear signal interaction effects between the void and mantle compartments inside the analogue are taken into account which is the case in the higher order BA or full-wave inversion. Another approach is to consider a transformed or complementary data

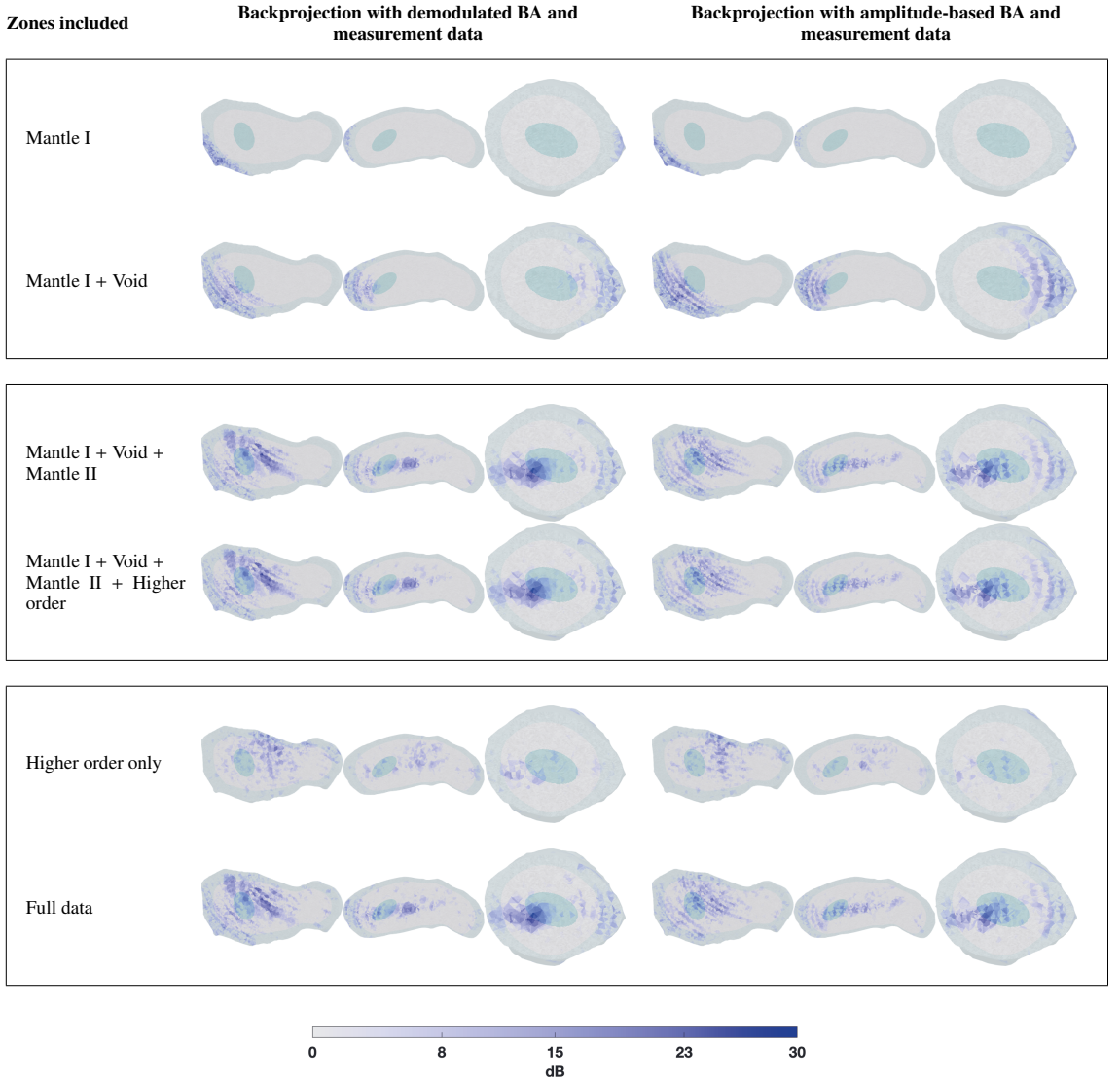


Fig. 8. Tomographic backprojection (adjoint operation of BA) done with microwave radar measurement data. Reconstructions are shown in blue for both the demodulated BA (**left**) and the amplitude-based BA (**right**) and for the temporal ranges of data as specified by zones in Table 2. The exact DM model structure with the surface layer and the void is overlaid in the reconstruction background.

modality, such as for instance the travel-time, which has been applied in CONSERT (Kofman et al. 2007, 2015), for example. The differences revealed by the present modalities, that is, the demodulated signal and its amplitude, support this assumption. Advanced travel-time inversion schemes have been developed, especially for seismic inversion (Luo et al. 2016; Tarantola & Santosa 1984; Tarantola 2005), in which the data are likely to be scarce —akin to space missions—, but also for electromagnetic investigation of a small Solar System body (Sava & Asphaug 2018a).

As we show that the interior structure of an asteroid analogue can be observed with a minimal number of full-wave measurements, despite its complex realistic shape, the relevance of

the present results is significant with respect to future missions, such as for example HERA (Michel et al. 2018), as well as to the many proposed missions and mission concepts involving the use of radar data to probe the largely unknown interior structure of the small Solar System bodies (Asphaug et al. 2002; Barucci et al. 2005; Asphaug et al. 2008; Bambach et al. 2018; Snodgrass et al. 2018). With respect to mission design, the important aspects in this study are the frequency range and bandwidth of the signals modelled. The analogue scale applied here is partially limited by the equipment laboratory radar experiment. We consider the most relevant scales with respect to mission design to be those corresponding to 10 MHz (Binzel & Kofman 2005) and 20 MHz (Kofman 2012) centre frequencies.

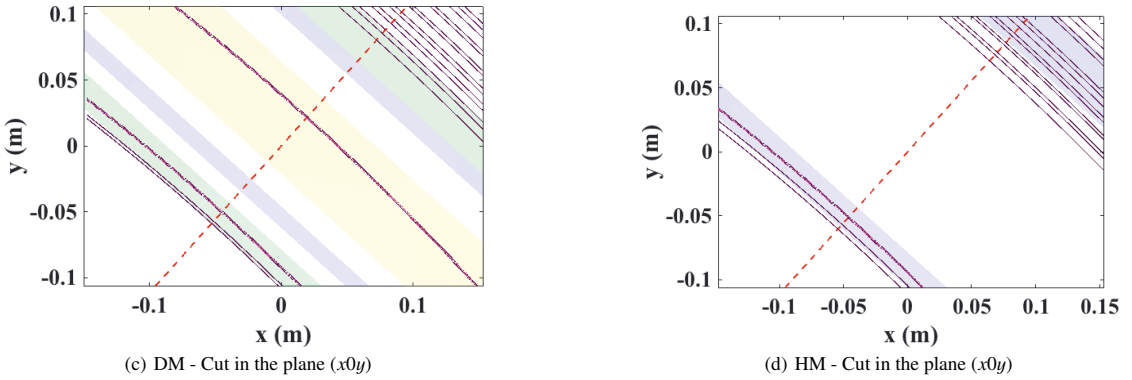
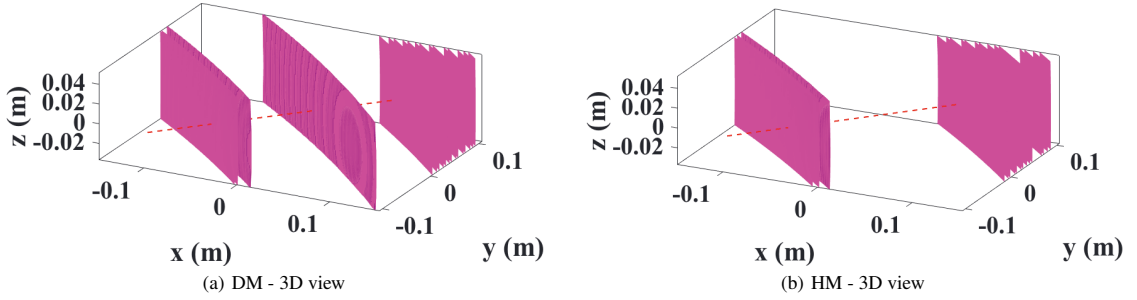


Fig. 9. Reconstructions obtained by backpropagation in the frequency domain using the calculated fields with a single transmitter and a single receiver and the frequency band between 2 GHz and 10 GHz. The direction of wave propagation is plotted with a dashed line. The coloured areas corresponding to the different parts of the analogue, taking into account the Born compensation and their boundaries, are summarised in Table 3: the green one refers to the boundaries air/mantle and mantle/air, the blue one refers to the reflections mantle/interior and interior/mantle, and the yellow one refers to the reflections interior/void and void/interior.

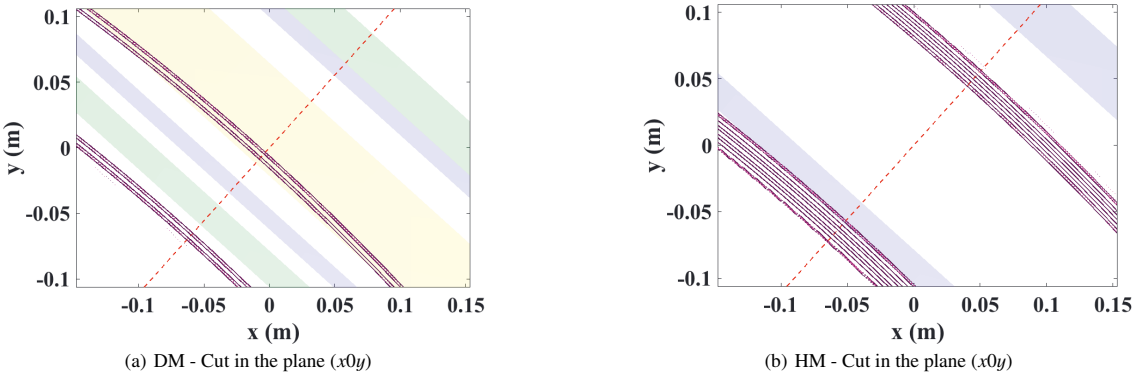


Fig. 10. Reconstructions obtained by backpropagation in the frequency domain using the measured fields with a single transmitter and a single receiver and the frequency band between 4 GHz and 18 GHz. The direction of wave propagation of the wave is plotted as a dashed line. The coloured areas are as in Fig. 9.

7. Conclusion

We demonstrate the feasibility of reconstructing the details inside a structurally complex asteroid analogue model with a realistic shape and internal permittivity structure based on the cur-

rent knowledge of asteroid interiors from sparse measurements, such as those from quasi-monostatic full microwave data measured at a single point. The results and the applied signal configuration and parameters are significant in the design of future

space missions aiming to reconstruct the interior structure of small Solar System bodies. The quality of the backpropagation results obtained depend on the applied modelling strategy, signal modality, data coverage, and inversion procedure, the latter motivating future inversion method development.

Important goals for the future include a full tomographic imaging experiment including wider coverage of measurements; for example, multi-monostatic or bistatic. Analogue development towards more arbitrary permittivity structures will be examined to further strengthen the mission-relevance of the results. Advanced reconstruction strategies will also be investigated, including for example the effect of data modality, taking into account the non-linearity of the inversion procedure, and the introduction of *a priori* information on the target.

Acknowledgement

The authors acknowledge Jean-Michel Geffrin, who performed the measurements and provided the data, and the opportunity provided by the Centre Commun de Ressources en Microondes (CCRM) to use its fully equipped anechoic chamber. We acknowledge the Mesocentre of Aix Marseille University for its support for these calculations. L-IS was supported by a Young Researcher's Grant from Emil Aaltonen Foundation. L-IS, and SP were supported by the Centre of Excellence in Inverse Modelling and Imaging (Academy of Finland 2018-2025, project number 312341) and the Academy of Finland project number 336151. L-IS and SP acknowledge CSC – IT Center for Science Ltd., for providing computing services on the Puhti supercomputer.

References

- Asphaug, E., Ryan, E. V., & Zuber, M. T. 2002, *Asteroids III*, 1, 463
- Asphaug, E., Scheeres, D., & Safaeinili, A. 2008, 37th COSPAR Scientific Assembly, Held 13-20 July 2008, in Montréal, Canada, 37, 139
- Bambach, P., Deller, J., Vilenius, E., et al. 2018, *Advances in Space Research*, 62, 3357
- Barrowes, B. E., Teixeira, L. F., & Kong, J. A. 2001, *Microwave and Optical Technology Letters*, 31, 28
- Barucci, M. A., D'Arrigo, P., Ball, P., et al. 2005, *Highlights of astronomy*, 13, 738
- Binzel, R. P. & Kofman, W. 2005, *Comptes Rendus Physique*, 6, 321
- Blair, D. M., Chappaz, L., Sood, R., et al. 2017, *Icarus*, 282, 47
- Cary, B. 2012, *Planetary and Space Science*, 73, 98
- Eyraud, C., Geffrin, J.-M., Litman, A., & Spinelli, J.-P. 2012, *Radio Science*, 47
- Eyraud, C., Litman, A., Hérique, A., & Kofman, W. 2019a, *Inverse Problems*, 26
- Eyraud, C., Saleh, H., & Geffrin, J.-M. 2019b, *JOSA A*, 36, 234
- Eyraud, C., Sorsa, L.-I., Geffrin, J.-M., et al. 2020, *Astronomy & Astrophysics*, 643, A68
- Fujiwara, A., Kawaguchi, J., Yeomans, D., et al. 2006, *Science*, 312, 1330
- Grima, C., Kofman, W., Mougnot, J., et al. 2009, *Geophysical Research Letters*, 36
- Harrington, R. 1987, *J. Electromagnetic Waves Appl.*, 1
- Haruyama, J., Kaku, T., Shinoda, R., et al. 2017, in *Lunar and Planetary Science Conference*, Vol. 48
- Hayabusa Project Science Data Archive. 2007, Itokawa shape model, <https://darts.isas.jaxa.jp/planet/project/hayabusa/shape.pl>, accessed 4 November, 2019
- Hérique, A., Agnus, B., Asphaug, E., et al. 2018, *Advances in Space Research*, 62, 2141
- Hérique, A., Gilchrist, J., Kofman, W., & Klinger, J. 2002, *Planetary and Space Science*, 50, 857
- Hérique, A., Plettemeier, D., Kofman, W., et al. 2019, in *EPSC Abstracts*, Vol. 13, EPSC-DPS Joint Meeting 2019, Geneva, Switzerland
- Jutzi, M. & Benz, W. 2017, *Astronomy & Astrophysics*, 597, A62
- Kaku, T., Haruyama, J., Miyake, W., et al. 2017, *Geophysical Research Letters*, 44, 10
- Kofman, W. 2012, in 2012 19th International Conference on Microwaves, Radar Wireless Communications, Vol. 2, 409–412
- Kofman, W., Hérique, A., Barbin, Y., et al. 2015, *Science*, 349, aab0639
- Kofman, W., Hérique, A., Goutail, J.-P., et al. 2007, *Space Science Reviews*, 128
- Luo, Y., Ma, Y., Wu, Y., Liu, H., & Cao, L. 2016, *Geophysics*, 81, R261
- M. Bertero, P. & Boccacci. 1998, *Introduction to Inverse Problems in Imaging (IoP)*
- Merchiers, O., Eyraud, C., Geffrin, J.-M., et al. 2010, *Optics Express*, 18, 2056
- Michel, P., Kueppers, M., Sierks, H., et al. 2018, *Advances in Space Research*, 62, 2261
- Picardi, G., Plaut, J. J., Biccari, D., et al. 2005, *science*, 310, 1925
- Saleh, H., Tortel, H., Leroux, C., et al. 2020, *IEEE Trans. Ant. and Prop.*, in Press
- Sava, P. & Asphaug, E. 2018a, *Advances in Space Research*, 62, 1146
- Sava, P. & Asphaug, E. 2018b, *Advances in Space Research*, 61, 2198
- Snodgrass, C., Jones, G., Böhnhardt, H., et al. 2018, *Advances in Space Research*, 62, 1947
- Sorsa, L., Takala, M., Eyraud, C., & Pursiainen, S. 2020, *IEEE Trans. on computational imaging*, 6, pp 579
- Sorsa, L.-I., Takala, M., Bambach, P., et al. 2019, *The Astrophysical Journal*, 872(1):44
- Takala, M., Bambach, P., Deller, J., et al. 2018, *IEEE Transactions on Aerospace and Electronic Systems*
- Tarantola, A. 2005, *Inverse problem theory and methods for model parameter estimation (SIAM)*
- Tarantola, A. & Santosa, F. 1984, *Inverse problems of acoustic and elastic waves*, 104
- van der Vorst, H. A. 2003, *Cambridge University Press*
- Vernazza, P., Jorda, L., Ševeček, P., et al. 2020, *Nature Astronomy*, 4, 136

